Femtosecond Sum-Frequency Spectroscopy of Metal-Adsorbate Systems

---

Jonathan Philip Robert Symonds

Darwin College

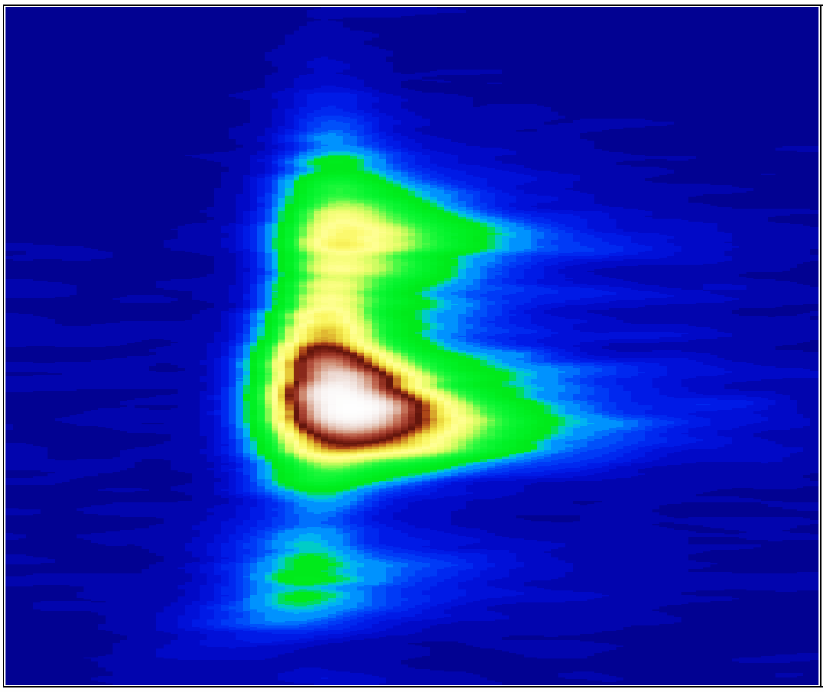

Submitted for the degree of Doctor of Philosophy

Department of Chemistry

University of Cambridge

July 2003

Preface

This thesis is submitted in conformity with the requirements of the University of Cambridge for the degree of Doctor of Philosophy. The work described in this thesis is the original work of the author and includes nothing which is the outcome of work done in collaboration, unless otherwise stated. No part of this thesis has been, or is being, submitted at this or any other university for a degree or equivalent qualification. This manuscript does not exceed 60,000 words in length, as specified by the Degree Committee for Physics and Chemistry.

Jonathan Philip Robert Symonds, July 2003

The image on the front is a temporally and spectrally resolved free induction decay representing vibrating carbon monoxide molecules relaxing on a ruthenium surface. See page 144 for more details.

To my dear Parents, John and Sheila

Acknowledgements

I thank my supervisor, Professor Sir David King for the opportunity to work in this field, for making his enthusiasm about the subject so infectious and for his ability to quickly develop self-consistent physical scenarios from very abstract data, thus helping me to draw the conclusions contained herein. I am indebted to my main co-worker and the PDRA on the femtosecond experiment, Dr. Heike Arnolds. Her dedication to this project, experimental skill and seemingly boundless energy are instrumental to its success. I thank her too for her detailed proof reading of this thesis and on a personal level for her good company both in the laboratory and on conferences. More recently, I thank the new PhD student on the project, Vanessa Zhang for her contribution in the laboratory whilst she has learnt about the system. I also extend my gratitude to the rest of my research group for all their useful discussions, particularly in relation to the surface science aspects of this work; it has been a privilege working with you. I am also thankful for the strong friendships built up in this group during my time here, and I will deeply miss seeing you all every day. I thank too the group's laboratory manager Liz Hawkins, and Professor King's secretary Henneli Greyling for their administrative help.

I thank Dr. Gareth Roberts for introducing me to the world of FemtoChemistry, both whilst I was an undergraduate and later as my co-supervisor during the first year of my PhD. I also thank Rodrigo Lopez-Martens and Timothy Schmidt from his group for their very hands-on introduction to the laser system. I am grateful to Dr. Paul Davies and his group for the many discussions on sum frequency generation. We have been privileged to have had three visiting academics in the laser lab over successive summers during the time of my PhD: Professor Robert J. Levis from the chemistry department at Wayne State University, USA; Professor Katsuyuki Fukutani from the Institute of Industrial Science, University of Tokyo, Japan and Dr. Frederic Thibault-Starzyk from the Laboratoire Catalyse & Spectrochimie, Caen, France. I thank all three for their very hands-on approaches in the lab and for their great social contributions to the group.

I am particularly grateful to Sylvie Roke, of the Gorlæus Laboratories in Leiden, Holland, for the many discussions we have had in person and over the telephone about sum frequency femtochemistry from both practical and theoretical perspectives; it was good to know that we were not alone with some of the experimental difficulties!

I am thankful to the technical support services in this department, particularly to the mechanical workshops for their craftsmanship and efficiency. Others who have been of practical assistance are acknowledged throughout this work. Besides Dr. Arnolds and Professor King, I thank Dr. Stephen Jenkins, Robert Dillon, Frank Lee and Dr. David Pritchard for proof reading this thesis.

I acknowledge experimental funding from the EPSRC and CERC3, and personal funding from EPSRC, Johnson Matthey plc., the Newton Trust and Professor King. It has been a pleasure teaching Physics and Physical Chemistry for Sidney Sussex College over the last four years, and I thank them for this opportunity and also for my own undergraduate education, in particular Dr. Paul Scott, Dr. Bill Jones and Professor Lindsay Greer. I have not forgotten those who encouraged me in science whilst still at school, and I especially thank Roger Burrage, Glyn Warnes and Steve Blaza for always making time for me.

Lastly I deeply thank my parents, friends and family for their love, understanding and unquestioning support throughout my education and life so far.

Abstract

A femtosecond time-resolution broadband vibrational sum-frequency (SF) spectrometer to study metal-adsorbate systems in ultra-high vacuum has been constructed from an existing 150 fs, 800 nm, 10 Hz repetition rate laser system. A commercial Optical Parametric Amplifier, and an in-house built pulse shaper (for high spectral resolution) have been added. A novel alignment strategy using a thin layer of alkali metal adsorbed onto the metal surface to generate large nonlinear optical signals has been developed. This technique also allows the complete characterisation of the laser beams *in situ* by a spectrally resolved cross-correlation method. The characteristics of the new system have been fully determined using this method and by Frequency Resolved Optical Gating.

A study of carbon monoxide adsorbed on a ruthenium $\{10\bar{1}0\}$ surface has been performed using the new experiment. A surface coverage dependent study of the CO stretch frequency shows good agreement with previous electron energy loss studies. From an isotopic study it has been deduced that dipole-dipole coupling is the principal cause of the observed frequency shift. The linewidths show a dramatic rise below 0.3 ML coverage; this is attributed to heterogeneous broadening, and a system of CO chains of varying length and spacing below this coverage is proposed to account for this. At high coverage the linewidth does not increase as would be expected from a system with such poor adlayer-surface registration at these coverages. An exchange interaction between low and high frequency dipoles would account for this. Sample temperature dependent studies of the stretch frequency have also been performed, and the change is attributed to the CO stretch coupling to one of the frustrated CO phonon modes.

Time-resolved Free Induction Decay measurements have also been made as a function of coverage. For example, these show that the total dephasing time, $T_2 = 1.2$ ps at 0.9 ML coverage. The FID curves have been accurately fitted using

the temporal characteristics of the spectrometer and from these linewidth values are obtained with little or no instrumental broadening as compared with the spectral techniques. The form of the FID curves also suggests little inhomogeneous broadening at high coverages.

Experimental setups for IR-pump, SF-probe and photon echo spectroscopies are discussed and have been implemented in their preliminary stages. An 800 nm pump, SF-probe experiment on the CO/Ru$\{10\bar{1}0\}$ system shows a transient redshift in the CO stretch frequency around $t = 0$ of 5.2 cm^{-1} for a fluence of 24 J m^{-2} at 0.9 ML coverage. This transient initially recovers with a time-constant of 5.3 ps, and this is accounted for using the data from the sample temperature dependent study by modelling the *adsorbate* temperature after laser heating. It is suggested that the redshift is due to coupling with one of the CO frustrated phonon modes. However, such a rapid effect could also be due to coupling to the laser excited electrons in the surface.

Contents

Chapter 1

Introduction

1.1 Motivation

1.1.1 Surface Science and Heterogeneous Catalysis

Metal surfaces play a vital rôle in many industrially and environmentally important chemical reactions. By providing a stage on which the molecular actors (the adsorbates) can perform their reactive dance they can promote reactions, increase yields and lower the necessary temperatures and pressures. Reactions can be promoted in many ways: by the surface correctly orientating the reagents; through surface diffusion and collision; or by the influence on the intermolecular bonds by the presence of the surface electronic states (for example the weakening of intermolecular bonds by a reduction in electron density caused by the formation of a surface-adsorbate bond).

Most of these heterogeneously catalysed reactions are not fully understood at a mechanistic level. Surface science concerns itself with unravelling these reaction pathways and understanding their energetics and kinetics [1]; this information can then lead to educated suggestions for better catalysts to replace those that currently are used largely due to serendipity. Improvements in catalysis lead to many advantages for industry and the environment; for example reducing a reaction temperature would cut costs in an industrial process, and, specifically could lead to car catalytic converters reaching their operational temperature much sooner after a vehicle is started, with great environmental benefits. The study of existing catalytic reactions can also lead to the development of catalysts for inefficient currently un-catalysed reactions.

The surface scientist's toolkit contains many techniques [2], and our group is fortunate to have several of these which can be used to tackle a problem from many angles. Spectroscopic techniques give insight into vibrational dynamics, such as Reflection-Absorption Infra-Red Spectroscopy (RAIRS) [3]. Density Functional Theory (DFT) calculations can model electron density and suggest likely reaction pathways [4]. A micro-calorimeter enables direct measurement of adsorption energies [5]. The molecular beams facility enables precise control of adsorption [6]. The unique Surface Infrared Emission (SIRE) experiment can directly detect the emission of infrared light from surface bonds [7].

We can spatially visualise molecules on surfaces with Low Energy Electron Diffraction (LEED) [8] and Scanning Tunnelling Microscopy (STM) [9]. STM produces images with nanometre resolution, the true length-scale of these fundamental processes. The work described in this thesis adds a technique to the group's arsenal which can spectroscopically follow chemical reactions on surfaces on their true femtosecond time-scale.

1.1.2 Pump-Probe Spectroscopy

In surface pump-probe spectroscopy, two ultrafast laser pulses are used, figure 1.1. The first (the pump), causes a reaction or physical process (e.g. desorption) to occur and establishes a time zero from which the reaction can be clocked. A second pulse arriving a short time after the pump then spectroscopically probes the surface-adsorbate system. By varying the time delay between the pump and probe pulses, a real-time spectroscopic picture of the process under study is revealed.

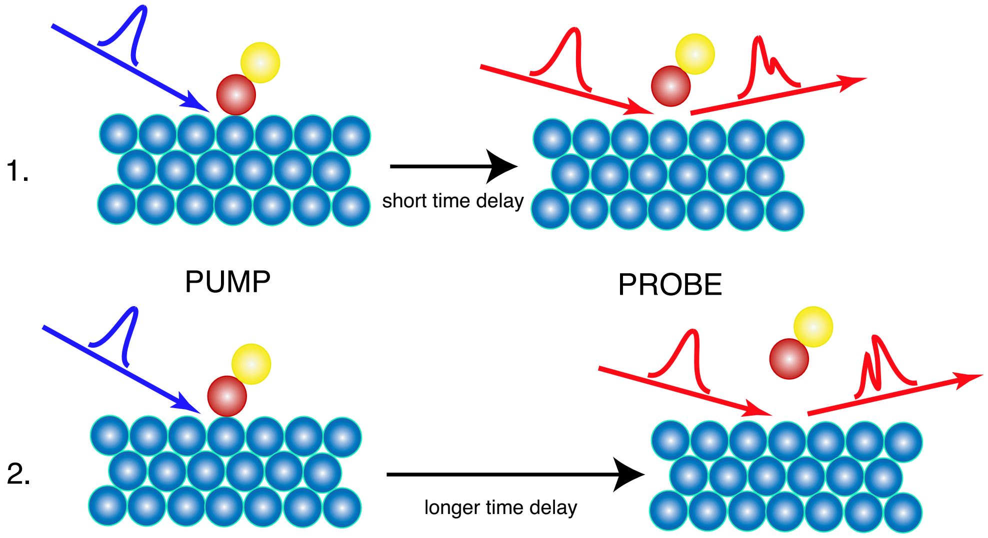

Figure 1.1: Surface pump-probe spectroscopy. (1) Pump beam starts molecular process, here desorption of the diatomic molecule from the metal surface. The state of the adsorbate layer is spectroscopically probed a short time later. (2) The system is pumped again, but this time the probe arrives slightly later, and the process of desorption has progressed further. By altering the pump-probe delay a real-time spectroscopic picture of the process can be built up.

The optical technique used for the probe pulses in this work is called Sum Frequency Generation (SFG). The probe actually consists of two laser pulses of differing frequency: one is infrared and is tuned to the vibrational resonance to be studied and the other is a visible pulse (figure 1.2). SFG is explained in more detail in chapter 2, but essentially what is detected is light at the sum of the two frequencies with vibrational information from the adsorbate present within its spectrum. SFG is ideal for surface study as: the process only occurs at surfaces and interfaces and thus gas phase molecules are not detected; the presence of the surface may enhance the signal; and IR detectors are not needed as the sum frequency (SF) light is produced in the visible region of the spectrum. SFG also has a much greater signal to noise ratio than infrared absorption, and can deal with hidden interfaces [10].

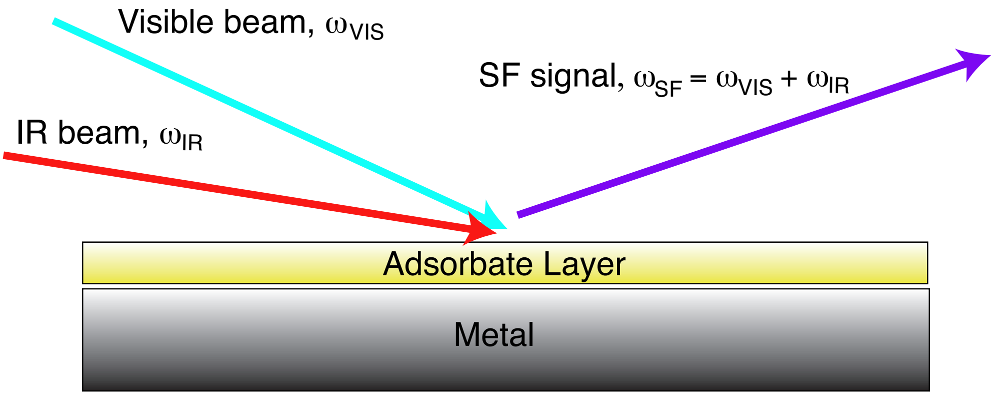

Figure 1.2: Sum frequency generation as a surface probe.

So for SFG pump-probe experiments three laser beams are necessary, one for the pump and two for the SF probe. Surface science experiments on single crystal metal surfaces are generally performed under ultra-high vacuum (UHV) conditions, so that contamination from sources not related to the chemical systems under study can be eliminated. Thus one of the major challenges of setting up such an experiment is how to align three small and temporally very short laser pulses in space *and* time on a sample in a vacuum chamber. A novel technique for doing this is described in this thesis.

SFG can of course also be used without a pump pulse for ordinary spectroscopic studies, and the first results from this experiment are of this nature. Femtosecond laser pulses are intrinsically broadband, due to the reciprocal Fourier relationship between the time and frequency domains. This means that a wide range of spectral features can be observed under the broad spectral envelope of the IR pulses and removes the need to scan the frequency of the IR source (section 2.3.2). If a spectrograph and CCD array are used as a detection system then an entire spectrum may be taken with one laser pulse.

Later results herein use a technique in which the visible and IR beams are delayed to take *free induction decay* measurements (explained in section 2.3.3). Finally in chapter 6, the first visible-pump SF-probe result from this laboratory is presented.

1.1.3 Choice of Chemical System to Study

Our group have been involved in a study of the photocatalytic decomposition of water to produce hydrogen. The work is a collaboration between the groups of Prof. Aart Kleyn and Dr. Mischa Bonn in Leiden, Prof. Martin Wolf in Berlin, Prof. Peter Saalfrank in Regensburg and our group, and is funded by the *Chairmen of the European Research Councils' Chemistry Committees* or CERC3. The work involves using femtosecond laser techniques and theoretical modelling to gain a fundamental understanding of the dynamics of energy transfer in the decomposition of water to form hydrogen on ruthenium oxide surfaces. The goal of this work is to suggest an efficient catalyst for this reaction, so hydrogen may one day be produced from water and sunlight for fuel.

RuO_x was chosen as it is already known to act as a water reduction catalyst in the decomposition of water to form O_2 and H_2 [11]. The rôle of our group in this is to investigate the effect of co-adsorbed alkali metal layers in promoting the reaction. We decided to use the Ru$\{10\bar{1}0\}$ surface to provide a contrast with the Ru{0001} surface used in Berlin and Leiden.

However, preliminary results from Berlin [12] indicated a relatively low signal from water on ruthenium. Given that the Berlin group have a femtosecond laser with a 400 Hz shot repetition rate, this, for reasons discussed in chapter 3, gives them more sensitivity and less shot-to-shot noise than we can expect with our 10 Hz system. Therefore our group decided not to investigate water on the Ru$\{10\bar{1}0\}$ surface immediately with the new experiment, but to try a molecule with a larger SF signal. For this reason the first chemical results from our spectrometer are from CO/Ru$\{10\bar{1}0\}$.

1.2 Review of Femtochemistry

1.2.1 Pioneering Work

In 1935 Eyring [13], and independently Evans and Polanyi [14], wrote on the transition state theory, and proposed an extension to the Arrhenius expression for the rate constant of a reaction based upon its activation energy. This theory gave an expression for the rate of a reaction corresponding to around 100 fs. Subsequently over the rest of the twentieth century the experimentalists attempted to catch up. Hartridge and Roughton developed the flow technique in 1923; Chance invented the stop flow technique in 1940, with a millisecond time resolution. The microsecond barrier was broken by Norrish and Porter [15] in 1949 with flash photolysis, a true forerunner of the pump-probe technique, in this very department. The relaxation technique was developed by Eigen in 1953 [16], in which the equilibrium of a chemical system was disturbed by a heat or pressure jump, or an electric field. This brought the technology almost to nanosecond timescales.

The invention of the laser by Maiman in 1960 brought rapid change in the field. The development of Q-switching (section 3.1.3) and mode locking (section 3.1.2) led to further gains in time resolution, and in 1974 sub-picosecond pulses were obtained from dye-lasers by Shank and Ippen at the Bell Laboratories. By

1992 6 fs pulses had been achieved from Ti:Sapphire lasers (section 3.1.2) and today the attosecond regime has been reached [17]. The parallel development of molecular beams was also important in attempts to clock chemical reactions [18].

The father of femtochemistry is Ahmed H. Zewail [19, 20] of Caltech. In 1987 his group published work [21] in which the dissociation of I-CN in the gas phase was monitored with 400 fs resolution. Within two years, they had studied the same reaction with a 40 fs resolution. Zewail then went on to study halogen exchange reactions, such as $Br + I_2 \rightarrow [BrI_2]^{\ddagger} \rightarrow BrI + I$, and from this work [22] was able to plot the full *potential energy surface* of the reaction. For reviews of recent work in general femtochemistry see [23, 24, 25]. Today femtochemistry not only concerns itself with the measurement of reaction dynamics, but has branched out into the area of *coherent control* [23].

1.2.2 Application to Surface-Adsorbate Systems

Lasers have been used to optically stimulate surface reactions since the 1970s [26, 27]. Such stimulation may theoretically occur by four distinct mechanisms [28]: adsorbate localised excitation; carrier-induced reactions; surface-state mediated reactions; and thermal reactions. The first of these cases is limited to where the free adsorbate has a large photochemical cross section, and is rare. The second case occurs when electron-hole pairs are induced by incident photons in the near-IR and shorter wavelength range on the metal surface. The "hot" electrons formed by this process have lifetimes in the range of 10–10^3 fs [29]. The effective electronic temperature caused by rapid thermalisation of the electron gas to a hot Fermi-Dirac distribution may reach peak temperatures of thousands of Kelvin above the equilibrium melting point with femtosecond laser systems. The third case arises when either an occupied or unoccupied electronic surface state is involved in a optically induced transition. The final case involves heating of the substrate by the laser and the thermal activation of the reaction.

Early surface time-resolved experiments involved desorption of adsorbed chemical layers with a pump laser pulse, for example NO on a Pd{111} surface in 1990 [30] using a technique known as REMPI (Resonance-Enhanced Multiphoton Ionisation) in which desorbed species are optically ionised and the remnants detected with time-of-flight mass spectrometry. For a review of this area see [28]. Section 1.3 describes the laser induced desorption experiments carried out in this group prior to the work described herein. A recent work related to the systems investigated in this thesis is a study of the laser induced desorption and oxidation of CO on a Ru{0001} surface by Bonn, Wolf and Ertl *et al.* [31] in which an 800 nm pump beam can desorb CO or react co-adsorbed CO and atomic O, with detection by time of flight mass spectrometry. They showed that the desorption process is caused by coupling to the substrate phonon bath, while the reaction is caused by hot substrate electrons.

The first surface time-resolved vibrational experiments, at least on a picosecond timescale, probed vibrational decay processes. Some of the earliest of these were by Heilweil, Beckerle, Cavanagh and Stephenson *et al.* (e.g. [32, 33, 34, 35]) from 1988. These experiments initially used platinum or rhodium particles on a SiO_2 substrate and progressed to CO on a single Pt{111} crystal. Transients in the vibrational spectra (taken with infra-red absorption spectroscopy) were observed when a vibrationally resonant IR pump pulse was present. From these, the lifetime of the vibrational population (T_1 — see section 2.3.3) could be calculated.

Slightly later SFG was used as the detection method to probe vibrational dephasing. These experiments probed the total dephasing time (T_2 — section 2.3.3) and the lifetime of the vibrational population (T_1). The dephasing measurements, known as *free induction decays* are reviewed and explained in section 2.3.3; the vibrational population measurements are explained in section 6.1.1.

In 1993 Germer *et al.* [36] performed experiments in which a visible picosecond pump pulse was used to heat a Pt{111} surface, and observed a shift in the stretch frequency of adsorbed CO measured by IR-probe absorption. This could be attributed to increased population of the CO adlayer frustrated translation mode at high temperature and its coupling to the C-O stretch.

The recent work of Bonn and Wolf *et al.* on CO/Ru{0001} with femtosecond lasers (as reviewed in sections 5.5.3 and 6.3.3) involved perturbing the surface-adsorbate system with a visible pump beam and observing the effect upon the vibrational dynamics with a sum frequency probe. A qualitatively similar observation to that seen by Germer *et al.* is also attributed to thermally exciting the frustrated translation mode. Also Bourguignon *et al.* [37] are currently undertaking a visible pump, sum-frequency probe femtosecond laser experiment on CO/Pt{111}.

Bandara *et al.* [38] have recently undertaken an SFG study of CO/Ni{111} with picosecond lasers. They observed an unusual shoulder in the SF spectra with a UV pump beam, but not for a visible beam. They attribute this to the direct involvement of hot electrons caused by the UV pump in exciting the C-O internal stretching mode.

Whilst time resolved SFG experiments on systems which are bench-top based have blossomed in recent years [39], experiments performed under ultra-high vacuum are few. This is largely due to the fact that UHV systems with surface science preparation / characterisation facilities, and ultra-fast lasers are both complex technologies in their own right; and indeed as chapter 3 demonstrates they often have conflicting needs when it comes to their ideal laboratory environments.

As an interesting aside, the Zewail group are currently setting up an experiment to perform LEED experiments in real-time by using a femtosecond laser to excite a medium and generate fast pulses of electrons to be used in the electron diffraction process [40]. In this way it should be possible to follow chemical reactions on surfaces simultaneously in real-space and in real-time.

1.3 Previous Work in the Cambridge FemtoLab

The femtosecond laser laboratory was originally a shared facility between the groups of Gareth Roberts and David King; up until a year and a half into my PhD laser time was shared between the two groups. Dr. Roberts' work concentrated on gas phase studies, and it is for this reason that the basic laser system is a high powered 10 Hz repetition rate system, which is most suitable for such work. A review of work done by the Roberts group in this laboratory is given in [41]. The main body of work from the King group in this laboratory concerned laser induced desorption of adsorbed molecules from metal single crystals. The principal system of study was benzene on a Pt{111} surface in ultra high vacuum [42, 43]. Benzene (and its fully deuterated isotope) was desorbed from the metal surface by 800 nm, 150 fs laser pulses — the fundamental output from the laser system. Desorbed species were detected with a mass spectrometer. Three distinct features were seen in the time-of-flight spectra: a hyperthermal feature with 0.2 eV translational energy; a thermal feature at intermediate energies; and a subthermal feature. This behaviour was explained by a model in which energy is transferred from the surface in a series of steps from layer to layer in the multilayer — a *molecular Newton's cradle*.

During the first year of my PhD we conducted a similar desorption experiment for ethylene, and later hydrogen, on Pt{111}. This was during downtime of the device used to produce mid-infrared light for vibrational experiments. Very fast charged species were produced, which were non mass-selected by our mass spectrometer. This work proved inconclusive and is peripheral to the main body of work described in this thesis. However, for completeness' sake a summary of the experimental details and results is given as Appendix A. A full account is given in my end-of first-year report [44].

1.4 About this Thesis

This thesis describes the development of the femtosecond laboratory from a simple 800 nm, 150 fs at 10 Hz repetition rate amplified femtosecond oscillator facility to a broadband sum frequency spectrometer for studying metal surface-adsorbate systems in ultra high vacuum, both in the frequency and time resolved regimes. The scope of this work began with the arrival of an Optical Parametric Amplifier (OPA) which converts the output from the existing laser system to mid-infrared for vibrational SF experiments.

Chapter 2 introduces the concepts of nonlinear optics and sum frequency spectroscopy. As much of this thesis is devoted to the construction of the spectrometer, this chapter presents a working introduction to the various nonlinear optical phenomena which are used in the optical setup as tools; such as second harmonic generation and optical parametric amplification. It also explains in more detail what sum frequency spectroscopy is, why it is used, and how spectra may be interpreted. Finally, the concept of the time resolved free induction decay to directly measure vibrational dephasing times is discussed.

Chapter 3 describes the development of the experiment, up to the level at which it was capable of spectrally resolved SF measurements and temporally resolved free induction decay measurements. It begins with an outline of how ultrafast laser pulses are produced, and describes the commercial laser system in theory and also in terms of its practical day-to-day running and alignment. The operation of the OPA is then discussed, followed by the development and construction of a pulse shaper to spectrally narrow the visible laser pulses used as part of the SF technique, which is a requirement for high spectral resolution. Then the ultra-high vacuum (UHV) chamber is detailed, along with the standard surface science techniques used to clean and characterise single metal crystals *in vacuo* such as low energy electron diffraction, Auger Electron spectroscopy and temperature programmed desorption. The final section of this chapter brings the laser and UHV systems together. The optical detection apparatus is discussed. Methods of mechanically delaying laser pulses with respect to each other for time resolved experiments are detailed, along with the software to coordinate data acquisition with changing temporal delay. The development of the novel strategy used for aligning multiple laser beams in space *and* time on a surface *in vacuo* is described. Given that this is the first PhD thesis to be completed from this laboratory in this group, it is hoped that the detailed description of the apparatus given in this chapter may usefully serve as a reference for future workers.

Chapter 4 discusses methods of characterising ultra-fast laser pulses. After a brief mention of fluence and autocorrelation measurements, the problems of chirp and pulse-front tilt are discussed. Frequency Resolved Optical Gating (FROG) is then explained and used to obtain some of the temporal and spectral properties of the spectrometer. Then a novel technique involving a thin layer of alkali metal on the crystal surface which allows *in-situ* characterisation of laser pulses in the UHV chamber is discussed and used to accurately determine the temporal characteristics of both beams used for SF experiments so that the finite temporal width of the laser beams can be taken into account when fitting time resolved data.

Chapter 5 presents an SF study of carbon monoxide on the ruthenium $\{10\bar{1}0\}$ surface. The cleaning and characterisation of the metal sample is detailed. Spectrally resolved measurements are described, where the stretch frequency and linewidth of the CO molecules are studied as a function of surface coverage. The temporally resolved free induction decay measurements of the oscillator dephasing time with coverage, accurately fitted using the temporal characteristics of the system from chapter 4, are given and compared with the spectral linewidth measurements. The origins of the stretch frequency changes are discussed, along with supporting data from an isotopic study. The changes in linewidth are explained with reference to surface order, and a suggestion is made about the nature of the adsorbate layer structure at low coverage. The data for Ru$\{10\bar{1}0\}$ are compared with recent data for CO/Ru$\{0001\}$ and to support this a brief sample temperature dependent study of the stretch frequency is presented.

Chapter 6 outlines experimental setups for IR-pump SF-probe and photon echo experiments. Finally, a setup for a visible pump, SF-probe experiment is presented along with the first three-beam time-resolved pump-probe results from this laboratory. The next stage of work in the laboratory is then discussed, followed by concluding remarks.

This thesis is aimed at audiences of both ultra-fast spectroscopists and surface scientists, and thus particularly in chapter 3, I have explained some of the more everyday concepts in each field for the benefit of readers from the other field given the overlap of speciality is not common.

Chapter 2

Nonlinear Optics and Spectroscopy

The process of sum frequency generation from surfaces and interfaces is the principal experimental technique used in this work. However, the laser system itself employs several other nonlinear optical processes, such as: second harmonic generation to double optical frequencies (for example to produce a 400 nm pump pulse from the 800 nm fundamental); optical parametric amplification to produce mid infrared light for vibrational studies; and SFG in nonlinear optical crystals as an alignment tool. This chapter provides a working introduction to the nonlinear processes described in the remainder of this thesis.

2.1 Interaction of Intense Light with Matter

2.1.1 Linear and Nonlinear Susceptibilities

Within the Born-Oppenheimer approximation, the electric field component of an electromagnetic wave incident upon a medium will exert a force on the electrons within that medium. The polarisation, **P**, induced in the medium when the electric field, **E**, is weak is given by [45, section 18.2]

$$\mathbf{P} = \alpha\mathbf{E} \tag{2.1}$$

where α is the *linear polarisability* of the medium. This may also be written as

$$\mathbf{P} = \epsilon_0\chi^{(1)}\mathbf{E} \tag{2.2}$$

where $\chi^{(1)}$ is the *linear susceptibility* of the medium and ϵ_0 is the permittivity of free space which will be omitted for clarity in all further equations. For an electric field of any form the induced polarisation will be of the same frequency as the incident radiation and this polarisation will re-radiate giving rise to classical optical effects e.g. reflection.

However, the assumption that the induced polarisation is linearly related to the electric field strength breaks down in stronger fields and the polarisation must be expressed as a power series in the field strength [46, page 2]

$$\begin{aligned}\mathbf{P} &= \mathbf{P}^{(1)} + \mathbf{P}^{(2)} + \mathbf{P}^{(3)} + \mathbf{P}^{(4)} + \cdots \\ &= \chi^{(1)}\mathbf{E} + \chi^{(2)}\mathbf{E}^2 + \chi^{(3)}\mathbf{E}^3 + \chi^{(4)}\mathbf{E}^4 + \cdots . \end{aligned} \tag{2.3}$$

where $\chi^{(n)}$ is the nth order nonlinear susceptibility. Again this can be written in terms of polarisabilities:

$$\mathbf{P} = \alpha\mathbf{E} + \beta\mathbf{E}^2 + \gamma\mathbf{E}^3 + \delta\mathbf{E}^4 + \cdots \tag{2.4}$$

where β, γ and δ are the 2nd, 3rd and 4th order *hyperpolarisabilities*.

2.1.2 Second Order Processes

All the nonlinear processes described in this thesis are second order. Thus if one considers only the first and second order terms, for an incident electric field

$\mathbf{E}(t) = \mathbf{E_0}e^{-i\omega t}$ + c.c. (c.c. = complex conjugate) inserted into equation 2.3 the polarisation may be written as

$$\mathbf{P} = \chi^{(1)}\mathbf{E_0}e^{-i\omega t} + \chi^{(2)}\mathbf{E_0}^2 e^{-2i\omega t} + \text{c.c.} \tag{2.5}$$

This expression contains a term which oscillates at twice the frequency of the incident radiation, and the component of the light re-radiated by the medium at this doubled frequency is known as the second harmonic (SH). If this analysis of the second order polarisation is now repeated for two incoming electric fields such that $\mathbf{E}(t) = \mathbf{E_1}e^{-i\omega_1 t} + \mathbf{E_2}e^{-i\omega_2 t}$ + c.c. then the following terms emerge:

$$\begin{aligned}
\mathbf{P}^{(2)} &= \chi^{(2)}\left(\mathbf{E_1}e^{-i\omega_1 t} + \mathbf{E_2}e^{-i\omega_2 t} + \text{c.c.}\right)^2 \\
&= \chi^{(2)}\mathbf{E_1}^2 e^{-2i\omega_1 t} + \chi^{(2)}\mathbf{E_2}^2 e^{-2i\omega_2 t} + \text{c.c.} && (2.6)\\
&\quad +2\chi^{(2)}\mathbf{E_1}\mathbf{E_2}e^{-i(\omega_1+\omega_2)t} + \text{c.c.} && (2.7)\\
&\quad +2\chi^{(2)}\mathbf{E_1}\mathbf{E_2}^{*}e^{-i(\omega_1-\omega_2)t} + \text{c.c.} && (2.8)\\
&\quad +2\chi^{(2)}\mathbf{E_1}\mathbf{E_1}^{*} + 2\chi^{(2)}\mathbf{E_2}\mathbf{E_2}^{*}. && (2.9)
\end{aligned}$$

Terms 2.6 represent the second harmonic generation (SHG) from each of the two fields. Term 2.7 represents a polarisation oscillating at the sum of the two frequencies. This term in the polarisation will re-radiate and generate the sum-frequency of the incoming beams — *this* is the phenomenon known as SFG. Term 2.8 generates the difference frequency (DF) of the incoming beams, and the final terms (2.9) are independent of the incoming frequencies and the effect is known as optical rectification.

In all of the above two approximations are made. The first is that we employ the electric dipole approximation — optical magnetic fields and multipoles are neglected. The second is the local field approximation: the **E** fields which induce the polarisations are the macroscopic electric fields of the incoming radiation alone and the microscopic fields of neighbouring dipoles are ignored.

2.1.3 Three Dimensional $\chi^{(2)}$ Processes

In equations 2.3–2.9 the electric fields and polarisations are referred to in their vector form and, for real media, $\chi^{(2)}$ is a tensor to truly reflect this relationship and the media's anisotropic nature. For SFG, $\chi^{(2)}$ is a third rank tensor to represent the relationship between the three spatial co-ordinates each of $\mathbf{E_1}$, $\mathbf{E_2}$ and $\mathbf{P}$, giving 27 components in total. For infrared (IR) and visible (VIS) incoming radiation, each component of $\chi^{(2)}_{ijk}$ represents the relationship as follows

$$\mathbf{P}^{(2)}_{i,\mathrm{SF}} = \chi^{(2)}_{ijk}\mathbf{E}^{(2)}_{j,\mathrm{VIS}}\mathbf{E}^{(2)}_{k,\mathrm{IR}}. \tag{2.10}$$

There is an important symmetry consideration in $\chi^{(2)}$ processes: given $\mathbf{P}^{(2)} \propto \mathbf{E}^2$ then $\mathbf{P}^{(2)}(\mathbf{E}) = \mathbf{P}^{(2)}(-\mathbf{E})$. In a centrosymmetric medium, opposite directions are identical so $\mathbf{P}^{(2)}(\mathbf{E}) = -\mathbf{P}^{(2)}(-\mathbf{E})$. These two conditions can only hold if the constant of proportionality, i.e. $\chi^{(2)}$, is zero. Thus only non-centrosymmetric media have a finite $\chi^{(2)}$ (a more rigorous argument for a fully tensorial $\chi^{(2)}$ is given in section 2.3.1). The most obvious examples of non-centrosymmetric media are surfaces and interfaces. Hence second order nonlinear processes such as SFG and SHG are *surface specific* and ideal for spectroscopic study of metal-adsorbate systems. Certain inorganic crystals also exhibit suitable symmetry, as described in section 2.2.1.

2.2 Processes Used as Experimental Tools

2.2.1 SHG and SFG in Crystals – Phase Matching

The angle of the incoming beams with respect to a nonlinear crystal is critical as I shall now demonstrate. From Maxwell's equations, for a dielectric

$$\nabla \times \mathbf{H} = \frac{\partial \mathbf{D}}{\partial t} = \frac{\partial}{\partial t}\left(\epsilon_0 \mathbf{E} + \mathbf{P}\right),$$

$$\begin{aligned}\nabla\times\mathbf{E} &= -\mu_0\frac{\partial\mathbf{H}}{\partial t}\\ \Rightarrow \nabla\times\nabla\times\mathbf{E} &= -\mu_0\epsilon_0\frac{\partial^2\mathbf{E}}{\partial t^2}-\mu_0\frac{\partial^2\mathbf{P}}{\partial t^2}.\end{aligned}\tag{2.11}$$

Taking the Fourier transform of both sides of equation 2.11 gives [47, section 8.3]

$$\begin{aligned}&\nabla\times\nabla\times\int_{-\infty}^{\infty}\mathbf{E}(\omega)e^{-i\omega t}\mathrm{d}\omega = \\ &-\mu_0\epsilon_0\frac{\partial^2}{\partial t^2}\int_{-\infty}^{\infty}\mathbf{E}(\omega)e^{-i\omega t}\mathrm{d}\omega-\mu_0\frac{\partial^2}{\partial t^2}\int_{-\infty}^{\infty}\mathbf{P}(\omega)e^{-i\omega t}\mathrm{d}\omega.\end{aligned}\tag{2.12}$$

One can then take each frequency component separately and expand **P** to second order to give

$$\nabla\times\nabla\times\mathbf{E}(\omega)=\mu_0\epsilon_0\omega^2\mathbf{E}(\omega)-\mu_0\omega^2\left[\mathbf{P}^{(1)}(\omega)+\mathbf{P}^{(2)}(\omega)\right].\tag{2.13}$$

The linear polarisation can be subsumed into the $\mathbf{E}(\omega)$ term by introducing the linear dielectric constant, $\epsilon(\omega)$ to give [48, page 43],

$$\nabla\times\nabla\times\mathbf{E}(\omega) = \frac{\omega^2}{c^2}\epsilon(\omega)\mathbf{E}(\omega)-\mu_0\omega^2\mathbf{P}^{(2)}(\omega).\tag{2.14}$$

If a transverse wave of the form $\mathbf{E}(\omega) = \mathbf{E_0}(\omega,z)e^{ikz}$ (where $\mathbf{E_0}(\omega,z)$ is an envelope function slowly varying with z) is inserted into the left hand side of equation 2.14 one gets

$$\begin{aligned}\nabla\times\nabla\times\mathbf{E}(\omega) &= \nabla\underbrace{(\nabla\cdot\mathbf{E})}_{\to 0\text{ for plane wave}}-\nabla^2\mathbf{E}\simeq-\frac{\partial^2\mathbf{E}}{\partial z^2}\\ &=\left[k^2\mathbf{E_0}(\omega,z)-2ik\frac{\partial\mathbf{E_0}(\omega,z)}{\partial z}-\frac{\partial^2\mathbf{E_0}(\omega,z)}{\partial^2 z}\right]e^{ikz}.\end{aligned}\tag{2.15}$$

As $\mathbf{E_0}(\omega,z)$ is slowly varying, we can neglect its second differential and thus reinserting expression 2.15 as the left hand side of equation 2.14 we get

$$\left[k^2\mathbf{E_0}(\omega,z)-2ik\frac{\partial\mathbf{E_0}(\omega,z)}{\partial z}\right]e^{ikz} = \frac{\omega^2}{c^2}\epsilon(\omega)\mathbf{E_0}(\omega,z)-\mu_0\omega^2\mathbf{P}^{(2)}(\omega)$$

which is a nonlinear wave equation in which the first term on each side is identical to the linear wave equation (in which $k^2 = \omega^2 \epsilon(\omega)/c^2$), and the second terms give

$$\frac{\partial \mathbf{E_0}(\omega, z)}{\partial z} = \frac{i\omega^2 \mu_0}{2k} \mathbf{P}^{(2)}(\omega) e^{-ikz}. \tag{2.16}$$

In section 2.1.2 we inserted the sum of two time-dependent electric fields into equation 2.3 to demonstrate the resultant terms responsible for second order processes. If now instead we consider the sum of two waves which also vary in space, $\mathbf{E} = \mathbf{E_1} \exp(ik_1 z - i\omega_1 t) + \mathbf{E_2} \exp(ik_2 z - i\omega_2 t)$, this will give a polarisation

$$\mathbf{P_{SF}}^{(2)} \propto \chi^{(2)} \mathbf{E_1} e^{ik_1 z} \mathbf{E_2} e^{ik_2 z} e^{-ik_{\mathrm{SF}} z} \tag{2.17}$$

where $k_{\mathrm{SF}} = n(\omega_{\mathrm{SF}})\, \omega_{\mathrm{SF}}/c$ for sum frequency generation in which $\omega_{\mathrm{SF}} = \omega_1 + \omega_2$. $n(\omega_{\mathrm{SF}})$ is the refractive index of the medium at frequency ω_{SF}.

Inserting the polarisation from equation 2.17 into equation 2.16 one gets

$$-\frac{\partial \mathbf{E_{SF}}}{\partial z} \propto \chi^{(2)} \mathbf{E_1} \mathbf{E_2} e^{i\Delta k z} \tag{2.18}$$

where

$$\Delta k = k_1 + k_2 - k_{\mathrm{SF}} = \frac{n(\omega_1)\, \omega_1}{c} + \frac{n(\omega_2)\, \omega_2}{c} - \frac{n(\omega_{\mathrm{SF}})\, \omega_{\mathrm{SF}}}{c}, \tag{2.19}$$

i.e. a value proportional to the change in total photon momentum ($= \hbar \Delta k$) before and after the process.

Integrating equation 2.18 over a path length L gives

$$\mathbf{E_{SF}} \propto \chi^{(2)} |\mathbf{E_1}| |\mathbf{E_2}| \left(\frac{e^{i\Delta k L} - 1}{\Delta k} \right),$$

which as the SF intensity, I_{SF}, is proportional to $|\mathbf{E_{SF}}|^2$, gives

$$I_{\mathrm{SF}} \propto \left| \chi^{(2)} \right|^2 L^2 \mathrm{sinc}^2 \left(\frac{\Delta k L}{2} \right). \tag{2.20}$$

The sinc function is maximal when its argument is zero, so equation 2.20 implies that maximum SF signal will be achieved when $\Delta k = 0$; i.e. when photon momentum before and after the process is conserved. From the rightmost term of expression 2.19 one can see that the only way to achieve this is to have $n(\omega_1) + n(\omega_2) = n(\omega_{\mathrm{SF}})$ which is impossible for most media due to dispersion. However, remembering that $\chi^{(2)}$ is in fact a tensor, it is possible to choose a material in which the SF beam is produced with an orthogonal polarisation to the incoming beams. In other words, a birefringent crystal is used in which the refractive indices are different for the two different polarisations.

When the SF beam produced in a uniaxial nonlinear crystal has an orthogonal polarisation to the incoming beams it is known as Type I *phase matching*. It is also possible to achieve phase matching by using incoming beams with a combination of the two polarisations, but with the combinations in each incoming beam being orthogonal with respect to one another. The SF beam may then have both components of polarisation, however only one will be phase matched. This is Type II phase matching.

One can achieve Type I phase matching by rotating the angle of the nonlinear crystal with respect to the beams. In the following, the *ordinary* polarisation is perpendicular to the plane containing the propagation vector, **k**, and the *extraordinary* polarisation is parallel to this plane. It can be shown [49, section 14.3][47, section 7.5] that for a uniaxial crystal

$$\frac{1}{n_e^2(\theta)} = \frac{\sin^2\theta}{\overline{n}_e^2} + \frac{\cos^2\theta}{n_o^2}$$

where $\overline{n}_e$ and n_o are the principal values of the extraordinary and ordinary polarisations respectively. Thus $n_e(\theta)$ can be changed from $\overline{n}_e$ at $\theta = 90°$ to n_o at $\theta = 0°$ to choose a value such that condition 2.19 is satisfied.

In this experiment we use two main nonlinear optical crystals. Beta Barium Borate (BBO) is used for second harmonic generation, a process used as a tool to optimise the laser system, and to generate a blue pump beam for pump-probe experiments. Second harmonic generation can be thought of as sum frequency generation with two incoming photons of the same wavelength. This can be useful to check the temporal alignment of two laser beams; whilst each individual beam will produce its own second harmonic, when the beams are temporally overlapped a third beam will be seen bisecting the others. Each photon in this beam can be thought as originating from one photon from each beam; but with twice the energy of each incoming photon and thus twice the frequency. BBO has a rhombohedral symmetry and its useful transmission range is 0.21–2.1 μm. It is also used in the OPA for the parametric process as described in section 2.2.2. Lithium Iodate ($LiIO_3$) is used to produce benchtop SFG for spatial and temporal alignment purposes. It has hexagonal symmetry and transmits from 0.31–5.0 μm.

2.2.2 Optical Parametric Amplification

Optical parametric amplification is a $\chi^{(2)}$ nonlinear optical process very similar in theory to difference frequency generation (expression 2.8 and [48, chapter 9]). It is equivalent to a difference frequency process in which a beam known as the *idler*, ω_i, is generated from a pump beam, ω_p, and a beam known as the *signal*, ω_s:

$$\omega_i = \omega_p - \omega_s. \tag{2.21}$$

The three beams must satisfy the phase matching condition

$$\mathbf{k_i} = \mathbf{k_p} - \mathbf{k_s} \tag{2.22}$$

in a similar way to condition 2.19 to conserve momentum. So as for sum frequency generation described in section 2.2.1, the nonlinear crystal must be correctly orientated for a particular set of wavelengths. Equation 2.21 is mathematically equivalent to

$$\omega_s = \omega_p - \omega_i. \tag{2.23}$$

The same phase matching condition applies and both may be represented in terms of energy levels as in figure 2.1. Now one can think of the process described in equation 2.21 and the left of the figure as generating an idler wave from the signal (and pump), and the process in equation 2.23 and the right of the figure as generating a signal wave from the idler (and pump). Then one can see how, if both these equivalent processes couple into and feed from one another, the signal and idler would mutually seed amplification of themselves from the pump beam over many passes of the crystal [46, page 86]. This has been exploited in devices known as *Optical Parametric Oscillators* (OPOs) [50] in which a nonlinear crystal is placed in an etalon or mirror cavity and oscillations are allowed to build up as the signal and idler are amplified [46, section 2.8]. In fact our commercial system uses a controlled finite number of passes through one crystal and is not an oscillator *per se* — hence the use of the term amplifier to describe it.

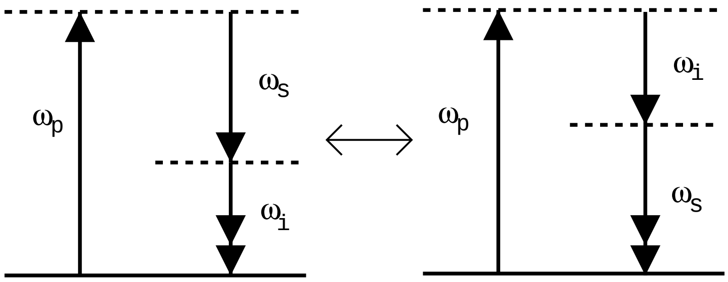

Figure 2.1: Optical parametric generation. Left hand panel is equivalent to equation 2.21, right hand panel to equation 2.23.

If such an amplifier is seeded with a broadband source of light, then in the first stage of amplification the process will select those signal and idler frequencies which satisfy equations 2.21 and 2.22 for a particular crystal orientation. By changing the angle of the crystal, the signal and idler frequencies can be systematically selected. For an 800 nm pump pulse, signal and idler frequencies are in the near infrared and a further simple difference frequency interaction can produce light in the mid infrared for vibrational studies. Our commercial OPA is described in the next chapter in section 3.1.4.

2.3 Sum Frequency Spectroscopy

2.3.1 Effect of Orientation and Polarisation

Equation 2.10 gives the total second order polarisation for VIS and IR beams incident upon a surface or interface and this is eventually detected as the SF intensity, $I_{\mathrm{SF}} \propto \left|\mathbf{P_{SF}}^{(2)}\right|^2$. However, for an isotropic surface, many of the components of $\chi^{(2)}_{ijk}$ make no contribution. If one now rewrites the symmetry criteria for $\chi^{(2)}$ introduced in section 2.1.3 one gets

$$\chi^{(2)}_{ijk} \equiv \chi^{(2)}_{-i-j-k} \tag{2.24}$$

and

$$\chi^{(2)}_{ijk} \equiv -\chi^{(2)}_{-i-j-k}. \tag{2.25}$$

These place constraints on the contributing components of $\chi^{(2)}_{ijk}$ for a surface. With the x and y axes in the plane of the surface, four examples serve to classify all the possible combinations [51, page 54]:

- zzz — reversing x or y axes has no effect — ✓
- xxx (and yyy) — reversing x axis ($xxx \rightarrow$-x-x-x) implies $\chi^{(2)}_{-x-x-x} \equiv -\chi^{(2)}_{x-x-x} \equiv \chi^{(2)}_{xx-x} \equiv -\chi^{(2)}_{xxx}$ which does not satisfy both criteria, if $\chi^{(2)}$ is finite — ✗
- zxx (etc.) — reversing the x axis ($zxx \rightarrow z$-x-x) implies $\chi^{(2)}_{z-x-x} \equiv -\chi^{(2)}_{zx-x} \equiv \chi^{(2)}_{zxx}$ which has no overall sign change so does not violate the criteria — ✓
- zzx (etc.) — reversing x axis ($zzx \rightarrow zz$-x) implies $\chi^{(2)}_{zz-x} \equiv -\chi^{(2)}_{zzx}$ which has an overall change of sign and so does not satisfy both criteria — ✗

Given the x and y directions are equivalent, this leaves only 4 non-zero $\chi^{(2)}_{ijk}$ components [52] for an isotropic surface:

$$\chi^{(2)}_{zxx}\left(\equiv\chi^{(2)}_{zyy}\right);\quad \chi^{(2)}_{xzx}\left(\equiv\chi^{(2)}_{yzy}\right);\quad \chi^{(2)}_{xxz}\left(\equiv\chi^{(2)}_{yyz}\right);\quad \chi^{(2)}_{zzz}.$$

With specific incident laser polarisations it is possible to probe particular susceptibilities. p-polarised light has electric field components along both the direction perpendicular to the surface (z) and one of the parallel directions (e.g. x), whilst s-polarised light has just one electric field component along the other parallel direction (e.g. y) — figure 2.2. Four combinations of incident and SF polarisations are available given the non-zero components of $\chi^{(2)}$ above, depending on which components of the **E** field are present in each direction — these are shown in table 2.1. However, only two of these are usually seen for metal surfaces. The reflectivity of metal surfaces is high for infrared light; for example the reflectivity of ruthenium at 5 µm is 96%. Only combinations with an IR field with some z component (i.e. p-polarised) contribute; the x and y components undergo a phase change upon reflection such that their intensities at the point of reflection are zero.

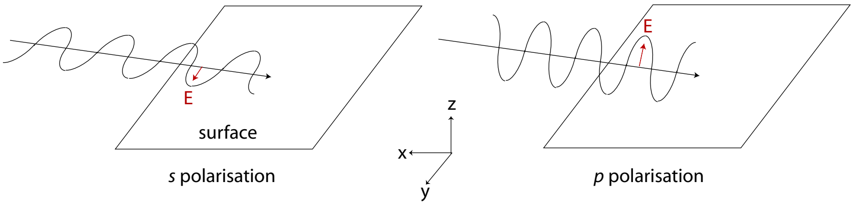

Figure 2.2: *s* and *p* polarisations of light incident on a surface.

It is possible to determine the orientation of molecules adsorbed on surfaces by measuring the SF signal strength as a function of polarisation, as has recently been reported for CO on Pd{111} [53]. In all experiments described in this thesis, PPP polarisation is used for maximum signal strength.

Polarisation Combination SF VIS IR	$\chi^{(2)}$ Components	Seen In Metals?
SSP	$\chi^{(2)}_{yyz}$	✓
SPS	$\chi^{(2)}_{yzy}$	✗
PSS	$\chi^{(2)}_{zyy}$	✗
PPP	$\chi^{(2)}_{zzz}, \chi^{(2)}_{xxz}$	✓
	$\chi^{(2)}_{zxx}, \chi^{(2)}_{xzx}$	✗

Table 2.1: Contributing polarisation combinations.

Phase matching also applies to surface SFG and thus the angles of the VIS, IR and SF beams are related by [54]

$$\omega_{\mathrm{SF}} \sin\theta_{\mathrm{SF}} = \omega_{\mathrm{VIS}} \sin\theta_{\mathrm{VIS}} + \omega_{\mathrm{IR}} \sin\theta_{\mathrm{IR}}. \tag{2.26}$$

2.3.2 Form of the Spectra

So far SFG has been presented as a physical property of the medium, with no discussion of the chemical significance. For a surface-adsorbate interface, *both* the surface and chemical layer will have their own independent second order susceptibilities, and the total $\chi^{(2)}$ will be the sum of these [55]

$$\chi^{(2)}_{\mathrm{T}} = \chi^{(2)}_{\mathrm{NR}} + \chi^{(2)}_{\mathrm{RES}} \tag{2.27}$$

where the subscripts denote Total, Non-Resonant (i.e. the metal surface), and Resonant (i.e. the chemical layer) contributions.

The intensity of the SF signal is proportional to $\left|\chi^{(2)}_{\mathrm{T}}\right|^2$ so from equation 2.27 this gives

$$I_{\mathrm{SF}} \propto \left|\chi^{(2)}_{\mathrm{NR}}\right|^2 + \left|\chi^{(2)}_{\mathrm{RES}}\right|^2 + 2\left|\chi^{(2)}_{\mathrm{NR}}\right|\left|\chi^{(2)}_{\mathrm{RES}}\right| \cos\Delta\phi \tag{2.28}$$

where $\Delta\phi$ is the difference in phase between the two complex susceptibilities. The right hand cross-term demonstrates a major advantage of SFG over other surface techniques. Not only is it surface specific, but the cross-term shows the non-resonant SF contribution can enhance the resonant contribution.

We now turn our attention to the adsorbate layer. The origins of $\chi^{(2)}_{\text{RES}}$ in such a layer lie in the molecular dipoles. The SF process in vibrational spectroscopy can be thought of as excitation to the first vibrational level by the IR beam, then *up-conversion* to a virtual electronic state by the VIS beam, followed by decay to the ground state throught emission of light at ω_{SF} — figure 2.3. In other words, it consists of an infrared-active process to excite to the first vibrational level followed by a Raman process absorbing the VIS light up to the virtual state and then the emission of SF light down to the ground state. The Raman process is anti-Stokes for SFG and Stokes for DFG. Thus molecules must obey the selection rules for both IR and Raman spectroscopies to exhibit a resonant SF signal.

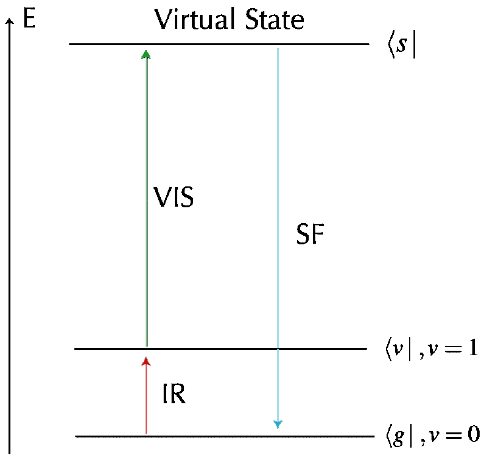

Figure 2.3: Vibrational SFG.

Shen derived an expression for $\chi^{(2)}_{\text{RES}}$ for molecular co-ordinates *l*, *m* and *n*, using a coupled wave approach and perturbation theory ([48, page 171],[56] with adaptations from [57])

$$\begin{aligned}\left(\chi^{(2)}_{\mathrm{RES}}\right)_{lmn} &= \frac{NA_nM_{lm}\Delta\rho}{\hbar\left(\omega_{\mathrm{IR}}-\omega_{\mathrm{v}}+i\Gamma_{\mathrm{v}}\right)}; \\ A_n &= \langle g\left|e\hat{r}_n\right|v\rangle, \\ M_{lm} &= \sum_s\left[\frac{\langle v\left|e\hat{r}_m\right|s\rangle\langle s\left|e\hat{r}_l\right|g\rangle}{\hbar\left(\omega_{\mathrm{SF}}-\omega_{s\to g}+i\Gamma_{s\to g}\right)}-\frac{\langle v\left|e\hat{r}_l\right|s\rangle\langle s\left|e\hat{r}_m\right|g\rangle}{\hbar\left(\omega_{\mathrm{VIS}}-\omega_{s\to g}+i\Gamma_{s\to g}\right)}\right]\end{aligned} \tag{2.29}$$

where A_n and M_{lm} are the IR and Raman transition moments, $e\hat{r}$ is the dipole operator, v, s and g refer to the vibrational, virtual (intermediate) and ground states, $\Delta\rho$ is the population difference between $\langle g|$ and $\langle v|$, ω_v and Γ_v are the vibrational resonance frequency and half-width, and N is the density of surface molecules. This means that the second order resonant susceptibility is proportional to the probability of an IR transition, A_n, *and* a Raman transition, M_{lm}, with an overall (square rooted) Lorentzian profile.

Hence the resonant polarisation in the frequency domain, $\mathcal{P}^{(2)}_{\mathrm{RES}}$, for one dominant transition can be expressed as

$$\mathcal{P}^{(2)}_{\mathrm{RES}}\left(\omega_{\mathrm{SF}}\right) \propto A_nM_{lm}\left(\omega_{\mathrm{SF}}\right)\frac{E_{\mathrm{IR}}E_{\mathrm{VIS}}}{\omega_{\mathrm{IR}}-\omega_{\mathrm{v}}+i\Gamma_{\mathrm{v}}}, \tag{2.30}$$

and the total susceptibility, from equations 2.27 and 2.29, can be written as

$$\chi^{(2)}_T = A_0e^{i\phi}+\sum_n\frac{A_n}{\omega_{\mathrm{IR}}-\omega_n+i\Gamma_n} \tag{2.31}$$

where A_0 and ϕ are the magnitude and phase of the non-resonant contribution, and A_n, ω_n, Γ_n are the amplitude, frequency and half-width of the resonance. It should be remembered that, due to the complexity of both contributions, and the phase relationship between them, the form of SF spectra is not necessarily as intuitively obvious as for absorption spectroscopies. The SF intensity is proportional to the square of equation 2.31 and so the resonant contribution of this intensity should be Lorentzian in form.

Equation 2.31 provides a good working model to fit SF spectra, providing the width of the VIS pulse is effectively a δ-function. However, due to the reciprocal relationship between time and frequency, ultra-short laser pulses have a large bandwidth (section 3.1.2). This has a major advantage for any form of spectroscopy as the large bandwidth removes the need to scan the IR source over a range of frequencies, and instead provides an envelope of frequencies within which all spectral features are visible. This was first exploited for SF studies with a femtosecond laser on self-assembled monolayers by Richter *et al.* [58].

There is however a disadvantage to this in that the VIS beam is usually in practice produced by the same laser oscillator as the IR beam, and if the VIS beam has a finite spectral width then this has an effect on the frequency resolution of the experiment. Each frequency component of a broadband beam is capable of up-converting the IR transition to give an SF emission (figure 2.3) and the resultant spectrum has its spectral features broadened by the width of the VIS pulse. In effect, the spectral profile of the VIS beam is convolved with the SF spectrum [59, 60]. Thus in broadband SF experiments with femtosecond laser systems, the VIS pulse must be spectrally narrowed to maintain spectral resolution. Part of the experimental setup described in the next chapter is the construction of a *pulse shaper* to do just that.

2.3.3 The Free Induction Decay

The total width of a vibrational resonance is given by [61, 62][63, page 12]

$$2\Gamma_{\mathrm{TOTAL}} = \frac{2}{T_2} = \frac{1}{T_1} + \frac{2}{T_2^*}, \tag{2.32}$$

where T_1 is the time-scale of the population decay, T_2^* is the *pure dephasing* time and T_2 is known as the *total* dephasing time. T_1 measures the time taken for individual oscillators to decay to the ground state. T_2^* measures the time taken for oscillators to become mutually out of phase with one another, for example due to substrate phonon processes. The latter process is analogous to dephasing in NMR [61].

It is possible to obtain the total dephasing time T_2 from the linewidth using more traditional spectroscopies. However, ultrafast lasers provide a tool to measure T_2 directly with far greater accuracy than any linewidth measurement. This is known as a *free induction decay* measurement (FID) and involves collecting SF spectra with varying IR-VIS time delays. The IR beam sets up a polarisation in the adsorbate, and the VIS beam arriving a short time interval later up-converts the energy of the polarisation to the virtual state and thus SF light is emitted. The longer the delay, the fewer oscillators will still be in the excited state (i.e. T_1) and still be coherent with other oscillators (i.e. T_2^*). Hence, by plotting the SF intensity as a function of delay, one gets a direct measurement of the combination of these two effects, i.e. T_2. This was first achieved for a surface-adsorbate system for a H terminated Si{111} surface in 1990 [64]. First results for a *metal*-adsorbate system (CO on Cu{111}) were produced by Owrutsky *et al.* [65] in 1992 using a picosecond laser system. This requires a much better time resolution because electron-hole pair-induced damping rates are an order of magnitude faster in metals than in non-metals. Unlike spectrally resolved SF experiments, these require a spectrally broad (temporally narrow) VIS pulse.

From [65, 60, 66] the SF polarisation as a function of time and IR-VIS delay τ is given by

$$P^{(2)}(t,\tau) = E_{\mathrm{VIS}}(t-\tau)\left\{\alpha \int_{-\infty}^{t} E_{\mathrm{IR}}(t')\chi^{(2)}_{\mathrm{RES}}(t-t')\,\mathrm{d}t' + \beta E_{\mathrm{IR}}(t)\right\} + \mathrm{c.c.} \quad (2.33)$$

The fast oscillations of the incoming electric fields have been omitted as their time scale is much faster than the free induction decay and will be averaged out in the next step. The term in curly brackets can be divided up into the resonant interaction of the IR field of strength α and the non-resonant interaction of strength

β. $\chi^{(2)}_{\mathrm{RES}}(t)$ is the response function in the time domain of the adsorbate layer to the IR field, and the total response at time t is the integral of this response function with the temporal profile of the IR electric field. This total response then beats with the field of the VIS pulse, which has been delayed with respect to the IR field by time τ. The intensity of the SF signal is given by time averaging the square of the polarisation

$$I_{\mathrm{SF}}(\tau) = \int_{-\infty}^{\infty} \left|P^{(2)}(t,\tau)\right|^2 \mathrm{d}t. \tag{2.34}$$

The form of $\chi^{(2)}_{\mathrm{RES}}(t)$ depends on the amount of inhomogeneous (i.e. heterogeneous) broadening of the vibrational transition of the chemical system in question. For a pure Lorentzian line (in the frequency domain), $\chi^{(2)}_{\mathrm{RES}}(t)$ will take an exponential form with a decay constant equal to T_2, i.e.

$$\chi^{(2)}_{\mathrm{RES}}(t) = e^{-t/T_2}. \tag{2.35}$$

In this case, equation 2.33 with equation 2.35 substituted is simply the Fourier transform of the general form of the SF polarisation in the frequency domain (equation 2.30, with Γ replaced by $1/T_2$), for VIS pulses well away from resonance [67]. However, for an inhomogeneously broadened system, for example in an adsorbate layer in which the local environments of oscillators are different, then a range of oscillator frequencies will lead to a non-Lorentzian lineshape, and a distribution of T_2 times.

Roke *et al.* [66] have used this to distinguish free induction decays from homogeneous and inhomogeneous systems. Based upon work from [68, 64, 69] they have fitted FIDs from an inhomogeneously broadened system (C-N stretch of acetonitrile on a gold film) using a Gaussian distribution of T_2 values. The fit of this system to a purely exponential $\chi^{(2)}_{\mathrm{RES}}(t)$ is very poor. They do, however, successfully fit the homogeneously broadened C-H stretch of the same system using a pure exponential, and thus can distinguish the two types of systems from FID measurements.

The experiment described herein was initially set up to perform broadband SF measurements in the frequency domain, and femtosecond time resolution FID measurements in the time domain. The development, implementation and day to day running of this experiment is the subject of the next chapter.

Chapter 3

Experimental Development

3.1 The Laser System

3.1.1 Overview

In order to perform time resolved vibrational sum-frequency spectroscopy, sources of infrared and visible ultrafast laser pulses are required. All these pulses originate from one source in our laboratory: the Femtosecond Oscillator (Spectra Physics *Tsunami*). This is pumped by a 10 W argon ion laser. The pulses are then amplified by a Spectra Physics *TSA* regenerative laser amplifier, which in turn is pumped by a Nd:YAG laser with a repetition rate of 10 Hz. This arrangement is shown schematically in figure 3.1 and photographically in figure 3.2. The train of pulses from the amplifier is then split into two variable parts. One of these is passed into an Optical Parametric Amplifier (OPA), which is our tunable source of mid-infrared light. The other is passed through a self-built pulse shaper which allows the pulses to be spectrally narrowed for good spectral resolution, or to be passed unaltered for good temporal resolution. This section should be read in close conjunction with the next chapter, which describes laser pulse characterisation techniques.

The laboratory is air conditioned to a tolerance of one degree Celsius as all the lasers are sensitive to quite small temperature fluctuations, especially the oscillator. The oscillator ceasing to mode lock is often the first sign of the air conditioning failing, often hours before people would otherwise notice. We have very recently enclosed the entire main laser table with a self-built metal framework (not shown on figure 3.2), from which hang 20 cm wide polythene strips to keep dust and air currents away from the lasers, whilst simultaneously allowing easy access and beams to emerge where needed. This frame has a double-ply polycarbonate "roof" which stops the quite large air currents from the air conditioning affecting the optics, and acts as a resting place for the polythene strips when access is needed to the table. In the centre of the "roof" there is now a laminar flow fan / filter unit so that the lasers are sufficiently cooled without having draughts directly aimed at them.

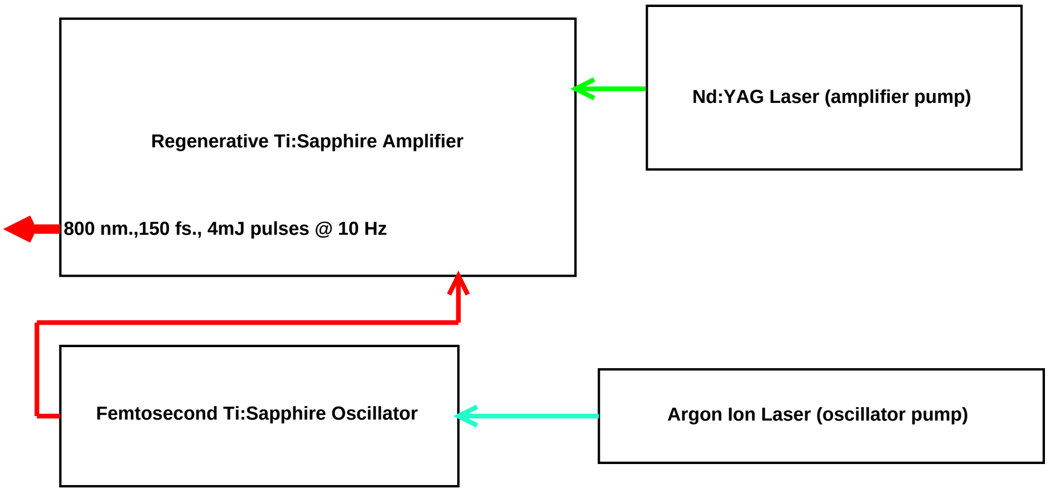

Figure 3.1: The femtosecond laser system.

Figure 3.2: Photograph of the laser system, showing clockwise from bottom right: the argon ion oscillator pump laser, the *Tsunami* femtosecond oscillator, the TSA amplifier and the Nd:YAG amplifier pump laser.

3.1.2 The Oscillator

Pulse Generation

Central to all that is to come in this discussion is the idea of the reciprocal relationship between time and frequency — the Fourier transform. Ultrashort pulses essentially originate from the ultrawide emission spectrum of the lasing medium. The medium in question is Titanium Sapphire, a crystal made by adding Ti_2O_3 into a melt of Al_2O_3. A small percentage of the Al^{3+} ions are replaced by Ti^{3+} ions. This produces a medium in which the spectra of absorption and emission are both remarkably wide (figure 3.3). In theory at least, an emission spectrum of $\sim$ 150 nm can produce pulses as narrow as $\sim$ 1 fs. The spectral properties of Ti:Sapphire are discussed in more detail in [70].

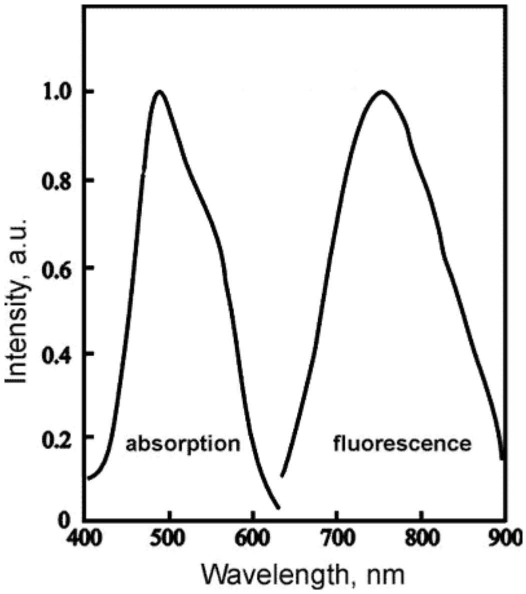

Figure 3.3: Ti:Sapphire absorption and emission spectra.

A temporally confined laser pulse should, by the uncertainty principle, have a wide spread of energies, and hence frequencies. That is to say, a wave packet localised in time will consist of many Fourier components. This is generally achieved by forcing all the modes (or frequencies) present in a laser cavity to lase together simultaneously, and hence to superpose themselves into the form of a wave packet. This process is known as temporal mode-locking [71, chapter 8.6]. It is usually achieved by introducing some controllable energy loss process into the laser cavity such that undesired modes are eliminated [72]. Early attempts at this used an acoustic wave shutter which scattered light from modes not required in the pulse. Another method involved placing dye jets in the cavity, to absorb or amplify certain frequencies. An intense pulse would bleach the dye, thus reducing loss of the modes in that pulse, and hence selectively propagating that mode [73]. Ti:Sapphire was originally incorporated into lasers as a replacement for dye lasers, mainly for aerospace applications. However, it was found that a simple laser design using Ti:Sapphire produced very short pulses, without deliberately setting about to do so. The effects of *self mode-locking* had been observed [74, 75, 76].

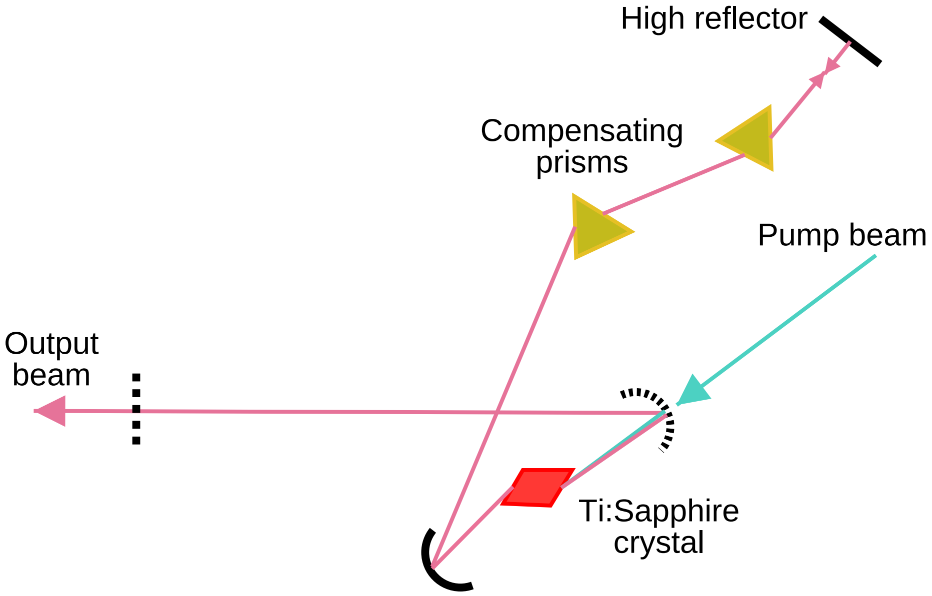

Figure 3.4: Design of a simple Ti:Sapphire laser.

A design for a basic Ti:Sapphire oscillator is shown in figure 3.4. It consists of a fairly long cavity, as this determines the temporal spacing between pulses. Due to its length, two additional mirrors are used to focus the cavity beam tightly in the Ti:Sapphire rod. Self mode-locking relies on the fact that the refractive index of Ti:Sapphire is nonlinearly dependent upon pulse intensity. Laser beams have an approximately Gaussian intensity profile [71, chapter 4], and thus the beam is more intense in the centre of the lasing rod. This in turn gives a differential refractive index through the crystal's cross section, essentially turning the rod into a lens (a so called *Kerr Lens* [71, p344-345]). This selectively focuses high power modes, localised in time, and by arranging the cavity mirrors to exploit this, self mode-locking of the shortest pulses can be achieved. An initial short "seed" pulse can be generated by many methods, the simplest of which is to physically tap the laser. The prisms in the basic design compensate for the positive dispersion produced in the Ti:Sapphire rod [77, 75]. This effect is caused by the fact that the refractive index of most materials, and hence the speed of light in that medium, is a function of wavelength. In the laser rod the longer wavelengths travel faster than the shorter wavelengths, and over many passes through the cavity this would separate in time (or *chirp*, section 4.1.3) the wavelengths and modes present in the cavity. The prism pair produces a spectrum of the pulses, and then forces the longer wavelengths to travel further, hence slowing them down. The spectrum is then recombined in the second prism. This concept is further exploited in the laser amplifier, see section 3.1.3.

The *Tsunami*

The commercial femtosecond oscillator we use is produced by Spectra Physics [78], and is their *Tsunami* model. The absorption spectrum of Ti:Sapphire, figure 3.3, makes it particularly suitable for pumping by an Argon Ion laser source. Our oscillator pump is a Spectra Physics BeamLok™ capable of supplying a continuous wave pump beam of up to 10 W in power, although the day to day running power is around 7.5 W. The *Tsunami* produces 800 nm pulses of around 90 fs in length, vertically polarised; see page 106 and figure 4.5 for a measurement of this. The cavity length is such that a repetition rate of around 82 MHz is achieved, and the average power is about 1 W. Figure 3.5 shows the internal configuration of the *Tsunami*. The AOM is an acoustic-optical modulator which assists the initial mode locking of the laser and provides stability of the repetition rate. The dispersion compensator consists of four prisms, and in the centre of this configuration (whilst the beam is spectrally spread) there is a slit consisting of two movable knife edges. This allows a particular part of the spectrum to be selected, thus enabling user control over the bandwidth and centre wavelength. We display the spectrum of the *Tsunami* using a dedicated rotating grating spectrograph (Rees Instruments) connected to an oscilloscope, and adjust the micrometers which control the slits accordingly. Successful mode-locking is indicated by a broad spectrum, with no continuous wave “breakthrough”, which would manifest itself as a delta-function in the spectrum. A typical spectrum from the spectrograph is shown in figure 3.6. Apart from this adjustment, the main day to day alignment merely consists of fine adjustment to the end reflectors to optimise the output energy. The argon ion pump and the *Tsunami* take around an hour to warm up before use, and are generally trouble free if kept at a very constant temperature and are not subjected to mechanical shocks.

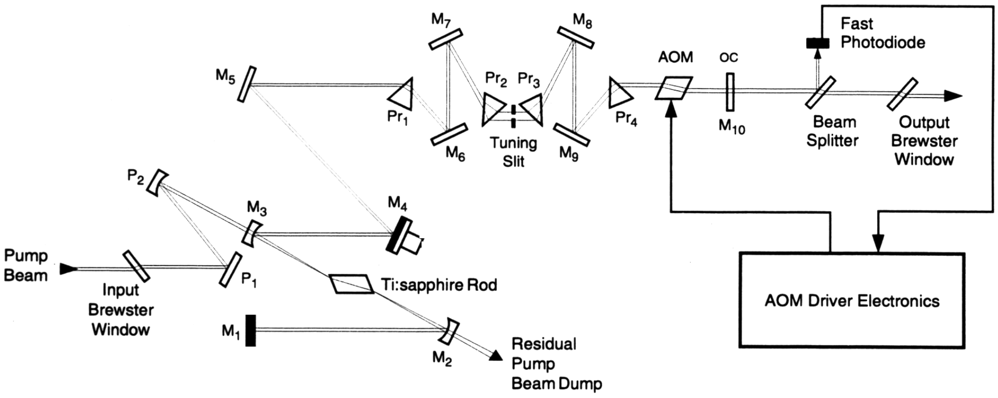

Figure 3.5: Schematic of Spectra Physics *Tsunami* femtosecond oscillator. Adapted from that given in the manual.

3.1.3 The Amplifier

The *Tsunami* produces pulses of around 10 nJ in energy. A much higher energy than this is required for nonlinear applications, so an amplifier forms the next stage of the laser system. The amplifier is a Spectra Physics Titanium Sapphire

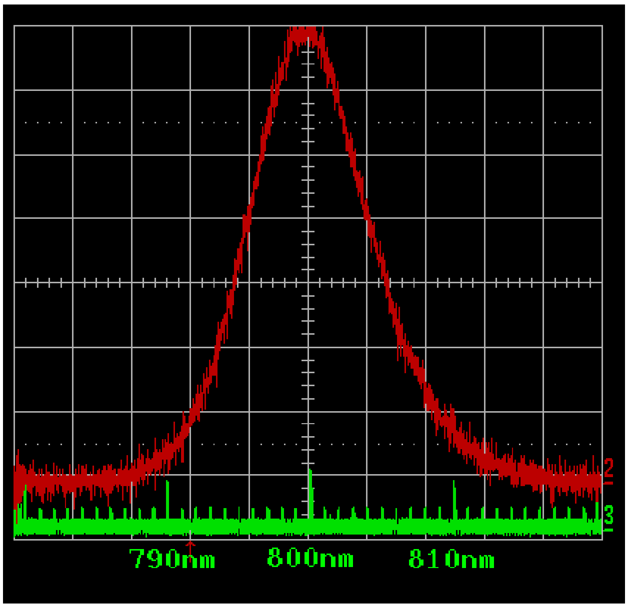

Figure 3.6: A typical spectrum of the *Tsunami* oscillator displayed on an oscilloscope. The numerical scale has been added for clarity.

Amplifier (TSA). It is pumped by a Nd:YAG laser. I shall discuss this pump laser and then outline the main principle of the amplifier's operation, chirped pulse amplification (CPA).

The Nd:YAG Pump Laser

The TSA is pumped by a Spectra Physics *Quanta Ray* Nd:YAG laser (Nd:YAG is the lasing medium, Neodymium doped Yttrium Aluminium Garnet [79]). This laser uses pulsing electrical discharge lamps to excite a Nd:YAG rod. The laser cavity has a controllable *quality factor*, allowing deliberate losses to be introduced into the cavity by an electro-optical switch. This enables a large population inversion to be built up in the lasing medium by suppressing lasing whilst the cavity is lossy. The energy stored in this way can be suddenly released as an intense pulse by *switching* the quality factor of the cavity to high. Hence this form of mode locking (section 3.1.2) is known as *Q switching* [71, chapter 8.4]. Nd:YAG lasers produce nanosecond pulses at 1064 nm, but to bring this into the absorption band range of the Ti:Sapphire (figure 3.3) used in the amplifier, it is frequency doubled with a nonlinear optical crystal to 532 nm. Our Nd:YAG laser operates at a 10 Hz repetition rate, which defines the repetition rate of the whole laser system. This generally gives higher amplifier energies, but lower stability when compared with 1 kHz systems. The latter is largely due to a low repetition rate allowing thermal cooling of optical components between pulses. The amplification system in use was originally purchased for gas phase studies where a high energy was needed, but for pumping an OPA for infrared studies stability would be much more desirable. A higher repetition rate also allows spectra to be collected faster. We have recently converted the Nd:YAG cooling system from the original closed loop water and air cooling system to a system thermostatically cooled by the high pressure water system in our building. This has seen great improvements in the stability of the amplifier during a working day. The discharge lamps used in the Nd:YAG laser gradually deteriorate, and during intense experimental activity may have to be replaced every month or so to keep the TSA running to the stability needed by the OPA.

A further improvement to the reliability of the amplification system has involved removing the feet from the TSA and screwing its base directly to the optical table. This has reduced the tendency of the entire TSA casing to warp with physical and thermal pressures, thus affecting the cavity length and lasing performance.

Chirped Pulse Amplification

I described in section 3.1.2 above how Ti:Sapphire self-focuses an already intense laser beam. If a Ti:Sapphire rod were to be employed in a naïve laser amplifier as the lasing medium, the extraordinary intensities produced by this would quickly destroy the crystal. CPA [80] gets around this problem by *stretching* the ultra-short pulse in time, thus reducing its peak power, then amplifying it, and finally *compressing* the pulse again to *almost* return its original short duration, figure 3.7 [71, sections 12.3.1 and 12.5]. Given the reciprocal relationship between time and frequency, given by the Fourier transform, one way to stretch a pulse is to split the pulse up into its spectrum, allow the higher frequency ("bluer") light to travel further in space than the lower frequency ("redder") light, and then recombine the spectrum in a further grating, figure 3.8. This introduces a *positive group velocity dispersion*, otherwise known as a positive *chirp* - the frequencies present in the pulse change over the pulse duration (see section 4.1.3 for details on how to measure chirp). This spreads the power present in all frequencies over the pulse duration, and hence reduces the peak power. After amplification the chirp can be removed by a similar arrangement, this time the low frequencies are delayed with respect to the high frequencies. This latter process is exactly the same as that employed in a femtosecond oscillator using prisms to remove the positive chirp introduced by the lasing medium, see section 3.1.2 above.

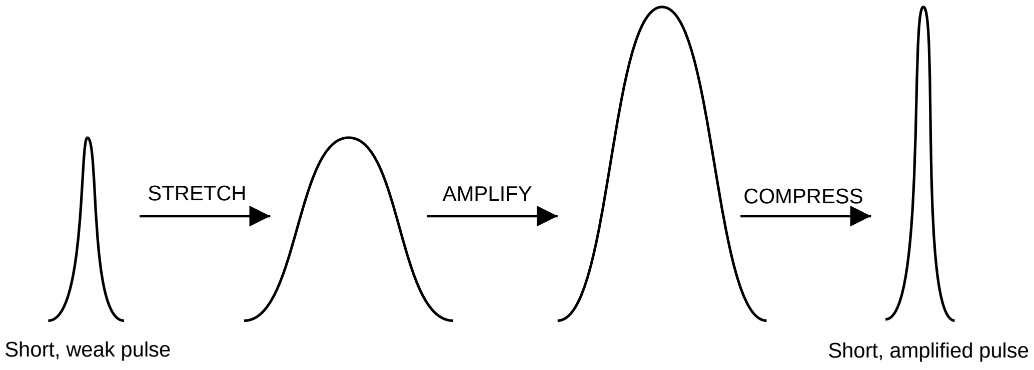

Figure 3.7: Chirped pulse amplification.

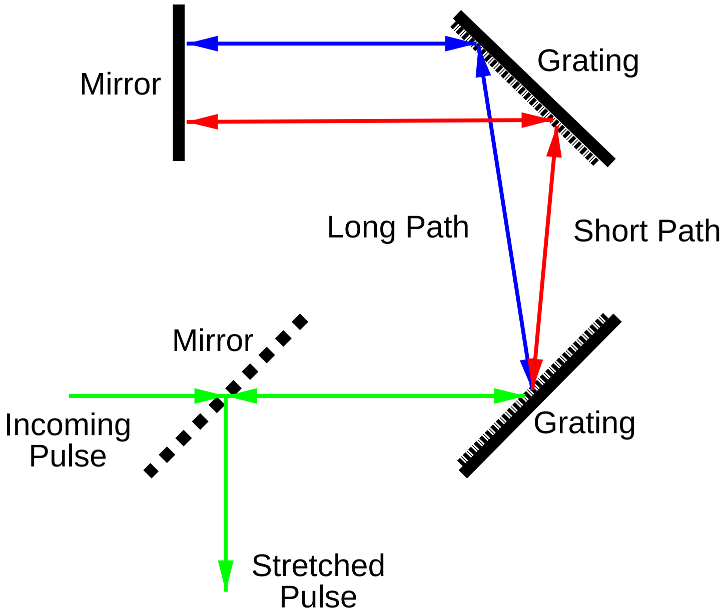

Figure 3.8: A pulse stretcher. Compression may be performed by the inverse process.

The *TSA*

Our TSA is not a standard production unit, as it was in fact built by a previous coworker in the *Spectra Physics* factory using their parts but to a slightly different design. The TSA has four main stages. As described above, it has a pulse stretcher to avoid damage to the optical components during amplification. Then it has a *regenerative amplification* stage, followed by a two-pass *multipass amplification* stage (or “double pass” stage). Finally, there is a pulse compressor which nearly restores the original pulse width. See figure 3.9 for a detailed schematic. Overall, it produces pulses of around 4 mJ at 800 nm, at a repetition rate of 10 Hz.

The following description of the operation of the TSA is with reference to the key letters on figure 3.9. Also table 3.1 on page 47 lists the polarisation of the seed (amplified) beam as it passes through various stages of the TSA. The vertically polarised pulse train from the *Tsunami* (in red) enters at the top of the diagram and passes through a *Faraday Isolator*, [a]. This is in effect an optical “diode” which allows passage of light in one direction only, thus stopping any back-reflected pulses from the amplifier reaching and damaging the *Tsunami*. This also changes the polarisation to horizontal. The pulse train passes over a mirror [b] and is incident on the stretcher grating [c]. This grating with the curved focussing mirror at [d] and a plane mirror [e] form the pulse stretcher as described above. In fact only one grating is used compared with figure 3.8; mirrors [d] and [e] are arranged so that the light is incident on the one grating four times to give the same effect as the arrangement with two gratings in figure 3.8. This makes the system cheaper to manufacture and also ensures consistent alignment. The pattern of beams on the grating is shown in figure 3.10. The stretched pulses then pass back below their incident path on to the mirror at [b], and finally via a “twisted” periscope (which changes the polarisation again) and another mirror on to the Ti:Sapphire rod [f]. Meanwhile, the Nd:YAG 10 Hz pulse train enters from the left hand side of the diagram, shown in green. Approximately 25% of this energy is reflected from a beam splitter [m] on to the Ti:Sapphire rod. The remainder is used to pump the double pass amplifier.

I shall now describe how a single stretched pulse from the *Tsunami* is regeneratively amplified. The now vertically polarised pulse reflects at the Brewster angle from the Ti:Sapphire rod [f] and passes along the dashed path through a *Pockel’s cell* [g]. This is a device which can rotate the polarisation of light when subjected to a large electrical potential difference. This potential is turned off at this stage, and remains so for the duration of the first pass of the amplifer. The pulse passes through a quarter wave plate [h] which rotates its polarisation by $\lambda/4$. Having then been reflected from the first cavity mirror [i] and passing back through the $\lambda/4$ plate once more, its polarisation has been rotated by $\lambda/2$ in total. It passes

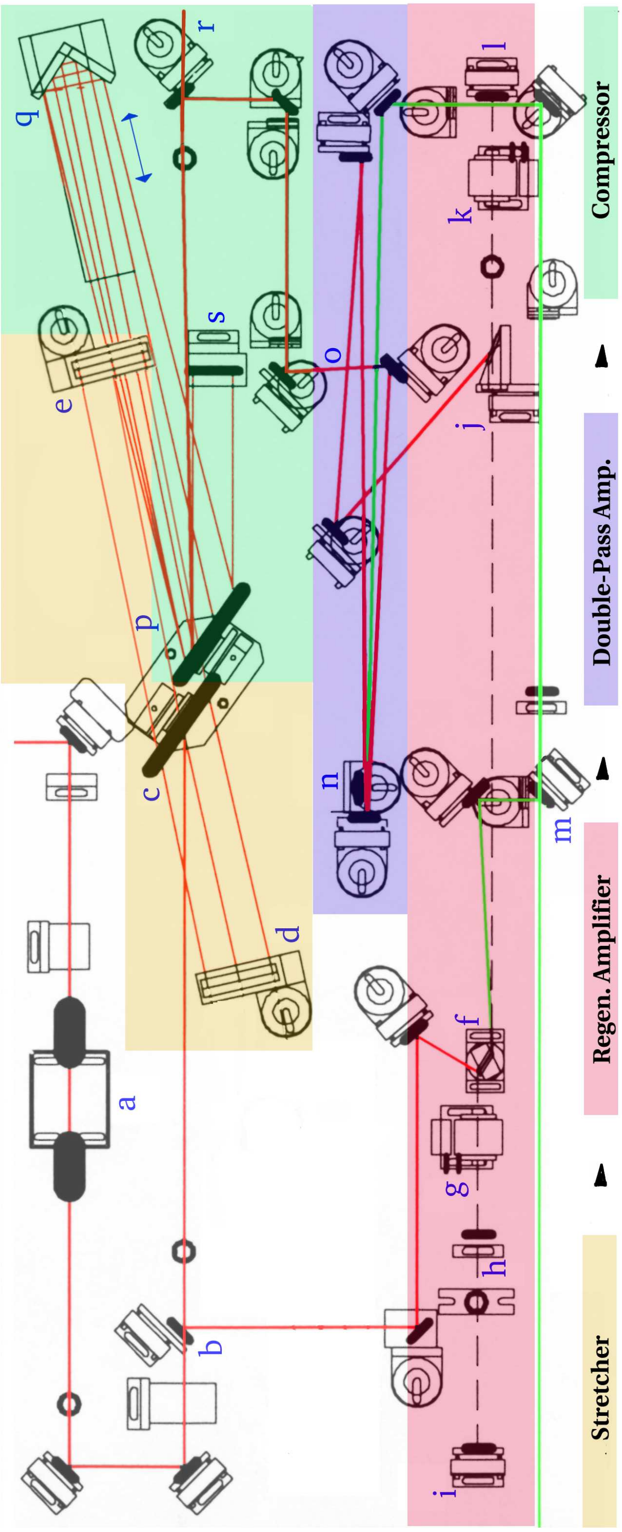

Figure 3.9: The TSA regenerative amplifier, see text for key. Based upon that given in the manual, but corrected for our non-standard unit; colourised and key added for clarity.

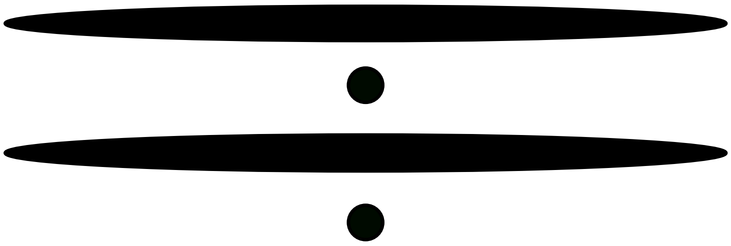

Figure 3.10: Correct light pattern on the stretcher grating.

through the laser rod, picking up energy from the rod's excitation by the Nd:YAG pulses, then straight through the polariser at [j], through a second Pockel's cell [k] (which is off) and is reflected from the second cavity mirror [l]. It passes back on to the polariser, at the Brewster angle. Because the pulse has undergone a $\lambda/2$ rotation from the quarter wave plate, it passes straight through the polariser and then back through the rod. By the time the pulse reaches the first Pockel's cell [g] again it has been activated such that is acts as a quarter wave plate, effectively resetting the pulse back to its original polarisation over two passes so that in combination the quarter wave plate has no further effect. Thus the horizontally polarised pulse is trapped in the cavity. After a user defined interval (see alignment description) over which the pulse may be amplified by as much as 10^6, the second Pockel's cell [k] is activated to rotate the polarisation by $\lambda/2$ before the pulse passes through the polariser [j] for the last time. This change of polarisation to vertical causes the pulse to be reflected from the face of the polariser at the Brewster angle and hence to be ejected from the cavity. At the end of this stage the pulses can be up to 5.5 mJ in energy.

The next stage is a simple double pass amplifier in which the pulse passes through (once in each direction) a second Ti:Sapphire crystal [n], which is pumped by the remaining 75% of the Nd:YAG beam. This stage will amplify the pulses to about 12 mJ. A telescope arrangement [o] enlarges the beam and a second twisted

After this stage…	The polarisation of the seed is…
Tsunami	V
Faraday Isolator	H
First Twisted Periscope	V
Trapped in Cavity	H
Released from Cavity	V
Second Twisted Periscope (& exit)	H

Table 3.1: Polarisation of the 800 nm beam as it passes through the TSA.

periscope converts the polarisation to its final horizontal state, before the beam passes on to the compressor grating [p] via mirror [r]. The compressor grating is mounted on the same rotatable stage as the stretcher grating [c], enabling the angle of one to be precisely complementary to the other; thus in theory compensating exactly. The remainder of the compressor consists of pairs of vertical [s] and horizontal [q] retro-reflector mirrors. The latter of these is mounted on a translation stage which allows it to be moved closer to or further away from the grating, giving control over the amount of pulse compression which occurs. The correct pattern of the four passes of the beam on the compressor grating is shown in figure 3.11. After the final grating pass the beam passes over the mirror [r] and out of the amplifier, at about 5 mJ per pulse, the losses being mainly in the compression stage.

Figure 3.11: Correct light pattern on the compressor grating.

Alignment

The TSA is one of the most complex and troublesome components of the entire experiment. Basic alignment has to be performed each day, and sometimes re-performed during the day. Temperature gradients and changes in the lab caused by baking the UHV chamber (see section 3.2.1) adversely affect the entire laser system. The TSA is used at maximum output power and up to its manufacturers' specifications; and, in terms of stability for use with an OPA, must exceed those specifications — *Spectra Physics* specify 10% stability, but in fact 2% is needed for the OPA. I describe here the basic alignment procedure. Complete realignment of the laser cavity is beyond the scope of this thesis, although it has been performed by us on occasion. Everyday alignment is performed with an energy meter (Ophir), thermal burn paper to check spatial mode, and a photodiode (Positive Light) connected to a fast oscilloscope (LeCroy Waverunner) which monitors stray cavity light from behind mirror [l].

The TSA cavity, with the incoming *Tsunami* seed beam blocked and the second (exit) Pockel's cell disconnected is in fact a free running laser in its own right. The intensity profile over time from the photodiode is shown in figure 3.12. The time axis is with respect to the Nd:YAG pump pulse entering the cavity, and shows how the 800 nm pulse loses energy as it is reflected around the cavity and as the population inversion builds up and decays in the amplifier's lasing medium. The key to aligning the TSA is to ensure that pulses spend as little time in the cavity as possible whilst still being amplified sufficiently. This is because refractive components in the cavity will inevitably introduce some dispersion (chirp) into the pulses, so the pulses should pass through these as few times as possible. With this in mind, the first step is to ensure that the free running laser pulse occurs as early as possible after the pump pulse enters the cavity. Adjustment of the angle of the frequency doubling crystal in the Nd:YAG laser can improve this by increasing

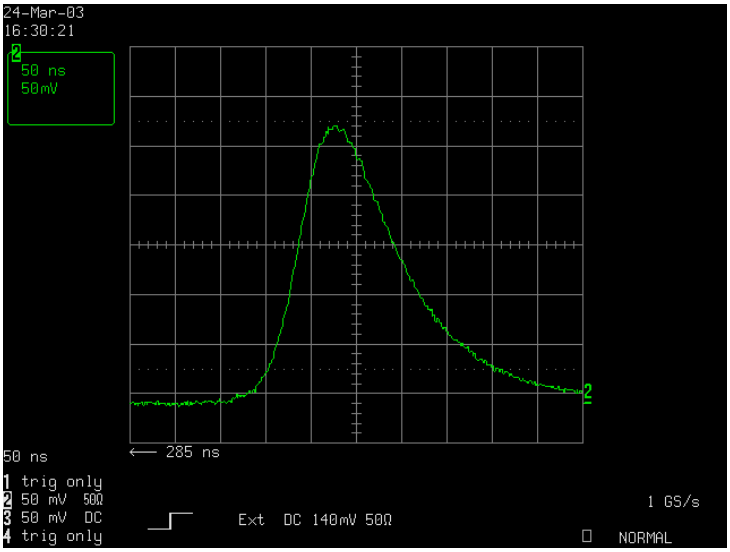

Figure 3.12: The intensity profile wrt. time of the TSA cavity in free running mode. The time axis on these oscilloscope traces is 50 ns per square and the Nd:YAG pulse occurs 285 ns before the left hand edge of the trace in this case.

the output power of the pump. This crystal and the Nd:YAG flash lamp energy should be occasionally adjusted so that the average energy of the Nd:YAG laser is 2.1 W. The free running cavity beam should also pass through the two alignment irises provided in the cavity; this can be checked with an infrared “night-sight” style viewer. Occasionally adjustment of the cavity end mirrors is necessary, but this should be a last resort.

Meanwhile the seed beam enters the TSA via two irises. The angle of the stretcher grating rotation stage should be adjusted until the pattern matches that in figure 3.10. When the seed is allowed into the cavity, with the second Pockel’s cell disconnected, the intensity measured by the photodiode resembles that in figure 3.13. Each of the small peaks corresponds to a round trip of the ultrafast pulse through the cavity. The seed beam should overlap the free running cavity beam on the laser rod and on the cavity end mirrors (this can be viewed with the infrared

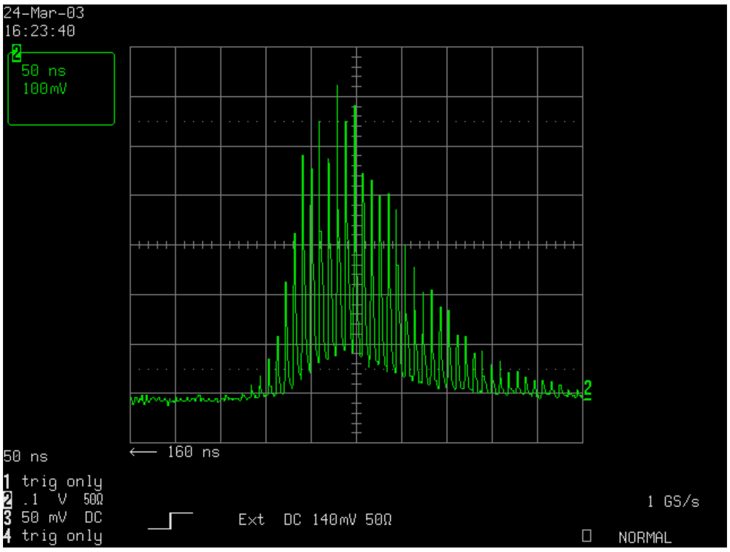

Figure 3.13: TSA with seed beam trapped in the cavity. Nd:YAG pulse occurs 160 ns to the left of the trace.

viewer). From figure 3.13 one can see that there is a optimum time for a pulse to spend in the cavity to gain maxiumum amplification. The user may set the time which the pulse spends in the cavity with a dial on the Pockel’s cell control electronics, and with the second Pockel’s cell connected an optimal pulse dump time gives a cavity intensity plot like that in figure 3.14. This must be studied carefully to allow fine tuning of the seed beam dump time to ensure multiple weaker pulses are not dumped. The dump time does affect the stability quite dramatically as well as the output energy and in general more stable pulses are achieved with longest dump times. Finally, the last steering mirror of the pump beam and the steering mirrors into the cavity for the seed beam should be adjusted to optimise output energy and to ensure the pulses leave the cavity as early as possible. Also, the cavity mode and spatial profile should be checked with thermal burn paper to ensure the single regular round spot TEM_{00} mode is being produced rather than, for example, the double spot TEM_{01} mode.

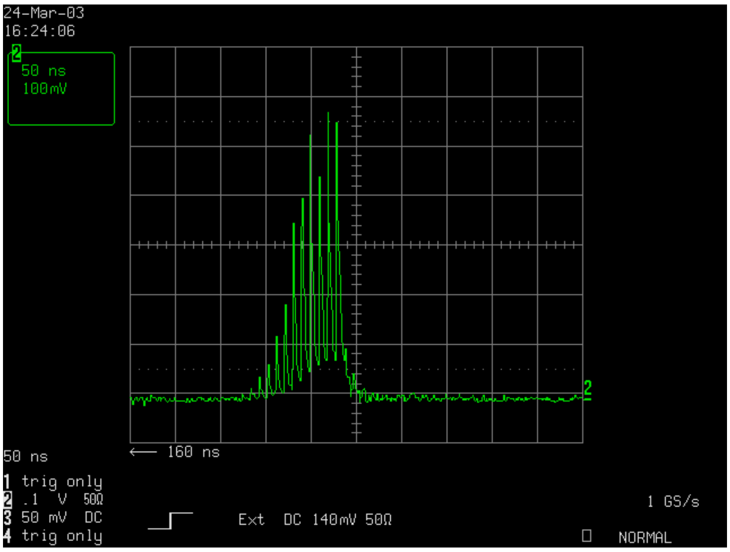

Figure 3.14: TSA with seed beam leaving the cavity after the optimal delay (in this case the delay is 321 ns from the Nd:YAG pulse). Nd:YAG pulse occurs 160 ns to the left of the trace.

With the seed beam now centred on the Ti:Sapphire rod [n] in the double pass amplifer, the pump for this part of the amplifier should be steered to maximise the energy output from this section. The mode should also be checked after this stage.

With the stretcher / compressor grating assembly removed (and the seed beam blocked), the free running cavity beam should now pass along the same path as the incoming seed to the stretcher, and through two irises provided for this purpose, although it is not necessary to do this every day. With the grating assembly reinserted the pattern on the grating should resemble that in figure 3.11. The adjustment to the compressor length [q] to ensure the shortest pulses may be undertaken by (a) watching the intensity of the frequency doubled output beam when put through a BBO crystal set to the correct angle, (b) by checking the performance of the OPA, (c) by using an autocorrelator (section 4.1.2) or (d) frequency resolved optical gating (FROG - section 4.2). FROG gives a plot of the frequencies present in a pulse as a function of the time duration of the pulse and gives feedback on more serious misalignments of the compressor, to ensure all chirp is removed. A typical FROG from the TSA is shown for reference in figure 4.6 during the discussion in the next chapter on pulse characterisation. The beam should be visually inspected on a white card for signs of diffraction (stripes) indicating that the beam is passing close to or being blocked by non-optical components.

3.1.4 The OPA

The Optical Parametric Amplifier (OPA) provides a source of infrared laser radiation tunable from 3–11 μm. The nonlinear process which underpins its operation is described in the previous chapter in section 2.2.2.

TOPAS

Our commercial OPA is a femtosecond version Travelling-wave Optical Parametric Amplifier of Superfluorescence (TOPAS) designed by Light Conversion Ltd. [81, 82, 83]. It is capable of producing pulses of 3–11 μm by taking the difference frequency of the signal and idler waves produced in the OPA. The combined signal and idler output is around 300 μJ per pulse and the mid infrared output is around 10 μJ per pulse. We have measured the temporal width to be 240 fs and the spectral width to be 150 cm^{-1} at 5 μm output (section 4.3.3). A basic outline of its operation is given in figure 3.15. The design of the TOPAS is such that only one BBO crystal is used for all 5 stages of amplification in the OPA section, due to the high cost of such crystals and the need for a consistent phase matching angle to be maintained. The first pass generates a broadband source of light by intensely focusing around 5% of the pump onto the BBO crystal and generating what is known as *superfluorescence* [48, section 21.7]. The second and third passes selectively amplify the signal wavelength component of the broadband light — the

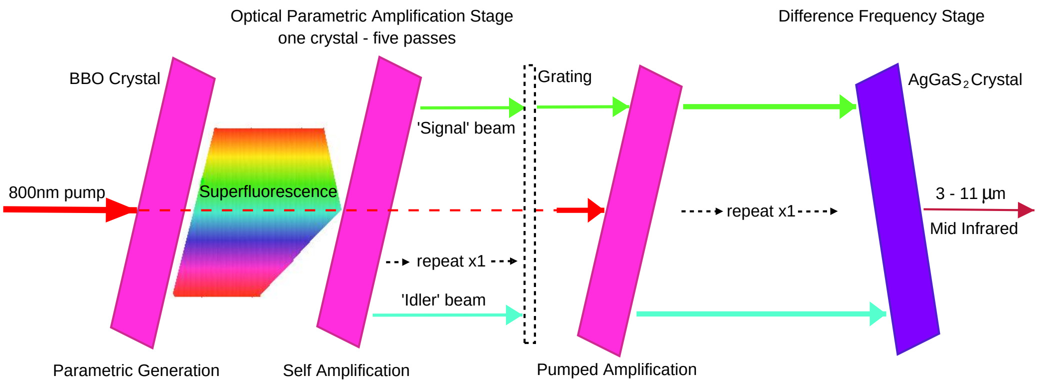

Figure 3.15: Outline of TOPAS optical parametric amplifier.

idler is *not* amplified at this stage and is effectively dumped. The bandwidth of the OPA is constrained further by reflecting the signal from a diffraction grating. Then the remainder of the pump beam is used to actively amplify the signal and idler; 5% on the fourth (pre-amplifier) pass and the remaining 90% on the fifth (power amplifier) pass. This last pass leads to saturation of the parametric conversion process which reduces pulse to pulse fluctuations. Finally the signal and idler pass into a separate section which generates the difference frequency in an AgGaS$_2$ crystal to produce mid infrared light. For example, to produce 5 µm light, the BBO crystal is set to produce the signal wave at 1380 nm and an idler wave at 1900 nm, $\frac{1}{800\text{nm}} = \frac{1}{1380\text{nm}} + \frac{1}{1900\text{nm}}$. Then the phase matching angle of the AgGaS$_2$ crystal is set to give the difference frequency, $\frac{1}{1380\text{nm}} - \frac{1}{1900\text{nm}} = \frac{1}{5000\text{nm}}$. The disadvantage of this system is that a very complex arrangement of passive optics and active path length controls is needed to route the beam through the crystal 5 times, at the same phase matching angle each time. A (still simplified, 2D) schematic of the optical layout of the OPA section is given in figure 3.16. The majority of the pump pulse (90%) is split off by BS1 for the final 5th power amplification stage. Then 10% of what is left is split off by BS2 for the fourth pre-amplification stage. The remainder is focused by a lens system on to the BBO crystal (marked NC on

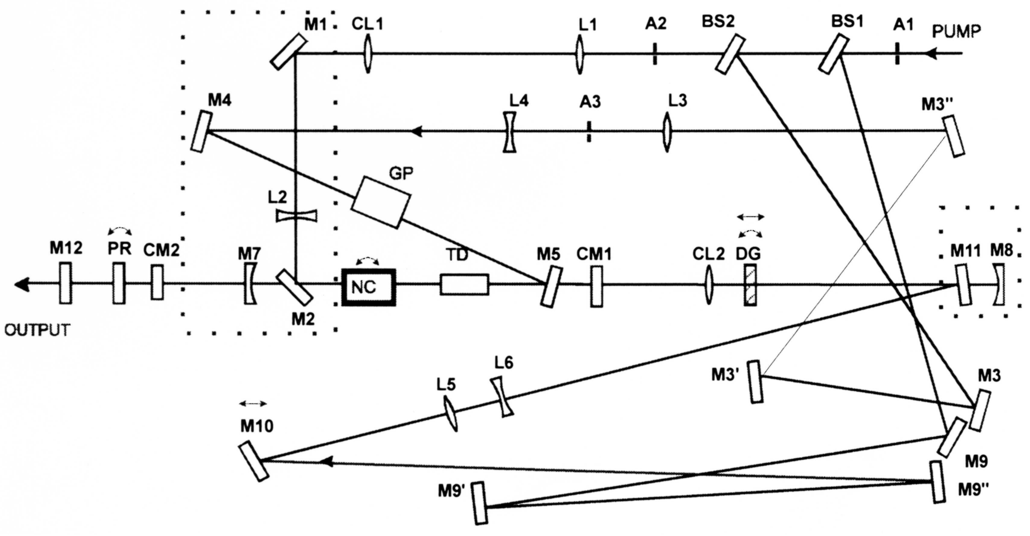

Figure 3.16: Schematic of TOPAS OPA section — taken from the manual.

the diagram). This crystal is on a motorised rotation stage to enable frequency tuning. Superfluorescence is now generated by the intense beam and passes on to mirror CM1 and back through the crystal (pass 2). The signal and idler pulses, plus the rest of the broadband light are reflected from CM2 and pass back through the crystal a third time. By now the correct signal and idler frequencies will have been selected by the BBO crystal from the superfluorescence spectrum, so a diffraction grating (DG — again motorised) is used to narrow the bandwidth further. Meanwhile the fourth pass pump has been delayed by mirrors M3, M3′, M3″ and M4 and a glass plate (GP) which is on the same rotation stage as the BBO crystal to compensate for path differences and directional changes caused by the crystal angle. This ensures the pump beam arrives for recombination at beamsplitter M5 at the same time as the signal and idler. The diffraction grating is on a mechanical delay stage which enables this delay to be adjusted. The pump, signal and idler now pass through the crystal again for the fourth time and the signal and idler are amplified. The fifth pass pump has been delayed by mirrors M9, M9′, M9″ and M10, the last of which is on a motorised delay stage to optimise the temporal overlap. After the signal and idler are reflected from M7 (this time *not* passing through the crystal, but through a piece of glass marked as TD on the diagram) they are recombined with the rest of the pump on mirrors M11 and M8. Finally the pump, signal and idler pass through the crystal for the 5th time when the latter two undergo power amplification before leaving the OPA section.

The signal and idler then pass into the difference frequency mixer section (figure 3.17). The remaining pump beam is dumped by a beamsplitter (not shown). This is of sufficient energy to provide a pump beam for pump-probe spectroscopy. Being of different frequencies and having passed through dispersive materials, the signal and idler are not perfectly temporally overlapped at this stage, so beam splitter BS1 separates the signal and idler allowing the delay between them to be removed by mirror M3 and the delay plate. M3 is on a manual delay stage for coarse adjustment, and the delay plate is a piece of glass on a motorised rotation stage which can introduce a small amount of delay due to the changing internal path length as the plate rotates. The signal and idler are recombined by beamsplitter BS2, which is motorised so that the angle of divergence of signal and idler can be changed. Finally, they pass non-collinearly through the $AgGaS_2$ crystal (which is on a motorised rotation mount to optimise phase matching) to give the difference frequency. The non-collinear arrangement is less efficient than a collinear arrangement but allows the signal, idler and mid IR to be spatially separated without the use of a lossy filter. The three emitted beams are separated in the vertical plane, the mid IR at the bottom, the signal in the middle and the idler uppermost. The signal and idler are useful for alignment purposes as they are of higher energy than the mid IR and they are each collinearly accompanied by a visible harmonic as a side effect of the nonlinear processes in the OPA — they can effectively be seen as blueish green dots on a card (see section 3.3.4). They are removed during experiments either spatially with an iris or by inserting a filter.

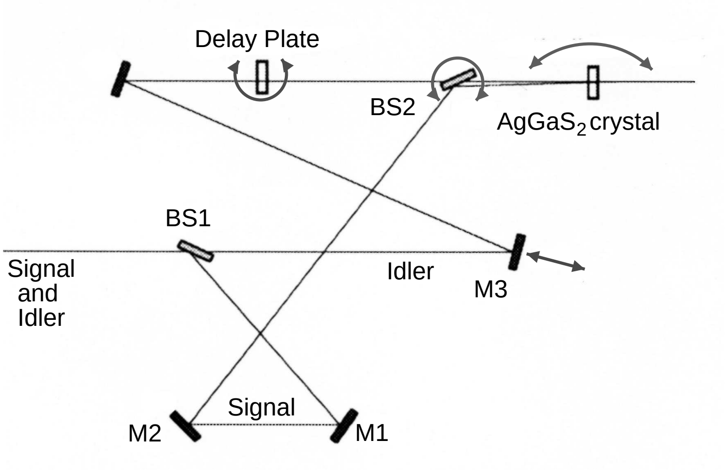

Figure 3.17: Schematic of TOPAS DFG section — adapted from the manual.

The TOPAS contains a total of six control motors: the BBO crystal angle (and hence the output wavelength); the fifth pass pump temporal overlap; the diffraction grating angle; the difference frequency crystal angle; the signal-idler delay in the mixer and the final signal-idler divergence angle. Each of these motors has an optimal position for a particular mid-infrared output frequency. Selecting a desired wavelength is achieved using a computer to access a look up table containing appropriate values for each motor and to interpolate for the exact required frequency. Upon installation and subsequent realignment of the OPA a set of empirical tuning curves is taken by measuring the output wavelengths and energies of the signal and idler waves whilst finely stepping the motors. The software for this is part of the package sold by Light Conversion. Whilst fortunately offering much more long term stability than the TSA, the OPA does require periodic realignment and retuning, especially after a few UHV system bakeouts. To counteract this, the OPA has been removed from the laboratory during bakeouts, but we came to the conclusion that more damage was done by the movement than the bakeout. Ideally, realignment and tuning should be performed by one of the Lithuanian based design engineers and takes around 3 days (30 hours). Due to the inconvenience of this I have now learnt to do this procedure which takes me just over a week. The details of the realignment procedure are beyond the scope of this thesis, and the reader is referred to the long and detailed instruction manual — but it should always be borne in mind that the threshold for superfluorescence is close to the damage threshold of the expensive BBO crystal. TOPAS is very sensitive to the condition of its pump beam, and requires ideally 2 mJ in energy with a stability of around 2–5%, optimally short pulses with a good round spatial mode, and with no *phase front tilt* — see section 4.1.4. Day to day pump alignment is performed coarsely through the two irises A1 and A2 in figure 3.16, and finely by measuring the mid-infrared energy output.

3.1.5 The Pulse Shaper

As discussed in section 2.3.2, the spectral resolution of vibrational SF spectroscopy is dependent upon the spectral width of the visible pulse. A spectrally narrow and therefore temporally long visible pulse gives high spectral resolution. Some groups, such as Richter *et al.* [58] achieve this by inserting a mirror into the compressor assembly in their regenerative amplifier to divert a small range of the spectrum out of the amplifier for use as the visible pulse. This would not be practical for us, due to the geometry of our compressor. At the same time, an option is required to use temporally short visible pulses for free induction decay and photon echo experiments. To achieve that aim, we have constructed a pulse shaper capable of either selecting a narrow region of the visible pulse spectrum, or to allow it to pass unaltered when needed. A grating based pulse expander is used to transform the pulse into the frequency domain for bandwidth selection, and then transform exactly back to the time domain with no increase in pulse width when the full bandwidth is allowed to pass.

In the following, the term *group-delay dispersion* (GDD) refers to the second order coefficient in the Taylor series expansion of the relationship between the phase, ϕ of a pulse and its frequency, ω in a general dispersive situation, i.e. $\frac{d^2\phi}{d\omega^2}$ in

$$\phi = \phi_0 + \left(\frac{d\phi}{d\omega}\right)_{\omega_0} (\omega - \omega_0) + \frac{1}{2}\left(\frac{d^2\phi}{d\omega^2}\right)_{\omega_0} (\omega - \omega_0)^2 .$$

The relationship [71, page 349] between the time stretching factor, $\Delta\tau$, the pulse width, $\Delta\omega$, and the GDD is given by

$$\Delta\tau \cong \left|\left(\frac{d^2\phi}{d\omega^2}\right)_{\omega_0}\right| \Delta\omega. \tag{3.1}$$

For a general pulse expansion system consisting of two gratings and two lenses (figure 3.18), the GDD is given by Martinez [84] as

$$\left.\frac{d^2\phi}{d\omega^2}\right|_{\omega_0} = \frac{4\pi^2 c}{\omega_0^3 d^2 cos^2\theta} (2f - s_1 - s_2) . \tag{3.2}$$

where d is the grating spacing, θ is the angle the normal of the grating makes to the optic axis, $s_{1,2}$ are the distances from the first and second gratings to the first and second lenses and f is the focal length of each lens. From equation 3.2 and figure 3.18 it can be seen that, in general, for $s_{1,2}$ and f the paths of higher and lower frequencies will no longer spatially or temporally exit the system simultaneously — in the setup shown in figure 3.18 the high and low frequencies are separated along the spatial width of the exit beam, and the low frequencies travel further than the high frequencies. However, if the system is set up such that $s_1 = s_2 = f$, then equation 3.2 shows that no GDD will be introduced, and hence via equation 3.1, no time expansion will occur. Also, the high and low frequencies will then emerge along the same spatial path. Given that the arrangement is then perfectly symmetric, it is better to use just one grating and one lens; and use a mirror to exactly bisect the arrangement in figure 3.18 and reflect the beams back through the same lens and onto the same grating once more. This mirror should be vertically tilted to allow the incoming and outgoing paths to be spatially separable. A slit can then be inserted in front of the mirror to select a proportion of the spectrum to increase the spectral resolution when needed. This is the arrangement we have used and it is shown schematically in figure 3.19 and photographically in figure 3.20. The grating has 1200 groves/mm (made by Spectrogon) and is mounted on a rotation stage which also allows slight vertical tilt, and is set to an azimuthal angle, θ, of around 17° for maximum energy in the first grating order. The focal distance, f, and separation distance, s, are around 16 cm and can be changed by moving the optics on the rail. Each is also on a miniature translation stage aligned along the direction of the rail for fine adjustment. The lens is on a vernier rotation stage to allow for exact alignment of the lens axis with respect to the optical axis, and the mirror is held in a standard 2D adjustable mirror mount. The slit assembly (Edmund Optics) consists of two metal knife edges, the distance between which, and hence the selected bandwidth, is adjustable with a micrometer. The maximum slit width is 6.35 mm, as is the height of the slit. It is mounted, via a system of metal posts, on a lateral translation stage to select the

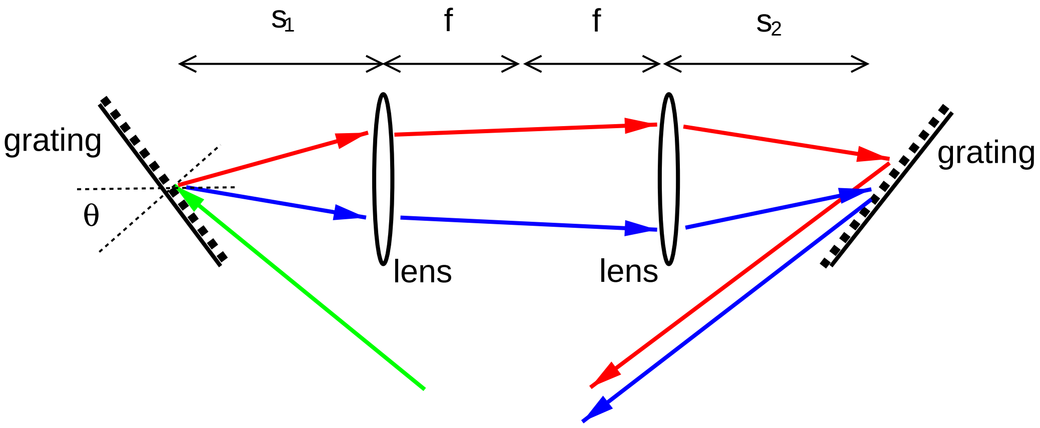

Figure 3.18: A general pulse expander.

section of spectrum required. This stage is mounted on the rail *behind* the mirror, and the post system ensures that the slit is suspended in front of the mirror. The slit is removed and inserted by either sliding the assembly down a collared post, or by rotation. The exiting beam is in a plane slightly below that of the incoming beam (adjusted by the incoming mirrors and the vertical tilt of the shaper mirror) and it is picked off by a square mirror placed just under the path of the incoming beam (shown in the centre of figure 3.20).

With the slit removed, the pulse shaper is first geometrically aligned by eye and a ruler, then finely adjusted using FROG (section 4.2), which determines the temporal and spectral characteristics of the pulse. The FROG trace of the TSA output is compared with the FROG trace of the pulse shaper (figures 4.6 and 4.7 in the next chapter). The shortest pulses with the least chirp are achieved by adjusting the distances along the rail and the angle of the lens. Small changes make a very large difference indeed. Once this has been optimised, two irises are inserted in the incoming beampath for future reproducibility. The output energy

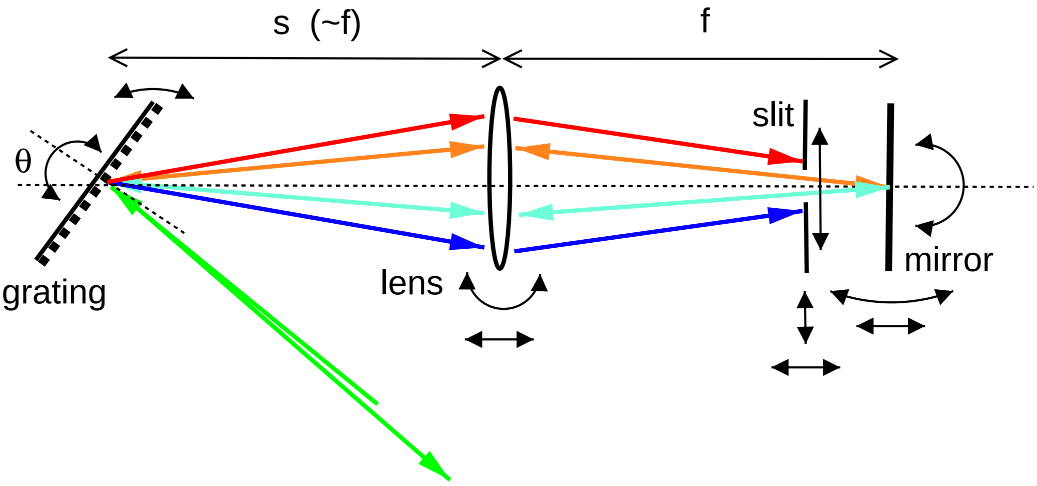

Figure 3.19: Schematic of the pulse shaper.

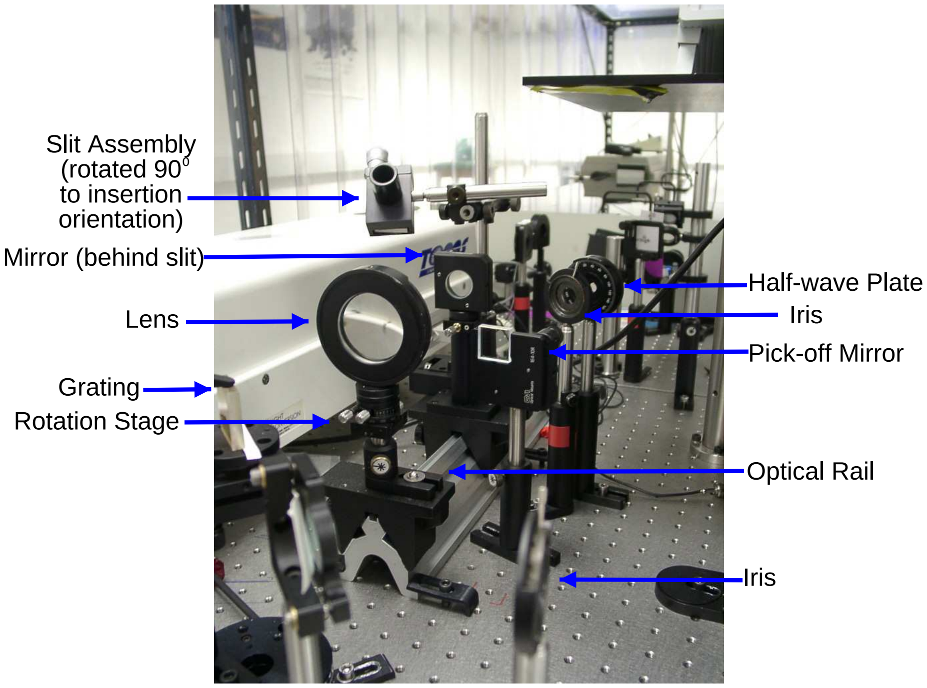

Figure 3.20: Photograph of the pulse shaper. The white OPA is seen as the left backdrop and the TSA and Nd:YAG laser are in the far background.

from the shaper is then measured, and along with the centre wavelength is used as a reference to check for accurate reproducibility upon reinsertion of the slit at a later stage. Details of the characteristics of the narrowed visible pulses used in spectrally resolved experiments are given in section 4.3.3.

The operation of the pulse shaper has been simulated using Sarkomand Software's Apple Macintosh based CyberRay program. One view of the photon traced 3D image produced is given in figure 3.21. It was produced by simulating broadband 800 nm pulses, with a Gaussian beamwaist, and neatly shows how our pulse shaper takes a broadband source, and produces a narrowband output with the same spatial size and divergence as the incoming beam.

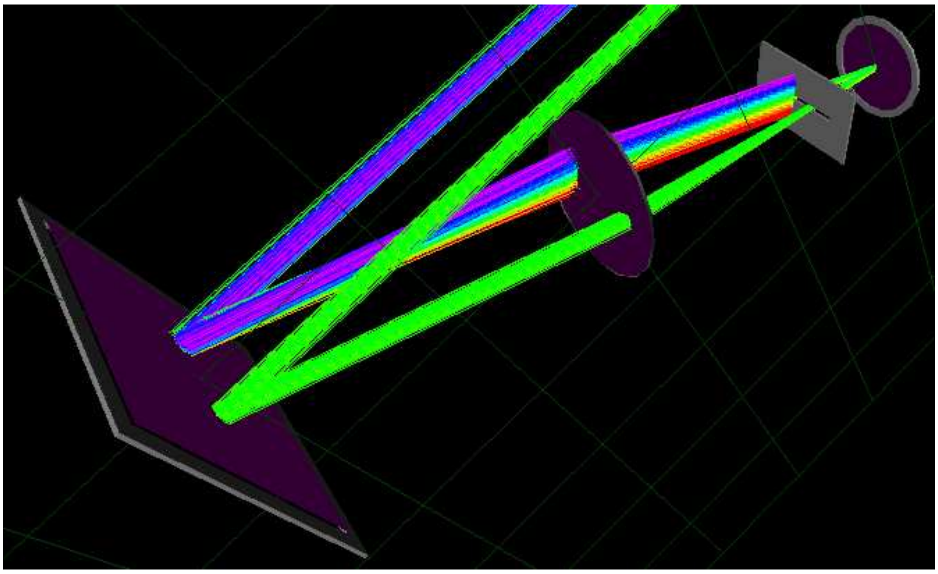

Figure 3.21: Photon traced simulation of the pulse shaper, using CyberRay. For clarity, the image is shown at a 90° anticlockwise from left rotation around the main optical axis as compared with figures 3.19 and 3.20. The incoming broadband beam is multicoloured in the background, and the outgoing narrowband beam is green in the foreground. Left to right are the grating, lens, slit and mirror.

3.2 The UHV Chamber

Sum frequency spectroscopy is adaptable enough to be used in a variety of environments. Unlike many surface probe techniques, a vacuum environment is not required *per se*. Indeed, when setting up the SFG system the technique was practised in our lab on the benchtop — see section 3.3.4. However, to study well ordered single crystal metal–adsorbate systems, ultra high vacuum is required. This is both to maintain the cleanliness of the surface from contaminants which might alter the chemical processes which we wish to study, and because many of the traditional surface characterisation techniques require vacuum.

3.2.1 Overview

Our laboratory is equipped with a UHV chamber made by Vacuum Generators, originally used for Electron Energy Loss Spectroscopy (EELS) studies — a photograph is given as figure 3.22. The sample is suspended vertically by a 3D manipulator (at the top) and can be moved between two main experimental levels. The upper level has a quadrupole mass spectrometer, LEED system, ion sputter gun, gas dosing valve plus optical windows. The lower level has optical windows, an electron gun for AES and a Getter source for alkali metal layer deposition. It is this level which is used for SFG experiments. The chamber contains a hemispherical analyser for Auger studies mounted on a gimbal and goniometer assembly to allow movement around the sample.

Pumping

The pumping system is represented schematically in figure 3.23. The main chamber is pumped to rough vacuum (10^{-3} mbar) by an Edwards rotary pump. Then an oil diffusion pump (backed by another rotary pump) is used to take the vacuum down to around 2×10^{-10} mbar, after bakeout. The diffusion pump has a liquid nitrogen cooled trap between the chamber and the pump. This has to be filled twice a day whilst undertaking experiments so that oil particles from the pump stick to the cold trap. The rotary pumps both have sorption traps to collect pump oil and other impurities from the line. The diffusion pump requires both continuous electrical and water supplies (the latter for cooling). Due to continual disruptions in recent years to these two services in our building, we have recently fitted an ion pump to the base of the vacuum chamber (Varian Diode). This requires only electricity, and the power is backed from the building's emergency generator supply. Thus, providing the gate valve is closed between the chamber and the diffusion pump, vacuum is always maintained even during power or water failures.

Figure 3.22: The UHV chamber. The optical table has been removed.

The pressure in the chamber is monitored by an ion gauge (Varian), as is the pressure in the UHV section of the gas line. Two pirani gauges monitor the backing pressure of the diffusion pumps, and a third monitors the roughing rotary pump pressure. To reduce leakage from the rotary feedthrough, the sample manipulator is differentially pumped by the roughing pump. This reduces the pressure gradient across the seals, see section 3.2.2.

Gas Admission

Gases are supplied to the chamber via a small gas line. Each of the gases is connected to this line with Nupro type valves which are in turn connected to the

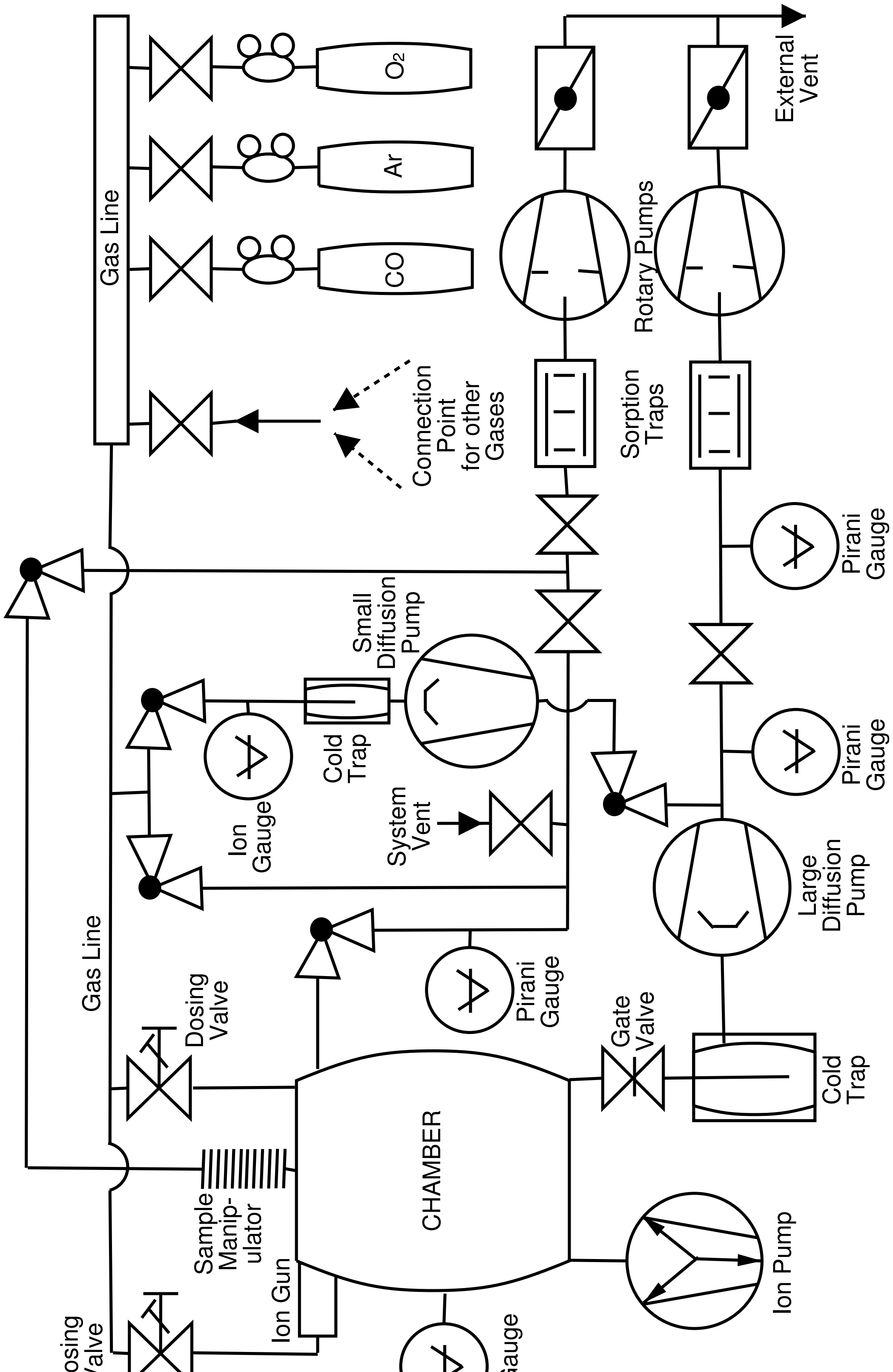

Figure 3.23: The vacuum system. See text for explanation.

gas bottle regulators. Carbon Monoxide, Argon and Oxygen are permanently available and other gases are connectable to a Swage-Lok type connection when required — at the moment this includes hydrogen, ethylene, NO and various isotopes of CO. Vapour from volatile liquids (e.g. benzene, water) can also be admitted via this connection. The gas line is pumped to rough vacuum by the same rotary pump which rough-pumps the chamber. It is also connected via a valve to a second, smaller, diffusion pump which can take the pressure in the gas line down to about 10^{-7} mbar. This is useful for studies involving small quantities of gas isotopes. Gas is admitted to the chamber by a copper plate and knife-edge style dosing valve placed between the chamber and the gas line. Argon may be admitted through a secondary dosing valve, which passes directly into the plasma chamber of an ion gun (discussed in section 3.2.2).

Optical Windows

In order to introduce laser beams into the chamber, it is fitted with several optical windows. Infrared beams are admitted via a magnesium fluoride window. MgF_2 has a useful transmission range of 0.12–7.0 μm, whilst being physically strong enough, at 3 mm thick, to withstand UHV conditions. All other windows are glass. The plan view of the lower level of the chamber is shown in figure 3.24 as it is this level which has the largest number of available ports, giving the most options for incoming and outgoing beam directions; hence this is the level at which SFG experiments are performed.

Maintenance

Before opening the chamber it is vented via a valve connected to the roughing pump / gas line system. The venting is done with liquid nitrogen to avoid contamination. After venting, the chamber must be baked to remove deposits from its

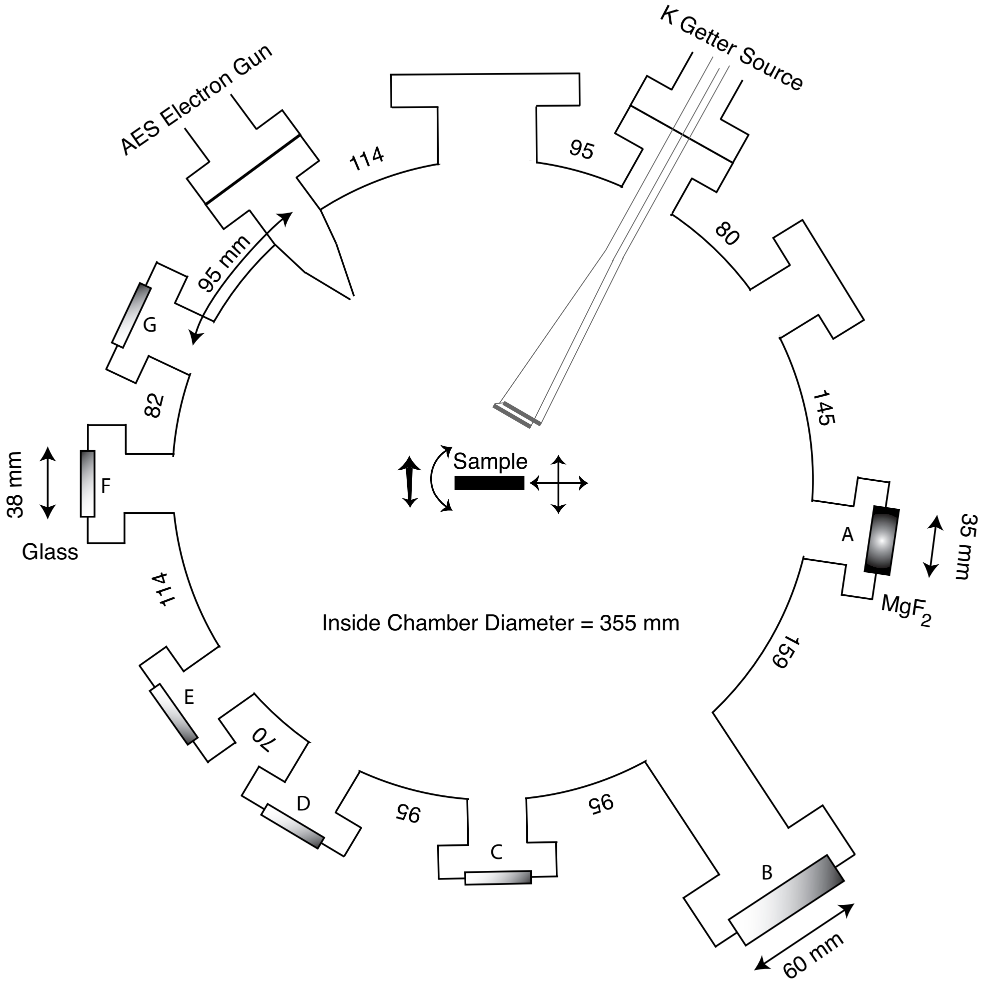

Figure 3.24: Plan view of optical level of UHV chamber. Five small plain glass windows (C–G), one large glass window (B), one small MgF$_2$ IR window (A), the AES electron gun, the potassium Getter source and two blanked-off ports are shown. The bulky AES analyser, which in fact takes up most of the interior, is not shown.

walls. The chamber is surrounded on its plinth by heating elements and is completely enclosed in a custom insulated cover before baking; glass windows and other delicate items being covered with aluminium foil to reflect the heat. It is usually baked for 48 hours at a temperature of 115° Celsius, whilst monitoring the pressure. The ion pump has an integral heating element to remove material deposited on its walls during the pumping process. Unfortunately, the baking process does create quite a large temperature gradient in the laboratory, further increased by the fact that the air conditioning tends to overcompensate and reduce the temperature to sub-normal levels at the opposite end of the lab. This significantly affects the laser system, and usually means much realignment, so bakeouts should be kept to a minimum. Flange seals on the chamber are made by a copper gasket and knife-edge system; those on the gas line system are a combination of these and Swage-Lok style connections. All *in vacuo* electrical connections are spot welded.

3.2.2 Sample Manipulation and Preparation

Sample Motion

Azimuthal rotation is achieved by a differentially pumped rotary feedthrough (Vacuum Generators). The roughing rotary vacuum pump is used to pump the non-UHV side of the seals to reduce the pressure difference and hence the likelihood of a leak. The x and y motion is achieved with orthogonal micrometer screws at the top of the chamber. The z motion is achieved by a vertical screw thread which lifts the whole crystal mount, a set of external bellows providing vacuum integrity during the motion. This screw is driven by a geared electric motor, as it takes a considerable time to raise and lower by hand. It may prove necessary in the future for certain types of pump-probe experiment to motorise the other two axes, in order to allow the sample to be automatically moved during experiments so that fresh areas of adsorbate are exposed to the laser beam — see section 6.4.1 for more details on this matter.

Heating and Cooling

For studies involving many metal-adsorbate systems it is necessary to be able to cool the sample to 100 K for the adsorbate to stick in an ordered layer, and to be able to heat to 1550 K to remove oxygen from the sample. Single crystals to be mounted in our chamber must first have 0.5 mm groves cut in the top and bottom thin edges. This is done for us by Metal Crystals and Oxides (Harston, Cambridgeshire) before the polishing process, which they also perform. The grooves are lined with tantalum foil to improve thermal conductivity, then lengths of 0.38 mm Tungsten wire bent as shown in figure 3.25 are inserted. These wires both support the crystal and heat it when a current is passed through each of them. This arrangement, suggested by Yates [85][86, pages 504-5], has the advantage that when the crystal is heated the two loops differentially remove any linear expansion which would force the wire from the slot, or cause the crystal to tilt — very important for laser work. Also, it removes the need to spot weld to the sample, which is difficult for ruthenium. The crystal is held by a slight spring tension from the tungsten wires.

The tungsten wires are screwed onto copper blocks, which supply the heating current. The copper block assembly is mounted on the end of a long steel reservoir (“cold finger probe”) which can be filled with liquid nitrogen via the funnel shown uppermost on figure 3.22. This cold finger also mechanically connects the sample mount to the top of the manipulator. The thermal connection between the left and right copper block assemblies and the central copper block is achieved with 2 mm thick sapphire discs. This provides good thermal contact, whilst providing complete electrical insulation. The thermal contact is improved further with a thin piece of indium foil coating each side of each sapphire disc. This smooths out any surface area imperfections. The heads of the screws connecting the outer copper blocks to the central column are tightened onto countersunk ceramic electrical

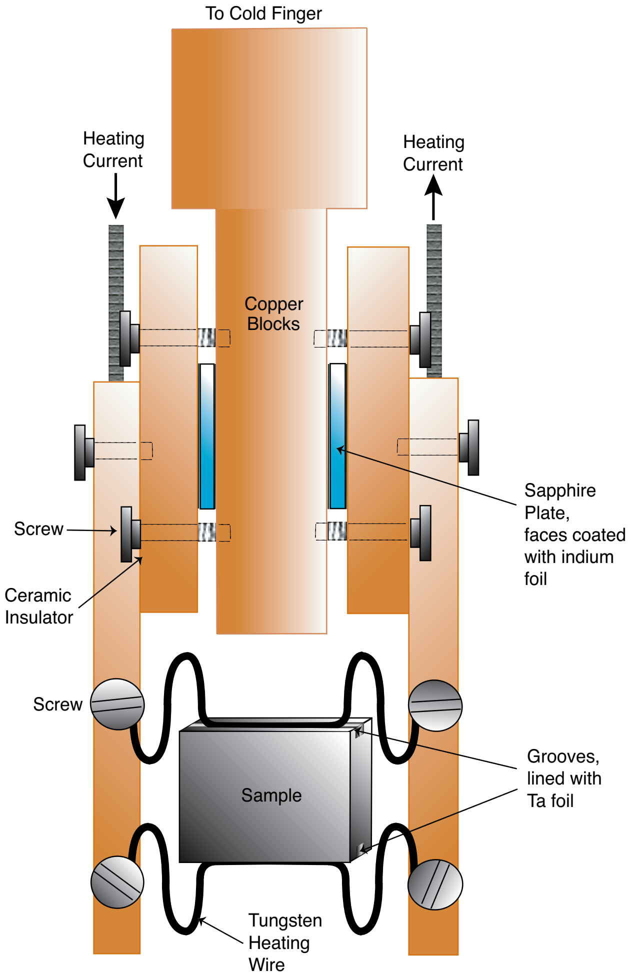

Figure 3.25: Sample mount.

insulators. This is also all shown in a photograph in figure 3.26.

A chromel-alumel thermocouple junction is spot welded to the reverse side of the sample. This was chosen as it is one of the few thermocouple types to work over the large temperature range we use. It is connected to a programmable thermal controller (Eurotherm) which drives a 0–30 A power supply (Kenwood). The thermal controller has an adaptive algorithm which can be used to tune the

Figure 3.26: Photograph of sample mount and Ru$\{10\bar{1}0\}$ crystal.

heating process so that it is more or less critically damped. With this arrangement, a 30 A current can heat a 1 cm square by 4 mm thick sample to around 1450 K, and the sample can be cooled to a minimum of 95 K. An additional 10 A power supply, connected in parallel, can be used to heat the sample to 1550 K, which is necessary to remove oxygen from Ru$\{10\bar{1}0\}$. This must be used sparingly though, as this temperature approaches the melting point of the thermocouple (1650 K), and the weld supporting the junction may fail slightly below the melting temperature. A typical heating and cooling curve is shown in figure 3.27. The heating current shown in this is not constant, as it is not prudent to expose the mounting system to the full 30 A of current from cold. The fastest linear ramp we use is 4 Ks^{-1}. The exact cooling and heating times may vary by ± 5 minutes from the time shown depending on the pressure exerted on the sample by the tungsten wires. The tungsten wires are much hotter than the crystal, so the high temperature limit arises mainly from T^4 thermal radiation from the relatively large area of the sample.

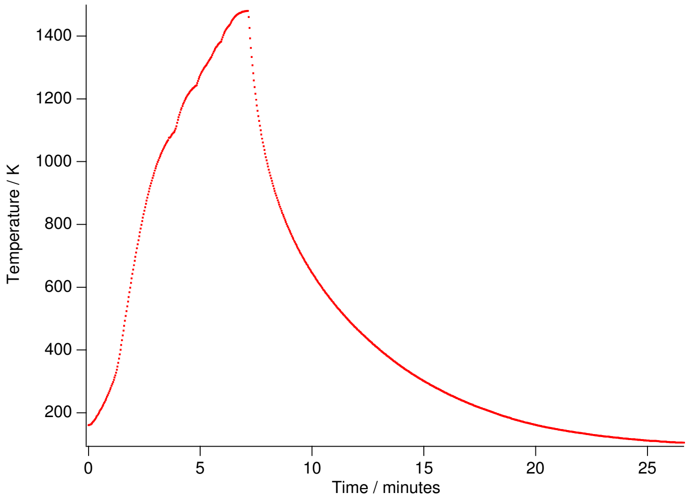

Figure 3.27: Typical sample heating and cooling curve wrt. time. Heating current *not* constant — see text.

The main disadvantage of this system is that the sample mounting tends to settle after a couple of heatings, and the sample does not always end up perfectly vertical; and small changes in the vertical tilt make a large difference to the exit angle of laser beams incident on the surface. After the initial settling, the orientation of the sample does not seem to alter significantly. Also, the copper blocks next to the crystal restrict the laser beam geometry. An alternative was tried, similar to that used by the Surface InfraRed Emission (SIRE) project in our group [87]: this involved vertically mounted 3mm tungsten rods, which have been spark drilled (with thanks to the Department of Engineering in the University) — see figure 3.28. In each of the two holes on each rod was inserted a short horizontal length of tantalum rod, which is relatively easy to spot weld. To these two rods were welded a vertical length of tungsten wire, which was then welded to the back of the sample, using tantalum foil as an interface. A pair of these tungsten / tantalum mounts was used, each being attached to copper blocks similar to those shown in figure 3.25, thus putting the heating current across the *sample*. I performed a computer simulation of this system, which iteratively models the nonlinear heat flow. This was based upon the Pascal algorithm given in [87], but adapted for our manipulator and Ru$\{10\bar{1}0\}$ crystal, and rewritten in C. The simulation appeared to give satisfactory heating and cooling times, but when the idea was built and tried in situ, cooling times were impractically slow to enable coverage dependent studies to be undertaken in which many desorption cycles are needed; the idea was abandoned.

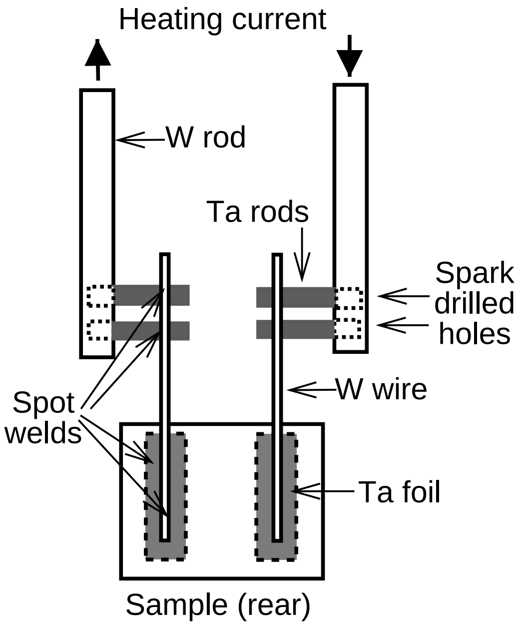

Figure 3.28: Alternative sample mount.

Ion Sputter Gun

The top level of the chamber is fitted with an ion sputter gun. This is used to clean a sample by removing a few layers of the top surface by bombardment with argon ions. Bulk impurities may be removed by elevating the sample temperature during sputtering, allowing them to diffuse to the surface for removal. Originally a gun made by Physical Electronics was fitted, for which the chamber had to be back filled with argon to a pressure of 10^{-5} mbar. It is possible to measure the effectiveness of sputtering by directly measuring the electric current from the sample to earth, this being proportional to the number of ions per second hitting the sample. This was found to be negligible due to either a fault in the gun or the controller, so the entire gun / controller system has been recently replaced by another. This gun (VSW Instruments AS10) is of a slightly different type, which produces a low pressure argon plasma. It has a feedthrough allowing argon to be directly fed through the gun, via a second dosing valve (as in figure 3.23). The procedure is to turn on the hot cathode filament and the accelerating bias, then to increase the chamber pressure with argon through this valve to $\sim 4 \times 10^{-5}$ mbar until an arc is struck; the filament emission current then rises, and the gas pressure can then be reduced to about 1×10^{-5} mbar. By measuring the drain current the sample position and focus can be optimised. Up to 10 μA of drain current has been measured with this gun. After sputtering, a sample must be annealed at high temperature to restore surface order. The cleaning recipe used for the Ru$\{10\bar{1}0\}$ sample is detailed in section 5.2.1.

Getter Source

The Getter source is used to deposit an ultra-thin layer of an alkali metal on the sample. This is useful in surface science as alkali metals act as promoters for many catalytic reactions. We were originally intending to use this to study the effect of co-adsorbed alkali metals on the water photodissociation reaction described in section 1.1.3. The source is quite simple, consisting of three wire loops all at the central chamber level, in the position shown in figure 3.24. A 17 mm long potassium metal dispenser (SAES Getters) is spotwelded across, linking one loop to another, with the emission slot facing the sample. A second dispenser is welded from the third loop to one of the other two, the latter now acting as a common connection. When 6–7 A of current is put across either source, it glows and potassium is emitted from the slot in the dispenser at a rate of a few monolayers per minute. Two dispensers are provided in case of burnout or exhaustion; replacement involves dismantling the chamber and exposing to air. The connections are in the form of loops rather than straight wires, as the two terminations of each loop can have 10 A of current passed through them to degas the long wires. A second source has recently been added, to dose caesium. This was built by us by adapting an old titanium sublimation pump and does not have the degassing loops.

3.2.3 Sample Characterisation

Detailed below are three main techniques available to us to study the cleanliness and order of a sample.

Temperature Programmed Desorption

TPD is the process of ramping the temperature of a sample, and monitoring the desorbed species. This monitoring is performed with a quadrupole mass spectrometer (VG Quadrupoles Masstorr 200) which in our case is mounted at the top level of the chamber. The controller unit generates a voltage which is proportional to the partial pressure at the current set mass, and this voltage is fed into a lock-in amplifer, used in this case as a simple analogue to digital converter.

The lock-in amplifier is interfaced to a computer via an RS232 serial connection. The Eurotherm sample temperature controller described in section 3.2.2 is also interfaced to this computer via the other RS232 port. The Eurotherm controller is set up to provide a temperature ramp of a few degrees per second. A custom written piece of software (written in the LabWindows CVI environment) is used to plot the partial pressure of desorbed species versus temperature — this is the TPD curve. The same piece of software is also used to monitor the background pressure of a particular gas during dosing, and to calculate the live integral of this pressure with respect to time, this being proportional to the gas dose.

As the temperature of the sample increases, it becomes possible to break surface-adsorbate bonds and so species are liberated from the surface, causing a desorption peak in the TPD curve. As the vacuum chamber is being continuously pumped, this peak also corresponds to the maximum desorption rate. The fact that a peak is seen can be qualitatively explained as the result of the competition between the Arrhenius type desorption energetics and the simultaneous depletion of adsorbate.

The most useful piece of information for us which can be obtained from TPD is the surface coverage. Providing a reference TPD curve is available for comparison, the coverage, Θ, is given by

$$\Theta_{\text{unknown}} = \frac{\text{area of TPD curve for } \Theta_{\text{unknown}}}{\text{area of TPD curve for } \Theta_{\text{known}}} \times \Theta_{\text{known}}.$$

This is also the principal day to day method we use to determine surface cleanliness. A clean surface will have a certain maximum coverage, which will decrease as adsorption sites are blocked by rogue “dirt” atoms. This comparison can be qualitatively made by comparing the profile of TPD curves with known clean curves from other workers for a given surface-adsorbate system.

Low Energy Electron Diffraction

Low Energy Electron Diffraction (LEED) is a surface structure determination technique in which electrons in the energy range of 20–1000 eV are elastically back-scattered from the sample surface onto a phosphor screen to give a diffraction pattern representative of the structure of the metal-adsorbate system; see figure 3.29 for a schematic of our Varian system, at the top level of the chamber. These energies are chosen to obtain the correct de Broglie wavelengths for the interatomic spacings typically found at surfaces. A series of grids in front of the screen are biased so that only elastically scattered electrons are allowed on to the screen. The screen, on which the diffraction spots appear green on a black background, may be viewed by eye from the opposite chamber window, or may be photographed by conventional or electronic means. Dedicated LEED chambers, such as are available elsewhere in our group, use a digital monitoring system, from which surface structures and bond angles are determined using a complex computational algorithm. For the simple molecules in this study, a visual interpretation

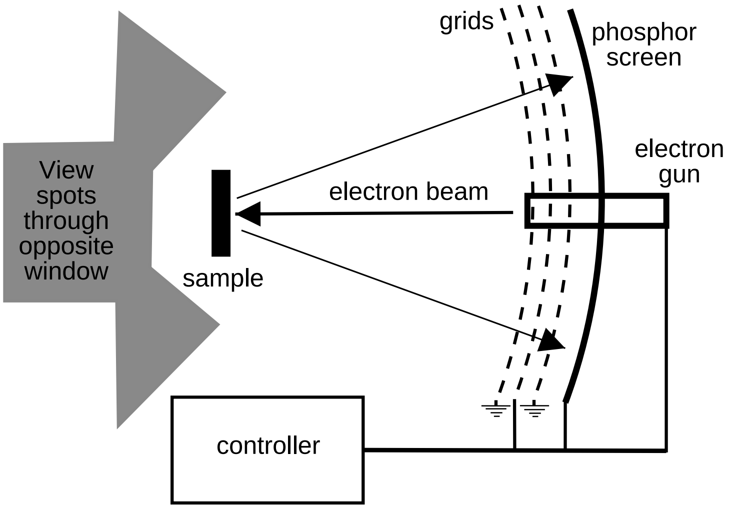

Figure 3.29: Schematic of our LEED system.

of adsorbate spots manifesting themselves between the surface spots is sufficient; and at the very least allows comparison with the work of others. For more details of the concepts of LEED see, for example, [88, section 2.3].

Auger Electron Spectroscopy

An electron incident on an atom may cause the emission of a core electron. The hole left by this process may then be filled by an electron of lower binding energy. This electron is known as the “down” electron. The transition of the down electron releases energy which may liberate an electron from a still lower bound state into the vacuum. This third electron is known as the Auger electron, after its discoverer Pierre Auger. This scheme is shown in figure 3.30. From the arrangement given in this diagram, the kinetic energy, T, of the Auger electron is given by

$$T = E_K - E_L - E_M - \phi.$$

Thus the kinetic energy of the Auger electron is independent of the incident electron energy, and is just a function of the electronic structure of the adsorbate, so AES can be used to identify particular elements on particular surfaces with a unique “fingerprint” [89]. In fact, the differentiated electron spectrum, dN/dE, is usually plotted, as this tends to make the Auger peaks clearer. Auger spectroscopy can identify impurities present on a surface, so can be used to check surface cleanliness by comparison with spectra known to be clean.

Our Auger system is made by Varian and the electron gun is driven by the same power supply as the LEED system. The electrons are detected by a hemispherical analyser which acts as a monochromator. The electrons enter via a small hole and pass between two hemispherical plates, which have a variable potential difference across them. Only electrons in a certain energy range can traverse the curved path between the plates and emerge. These are detected by a channeltron detector. We

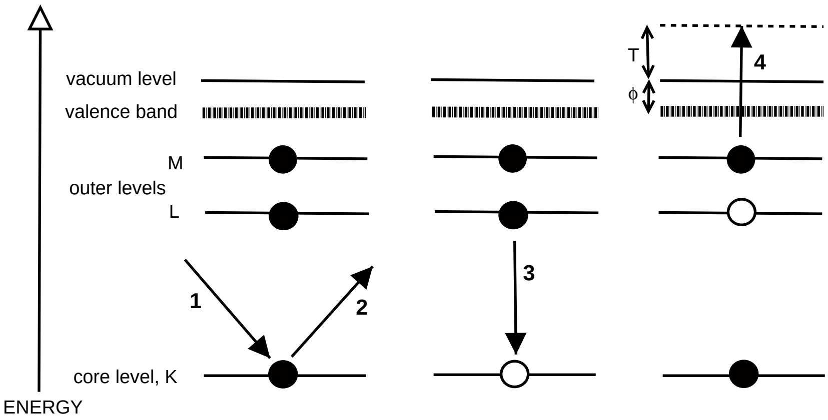

Figure 3.30: The Auger effect. In the left hand panel, an incident electron (1) from a gun removes a core electron (2). In the central panel an electron (the “down” electron) from an outer level (3) moves to occupy the hole left by this process. In the right hand panel, the energy released by the down electron causes an Auger electron (4) from a still further-out level to be liberated at a kinetic energy T.

use an external 1 KHz oscillator to modulate the potential of the sample, with the lock-in amplifier in phase sensitive detection mode to reduce experimental noise. The spectrum is obtained by setting the analyser controller to scan a spectrum, whilst recording the output from the lock-in using the same software as used for TPD measurements. The analyser is mounted on a two dimensional gimbal system, operated by external drive knobs, internal goniometers being visible through a window on the chamber. This allows exact positioning of the analyser around the sample for angular dependent studies.

3.3 The Complete Spectrometer

3.3.1 Overview

Practical Constraints

This section describes how the laser system and UHV chamber have been combined to make the time resolved surface SFG spectrometer. The initial hurdle was that the main laser table and the UHV chamber have a physical gap between them in the lab of nearly a metre. This unfortunately cannot be altered as this is the only practical route to the fire exit of the lab: both the laser system and UHV chamber have many pipes and cables at their rears connecting them to departmental services. Also, the UHV chamber's central level is around 1.43 m from the ground, presenting another safety issue — the laser beams must enter and exit the vacuum chamber at roughly human eye level. The first priority in setting up this experiment was the safe and practical entry and exit of laser beams to and from the vacuum chamber. The original plan, as used for the previous laser desorption experiments on benzene/Pt{111} and those in Appendix A, was to use a periscope on the main laser table to directly aim the beam into the chamber across the gap. It was clear that, aside from the obvious safety issues, it would be nearly impossible to spatially and temporally overlap two or maybe three beams of a few hundred microns diameter on a crystal in vacuo, with the final turning mirrors over one metre away.

To overcome this I designed a custom laser table and commissioned the departmental workshops to construct it such that it fitted around the UHV chamber and allowed the final alignment to be done much closer to the sample. The original working diagram for the surface plan of this table is given as figure 3.31. It is made of aluminium and is covered in an inch grid of M6 threaded holes. The table is mounted on a light box section steel frame, with three 60 cm high legs which sit on and are bolted to the lower mounting platform of the UHV chamber system. It is also supported nearer the chamber by a screw thread which comes out of the cold trap on the large diffusion pump. This threaded rod is passed through a specially drilled hole on the table and nuts and washers are used to secure the table to the trap. This table has proven to be an essential keystone of the whole experiment, and any initial fears about stability or vibration from the pumps have proven to be unfounded. All the final alignment optics are on the chamber mounted optical table. The table and all the optics on it are removed from the chamber prior to a bakeout.

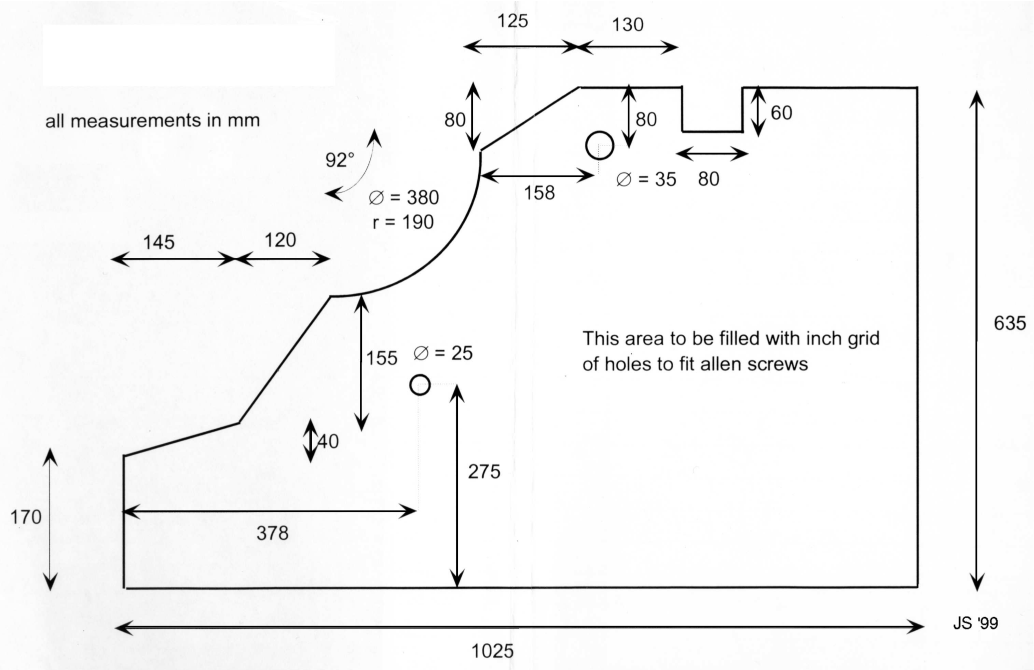

Figure 3.31: The custom optical table mounted around the UHV chamber. To scale.

In practice it was found to be much simpler not to have the periscopes to raise the beam to window height mounted on this table, so the beams do still travel across the lab gap at window height. We have overcome this safety issue by putting a wooden platform between the main laser table and chamber to raise *our* height well above that of the beams — this also makes adjustment to the optics on the still relatively high UHV laser table much more comfortable. Furthermore, a mechanical shutter which covers all beam paths from the periscopes on the main table is used to block beams when they are not needed and all non-used windows on the chamber are covered with black plastic caps. A black and white CCD camera with a Cosmicar-Pentax zoom lens is used to view the beams incident on the sample safely through window (D) in figure 3.24 via a framegrabber card and a computer screen. The number of lost pixels on the CCD camera to date shows the prudence of this measure.

Optical Layout

The experimental arrangement described here is suitable for performing spectrally resolved SF measurements and time resolved SF free induction decay measurements, as these techniques form the bulk of the recent work and the main results presented in this thesis. Alternative beam paths for various types of pump-probe and photon echo experiments are given in chapter 6.

Figure 3.32 shows in detail the optical paths from the regenerative amplifier to the edge of the main table, with the periscopes on the right taking the beams across to the UHV mounted optical table. The output from the TSA is split by the vertically mounted beamsplitter shown in the insert. The OPA requires 2 mJ of energy per pulse, so given the output of the TSA changes from day to day and ultimately decreases as the flash lamps in the Nd:YAG pump laser wear out, some form of energy "balance" control is needed to divert varying amounts of energy to the OPA. This is acheived with a combination of this beamsplitter and the three half wave plates (a), (b) and (c). The beamsplitter is coated for optimal reflection at a certain polarisation, so by changing the polarisation with half-wave plate (a) before the beamsplitter, it is possible to vary the amount transmitted and reflected. Half wave plates (b) and (c) allow the polarisation to be corrected back to the original horizontal polarisation. This works well for day to day fluctuations in the output of the TSA, but cannot make up the difference between worn and brand new flash lamps, so two different beamsplitters are available with their reflectivities ($R = 30\%$) optimised for s or p-polarisation and so can be changed as the flashlamps age.

Two mirrors are used to steer the beam into the OPA. Two energy meter heads (Scientec) are available, one to measure the input to the OPA, and a more sensitive head to measure the IR output. A “flipper” mirror (Newport Optics) is placed in the OPA output path, and this can be sprung up into the beam path reproducibly when needed to reflect the beam into the energy meter head. Near the OPA the signal, idler and IR are not that well spatially separated so a filter (University of Reading Thin Films Laboratory) is usually inserted before the meter to remove the signal and idler. The mirrors in the IR beam periscope are rectangular (50×30×12.5 mm) substrates coated with gold by CVI Technical Optics Ltd. The rectangular substrate gives a greater range of beam angles without moving the periscope. The VIS beam passes into the pulse shaper, as described in section 3.1.5, via two mirrors and two irises, (e) and (f), at an elevated height, gained from the post TSA periscope. The irises allow for reproducible alignment into the pulse shaper. Following the pulse shaper, the beam passes past another flipper mirror which is used to send the beam into the FROG (section 4.2) for alignment purposes when needed. It passes out of the pulse shaper at a slightly lower height via the square pick-off mirror. It then passes onto a translation stage to allow the IR and VIS pulses to be overlapped temporally or delayed as required. The translation stage is a combination of a computer controlled stage (Aerotech, see section 3.3.3) of range 25 cm, and on this mounted a manual micrometer driven transla-

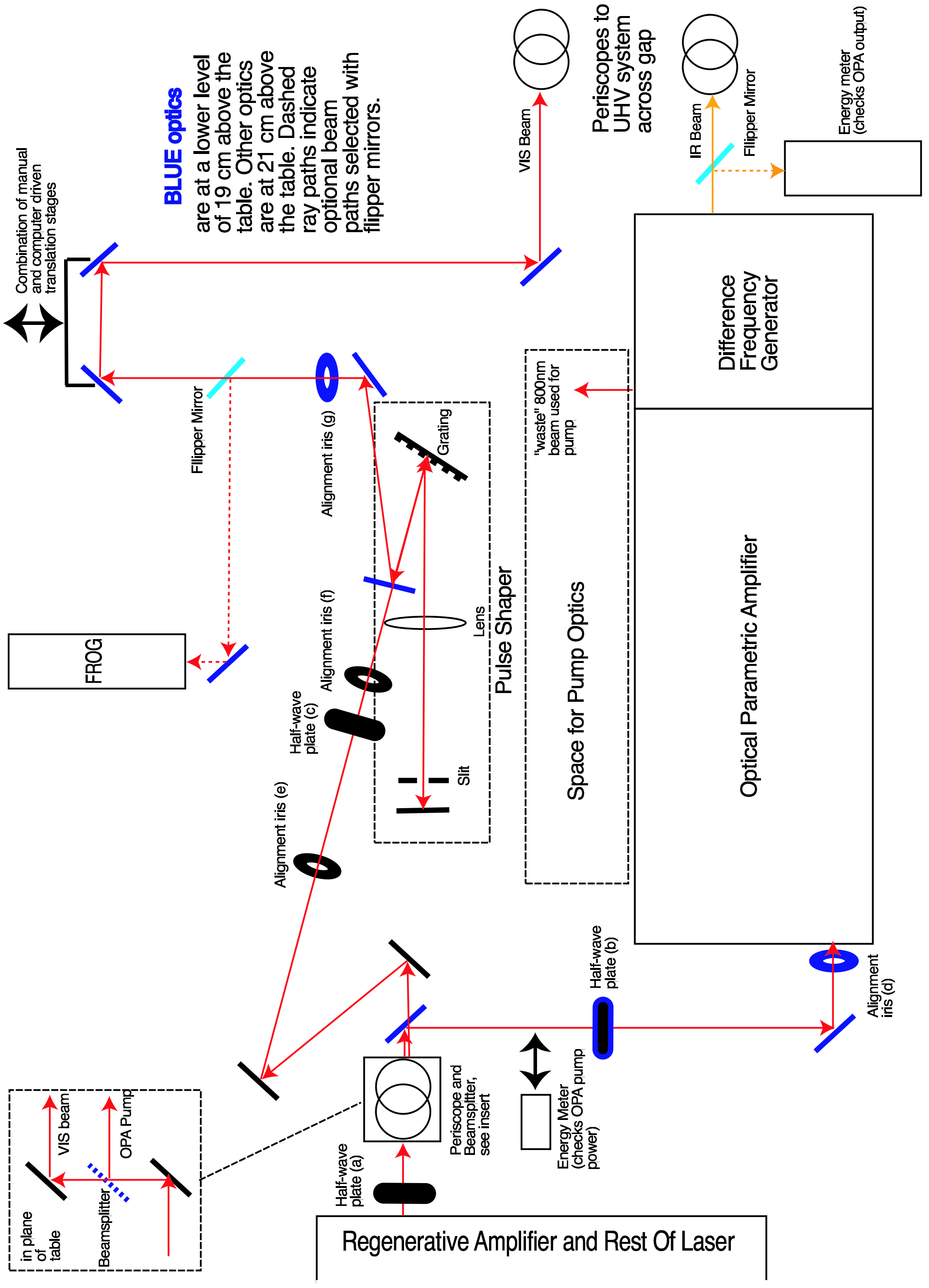

Figure 3.32: Optical paths on the main optical table. See text for explanation. The pulse shaper is shown in more detail in figure 3.19.

tion stage (range 25 mm). The beam then passes via one turning mirror onto the exit periscope. All 800 nm mirrors are made by CVI Technical Optics, and are coated to their TLM1 thin layer dielectric ultrafast specification. All 800 nm mirror substrates, with the exception of the square shaper pick-off mirror, are 1 inch circular BK7 glass.

The two beams then pass across to the chamber mounted optical table, figure 3.33. Irises (j), (k), (l) and (m) are provided for day to day alignment reproducibility. A holder is placed in the IR path for a chemical containing infrared transmissive cell for wavelength calibration, see section 3.3.4. A holder for a 10% neutral density filter is in the VIS path to attenuate the power when needed; for example when the narrowing slit is removed for time resolved free induction decays the fluence from the VIS path might well ablate the sample surface when focused down. When attenuation is not required a 4 mm thick borosilicate glass plate is inserted in its place to keep the path lengths equal. A pair of convex / concave lenses are in the VIS path, one on a translation stage, which together act as a variable telescope to vary the 800 nm spot size, so that the VIS and IR spot sizes can be made approximately equal for efficient SF production, given they both have to pass through the final MgF_2 lens which has a chromatic aberration.

After a pair of final turning mirrors (IR mirror is gold and rectangular exactly like the periscope mirrors), the beams then pass into the chamber via a CaF_2 lens of focal length 25 cm (which is on a manual translation stage and optical rail to change the focal spot size), the MgF_2 window (A) and finally onto the sample. The beams are angularly separated as much as possible given the size of the MgF_2 window. The IR beam is at 84° to the surface normal, and the VIS is at 80°; which from equation 2.26, the SF direction is 81°, or $-81°$ on reflection. Orthogonal to this arrangement on the table is a non-vacuo replica of the lens and window system, with a $LiIO_3$ crystal ($\phi = 0°$, $\theta = 20.3°$) replacing the metal sample.

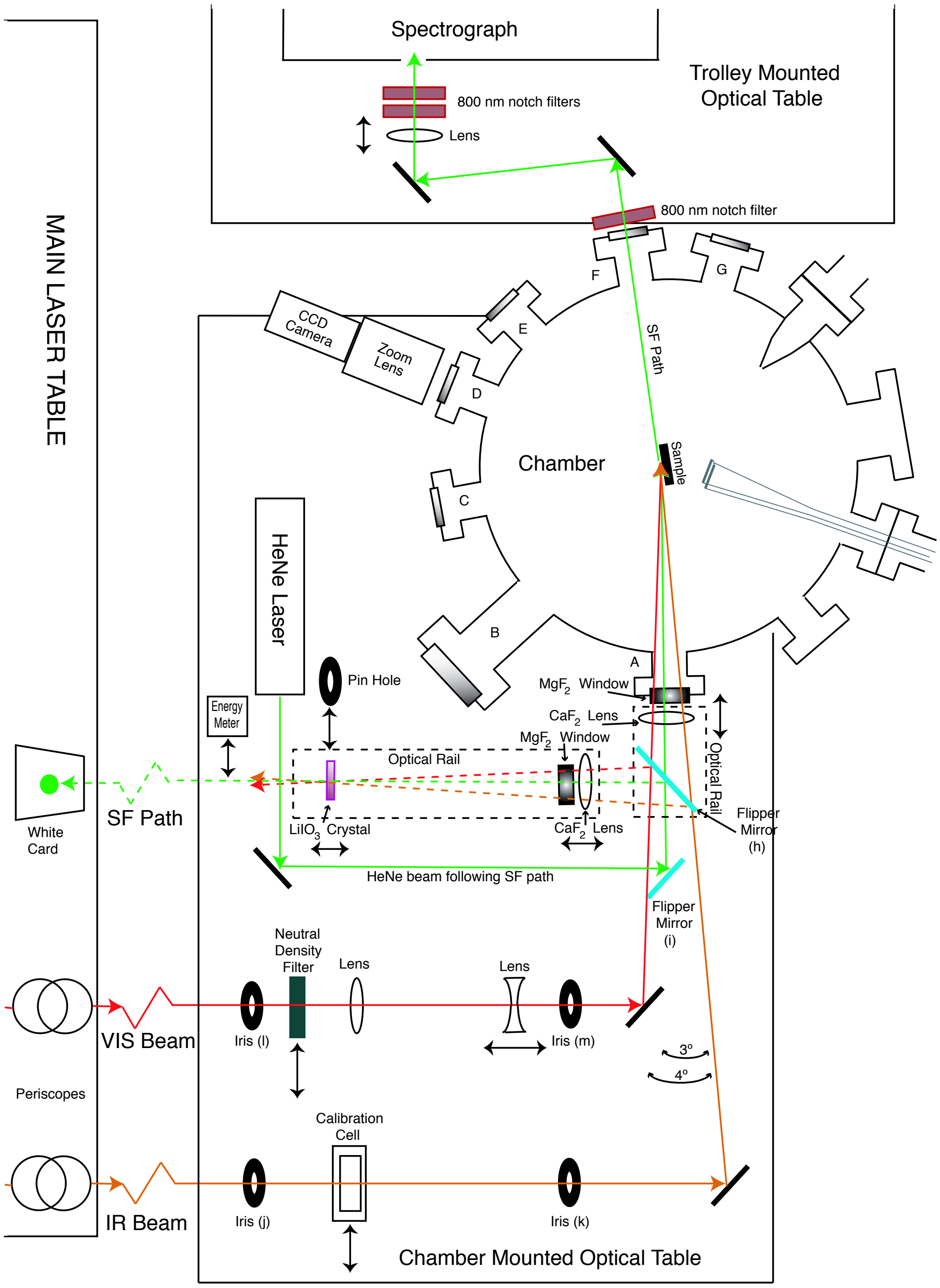

Figure 3.33: Optical paths around the UHV Chamber. See text for explanation.

The beam can be passed through this alternative path with flipper mirror (h). This mirror must catch both VIS and IR beams at a relatively large diverging angle, and is a microscope slide coated with evaporated gold (with thanks to Frank Lee at the Cavendish Laboratory). The relatively thick (1 mm) $LiIO_3$ crystal is efficient at producing the visible sum frequency of the IR and VIS. To obtain spatial overlap, the $LiIO_3$ crystal can be replaced by an iris, and then a 150 μm pin hole through which both beams must pass — the VIS beam being detected with a fluorescent card and the IR with a sensitive energy meter connected to an oscilloscope. The pin-hole mount is on a lateral optical rail, a transverse translation stage, and a screw driven height control for accurate positioning. Temporal overlap is achieved by watching for the SF light in the $LiIO_3$ crystal. The direction of the SF beam can be marked on a white card placed at a $\sim$ 1 m distance on the main optical table.

If the pin-hole is then replaced, a low power Helium Neon laser can be aligned exactly along the SF path by flipping up flipper mirror (i). When the flipper mirror (h) is flipped down, the VIS, IR and HeNe beams will pass into the chamber and the HeNe path should reproduce the SF exit path from the metal surface. The overlap of the two visible beams on the surface can be checked by the CCD camera. The HeNe beam is then aligned into the spectrograph via two turning mirrors (broadband dielectric, CVI). A 100 mm focal length lens is used to focus the beam into the spectrograph. Three notch filters remove any trace of the 800 nm beam, which is spatially close to the SF/HeNe path. We estimate, by use of pin holes and irises on the benchtop beampath, that the spot size on the surface is around 300 μm. The alignment procedure is described in detail in section 3.3.4.

3.3.2 Optical Detection

Spectrograph

Our imaging spectrograph is made by Acton (SpectraPro 300i) and has a 0.3 m internal path length in a Czerny-Turner configuration. It is fitted with two gratings of 600 and 1800 grooves per mm, on a selectable turret. It is controlled via an RS232 serial connection to a PC, and comes with custom control software. A mirror diverts the incoming beam at right angles, such that the spectrum emerges perpendicularly to the incoming beam. A micrometer driven variable width entry slit is provided.

The ICCD

We have an Intensified Charge Coupled Device (Andor i-Star) as our detector. This is bolted onto the spectrograph perpendicular to the incoming beam path. Inside the i-Star is a cooled CCD chip and a Gated Image Intensifier. The CCD has 256 rows and 1024 columns of pixels, the rows running in the direction of the spectrum. The data from the CCD can be read either as an image, or by “binning” whole columns on chip, or by taking just a thin strip of rows. Binning a whole strip increases the signal, whilst selecting a thin strip of rows reduces extraneous optical noise. Horizontal binning is also available to increase signal and acquisition times, whilst reducing spectral resolution. The CCD can be cooled to reduce noise to -25° C via a peltier element which is in turn externally water cooled.

The image intensifier is of a *second generation tube* type. Photons enter the intensifier and fall on a photocathode, which then liberates electrons. The electrons cross a small gap under an electric field and enter a *microchannel plate*, which is a thin disc of honeycombed glass, each channel being resistively coated.

The electrons cascade along each channel under a large electric field and produce many secondary electrons along the way. The electrons then strike a phosphor plate which re-emits photons for detection by the CCD. This cascade of electrons can amplify the light by a factor of up to 10^4. The high electric field ensures little transverse movement of the electrons, thus preserving the integrity of the spectral information. By pulsing the electric field, the intensifier can be gated and acts as a shutter. By selecting the opening and closing times of this gate with respect to the laser pulse trigger, non-laser ambient optical noise can be significantly reduced. We use the Nd:YAG laser Q-switching signal as a trigger. The gate has a minimum width of 1.2 ns, though this does depend on the user variable intensifier gain. We typically use gate widths of 10–20 ns.

The i-Star connects to a custom PCI card mounted in a PC, and is supplied with comprehensive control software. This software is capable of setting up the CCD, gating and cooling, of gathering data, and of directly controlling the spectrograph. Perhaps the most powerful feature of this software is the built in Andor BASIC programming language which can control acquisitions and be used to drive external devices and programs. This language is used to automate free induction decay and pump-probe experiments as described in section 3.3.3. The software allows spectra to be accumulated over many laser pulses, and for a *photon counting* threshold to be set: the user can set a level below which light is not to be counted, thus reducing background noise. Also, a background subtraction mode is available. An infrared remote control allows simple one person operation.

Calibration

The i-Star software permits calibration by allowing the user to specify known spectral lines. It then fits a polynomial which it uses in subsequent acquisitions to generate the frequency axis based upon the spectrograph settings. We use a neon discharge lamp (UVP Ltd) to calibrate the i-Star and spectrograph as neon has several spectral lines around 690 nm where the 5 μm and 800 nm SF lies. As a further check, we can also insert a chemical cell in the IR path, and observe an absorption dip in the SF spectrum corresponding to the IR absorption position — see section 3.3.4.

3.3.3 Computer Control

We have two stepper motor driven translation stages. The largest is made by Aerotech, and has a 1 μm resolution — 10 μm corresponds to 66 fs in time (1 μm of stage movement extends the beam path length by 2 μm in the configuration shown in figure 3.32). This has a separate controller box (Unidex 100) which contains a sophisticated programmable microcontroller. This is in turn controlled via a RS232 connection to a PC. The Andor BASIC language has facilities for sending ASCII data to an RS232 port.

The smaller stage, used to delay a third pump beam with respect to the VIS and IR beams is made by Standa and has a resolution of 0.5 μm. It is directly controlled via a PCI type card mounted in a PC. This card, if used for custom applications, must be driven at a very low level by writing to the computer's internal I/O ports. Although Andor BASIC claims to have low level port control, I have not been successful in controlling it in this way, so to drive it I have written an external C program, which is then called by the Andor BASIC program. The Standa stage driver program is given as Appendix B.

I have written Andor BASIC programs to just move the two stages (with no spectra taken), in order to find temporal overlaps, and other Andor BASIC programs to take surface autocorrelations (chapter 4), free induction decays (chapter 5) and pump-probe data (chapter 6). These are given in Appendix C.

3.3.4 Alignment Procedure

Development of the Procedure

The development of the complex daily alignment procedure has taken some time to perfect, but is now such that it can be done in perhaps a couple of hours. Along the way several schemes were tried, and each contributed in some way to the final solution.

The main hurdle in this problem was how to overlap two very small beams in both space and time, *in vacuo*, one of which is invisible to the naked eye. Additionally, given the length of the beampaths, the stability of the laser system, the fact that the sample must be moved in the chamber for cleaning and characterisation and the complexity of the overall experiment, it was clear that this alignment would have to be repeated each day.

We started with the $LiIO_3$ crystal, mounted on the main laser table, with the IR beam and a VIS beam directly from the TSA. The beam paths were measured with a tape measure until they were roughly equal. Given the fact that it was impossible for us to see the IR beam by eye, we used an energy meter to detect its presence. By replacing the $LiIO_3$ crystal with an iris, and later a pin-hole, we found a way to ensure the VIS and IR paths crossed in space. We then used our portable 0.125 m spectrograph and line-CCD (Linespec) to detect the SF in this crystal, then optimised the temporal and spatial overlap until we could see it by eye. Eventually the Linespec was not needed as we could see the red SF spot more or less immediately as we improved the geometry.

Then we tried with a piece of (undoped) Gallium Arsenide wafer (with thanks to Frank Lee at the Semiconductor Physics Group) as GaAs has been used in reflection in the past to align nonlinear optical surface experiments, see for example [90]. It has very high surface and bulk $\chi^{(2)}$. This small crystal, 5 mm square, was glued to a glass mirror substrate and placed in a rotatable mount. The next problem to address was where to place the detector. This was solved by repeating the setup of the $LiIO_3$ crystal path, and following the SF direction with a HeNe laser, then flipping the beam paths in the direction of the GaAs wafer, and aligning the spectrograph along the direction of the HeNe path. In this way we found our first surface SF signal from GaAs. We later briefly mounted a piece of GaAs on the reverse of our chamber mounted sample for alignment purposes. Meanwhile, we also successfully obtained bench-top SF signals from a gold coated mirror, but tried a Palladium crystal without success. SF and DF (difference frequency) signals from the GaAs and gold surfaces are shown in figure 3.34.

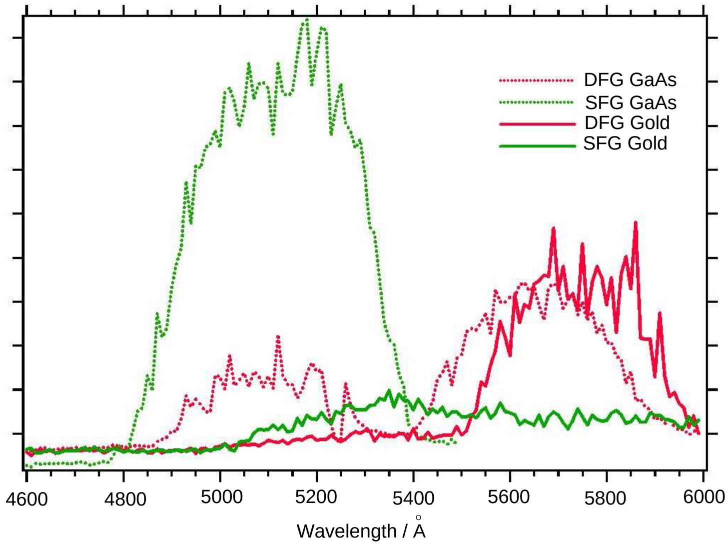

Figure 3.34: SF and DF signals from GaAs and gold samples.

We then transferred this geometry on to the chamber mounted optical table. Lens focal lengths were estimated with computer simulations of Gaussian beams to obtain the smallest spot size possible. At this time the chamber was fitted with the Pt{111} sample which had been used for the benzene desorption experiments. We were unsuccesful in getting an SF signal from this; since it has become clear that the low $\chi^{(2)}$ of Pt at these wavelengths could be a problem — see section 6.4.1. We had purchased a Ru{$10\bar{1}0$} crystal for the water catalysis project, so we tried this whilst our Pt{111} crystal was being re-polished. As the original plan with the water catalysis project was to study the effect of co-adsorbed alkali metals we used the Getter source to deposit a thin layer of potassium on the surface, and we suddenly obtained a large SF signal. The reasons for this are discussed in detail in the next chapter in section 4.3.5. Once the alignment was optimised, a clean surface Ru{$10\bar{1}0$} SF signal was seen after the K layer had been heated off. The use of an alkali metal layer is the cornerstone of the alignment procedure, and from this we have developed a method of characterising our entire system in vacuo — see section 4.3.1.

Day to Day Alignment

The laser is aligned as described in section 3.1. An energy meter is placed in the OPA pump beam path and half wave plate (a) is rotated until 2 mJ registers. Then the polarisation is corrected by inserting a BBO frequency doubling crystal optimised for horizontal polarisation into each beam path in turn and optimising for maximum blue light whilst adjusting half wave plates (b) and (c). Two mirrors, in conjunction with external iris (d) and the two internal OPA irises A1 and A2, are used to steer the pump into the OPA. Fine adjustment is done by inserting the energy meter to measure the OPA output via the flipper mirror. Occasionally it is wise to reset the internal motors of the OPA via the control software. Half wave plate (b) and the TSA compressor can also be optimised at this stage by maximising the energy output of the OPA.

The incoming beam to the pulse shaper is steered so that it is centred on irises (e) and (f). The slit is removed, and the neutral density filter inserted on the chamber table to protect the sample. The pulse shaper can then be occasionally checked for optimisation by comparing the incoming and outgoing FROG traces — see section 3.1.5. The VIS beam is then centred on irises (l) and (m).

If the alignment is very poor, or if a new set up is being trialled, then it is usual to initially perform the IR alignment with the signal beam from the OPA, as this has an accompanying visible harmonic, and at 1.4 μm is still visible on our IR viewing card. The SF of the signal and the VIS appears green in the $LiIO_3$ crystal.

In general the IR beam is aligned through irises (j) and (k) by placing an energy meter head behind them, directly connected to an oscilloscope for easily visible feedback. An iris is placed in the $LiIO_3$ crystal position and the IR beam is steered through the iris, again checking with the energy meter. The iris is replaced by the 150 μm pin-hole and the alignment is optimised. The VIS beam is then aligned through the pin-hole. The pin-hole is replaced by the $LiIO_3$ crystal, and the temporal overlap is adjusted until the red spot of the SF light is seen. The spot is allowed to travel to the far field on the main optical table, where its position is marked on a white card. The pin-hole then replaces the $LiIO_3$ crystal and the HeNe laser is steered so it passes through the pin-hole and onto the spot marked on the card.

At this stage, potassium is dosed onto the metal sample. We usually dose for 1 minute at 7 A current, but this is not critical as long as a multilayer is dosed — see chapter 4 for more details. The sample is then returned to the normal experimental orientation.

Flipper mirror (h) is then sprung up so that all three beams travel into the chamber. The CCD camera is used to observe the spatial overlap on the crystal. Given all three beams are overlapped in the pin-hole, then providing the two observable beams (VIS and HeNe) are overlapped on the surface, one can be sure the IR is overlapped there too. If this is not the case, the two observable beams are overlapped on the surface, and the pin-hole position is changed to the new overlap position. The IR is realigned through the pin-hole and the procedure is iterated until the pin-hole and surface overlaps agree. It should be noted that the HeNe flipper mirror (i) does actually block the IR beam and most of the VIS beam, so it has to be alternately sprung up and down during alignment.

The HeNe beam is steered into the spectrograph entry slit, which is open to about 150 μm. The grating in the spectrograph is then set to zero order, and the profile of the zero order light is observed in real time by the pre-cooled i-Star set to full vertical binning mode. The HeNe beam is optimised so that it enters exactly in the centre of the ICCD and is symmetric. The spectrograph entry slit is gradually closed until it begins to attenuate the signal, whilst optimising the input direction. The 800 nm filters are removed temporarily and the spectrograph set to 800 nm. The i-Star gate delay and width are then optimised so that the VIS beam is just detectable, to cut out any non-laser optical noise. A spectrum may then be taken of the VIS beam.

The spectrograph is then set so that the SF signal will appear in the centre (usually 690 nm), and the slit is opened wide again. The gain is turned up, the 800 nm filters reinserted, the HeNe is turned off and flipper mirror (i) is sprung down. Whilst observing the i-Star spectrum, the final IR turning mirror is slightly tweaked until the SF signal is seen from the K covered surface. Empirically we have found it to be most efficient to adjust the horizontal direction first. The signal is optimised by iteratively tweaking the IR and VIS final tuning mirrors, the temporal delay, the CaF_2 lens distance from the sample, the VIS beam size via the telescope, the VIS polarisation via half wave place (c), the mirrors leading into the spectrograph and the sample position. Usually this will saturate the i-Star if the 600 g/mm grating is used and horizontal binning is set to 8 pixels per bin. Such a spectrum is shown in the next chapter as figure 4.8.

The i-Star is set to full imaging mode and the image of the spectrum is observed on the screen. The final lens into the spectrograph is then moved back and forth until the vertically narrowest spectrum is seen, and the entry slit width reduced until the signal is just attenuated. The centre and width in pixels of this band are noted, and the i-Star is set up only to record pixels within this band to cut out extraneous noise. Usually the beam path from the chamber exit window to the spectrograph is then covered with a black cloth.

Next the narrowing slit is put in the pulse shaper. The slit width is set with the micrometer to a value determined by the system characterisation, see section 4.3.3. An energy meter is placed at the exit of the pulse shaper, and the lateral slit position is optimised to give maximum energy — this ensures reproducibility of slit insertion. The neutral density filter in the VIS path is replaced by the glass plate as attenuation is no longer required. A few thousand counts per shot should still be visible on the 600 g/mm grating. A chemical cell is then inserted in the IR beam path. For studies on CO we use 10 mmol of $W(CO)_6$ in $CHCl_3$ — see chapter 5 for more details. The temporal delay is then re-optimised whilst watching the i-Star spectrum as the cell increases the IR path length by about 2 mm. The i-Star is then set to accumulate, and a cell spectrum is taken for calibration purposes, for examples see chapter 5. If the higher resolution of the 1800 g/mm grating is required, with 8 pixels per bin horizontal binning, and full gain, 5 μJ of IR should give up to 6×10^4 counts per shot. The cell is then removed and the temporal delay returned to normal.

The potassium layer may then be heated off and adsorbates dosed as required. The system is now set up for frequency resolved experiments. For time resolved free induction decays, the pulse shaper slit is removed, and the neutral density filter re-inserted. We have previously found that ~ 100 μJ of the 800 nm beam focused to ~ 200 μm does not cause surface ablation, whereas without the slit present there may be up to 1 mJ focused onto the surface with no filter present.

Chapter 4

Characterisation of UltraFast Pulses

When making measurements upon any physical system, it is necessary to have all tools characterised and calibrated before accurate data can be taken. This is no different with an ultrafast laser system. The experimental design described in the previous chapter can be considered as a measuring instrument, and it has been necessary to probe the properties of this instrument before meaningful chemical experiments could be performed.

The commercial laser system needs to be characterised on a day to day basis, and this is described in section 4.1. This applies equally to the infrared from the OPA and the narrowed 800 nm light from the pulse shaper. And ultimately the spectral and temporal resolution of the experiment as a whole must be determined. This chapter describes the traditional methods used to characterise each stage, plus an original methodology for characterising the properties of the laser beams in vacuo [91].

4.1 Laser System Parameters

4.1.1 Pulse Energy, Fluence and Spatial Beam Profile

Pulse energy is easily determined using a commercial energy meter (Scientec). If a fluence measurement (energy per pulse per unit area) is required, the beam area can be estimated by aiming the beam via a neutral density filter at a CCD camera of known pixel size. Qualitatively the beam profile should be Gaussian, corresponding to a TEM_{00} cavity mode.

4.1.2 Spectral and Temporal Profile

Spectrum

The spectrum of our femtosecond oscillator is determined with a commercial spectral analyser which uses a rotating diffraction grating and detector to provide a real time beam spectrum. However the amplification system will introduce changes to this spectrum, so it is prudent to check the spectrum again at further stages in the system. We use a 'LineSpec' single row CCD system attached to a 0.125 m spectrograph, and for more accurate and sensitive measurements we have the Andor i-Star system and 0.3 m spectrograph as described in section 3.3.2, normally used as the experimental detector. See also FROG, section 4.2, below.

Temporal Width

The temporal width of a laser system is usually measured with an autocorrelator. We have recently acquired a commercial autocorrelator (see section 4.1.4 below) for day to day alignment, but in the past we have built temporary autocorrelators when needed from standard optical components. With any measurement technique in science, a quantity is usually measured by comparing it with some standard of comparable magnitude. With a pulse duration of the order of 150 fs this would prove impossible to find. The technique of autocorrelation performs the temporal measurement by comparing the beam with *itself*, see figure 4.1. A beam is first divided up into two components using a beam splitter. One of the beams is allowed to travel further along the bench, via a variable delay stage, thus delaying the pulses with respect to the other beam. The two beams are then recombined by passing in a non-colinear arrangement through a nonlinear frequency doubling crystal, such as BBO or KDP. Each of the beams is separately doubled in the crystal, but when both pulses arrive at the same time, a second order nonlinear process occurs in which a photon from each beam is combined to give the a third beam spatially bisecting the straight-through beam paths, as described on page 22. This is the sum frequency of two identical beams. If a detector is placed in a position such that it only detects this third central beam, then by plotting the measured intensity as a function of beam delay time an autocorrelation trace can be acquired. In practice this is done by taking the output from the Linespec CCD and feeding it into an oscilloscope, where it is frequency integrated and read into a custom written computer program. This program also controls the delay stage and produces a pairwise data file of time delay and intensity. A Gaussian or secant function (depending on the assumed pulse shape) can be fitted to this data, and the FWHM temporal width can be obtained.

The electric field of the SFG, with respect to time delay τ, will be

$$E_{\mathrm{SFG}}(t,\tau) \propto E(t)E(t-\tau),$$

and the intensity, when integrated over time by the detector, will be

$$A^{(2)}(\tau) = \int_{-\infty}^{\infty} I(t)I(t-\tau)\mathrm{d}t.$$

In other words, the temporal profile of the beam is convolved with itself. This means that the autocorrelation will be broader than the true temporal profile. Thus in order to extract the FWHM of the pulse width, an assumption must be made about the mathematical form of the temporal profile. For a Gaussian, this means that the width of the autocorrelation must be divided by $\sqrt{2}$ to obtain the pulsewidth (FWHM). Of course, real beams are not always easily represented by a simple mathematical function.

The temporal profile can also be more successfully measured by FROG, see section 4.2 below. This also allows the phase and intensity of the electric field to be reconstructed.

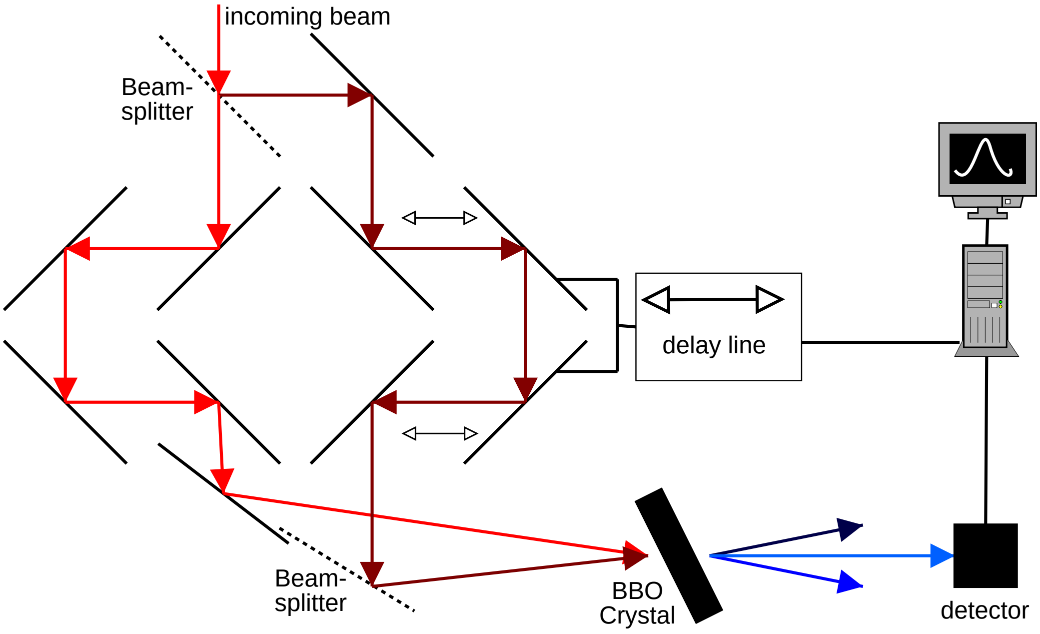

Figure 4.1: An autocorrelator setup.

Time-Bandwidth Product

In general, temporal width and spectral width should be related by a simple reciprocal relationship. The quantity time-bandwidth product is defined, as the name suggests, by the product of the temporal pulse width with the spectral pulse width.

The value of this quantity gives some measure of the ‘complexity’ of the pulse shape; the greater the value, the more complex. For example, a square wave, which contains many Fourier components, has a time-bandwidth product of 1.

The time-bandwidth products for various pulse shapes are given in table 4.1 below.

Function	Time-Bandwidth Product
Square	1
Gaussian	0.441
Hyperbolic Secant	0.315
Lorentzian	0.221

Table 4.1: Time-bandwidth products for various pulse shapes.

4.1.3 Chirp

Chirp is a variation in frequency with time (temporal chirp), or a frequency variation over the spatial width of the pulse (spatial chirp). The term arises from an audio analogy; if for example the pitch of a bird’s song were to steadily increase or decrease during its call, then this would make a ‘chirping’ sound. Chirp can be introduced by misaligned components, especially in the frequency domain sections of the regenerative amplifier where different components of the spectrum pass over different path lengths — indeed this is the principle of operation of our CPA amplifier (section 3.1.3). The chirp introduced by the amplification process should be removed in the compressor stage, but misalignment often means this is not the case. Chirp is undesirable for many reasons. The OPA does not function efficiently with chirped pulses. Also, if the frequency of pulses involved in time resolved SFG varies with time, then recorded spectra will shift as the time delay is varied, which may mask any genuine chemical effect present. Chirp is best measured with FROG, as described in section 4.2 below.

4.1.4 Pulse Front Tilt

Pulse front tilt is where the *phase front* (line of common phase) is tilted with respect to the normal of the direction of wave propagation, see figure 4.1.4. Such a pulse tilt is commonly introduced by a misalignment in the compressor part of the regenerative amplifier. For most purposes, such a tilt is of no great importance, but the performance of the Light Conversion OPA we use is significantly affected by tilt. With this in mind, a special autocorrelator was designed and constructed to measure pulse tilt, which is described in detail in my end of first year report [44]. It consisted of a very similar arrangement to the standard autocorrelator, with the exception that one of the two paths passed though an odd number of mirrors. This has the effect of spatially inverting the beam, and hence inverting the pulse tilt if present. Now when the two beams are recombined any tilt should

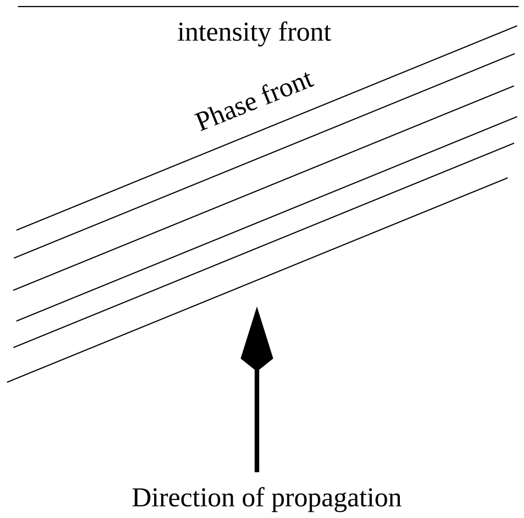

Figure 4.2: Pulse tilt.

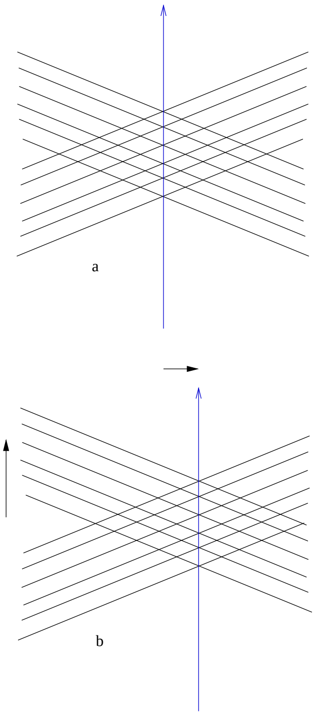

Figure 4.3: Measuring pulse tilt: phasefronts are shown, a and b are delayed in time wrt. each other.

manifest itself as a sideways movement of the autocorrelation beam with changing time delay (figure 4.3). This is because a pulse tilt will effectively ‘resolve’ any change in temporal delay along the axis of propagation into lateral motion of the point of overlap, and hence into motion of the sum frequency beam. Whilst this worked well, it was difficult to set up with sufficient accuracy each time it was needed and eventually we were able to purchase a commercial unit from Light Conversion. This works in a similar manner, but is in effect ‘solid state’ with no temporal scanning required. This is achieved by having the wide beams cross at different angles with respect to the azimuth of the doubling crystal; this maps the temporal delay to the spatial width of the line projected, giving a literal image of the pulse width. The pulse tilt is directly represented by the tilt of the projected line. For more details of this temporal to spatial mapping, see the section on FROG (4.2). Such a direct read out gives immediate feedback during alignment of the regenerative amplifier, thus ensuring optimal OPA performance.

4.2 Frequency Resolved Optical Gating

FROG is a relatively new technique, developed by Rick Trebino amongst others [92]. A FROG trace contains information about how the spectrum of a pulse varies along the timespan of the pulse. An analogy for this is that of a musical score. This shows the notes (frequencies) of a musical piece with respect to the duration of the piece. This information can be used to diagnose laser problems, for example, a chirped pulse (section 4.1.3) would have a steady increase or decrease of frequency with respect to time. One way to measure this is to set up an autocorrelator as in section 4.1.2, and record the entire spectrum at each time delay rather than integrating it. These data can then be plotted as a two dimensional trace, plotting frequency versus time. The additional frequency dimension can be used to reconstruct the electric field of the pulse.

The temporal scanning method has several disadvantages, principally that it takes a long time, and it assumes that each successive pulse is identical, and thus meaningful to the overall trace. It would be much better to taken an entire FROG trace in one shot, and the commercial FROG we use in our lab, *GRENOUILLE*, does just that — and has no moving parts [93, 94].

Like the commercial pulse tilt autocorrelator we use, the *GRENOUILLE* splits a beam elongated by a cylindrical lens up into two parts and crosses them at an angle in a nonlinear doubling crystal (figure 4.4) which maps or resolves the temporal profile of the beam on to a spatial direction. The splitting is done using a Fresnel biprism. The spectral dimension of the FROG trace is obtained by using a thick nonlinear crystal. As described in section 2.2.1, beams in a nonlinear crystal are subject to a phase matching constraint upon their entry angles to conserve photon momentum. The thick crystal has a relatively small phase-matching bandwidth, so the phase-matched wavelength produced by it varies with angle. Thus the nonlinear crystal acts as a spectrograph in the plane orthogonal to the arrangement shown in figure 4.4. Finally, the two dimensional FROG pattern is imaged with a CCD camera and read into a computer.

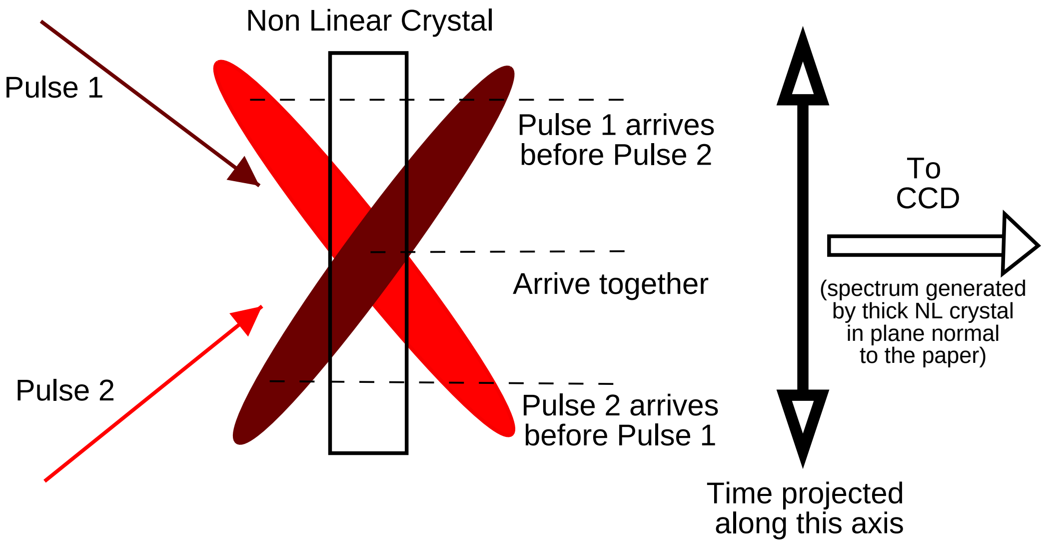

Figure 4.4: How the *GRENOUILLE* FROG maps time on to a spatial direction.

This two dimensional SHG FROG trace is mathematically represented by

$$I_{\mathrm{FROG}}(\omega, \tau) = \left| \int_{-\infty}^{\infty} E(t)E(t-\tau)\exp(-i\omega t)\mathrm{d}t \right|^2$$

which is the Fourier transform of the electric field intensity gated (convolved) with itself. The computer program must therefore invert this equation to recover the electric field and hence its phase. This cannot be done analytically, so a complex iterative algorithm is used — for more details see Trebino's book [92, chapter 8]. No assumption needs to be made about the mathematical form of the pulse shape.

FROG measures many of the parameters described in section 4.1 above. The pulse temporal and spectral widths are obtained from the reconstructed electric field. Spatial chirp is indicated by a tilt in the FROG trace. Pulse front tilt is indicated by a displaced trace along the temporal axis, but the tilted front pulse autocorrelator is much more intuitive for real time correction of any tilt from the TSA. The most useful practical feature of FROG is the real time feedback for laser alignment.

A few examples are now given. Figure 4.5 shows a very round and even FROG trace (with its electric field reconstruction) from the *Tsunami* femtosecond oscillator. The pulse length is 91.2 fs FWHM, the spectral width is 4.87 THz FWHM and the time-bandwidth product is 0.44. Figure 4.6 shows a FROG trace after the regenerative amplification stage. The amplifier adds complexity to the pulse, and it is the object of amplifier alignment to reduce this added complexity as much as possible. The pulse width is 140 fs FWHM, spectral width is 4.36 THz FWHM and time-bandwidth product is 0.61.

It was noted in the previous chapter that the position of all the reflective and refractive elements in the pulse shaper for the visible component of the SF are critical to the temporal and spectral resolution of the experiment (section 3.1.5). Real time feedback from FROG allows this part of the experiment to be aligned very efficiently. If the narrowing slit is removed entirely, then the pulse shaper should return pulses of the same (or very similar) form to those from the amplification stage. Figure 4.7 shows an example of a FROG trace and reconstructions for the output of the pulse shaper. Again, some complexity has been introduced, but this has at least been systematically minimised. However, in this example the pulse front is clearly tilted as shown by the displacement of the trace along the time axis; this is not a problem for the up-conversion pulse. The pulse width is now 127 fs FWHM, the spectral width is 4.91 THz FWHM and the time-bandwidth product

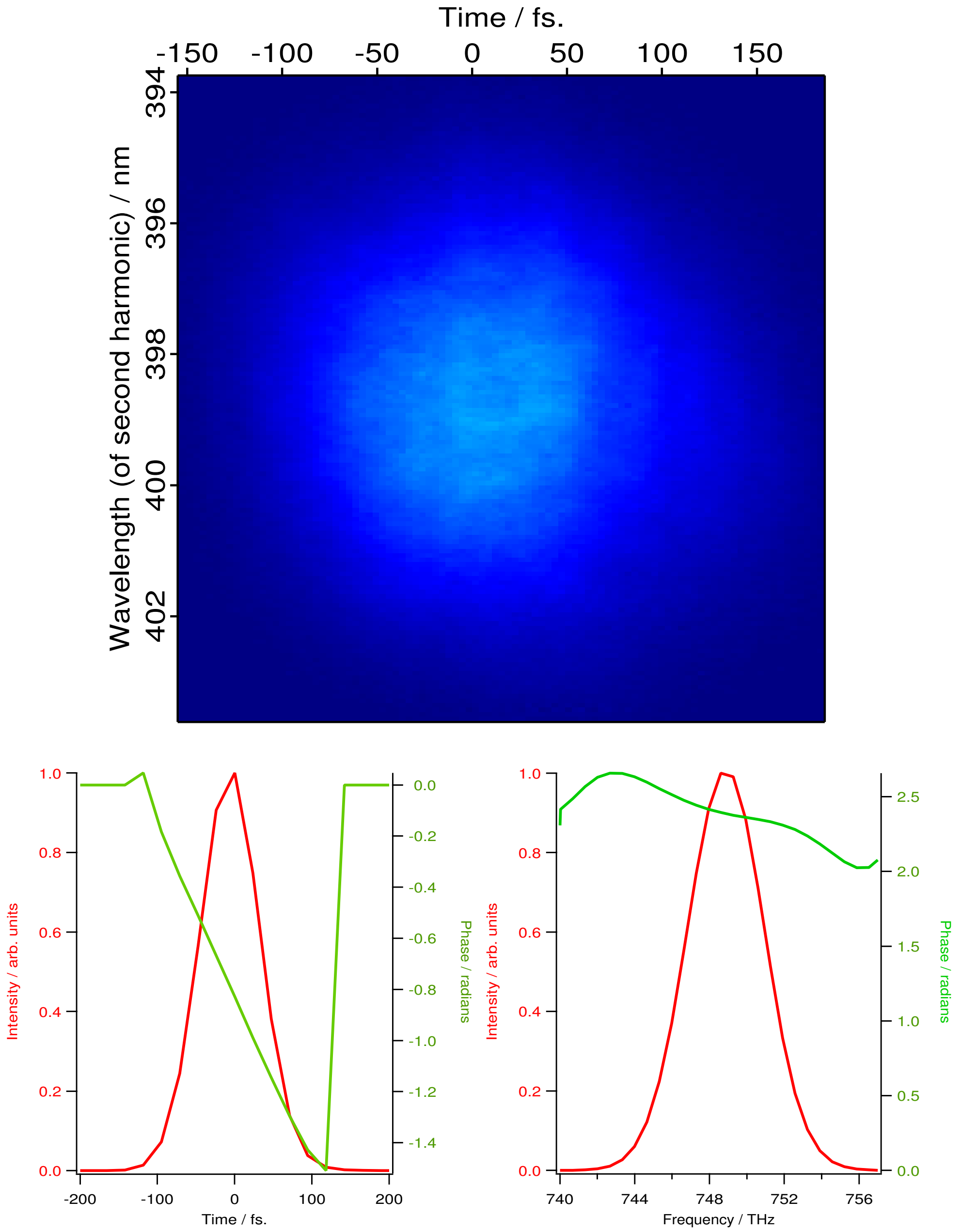

Figure 4.5: FROG trace of the femtosecond oscillator. The upper plot is the raw FROG data, whilst the lower left and right plots are the reconstructed electric field in the time and frequency domains respectively. In each of these plots the red trace is the intensity profile (which is the most useful for our purposes), and the green trace is the phase.

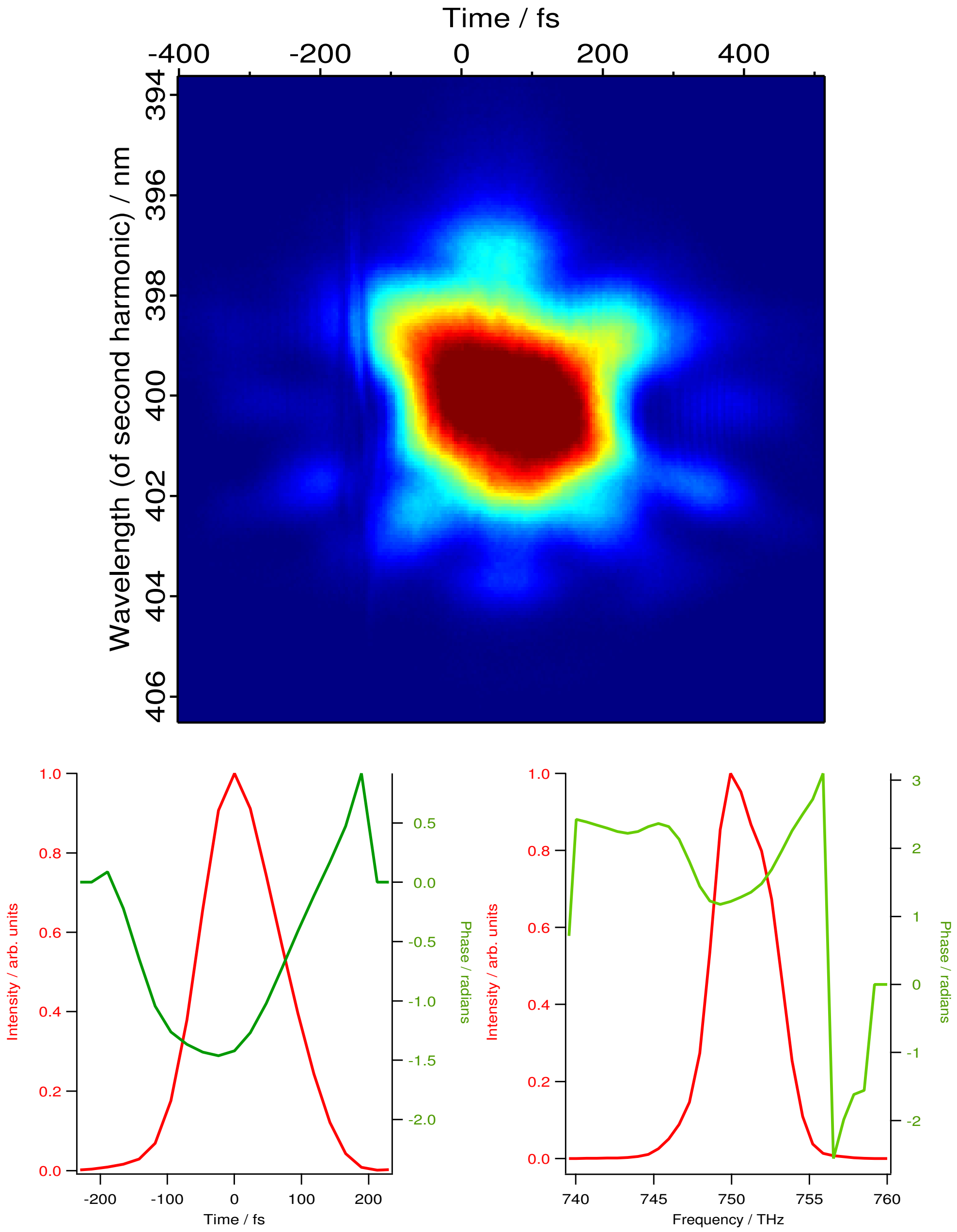

Figure 4.6: FROG trace, and electric field reconstructions, of the output of the regenerative amplifier stage.

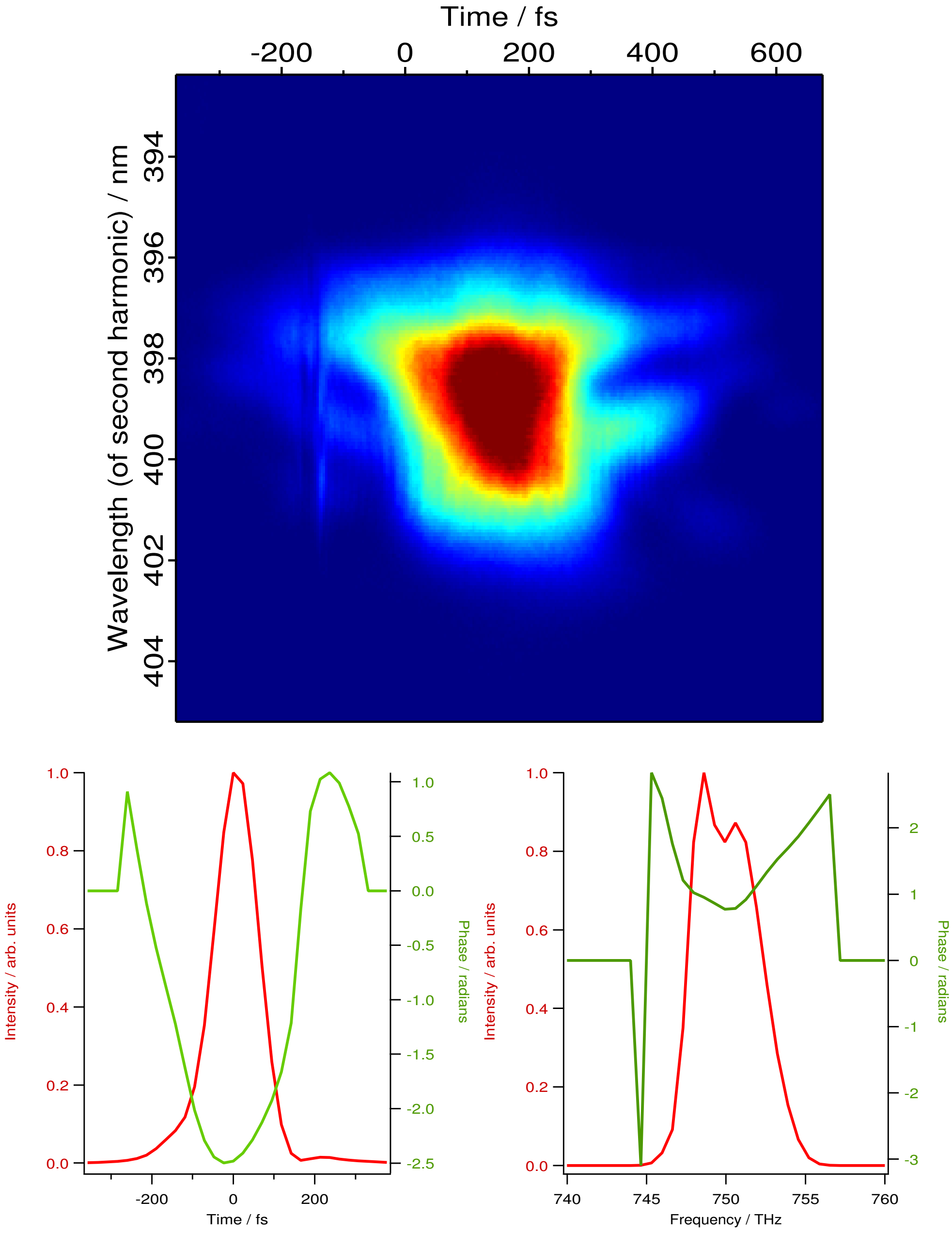

Figure 4.7: FROG trace, and electric field reconstructions, of the output of the pulse shaper stage, without narrowing slit. In this example the pulse front is clearly tilted, as shown by the displacement along the time axis.

is 0.63. One notes a gradual increase of this product (and hence the pulse complexity) as the pulses pass through the system from oscillator (0.44), to amplifier (0.61) and to pulse shaper (0.63).

4.3 Novel In-Situ Pulse Characterisation

4.3.1 The Problem

For accurate temporal and spectral measurements the temporal and spectral properties of both IR and VIS beams need to be known in order to fit data, as seen in chapter 5. Whilst the properties of the VIS beam are know by FROG this still leaves the IR beam uncharacterised. This would be traditionally achieved by methods similar to those described in section 4.1.2; one would perform a *cross correlation* (comparison of one beam with another) of the pre-characterised VIS beam and the uncharacterised IR beam, and then recover information about the IR beam from this. The VIS and IR beams would be combined in a nonlinear crystal, with one subject to a temporal delay, and the intensity of the sum frequency can be monitored as a function of time delay [35, 95]. The apparatus for such a measurement already exists in our experiment, the time delay line and the $LiIO_3$ crystal are already in place. However, this still does not allow for *in situ* characterisation — the $LiIO_3$ crystal is not subject to exactly the same geometry as the in-chamber arrangement. The $LiIO_3$ crystal has a finite thickness and the effect of this is to spread (convolve) the temporal measurements by this finite width (see section 4.3.4). Not to mention the fact that $LiIO_3$ abruptly stops transmitting above 5.5 μm, which is acceptable for measurements specific to CO but perhaps not for other molecules such as NO.

4.3.2 The Solution

In the previous chapter, it was mentioned that we use a layer of potassium on our metal crystal to assist in the day to day alignment of the experiment. We have also found that such a metal layer gives us an excellent tool for the characterisation of the instrument as a whole. One uses the potassium layer placed on the surface to align the system, as the nonlinear medium in the crosscorrelation of the VIS and IR beams and then one observes the surface SF signal as a function of time delay between the two beams. For each time delay an SF spectrum is produced similar to the one given in figure 4.8. A program to control the delay stage and ICCD for this is given in Appendix A. The width of the IR pulse can be determined by mathematically deconvolving the known temporal form of the visible pulse from the cross correlation trace. By measuring the entire spectrum of the SF signal as a function of time delay, a FROG trace can be taken (albeit not a single shot FROG as taken by the *GRENOUILLE*), comparing the visible pulses with the IR pulses. The cross-correlation of the broadband 800 nm beam with the IR gives the effective instrumental temporal resolution of the instrument for free induction decay studies — section 5.4.1.

4.3.3 Characteristics of Our System

FROG indicates that the pulse width before the pulse shaper is 140 fs, and 125 fs afterwards, with no slit inserted in the shaper (see section 4.2). The spectral width of the unchanged 800 nm pulses is 7.4 nm (116 cm^{-1}). If a slit is placed in the shaper, then the pulses become spectrally narrowed to 0.64 nm (10 cm^{-1}), for a slit width of 200 μm, again measured by FROG. The experiment was set up as in the previous chapter, during the surface alignment stage, with just greater than a monolayer of potassium on the Ru$\{10\bar{1}0\}$ surface. A cross correlation of the IR

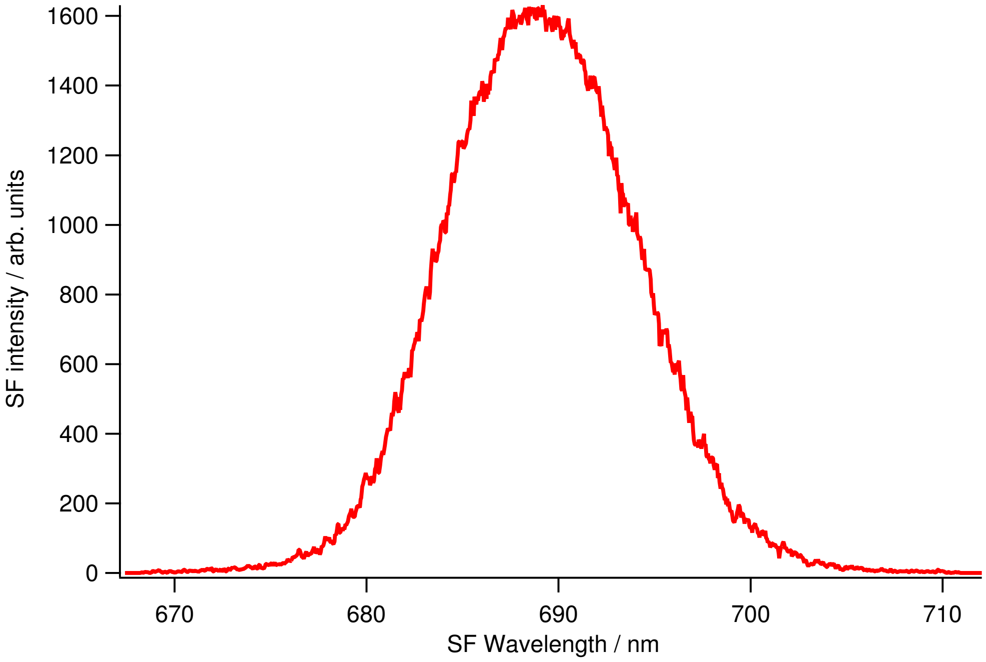

Figure 4.8: Example of non-resonant SF signal from potassium covered Ru$\{10\bar{1}0\}$. Data like these are collected for each IR-VIS delay time in the cross correlation. The example in this figure is at $\tau = 0$.

and broadband VIS pulses was taken by varying the IR-VIS time delay, with 50 shots being taken for each delay time. This takes about 6 minutes, and is shown in figure 4.9. This cross-correlation is mathematically equivalent to

$$I_{\mathrm{cc}}(\tau) = \int_{-\infty}^{\infty} E_{IR}(t)E_{VIS}(t-\tau)\mathrm{d}t.$$

Assuming a Gaussian temporal profile for the VIS pulses of 125 fs width, the form of the IR temporal profile can be obtained by deconvolution, yielding an IR pulse width of 240 fs at a centre wavelength of 5.1 µm. This has a spectral width of 156 cm^{-1} (thus indicating how spectral resolution would be lost with a broadband VIS beam) and a time-bandwidth product of 1.1. These SF spectra can be plotted as a function of time to yield a FROG trace (figure 4.10). The tilt of this trace indicates a slight temporal chirp of 0.7 (cm fs)$^{-1}$. When the same experiment is performed with the narrowed VIS pulses (200 µm slit in place, over 100 shots per delay time) it yields a temporal width of 2.76 ps, thus highlighting how temporal resolution is lost with the spectrally narrow beam (also figure 4.9). The fundamental limit of the resolution of the spectrograph / detector is 0.6 cm^{-1} per pixel for the 1800 g/mm grating.

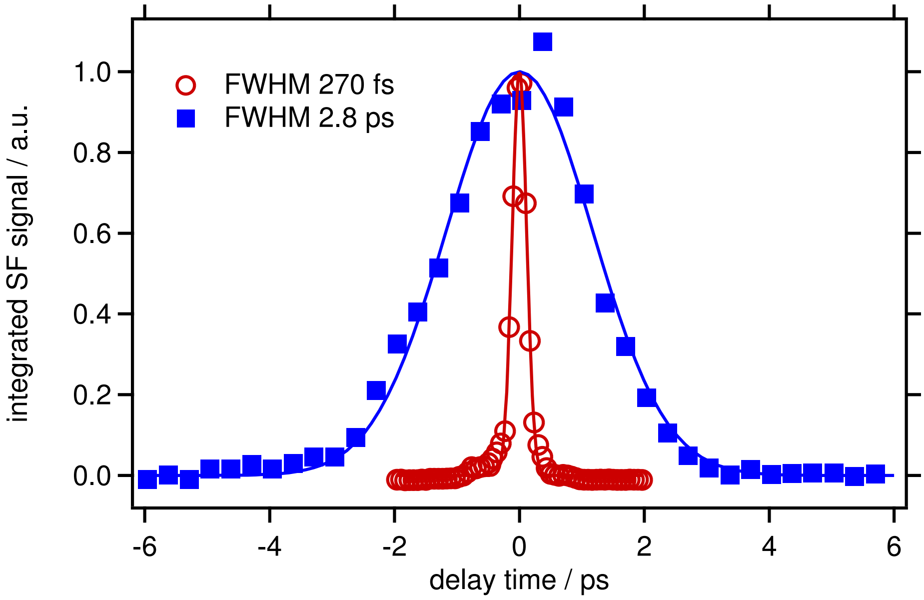

Figure 4.9: In situ cross-correlations of IR pulses with broad (○), and narrowed (■) visible pulses.

4.3.4 Advantages of this Technique

I have already stated many of the advantages of this system for characterising laser pulses. Measurement *in-situ* gives results as close as is possible to the conditions of the real experiment. The inherent thinness of an adsorbed metal layer on a surface removes the vast majority of the optical dispersion and phase matching effects which are present in nonlinear optical crystals of finite thickness. The

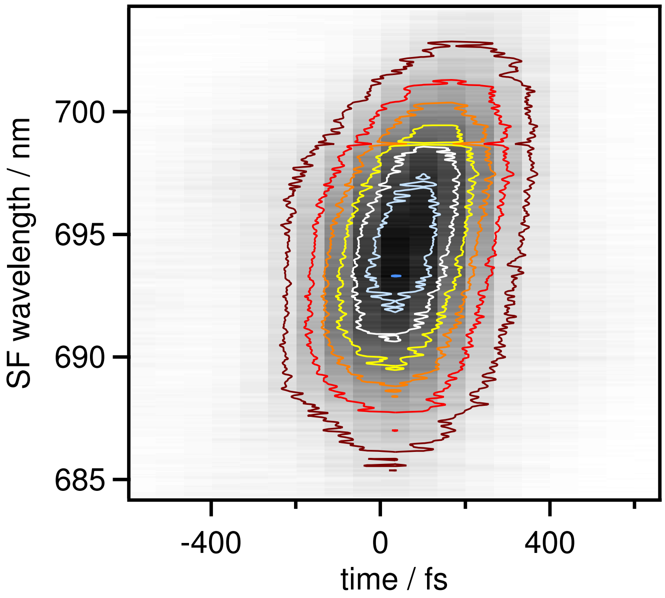

Figure 4.10: FROG trace generated from spectrally resolved cross correlation of IR with spectrally broad visible pulses. The original greyscale FROG trace is shown, with added coloured intensity contours for clarity.

difficulty in maintaining the phase matching condition throughout the finite width of a nonlinear optical crystal broadens correlations performed in such crystals. And with many crystals, the transparency range is finite.

It is possible to use a GaAs wafer in reflection to characterise laser pulses. However, these have a low damage threshold, and unless one is working on GaAs, these have to be mechanically inserted in the beam path, and this is difficult to reproduce.

The SF signal is not particularly sensitive to potassium coverage, peaking at 1 ML but only halving in intensity for multilayer coverages. We have found up to a 300 times enhancement in signal strength over a clean Ru$\{10\bar{1}0\}$ surface. Similar levels were found using a Pt{111} surface. This compares with enhancement factors of 70 [96] to 1000 [97] with alkali metals for second harmonic generation.

The cleanliness of the surface makes little difference; often whilst realigning the system we have dosed potassium on top of a CO layer and obtained similar signal levels. We fitted a second Getter source to the vacuum chamber and dosed caesium on to the surface, with the effect of roughly doubling the SF signal.

As a final note, it is possible to see many other nonlinear processes at work, simply by rotating the sample manipulator until the angles are suitable for these processes to be detected. Figure 4.11 shows IR-IR-VIS SF mixing (610 nm), VIS second harmonic (400 nm), and difference frequency mixing between the VIS SH and the IR (440 nm), as well as the IR-VIS SF signal (700 nm) used for the cross correlations.

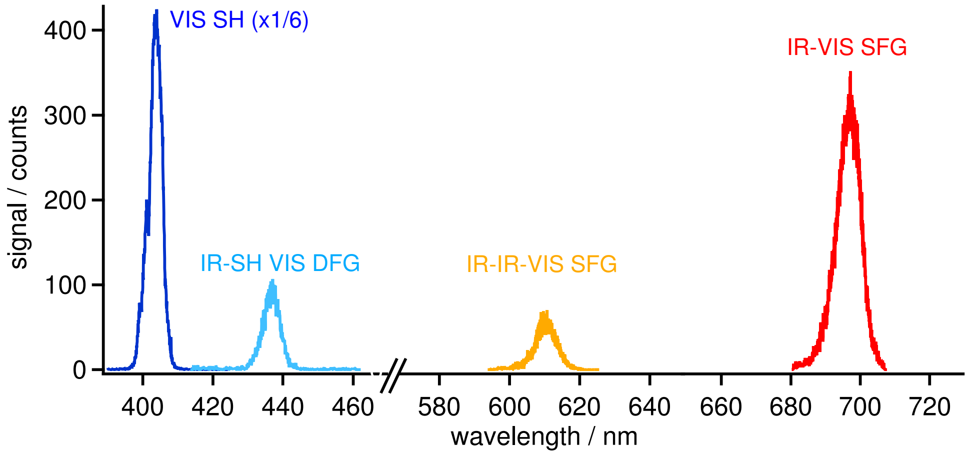

Figure 4.11: Various nonlinear optical interactions of the IR and visible pulses seen on a K covered Ru$\{10\bar{1}0\}$ surface.

4.3.5 Physical Origin of the Enhancement

Before concluding this chapter, I shall discuss in more detail the physical origin of the SF signal from the alkali metal layer. Density functional calculations of the SF response of a bare and Cs covered metal surface have been performed using a jellium model [98]. This predicts an increase in SFG efficiency of between 10^3 and 10^4 for two layers of Cs and an 800 nm light source. Much greater enhancements are possible if either the VIS or IR beams are close in frequency to the alkali metal's plasmon frequency, which for a simple free electron metal is given by

$$\omega_p^2 = \frac{ne^2}{\epsilon_0 m_e}.$$

For Cs ω_p corresponds to 2.9 eV. Our VIS beam has an energy of 1.55 eV and the IR-VIS SF is at 1.80 eV. Clearly the 300 times enhancement by the Cs layer is not a resonant effect.

However the difference frequency signal of the IR and the doubled VIS could be resonantly enhanced on the K layer as the photon energy of 2.88 eV is close to the plasmon frequency of potassium which corresponds to 2.7 eV [99]. One might wonder if such a resonant process could affect the temporal response, and hence reduce the suitability for cross-correlation purposes. However, a study of alkali metal clusters found the plasmon dephasing time to be between 1 fs and 15 fs [100]. This is insignificant compared with the pulse widths used in our experiments but could affect users of 20 fs laser systems. We could approach the plasmon frequency by using a 400 nm VIS pulse (i.e. 800 nm doubled), which whilst increasing the resonant enhancement would probably reduce the overall signal due to intensity loss in the 400 → 800 nm conversion and the lower sensitivity of the i-Star CCD at these wavelengths.

So for our system at present the enhancement due to the alkali metal layer is probably due to the non-resonant $\chi^{(2)}$ of the layer, as a resonant plasmon enhancement has been ruled out at these wavelengths.

Chapter 5

Study of CO on Ru{$10\bar{1}0$}

In this chapter I present the first chemical results from the ultrafast spectrometer. These were obtained from the Ru{$10\bar{1}0$} crystal originally purchased to study the photocatalytic decomposition of water as described in section 1.1.3. Ru{$10\bar{1}0$} was chosen to provide an interesting surface structure to contrast with the close packed Ru{0001} surface studied by Bonn *et al.* in Berlin and Leiden as part of the water decomposition framework (section 1.1.3). The Ru{$10\bar{1}0$} surface is shown in several different representations in figure 5.1. CO was chosen as it has a large dipole moment suitable for SF study; also it is a well studied molecule in the surface science community due to its many rôles in commercial catalysis, not least its oxidation into CO_2 on platinum type metals in vehicle exhaust catalytic converters. See [101] for a review of the surface science of CO on transition metals. The CO/Ru{$10\bar{1}0$} system has proved to be an interesting and challenging first system to study using the new spectrometer, with surprisingly little previous work being published on this metal-adsorbate system in the surface science literature.

Three main coverage dependent data sets of the CO stretch frequency and linewidth are presented in this chapter, referred to as data sets 1, 2 and 3. Data sets 1 and 2 were taken in the summer of 2002 and data set 3 in the spring of 2003.

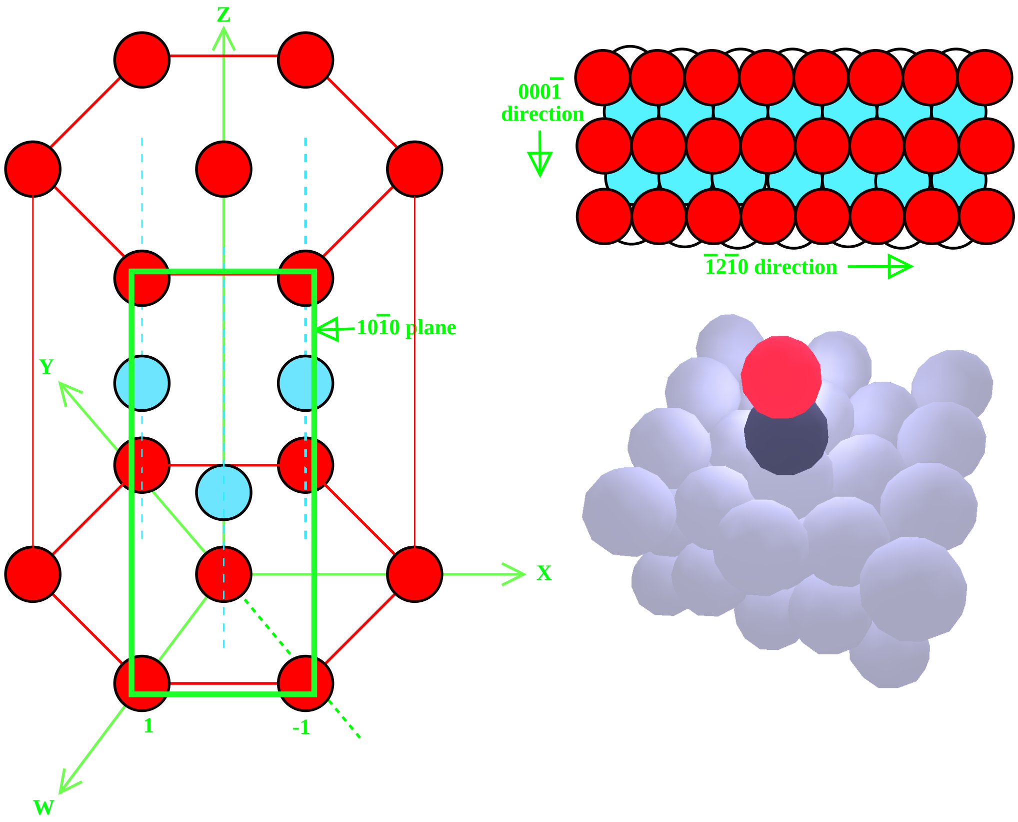

Figure 5.1: Ru$\{10\bar{1}0\}$. Left hand panel shows $\{10\bar{1}0\}$ plane in relation to the close packed plane. Top right panel shows surface view, and lower right panel shows a 3D representation with a single adsorbed CO molecule.

Sets 1 and 2 were taken before electrochemical polishing of the Ru$\{10\bar{1}0\}$ sample, and set 3 afterwards. However, as we shall see, the spectral data from all three sets are in very good agreement.

Spectral data set 3 is also accompanied by some corresponding free induction decay measurements. The work in the previous chapter on the temporal characteristics of the experiment is used to accurately fit the FID data and gives a much more accurate measurement of T_2 / linewidth than the spectral data can provide.

A brief isotopic study is presented to estimate the contribution of dipole-dipole coupling to the effects seen in the coverage dependent data. The effect of sample temperature on the CO stretch frequency is also investigated for two coverages.

The data sets represent the few occasions out of many attempts when every part of the experiment was working consistently well enough over the 24 or so hour period needed to align the system, characterise the laser and take enough data for a wide variety of coverages or temperatures

5.1 Previous Studies on this System

The first study of the CO/Ru{10$\bar{1}$0} system in the literature was conducted by Bonzel *et al.* in 1975/7 [102, 103], as part of a more substantial study of NO on the same surface. This group did not see an ordered CO layer with LEED even at 80–120 K. They also produced TPD data which agree with later workers. Their structural conclusions were later confirmed by Kiskinova *et al.* [104, 105]. The most detailed previous study of the CO/Ru{10$\bar{1}$0} system, and the most useful for our purposes, was performed by Lauth *et al.* in 1989 [106]. These workers used a combination of LEED, High-Resolution Electron Energy Loss Spectroscopy (HREELS), TPD and Contact Potential Change (CPD) measurements. They *did* see ordered CO layers at low temperature. Rotaris *et al.* added to this an X-ray Photoelectron Spectroscopy (XPS) study in 1996 [107].

5.1.1 Structure

Lauth *et al.* [106] reported that at 120 K their clean and annealed Ru{10$\bar{1}$0} surface showed a (1 × 1) LEED pattern. Upon exposing 0.7 L of CO they noticed a (3 × 1) overlayer appearing. They performed a coverage dependent LEED study, and used TPD to calculate the coverage for each exposure. Their interpreted results for various coverages are summarised in figure 5.2. They suggest that at coverages greater than 0.66 ML the CO molecules must tilt in alternate directions to allow packing in the limited space available. The saturation structure is a complex quasi-hexagonal densely packed array. They back up this suggestion with their HREELS data, see section 5.1.3. The saturation coverage is 1.22 ML. Rotaris *et al.* [107] suggest from their XPS study that this is equivalent to 1 ML on top sites, and the remainder on bridge sites.

5.1.2 Previous TPD results

Lauth *et al.* performed their TPD experiments by adsorbing at 100 K, and achieved saturation coverage after ~5 L of exposure. At saturation they note 3 thermal desorption peaks, designated as β_1 (380 K), β_2 (400 K) and β_3 (520 K). The high temperature β_3 peak fills first, by 1.0 L of exposure. Then the β_2 peak grows until 2.2 L of exposure. The β_1 peak appears as a shoulder to the β_2 peak, increasing until the surface is saturated. From their TPDs they calculated that the sticking coefficient, $s(\Theta)$, at 120 K is close to unity up until 1 ML, and then decreases to zero. At 250 K, the intitial sticking coefficient is only 0.9, and decays much more rapidly upon increasing coverage due to the competing desorption process, which occurs from the β_1 and β_2 peaks at this temperature.

5.1.3 C–O and CO–Ru Stretch Frequencies

The HREELS data from Lauth *et al.* reveal a steady linear increase in the CO stretch frequency with coverage, of around 1975 cm^{-1} at near zero coverage, rising to 2062 cm^{-1} at saturation. These results are plotted later (figure 5.17 in section 5.3.2) as a comparison with our data. The CO–Ru stretch (for completeness, as we cannot measure this in our wavelength range) varies by about ~ ±10 cm^{-1} with increasing coverage, and reaches a maximum of 453 cm^{-1} at $\Theta = 0.3$ ML.

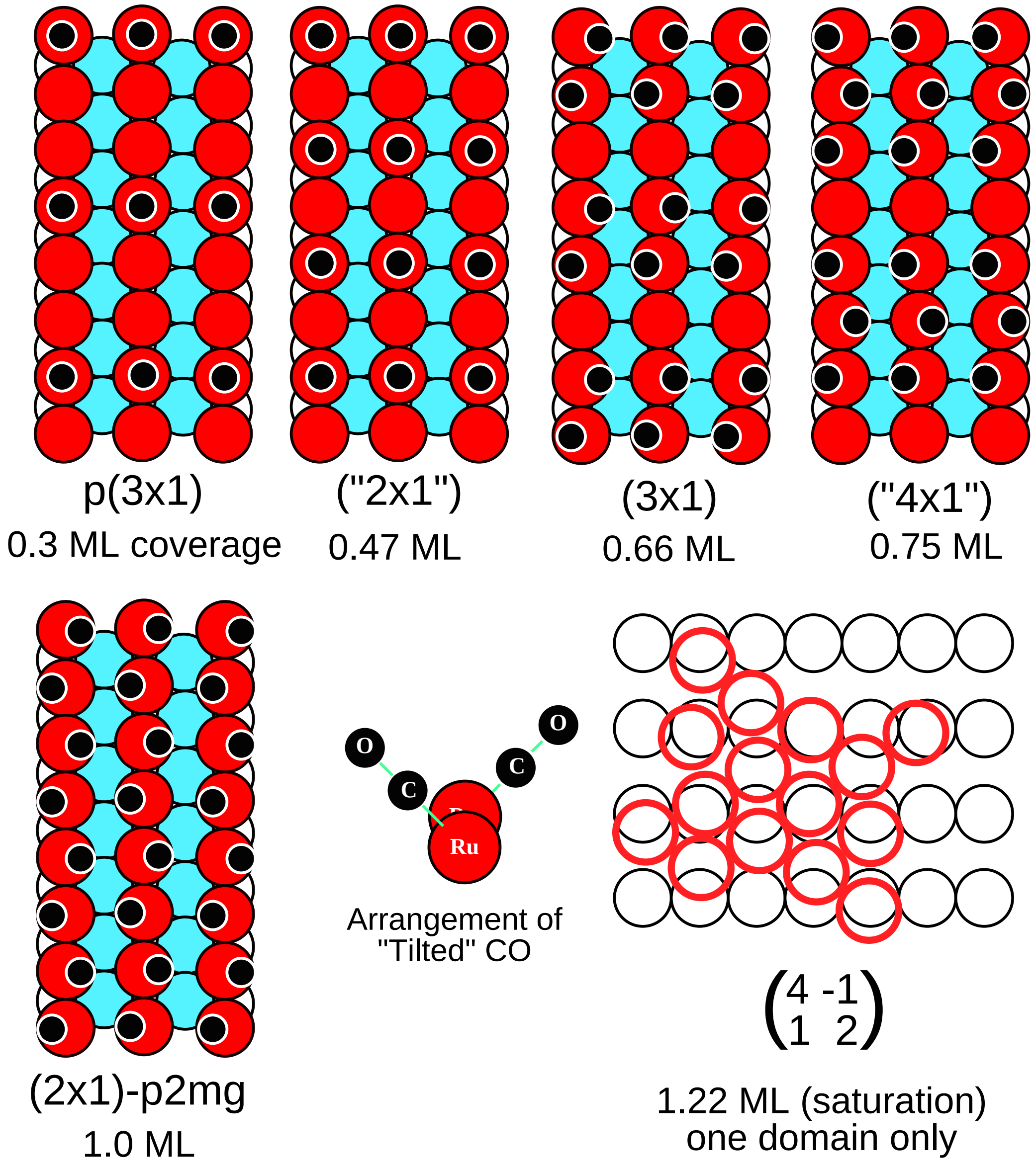

Figure 5.2: CO on Ru{10$\bar{1}$0}, based on data from LEED / TPD study by Lauth *et al.* (1989) [106]. See text for details.

5.2 Sample Preparation

5.2.1 Cleaning and Annealing

The Ru{$10\bar{1}0$} crystal was supplied mechanically polished by Metal Crystals and Oxides (Harston, Cambridgeshire) and measures $8 \times 11 \times 3$ mm. It was cleaned using cycles of argon ion bombardment, annealing to restore surface order, then heating in oxygen to remove carbon by oxidation to form CO. This method is broadly based on that used by Ku *et al.* [103] and Harrison *et al.* [108], amongst many others.

The actual cleaning recipe used is described below and is that given by Christmann ([109], based on [110]); with the exceptions that Christmann's method uses neon rather than argon for sputtering, and that the oxygen cycle is based on that used by Tikhov [111].

- Anneal to 1450 K for 2 min
- Wait for pressure to recover to $< 5 \times 10^{-10}$ mbar
- Briefly flash to 1450 K
- Hold crystal at 650 K (avoids CO and H_2 adsorption) and sputter with Ar at $\approx 1 \times 10^{-5}$ mbar for 20 min at 500 eV beam energy
- Expose to O_2 for 15 mins at 5×10^{-7} mbar and 1000 K
- Anneal 3 or 4 times to 1450 K for 2 min, to react off carbon and remove oxygen
- Sputter for a further 15 min as before
- Flash to 1450 K

Occasionally the crystal was flashed to 1550 K by connecting an additional power supply as described on page 71. Tikhov [111] suggests this is a more effective annealing temperature, but it is close to our thermocouple melting point so was not used frequently.

Due to the difficulties in obtaining a LEED pattern described in section 5.2.2, an electrochemical polishing procedure was later performed on the crystal by MaTeck GmbH (Juelich, Germany) to better than 0.1°. SF data sets 1 and 2 in subsequent sections were obtained before this polishing was performed, although little difference was observed with adsorbed CO via LEED or SFG (i.e. data set 3) after the process.

5.2.2 Surface Order: LEED, Laue and AFM

The clean surface LEED pattern of the Ru{10$\bar{1}$0} sample *before* electrochemical polishing is shown as figure 5.3. The spots are not very sharp and are vertically elongated in the [0001] direction. Removing the sample from the chamber, rotating it 90° and replacing it also changed the orientation of the elongation, thus showing this to be a property of the sample rather than the LEED optics.

Such elongation of the spots could be characteristic of the presence of terraces on the surface. The size of a LEED spot, as with any other diffraction pattern, is a convolution of the different length scales present in the sample. For a surface with no terraces, the convolution of the surface structure with the large scale flat surface represented in reciprocal space does not change the spot size. When small terraces are present, which are large in reciprocal space, this will cause a spreading of the LEED spots.

Coupled with the fact that we could not see any additional spots attributable to an ordered CO overlayer at any temperature, we decided to have the sample electrochemically polished as described in section 5.2.1. After this process the

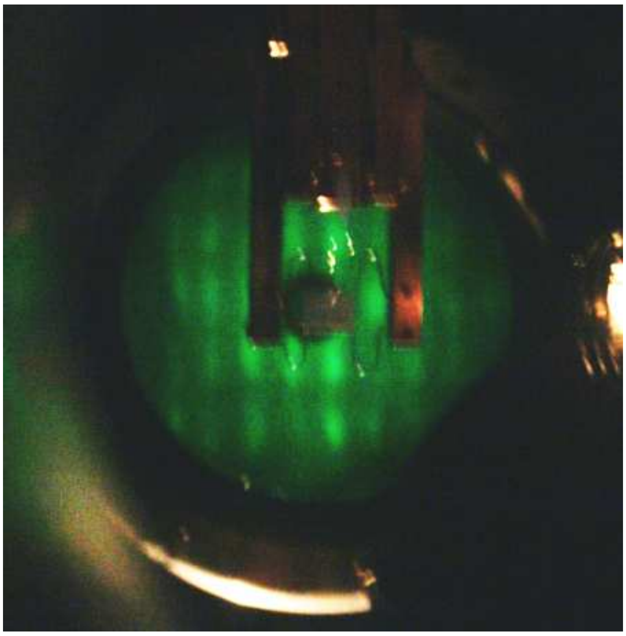

Figure 5.3: LEED photograph of Ru{10$\bar{1}$0} sample before electrochemical polishing. Beam energy is around 120 eV, sample temperature is 100 K. Spots are vertically elongated. These photographs are taken with a domestic camera and are not of good quality.

clean surface LEED pattern was less elongated, as shown in figure 5.4, but the spots were still not as round and sharp as they ought to be. No CO overlayer spots have been observed by us to date.

Given the disappointing LEED results, the crystal was returned to Metal Crystals and Oxides (pre electrochemical polishing), and they subjected it to Laue X-ray diffraction to determine the bulk order. This uses a broadband spectrum of X-rays to satisfy the Bragg condition for many diffracting planes, and thus all of these planes are seen simultaneously on one image. The set up is broadly similar to that used for LEED as shown in figure 3.29, but with the source of electrons replaced by an X-ray source, and the hemispherical screen replaced by a flat photographic plate. The Laue pattern is shown in figure 5.5. One can see that the

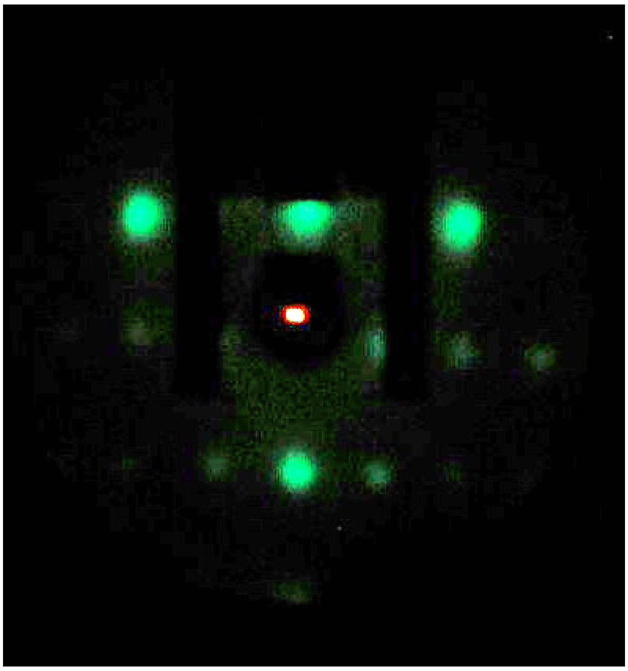

Figure 5.4: LEED photograph of Ru{$10\bar{1}0$} sample after electrochemical polishing. Beam energy is around 100 eV.

pattern is slightly displaced in the vertical direction from the central beam. This could indicate a mis-cut of up to 2°, which would produce terraces on the surface. For a structure 1 atom high, this corresponds to a terrace of $\tan 2^\circ = 29$ atoms wide, which corresponds to a terrace size of for example 77 Å along the ridge ($\bar{1}2\bar{1}0$) direction, assuming an atomic separation of 2.70 Å [106] in this direction.

Also before professional electrochemical polishing, the sample was examined on an Atomic Force Microscope (AFM) (with thanks to Dr. Hong-Wei Li of this department). The AFM image is shown as figure 5.6. This shows that the long range order of the crystal is not very good, and may have suffered adversely from polishing. It should be pointed out however, that this image was taken just after our own attempt at electrochemical polishing and this may well have made the surface temporarily worse, or at least exacerbated existing faults.

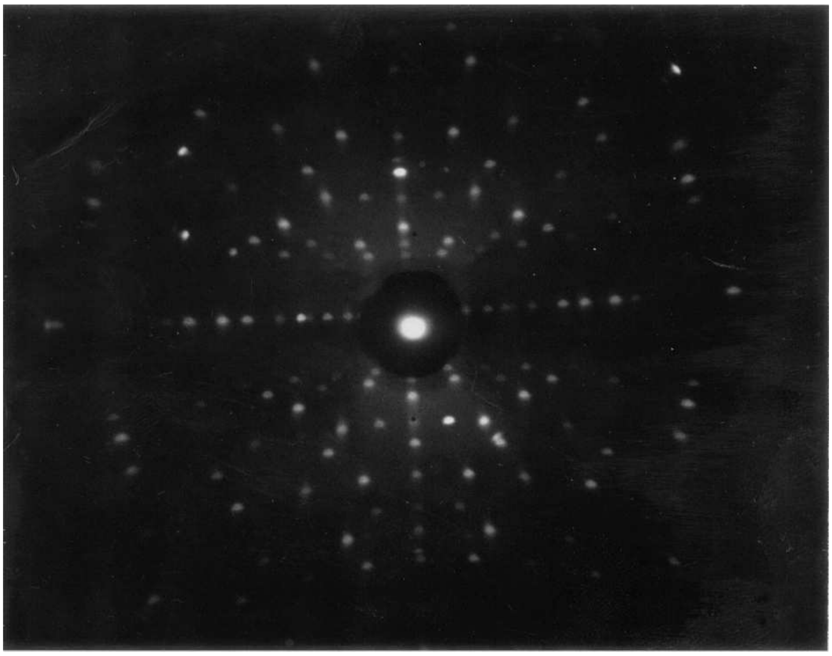

Figure 5.5: Laue X-ray diffraction pattern of our Ru{10$\bar{1}$0} sample.

We must therefore conclude from LEED and Laue that our Ru{10$\bar{1}$0} sample has some mid-range disorder, and from the AFM it is quite scratched over larger length scales.

5.2.3 Surface Cleanliness: AES and TPD

AES spectra of the Ru{10$\bar{1}$0} surface were taken after several of the cleaning cycles described in the previous section, and show the recipe to be effective. An example of these is given as figure 5.7. The characteristic peaks of ruthenium and oxygen are indicated by comparison with the spectra given in [89]. The small oxygen peak at 510 eV shows that there is little oxygen contamination. The largest characteristic peak for carbon contamination would be seen at 275 eV, but is normally obscured by the large ruthenium peak at 277 eV.

However, from [108, 109, 112, 113], the total peak height from carbon and

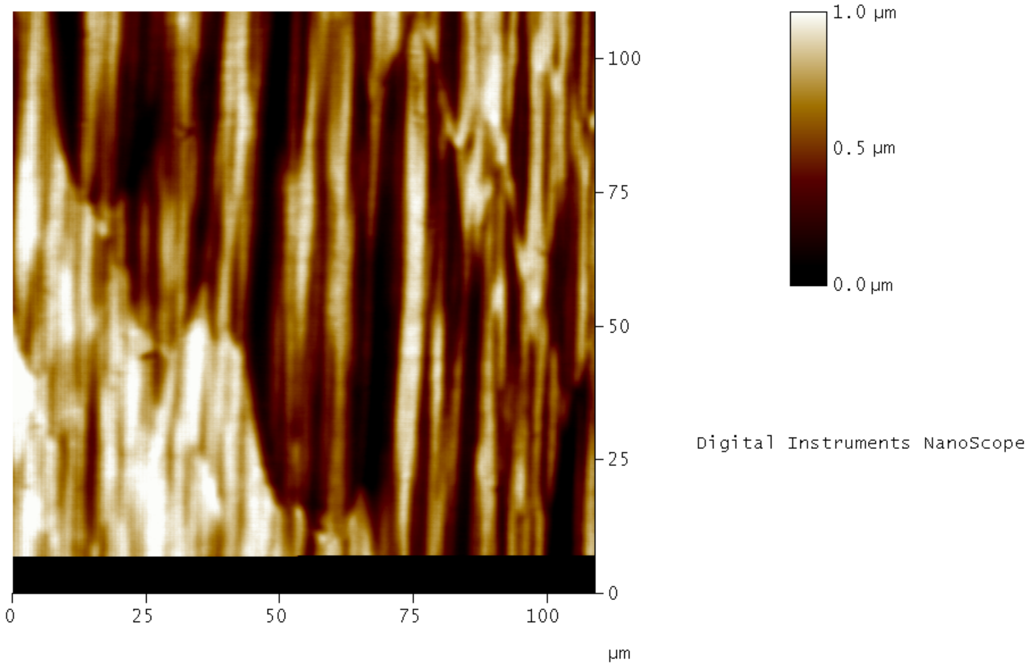

Figure 5.6: Atomic Force Microscope image of our Ru{10$\bar{1}$0} sample.

ruthenium at this energy, and the ruthenium peak height at 235 eV should be related by

$$R = \frac{\mathrm{Ru}_{277} + \mathrm{C}_{275}}{\mathrm{Ru}_{235}} \approx 1.8$$

for an uncontaminated ruthenium surface. This is the case for both spectra in figure 5.7.

Oxygen TPDs were taken to show the efficacy of the oxygen treatment to remove carbon. If carbon is still present, oxygen will react with the carbon to form CO and thus the amount of oxygen seen in a TPD will be less. Also, carbon will block oxygen adsorption sites and a characteristic low temperature mass 32 desorption peak will be attenuated. Example oxygen TPDs are shown in figure 5.8 for successive 0.6 kL oxygen treatments at 900 K. After several oxygen treatments, the TPDs agreed in shape and integral with those given by Tikhov [111] and thus

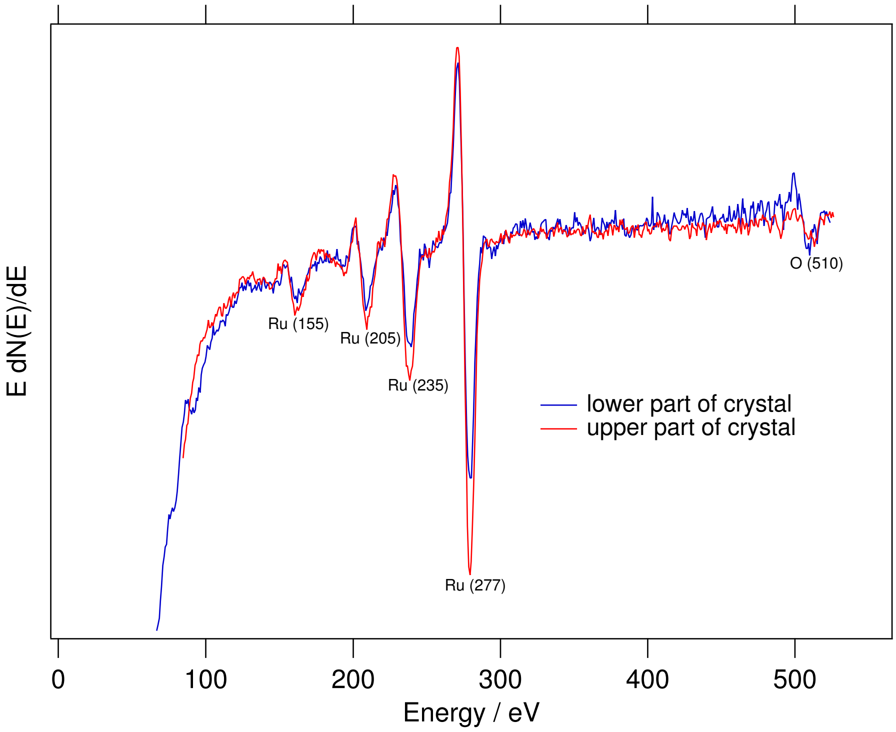

Figure 5.7: Auger Electron Spectra of our Ru{$10\bar{1}0$} sample after cleaning. It is shown in differential form, and was taken with 2.5 keV incident electrons, channeltron bias of 3.5 kV, sensitivity of 50 mV, the AES analyser at 110° and sample at 333°.

the surface was deemed to be free of carbon contamination.

CO TPDs provided the main method of surface cleanliness monitoring, by comparing the form of a saturation coverage TPD with those given by Lauth *et al.* [106] (described in section 5.1.2). Figure 5.9 shows the TPDs corresponding to data set 3 for all coverages examined in this experiment. Whilst CO was being dosed into the chamber, the mass spectrometer was set to the 10^{-9} mbar range at mass 28, and the exposure is recorded at 1 point per second using the same acquisition software used for TPDs, but replacing the ordinal axis with time. The software displays an on-screen cumulative exposure value as feedback to the user

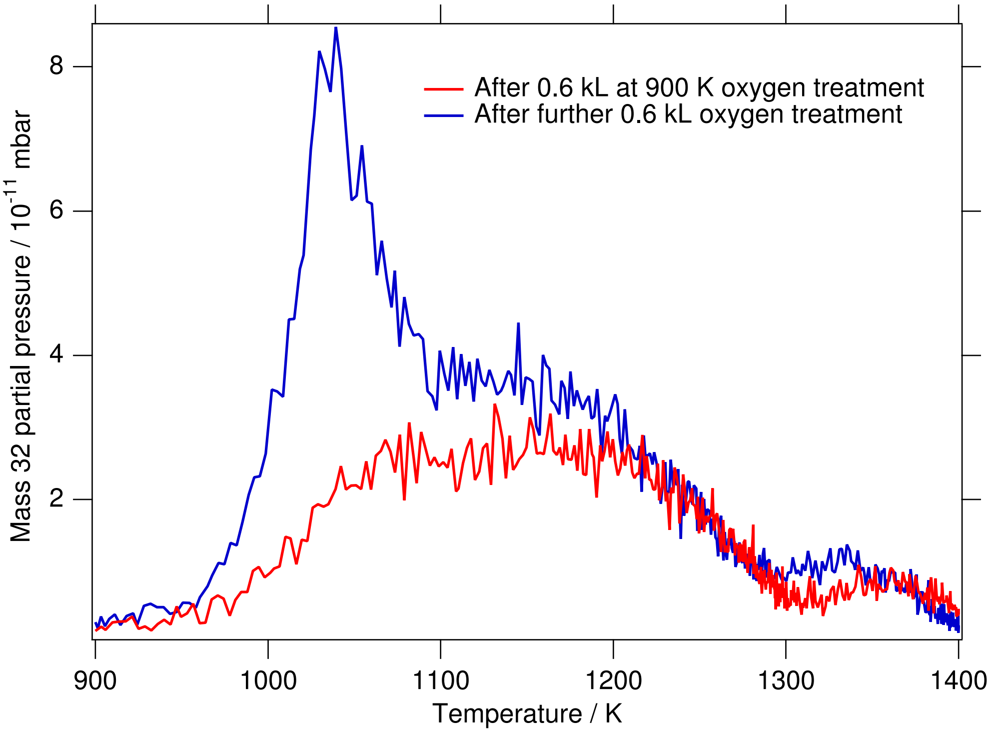

Figure 5.8: Oxygen on Ru{10$\bar{1}$0} TPD spectra after successive oxidation treatments. The peak in the blue curve at 1040 K represents the presence of a monolayer of oxygen according to [111].

operating the dosing valve. The mass spectrometer reads 44.3 times less than the main chamber ion gauge; using this conversion (and 1 L = 1×10^{-6} mbar per second), the integrated area under the exposure curves is converted to an exposure in Langmuirs.

A saturation exposure TPD is usually taken after each day's cleaning to check for cleanliness. Then for each coverage in a coverage dependent study, the exposure is measured whilst dosing, and a TPD is taken after the SF experiments have completed at that coverage. Each TPD curve has a background caused by desorption from the heating wires. The background is determined by fitting a function (usually exponential) to the far head and far tail of the curve, with the important

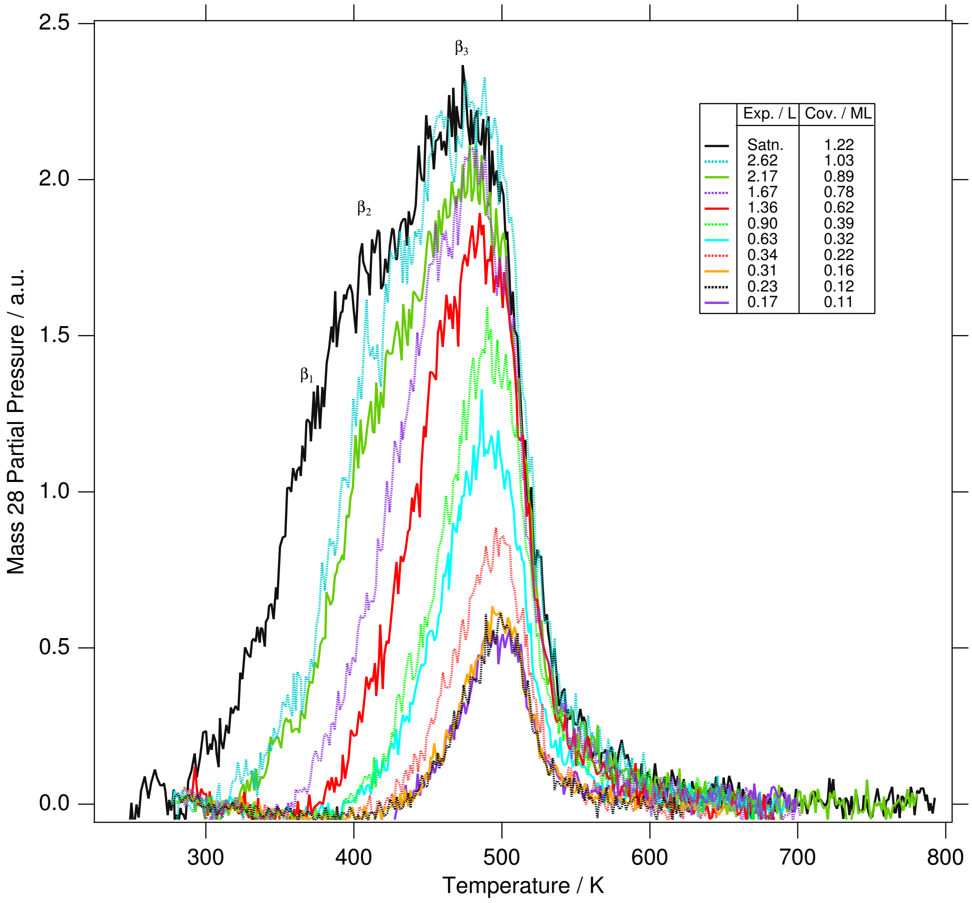

Figure 5.9: CO on Ru{10$\bar{1}$0} TPD spectra corresponding to SF data set 3.

central region masked out. This function is then subtracted from the TPD data. The curves in figure 5.9 have been treated thusly. Assuming that saturation coverage is 1.22 ML from Lauth *et al.* [106], coverages for all the sub-saturation TPDs are then obtained by scaling this value with respect to the integrated area. One can certainly see peaks β_3 and β_2 seen by Lauth *et al.* and possibly β_1 also. Figure 5.10 shows the coverage versus exposure, and from this one can safely assume that saturation is obtained after about 7 L, in excellent agreement with Lauth *et al.* considering the different vacuum systems used. It also shows that the sticking coefficient is roughly constant up to $\sim$1 ML.

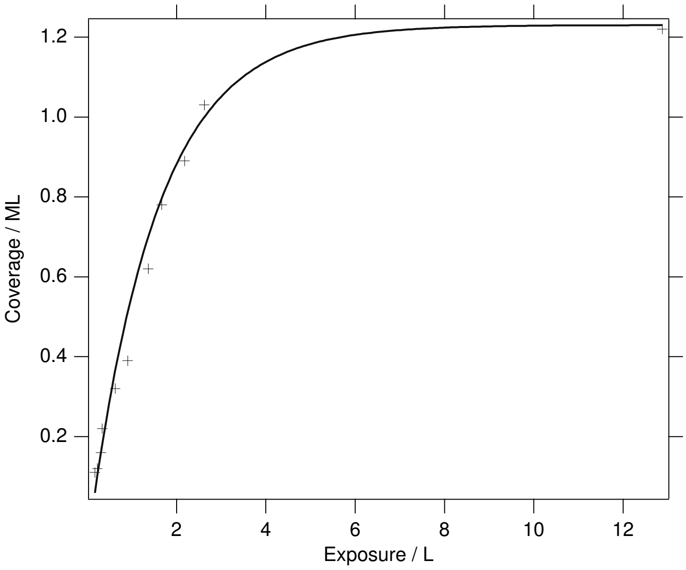

Figure 5.10: Coverage versus exposure for CO on Ru{10$\bar{1}$0}.

5.3 Frequency Domain Study

5.3.1 Experimental Details

Each of the three data sets described was obtained by the following method. Firstly the laser system was warmed up and optimised as described in section 3.1. Whilst the laser was warming up, the Ru{10$\bar{1}$0} crystal was cleaned by the recipe presented in section 5.2.1. Oxygen and CO TPDs are then taken to check the surface cleanliness as described in section 5.2.3. The OPA was set to 5.5 μm which corresponds to a broadband IR envelope with a centre frequency of around 2040 cm^{-1} and FWHM of 140 cm^{-1} when calibrated. Then the beams were aligned into the chamber — section 3.3.4.

With the potassium layer still on the surface, the slit in the pulse shaper inserted and narrowed to ~200 μm and the chemical cell containing 10 mmol of $W(CO)_6$ in CCl_4 inserted in the IR beam path, the SF "spectrum" from the K layer is recorded to provide the spectral calibration. This is similar to Hess *et al.* [114, 115] who use $W(CO)_6$ in their studies of CO on Ru{0001}; they use a $LiIO_3$ crystal to record the SF spectrum for calibration. They use the measurement of Tomakoff *et al.* [116, 117] who assign the main spectra feature in the wavelength range of interest of $W(CO)_6$ to be at 1980 cm^{-1}. Our cell is of a type which may be used directly with a bench top IR spectrometer, so it was taken to the teaching laboratories in this department and its spectrum is shown as figure 5.11. The

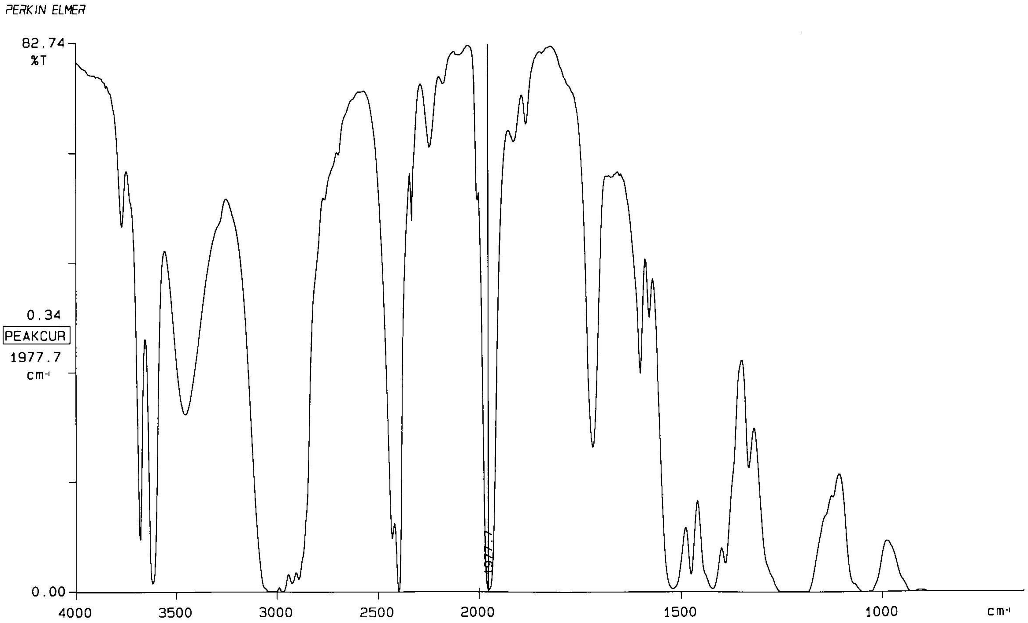

Figure 5.11: IR spectrum taken with Perkin Elmer spectrometer of the 10 mmol of $W(CO)_6$ in $CHCl_3$ chemical cell used for calibration. The main spectral feature of interest in our wavelength range is at 1977.7 cm^{-1}.

spectral feature of interest is at 1977.7 cm^{-1} and this has been used to calibrate all the spectral data presented in this chapter. The spectrograph is set up for a central wavelength of 690 nm as this corresponds to stretch frequencies around 5000 nm (or 2000 cm^{-1}) for a VIS pulse at 800 nm. The centre wavelength and width of the

VIS pulse is also measured by changing the spectrograph's centre wavelength to 800 nm and by removing one or two of the 800 nm filters. The central wavelength of the VIS beam is used to convert the SF wavelengths to IR wavelengths.

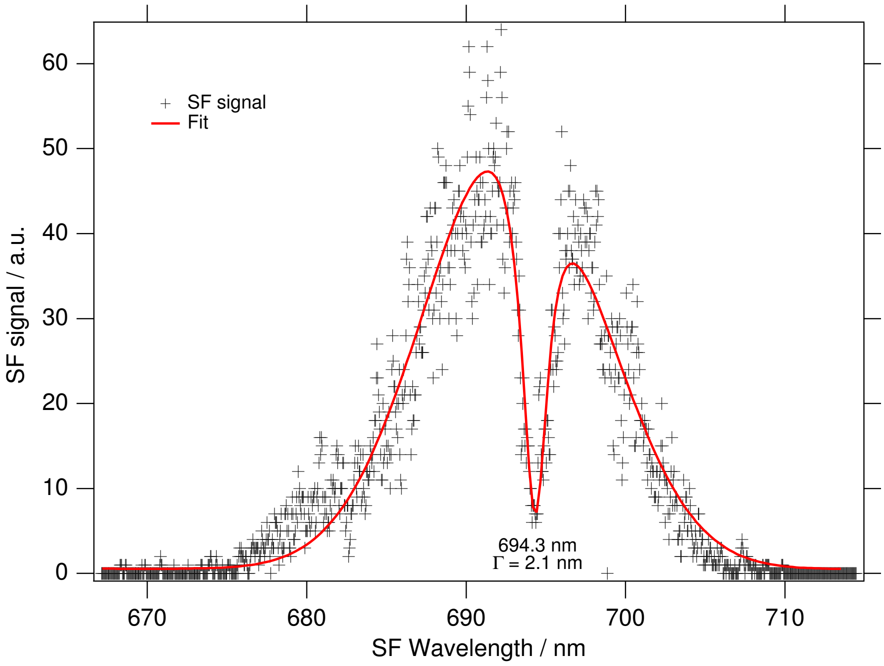

Figure 5.12: Spectrum of W(CO)$_6$ cell from K covered surface, 3000 counts. Taken on same day as data set 2. OPA centre frequency was set to 6 µm, and produced 5 µJ of IR. The energy of the VIS beam was 8 µJ (slit width = 200 µm). With a VIS beam of 802.8 nm this gives the spectral dip to be at 1945 cm^{-1} c.f. 1977 cm^{-1} from figure 5.11. This difference is used as a calibration. See text for details of fit.

An example cell spectrum using the K covered surface from data set 2 is given as figure 5.12. The cell spectra are fitted to a Lorentzian subtracted from a Gaussian function

$$A + B\exp\left(\frac{\lambda - \overline{\lambda_K}}{\sigma_K}\right)^2 - \frac{C}{(\lambda - \lambda_W)^2 + \sigma_W}$$

where $\overline{\lambda_K}$ is the centre of the non-resonant K envelope, σ_K is its width, λ_W is the centre of the W(CO)$_6$ spectral line, σ_W is its width and A, B, and C are constants.

We also at one point borrowed a 10 cm long glass cell containing 10 mbar of CO to place in the IR path. Whilst not actually used for calibration purposes, an example transmission spectrum from the K layer is shown as figure 5.13 where the individual rovibrational lines of the CO gas can be clearly seen.

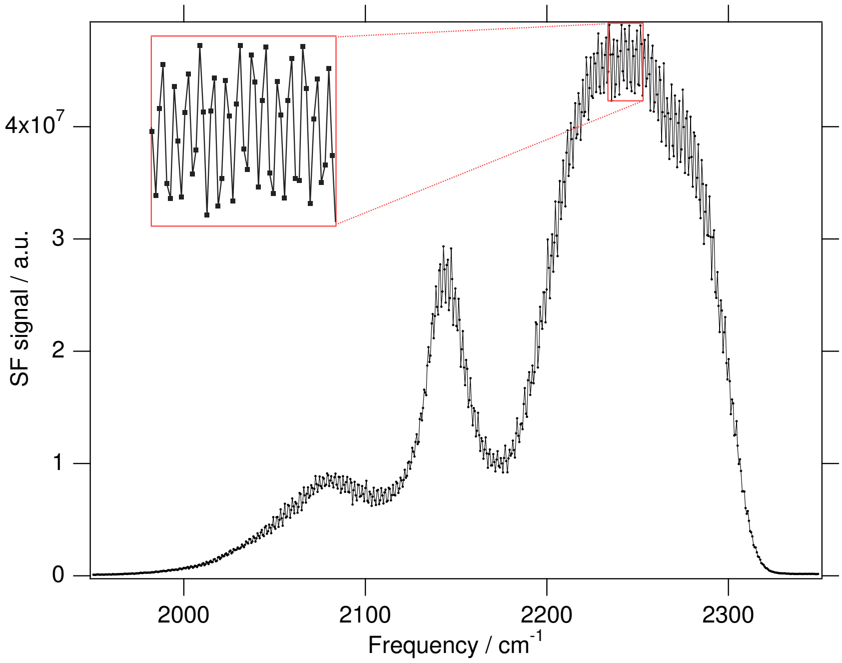

Figure 5.13: Gas phase spectrum of 10 mbar of CO placed in IR path, from the SF signal on the K layer. The central absorbance minimum at 2143 cm^{-1} is seen, and in the insert the individual rovibrational lines of the P and R bands at a separation of 3.83 cm^{-1} can also clearly be seen.

The crystal is then flashed to > 1200 K to remove the K layer. The gas line is pumped down and CO is admitted to it from the cylinder. The mass spectrometer is set to the 10^{-9} mbar range and the total integral exposure is monitored as gas is dosed into the chamber. A SF spectrum is then taken at this coverage, with a “photon counting” threshold set to around 320 counts per “photon”, to maximise the height of the central peak, and minimise the noise at the edges. Spectra are usually accumulated over 10,000 laser shots, which takes 16 mins for our 10 Hz laser system. A free induction decay can then be taken (see section 5.4.1 for full details) if needed. Then the mass 28 TPD is taken as described in section 5.2.3 to determine the coverage.

5.3.2 Results

Figure 5.14 shows an example of a raw (uncalibrated) SF spectrum (in this case saturation coverage), with the ordinate axis as directly taken from the spectrograph (but truncated at either end). Figure 5.15 shows the calibrated SF spectra from data set 3 as a function of coverage, with a sample temperature of 200 K. The coverage calibration corresponds to the TPDs given in figure 5.9. These were taken on the high resolution (1800 g/mm) grating, accumulating over 10,000 laser shots on full gain. The incident VIS energy is around 10 μJ and the IR energy around 5 μJ. This

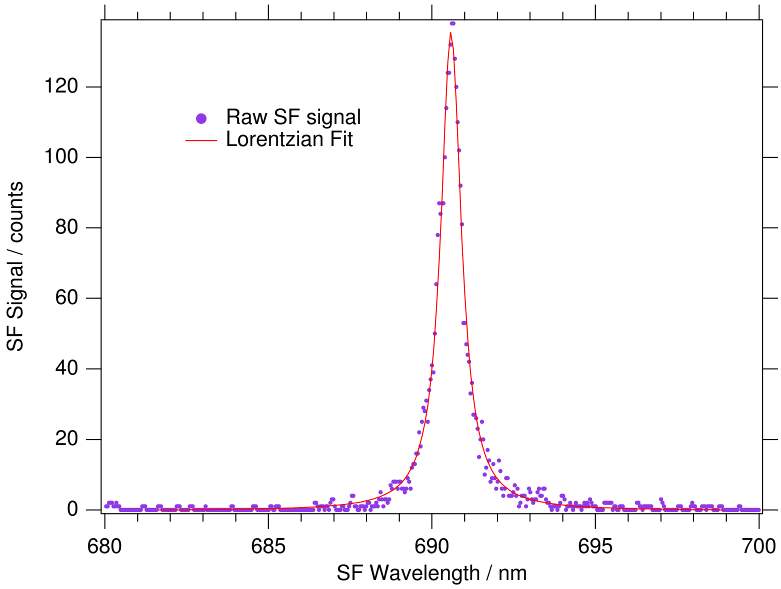

Figure 5.14: The raw uncalibrated SF signal, in the visible range for saturation coverage, and a Lorentzian fit. See text for full details.

is with an OPA output of around 8 μJ, with attenuation due to reflective optics and the chamber window. Figure 5.16 shows an example of the clean surface non-resonant SF signal from the Ru{10$\bar{1}$0} sample. At only 5 counts over 10,000 shots

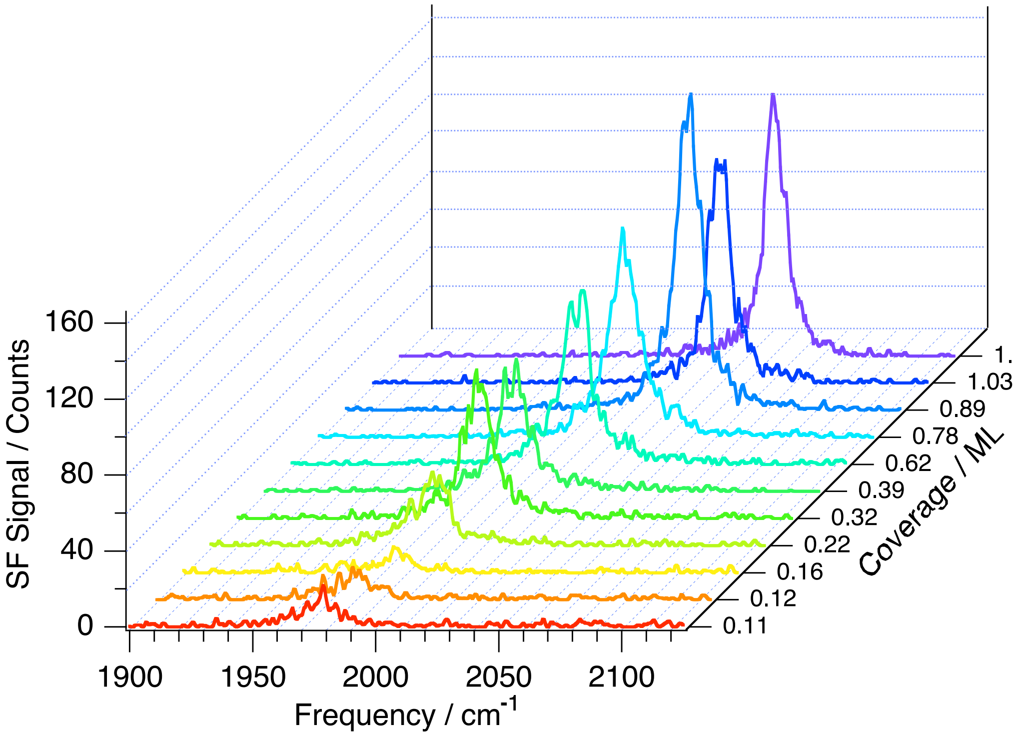

Figure 5.15: Coverage dependence of SF spectra of CO on Ru{10$\bar{1}$0} (data set 3). Each spectrum was accumulated over 10,000 laser shots, sample temperature 200 K. The discreet coverage axis is not to scale. See text for full details.

it is negligible compared with any of the spectra shown in figure 5.15. Therefore spectra have been fitted to equation 2.30 squared, i.e. a pure Lorentzian and no non-resonant background. Figure 5.14 shows such a fit (although of course in reality all spectra were fitted to the *calibrated* data as a function of frequency rather than wavelength). It is interesting to note that our first CO spectra had larger non-resonant background signals (comparable in amplitude to the lowest coverage resonant signals), which gradually decreased as the crystal became cleaner. This non-resonant signal was attributed to the effects of contaminants upon the surface.

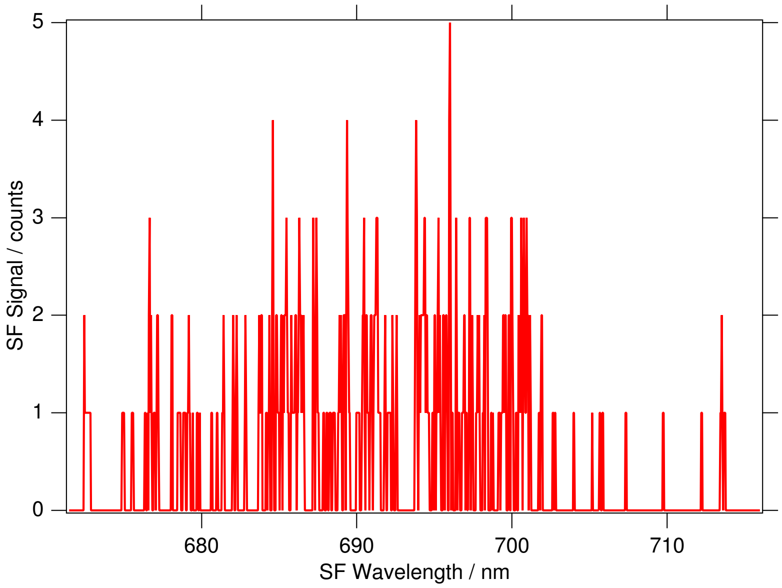

Figure 5.16: Non-resonant surface SF signal from clean Ru{10$\bar{1}$0} sample, accumulated over 10,000 laser shots.

The Lorentzian fits were performed by Wavemetrics Igor Pro, and from these a centre wavelength and FWHM were obtained, with associated errors. The error is set to the limit of the resolution of the detection system (0.6 cm^{-1} per pixel) when the calculated error is smaller than this. The centre frequencies from all three data sets are shown in figure 5.17, plotted alongside the EELS data from Lauth *et al.* [106] as described in section 5.1.3. The linewidths are given in figure 5.18. These data are fully discussed in section 5.5 but first I shall examine the time domain free induction decay data.

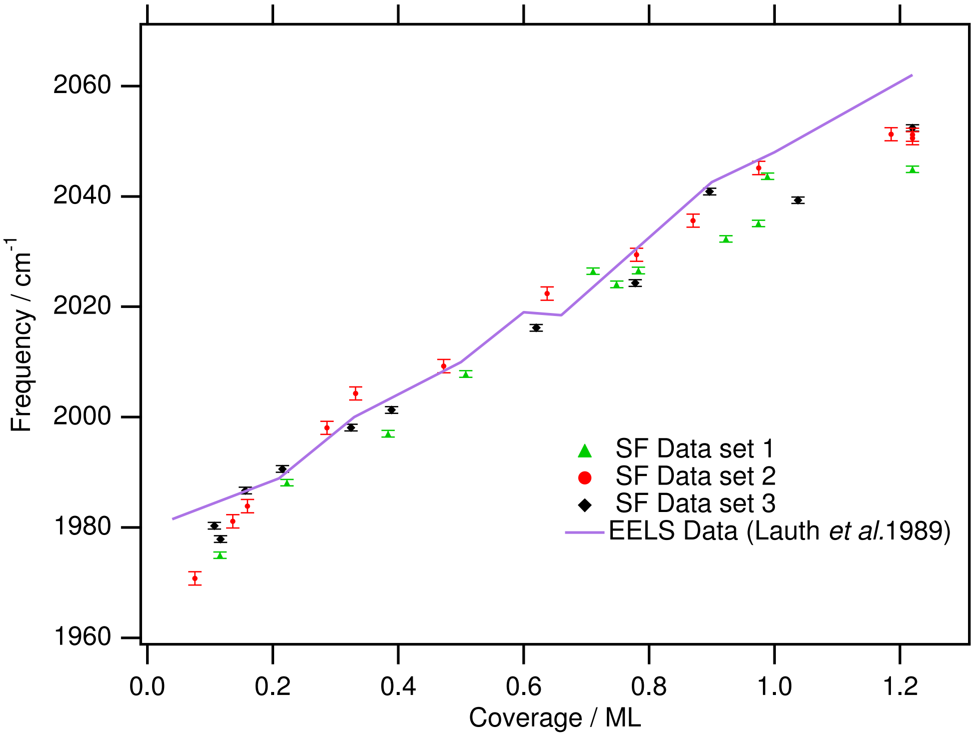

Figure 5.17: Coverage dependence of centre frequency. Sample temperature is 200 K in all three experiments. The SF data is compared with the EELS work of Lauth *et al.* [106]. See text for details.

5.4 Time Domain Study

5.4.1 Free Induction Decay Measurements

During the experimental session of data set 3, three free induction decays were taken, again at 200 K. After collecting the spectral data for that coverage, the slit in the pulse shaper and the glass plate in the VIS beam path were removed and the neutral density filter inserted in the latter's place to protect the Ru{$10\bar{1}0$} sample. In this way, the broadband VIS beam has a very similar energy to the narrowband pulses of around 11 μJ, and the IR remains at 5 μJ.

The FID acquisition software written by the author for the Andor i-Star, given

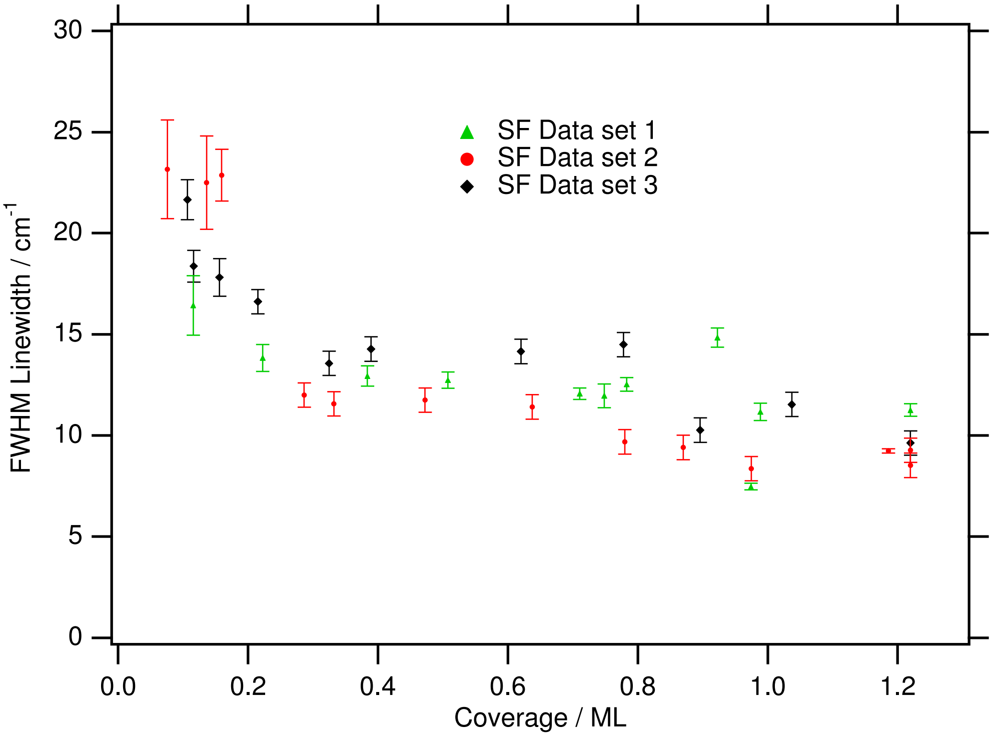

Figure 5.18: Coverage dependence of the linewidth. Sample temperature is 200 K in all three experiments.

in appendix C, was used to co-ordinate moving the translation stage and acquiring the spectra. In each case 80 stage steps were used, at 10 µm per step, and 400 laser shots per spectrum. 10 µm is equivalent to 66 fs. The data were then spectrally integrated using Igor Pro, to produce free induction decay curves. After each FID measurement the slit was carefully replaced in the pulse shaper, the filter removed and the glass plate reinserted to preserve the optical path lengths. A spectrum of the VIS pulse is then taken to fit subsequent spectral data in case the slit had been reinserted slightly to one side of its original position.

From combining equations 2.33, 2.34 and 2.35 in chapter 2, the form of a FID curve for a totally homogeneous exponential dephasing time is given by

$$I_{\mathrm{SF}}(\tau) = \int_{-\infty}^{\infty} \left| E_{\mathrm{VIS}}(t-\tau) \left\{ \alpha \int_{-\infty}^{t} E_{\mathrm{IR}}(t') \exp\left(\frac{t'-t}{T_2}\right) \mathrm{d}t' + \beta E_{\mathrm{IR}}(t) \right\} \right|^2 \mathrm{d}t. \quad (5.1)$$

Appendix D contains a computer program written by the author in C which will return a value for this function given τ and the constants, using adaptive numerical integration. It assumes a Gaussian temporal profile for E_{VIS} and E_{IR} and parameters for these can be passed to the program. This program is called by Igor Pro, as described in the appendix, and Igor is then used to fit this function to the free induction decay data using a least squares method. The unknowns which are fitted are: α; the overall amplitude; the amplitude offset; time zero (T_0) and T_2 (β is arbitrarily set to 1 as the overall amplitude and α are sufficient to represent the intensity dependency). The absolute fitting time is quite lengthy, at around three hours on a twin 1 GHz processor PowerPC Apple Macintosh. However, this time is assuming that the initial parameters are close enough to their final values. The FID program requires a parameter which is designed to scale all the time parameters to avoid numerical underflow or overflow, and it seems that the difference between underflow and overflow is only around half an order of magnitude, so many attempts were made before a suitable value was found. Also, the step change in the least squares fitting has to be carefully set for each parameter. This brings the fitting time to days rather than hours for each curve, when such false starts are taken into account.

5.4.2 Results

The three FIDS for different coverages are given as figure 5.19. The saturation coverage experiment suffered a mechanical shock during the rise time, so it has only been fitted after this point. The temporal widths of the VIS and IR beams are obtained from the methods described in chapter 4, and the fitting parameters are

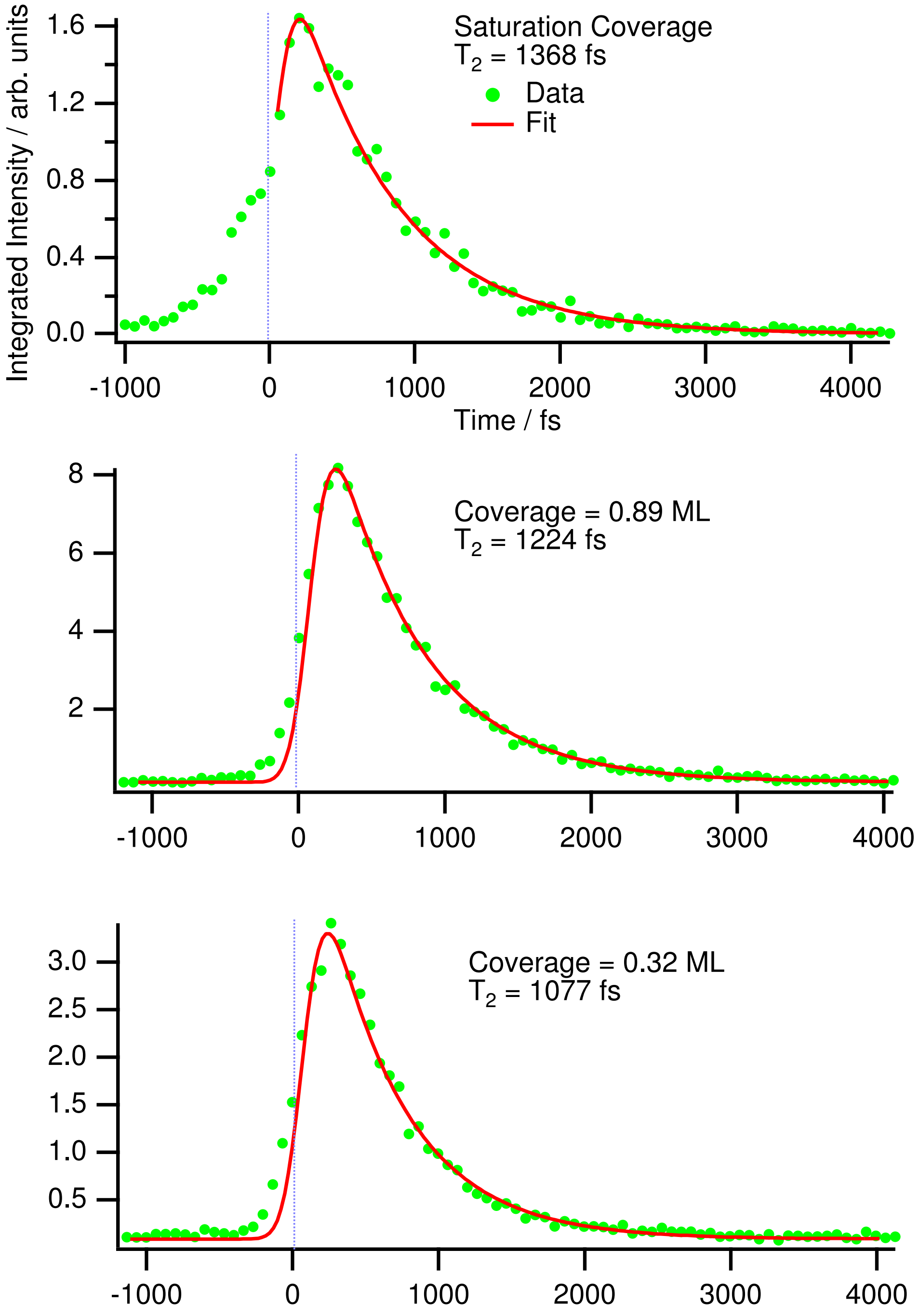

Figure 5.19: Free Induction Decays for CO on Ru{10$\bar{1}$0} at 200 K. Time zero set from fit. See text for details.

Parameter	Coverage		
	1.22 ML	0.89 ML	0.32 ML
Overall Amplitude / a.u.	**0.0763**	**0.163**	**0.0277**
T_2 / fs	1368.9 ± 117.1	1224.0 ± 63.5	1077.6 ± 89.9
T_0 / fs	**1059.6**	**1260.7**	**1201.4**
$2\sigma_{\mathrm{IR}}$ / fs	169.0	169.0	169.0
$2\sigma_{\mathrm{VIS}}$ / fs	109.0	109.0	109.0
α / a.u.	**202.21**	**314.54**	**496.25**
β / a.u.	1.0	1.0	1.0
Amplitude offset / a.u.	**0.00148**	**0.196**	**0.128**
Calc. FWHM 2Γ / cm^{-1}	7.76 ± 0.66	8.67 ± 0.40	9.85 ± 0.81

Table 5.1: FID fitting parameters. **Green** parameters were fitted, black parameters were fixed. The widths of the pulses are the raw Gaussian widths (2σ), not the FWHMs. Experiment carried out at 200 K.

summarised in table 5.1. At the foot of this table are given calculated values for the linewidth based upon the values of T_2. The errors in these (and in T_2) are taken from the fit. The large α/β ratio confirms just how negligible the non-resonant metal signal is compared with the resonant chemical signal.

The displacement of the time zero point obtained from the fit, and the peak of the FID curve, is in excellent agreement with a theoretical prediction from a density matrix study of the influence of pulse duration on FID curves by Mii and Ueba [60]. They predict such a positive displacement of the peak with respect to T_0 due to the combined effect of the polarisation decay constant and the finite temporal widths of the IR and VIS pulses.

It is important to restate that the fitting model is completely homogeneous, i.e. a single exponential with decay constant $1/T_2$ is fitted rather than a distribution of values of T_2. Thus the success of fitting to such a model must indicate a homogeneous linewidth at these coverages; fitting an inhomogeneous system to such a model fails as demonstrated by Roke *et al.* [66] who contrast fits of the homogeneous C-H stretch in acetonitrile on a gold film with the inhomogeneous C-N stretch. The largest error in the calculated linewidth value for our FID data is at $\Theta = 0.32$ ML, which is close to the upturn in linewidth values. This could indicate that the assumption of homogeneity is beginning to break down. These points are returned to in the discussion.

A comparison between the spectrally and temporally calculated linewidths is shown in figure 5.20. Section 2.3.2 discussed how the spectral width of the VIS

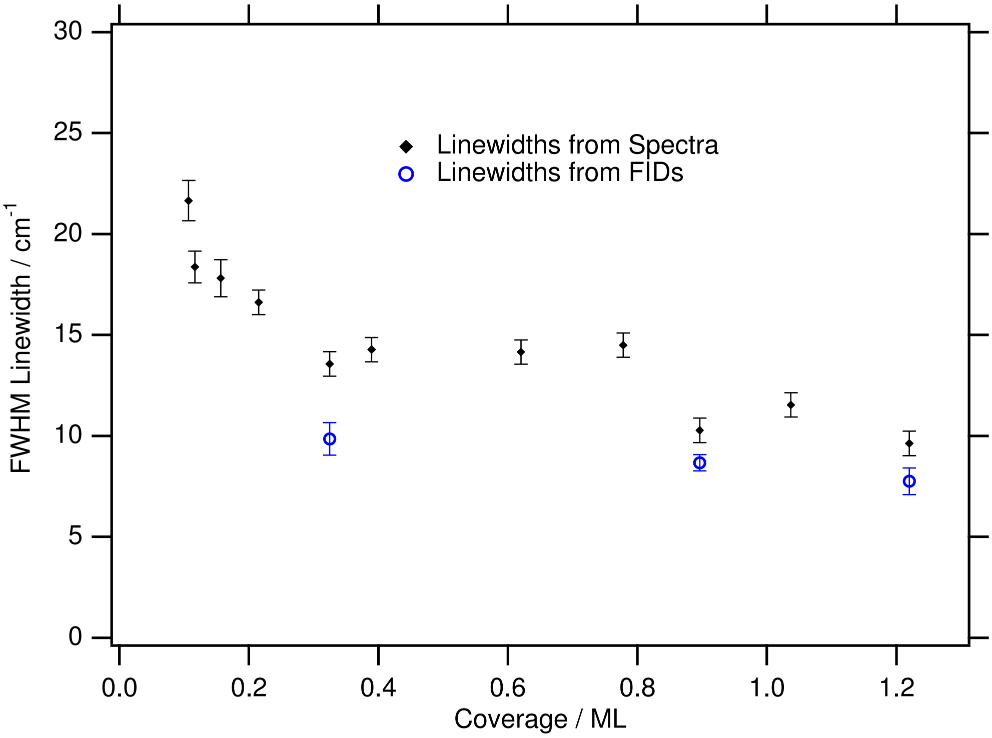

Figure 5.20: Comparison of spectral and temporal methods of obtaining linewidths (data set 3).

upconversion pulse affects the width of spectral features in SF spectra. Although the pulse shaper works well to spectrally narrow the VIS beam, a compromise does have to be made between pulse energy (and hence SF signal) and the spectral width of the pulses. However, it is possible to take this into account by deconvolving the VIS field from the SF spectra [59]. Figure 5.21 shows an example spectrum of the VIS beam, and its Gaussian fit. The convolution of a Gaussian with

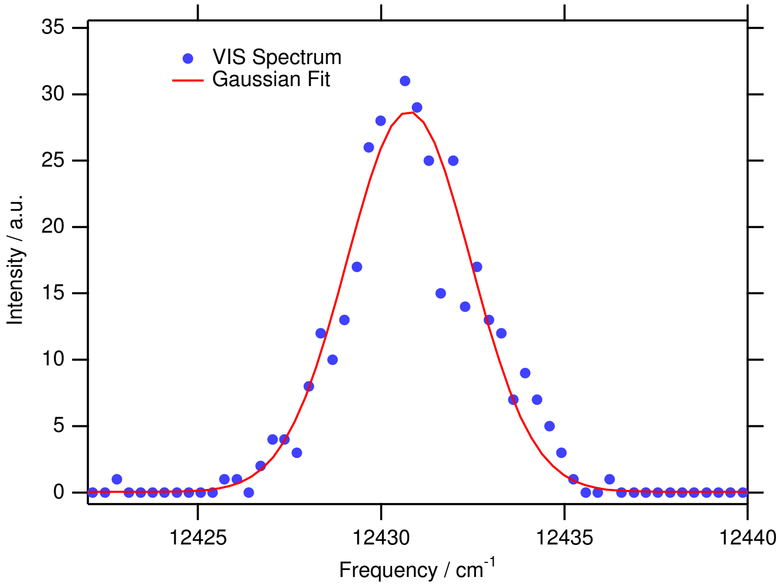

Figure 5.21: Spectrum of VIS pulse. Raw width is 2.39 cm^{-1}.

a Lorentzian (i.e. the true SF profile) is known as the Voigt function and is commonly used in spectroscopy to fit lineshapes which are neither truly Lorentzian nor truly Gaussian, see for example [118]. Igor Pro has a built-in Voigt function and so the linewidths from data set 3 have been deconvolved with a Gaussian of the correct width for the VIS beam measured on that day. This is presented in figure 5.22, along with the original Lorentzian fitted data and the FID linewidths. One can see that the Voigt fits bring the spectral data closer to the “true” values given by the FID measurements.

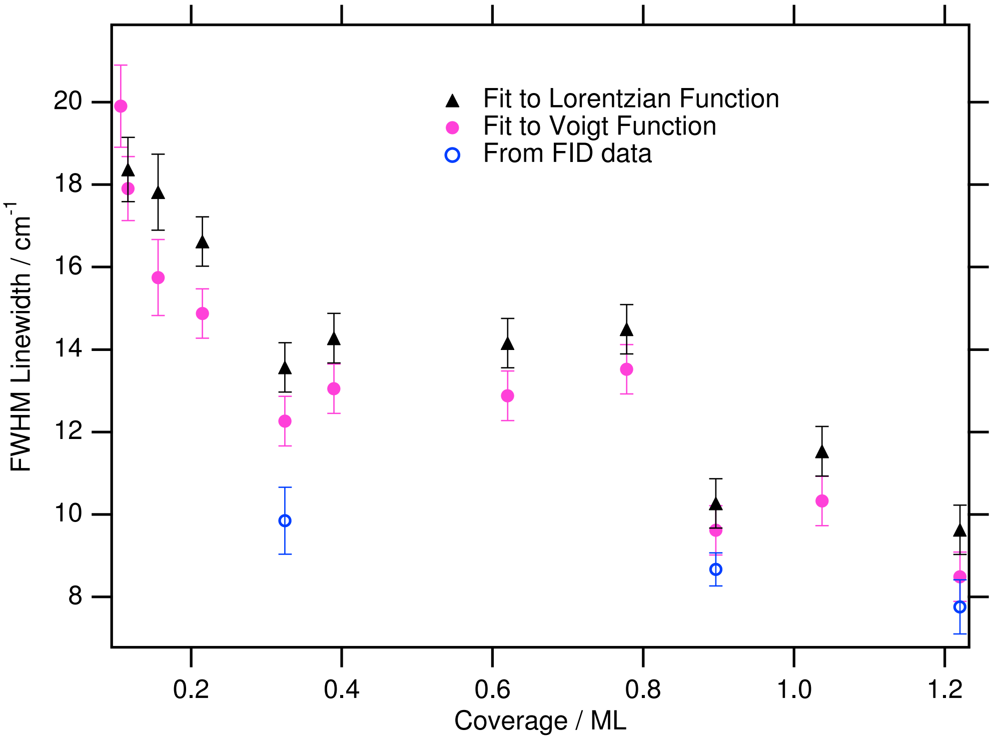

Figure 5.22: Comparison of Voigt fit, Lorentzian fit and FID linewidths.

If the spectral information in the FID measurements is not integrated out then a two dimensional plot of the change in the CO stretch frequency during the free induction decay can be plotted, and an example of this is given at saturation coverage on the front cover of this thesis. The temporal (horizontal) axis of this plot is over a range of 4 ps, and the spectral (vertical, top–bottom) axis is over the range 1950–2150 cm^{-1}.

5.5 Discussion and Further Supporting Results

5.5.1 Origins of the Frequency Shift

From the LEED study of this system by Lauth *et al.* [106] as summarised in figure 5.2 one can suggest two possible mechanisms acting in combination to account for the rise in frequency with increasing coverage. One is a chemical shift, due to changes in the influence of locally adsorbed CO molecules on the electronic state of the surface as the coverage is increased, and the other is a shift due to dipole-dipole coupling as the molecules are forced closer together with increasing coverage. To obtain an estimate of the relative contributions to the frequency shift of each of these we undertook a brief isotopic study of the system.

Three SF spectra were taken, after collecting data set 3. The first was a saturation coverage of ^{28}CO $\left({}^{12}\mathrm{C}^{16}\mathrm{O}\right)$, as before. In this system, both the chemical shift and dipole-dipole coupling may both be significant. Then for comparison we took a spectrum at 0.15 ML coverage of ^{28}CO, as this is the lowest coverage that produces a useful signal. The shift between these two data points is, for these purposes, the total shift, chemical plus coupling. Then we filled the surface to saturation coverage with ^{31}CO $\left({}^{13}\mathrm{C}^{18}\mathrm{O}\right)$ and recorded a third spectrum. These three spectra are shown in figure 5.23. It is important to note that at the OPA frequency range in use we do not see the ^{31}CO stretch; this is 86.6 cm^{-1} below the ^{28}CO stretch at $\Theta = 0.9$ ML.

So considering only the ^{28}CO molecules, they will on average be forced to occupy a range of sites as in the pure ^{28}CO saturation layer (bearing in mind that at 200 K the molecules will be fairly mobile on the surface), and hence the chemical shift will be identical. However, a majority of each ^{28}CO's neighbours will be ^{31}CO which will not couple well to the ^{28}COs because of the appreciable frequency difference.

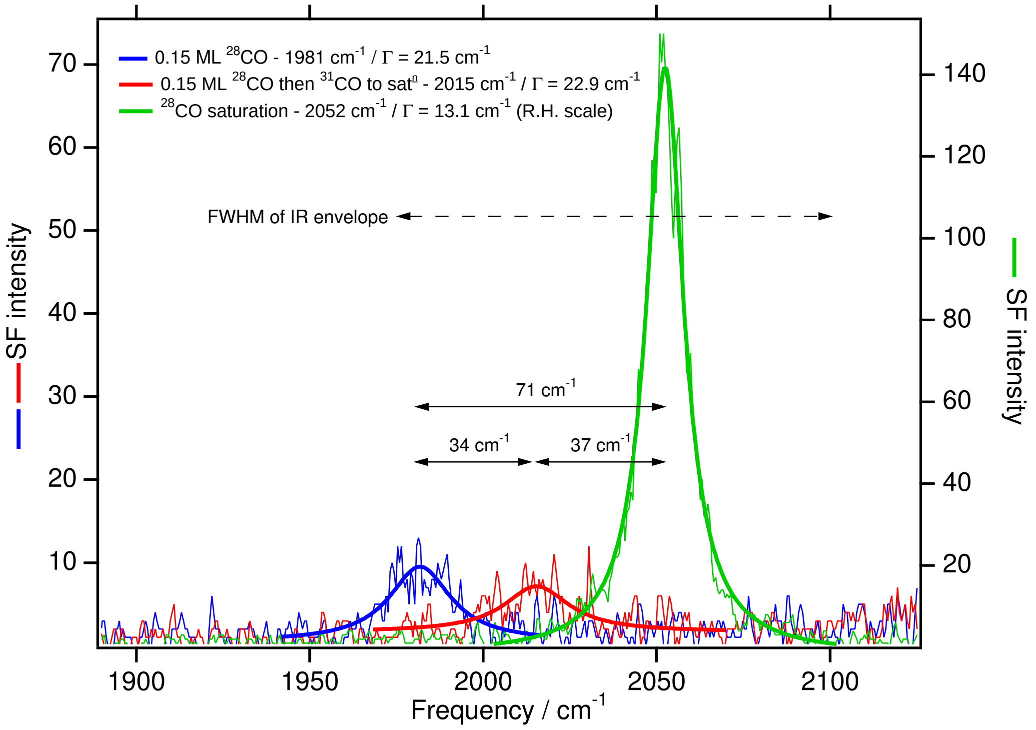

Figure 5.23: SF isotopic study, probing the ^{28}CO stretch at 200 K. 10,000 laser shot accumulations. The FWHM of the broadband IR envelope is indicated by the dotted line (~140 cm^{-1} centred at 2040 cm^{-1}); the ^{31}CO stretch is not seen in this range. The decrease in intensity of the red trace compared to the blue trace could be due to intensity stealing by the ^{31}CO oscillators in the former case.

One has to bear in mind that even at the ratio of isotopes, 0.15 ML ^{28}CO : 1.07 ML ^{31}CO there will be a minority (just) of individual ^{28}COs actually isolated from *all* other ^{28}CO molecules. One can estimate the likelihood of this quite simply; for a quasi-hexagonal CO overlayer at saturation (figure 5.2) each CO is surrounded by 6 others. The probability of a single ^{28}CO being next to a single ^{31}CO is 1.07:1.22, or 0.87. In order for the ^{28}CO to be alone, it must be next to a total of 6 ^{31}CO molecules. Hence the probability of it being totally isolated is $0.87^6 = 0.43$. So the contribution to the frequency shift by dipole-dipole coupling implied from the data in figure 5.23 of 37 cm^{-1} must be considered a *minimum*, as even in this isotopic mixture some dipole-dipole coupling between ^{28}CO molecules will still occur. With only 10 counts over 10,000 laser shots for the 0.15 ML spectra in figure 5.23, we could not obtain a useful spectrum at a much lower coverage than this with the present experiment. However for most full isotopic composition studies (e.g. CO/Pt{111} in [119]), little empirical change is seen in the dipole contribution below ~ 0.15 ML of one isotope.

This may be compared with CO on Ru{0001} where the dipole shift was determined to be 42 cm^{-1} [120].

The theory of dipole-dipole contributions to frequency shift in metal-adsorbate systems was pioneered by Hammaker, Francis and Eichens [121] in 1965. They considered a $1/R^3$ correction to the vibrational potential energy to take into account dipole pairings. The theory was later improved by Mahan and Lucas [122] who included a term for interactions between dipoles and the *images* of other dipoles, and later still Scheffler [123] included a third term to account for a dipole's interaction with its *own* image.

Crossley and King [119] undertook a combined RAIRS and theoretical study of CO on Pt{111} in which they used the theory developed by Hammaker *et al.* to calculate a value for the dynamic dipole moment of this closely packed and highly dipole coupled system of 2.9 DÅ^{-1} $\left(= 9.8 \times 10^{-20}\ \text{C}\right)$. This work was published shortly before the image corrections to the model were made. An attempt is made here to apply this model to the CO/Ru{$10\bar{1}0$} system as a comparison with the CO/Pt{111} system. No attempt is made here either to take into account the image dipoles; with an open and ridged surface such as Ru{$10\bar{1}0$} it would be extremely complex to take into account all the differing dipole-surface distances needed for such a calculation, especially given the complicated registration of the chemical overlayer with the surface at saturation.

Hammaker *et al.* [121] exactly solved the secular equation for the vibrational potential energy of a system of N adsorbed molecular oscillators to give

$$\lambda = \lambda' + \left(\frac{\partial\mu}{\partial r}\right)^2 \frac{1}{M_r\epsilon_0} \sum_{j=2}^{N} \frac{1}{R_{ij}^3} \tag{5.2}$$

where $\lambda = 4\pi c^2\nu^2$ for a band frequency ν, λ' refers to the isolated species (the "singleton" frequency, in cm^{-1}), M_r is the reduced mass of the oscillator, ϵ_0 is the permittivity of free space, R_{ij} is the distance between the centres of dipoles i and j, and $(\partial\mu/\partial r)$ is the dynamic dipole moment to be calculated.

Assuming that the "quasi-hexagonal" overlayer at saturation coverage described by Lauth *et al.* can be considered to be exactly hexagonal then one can numerically calculate the $\sum_{j=2}^{N}\left(1/R_{ij}^3\right)$ term in equation 5.2. Appendix E presents a C program to do just that, along with the details of how it is done, and for a centre to centre CO distance of 3.0 Å [106] the iteration quickly converges to give a value of 0.05108 Å^{-3}. For the mininum dipole shift of 37 cm^{-1}, substituting this shift, the dipole sum, CO reduced mass of 6.85 M$_\mathrm{H}$ and the constants into equation 5.2 gives $(\partial\mu/\partial r) \simeq 3.1$ DÅ^{-1}. This lowest estimate of the dynamic dipole moment of CO on Ru{10$\bar{1}$0} is higher than that of CO on Pt{111}, calculated by the same methods; the latter system is considered to be a highly coupled system, so dipole-dipole coupling is the major physical effect in the CO/Ru{10$\bar{1}$0} system at high coverages.

5.5.2 Origins of the Linewidth Changes

The coverage dependence of the linewidth presented in sections 5.3.2 and 5.4.2 (figure 5.18) raises a number of interesting questions. Firstly, the most obvious feature is the rise in linewidth with decreasing coverage below around 0.3 ML. Secondly, it is striking how the linewidth does not increase (and in fact seems to decrease) as very high coverages are reached. From the structures suggested by

LEED in figure 5.2 one notes that the CO molecules are adsorbed on an increasing variety of surface sites due to the overlayer becoming less registered with the surface as the coverage is increased beyond 1 ML. One might expect such an inhomogeneous distribution of sites to actually broaden the linewidths as saturation coverage is approached. And as discussed in section 5.4.1 the high coverage free induction decays have been successfully fitted to a model with a single exponential T_2 decay, as opposed to a distribution of T_2 values as one would expect in an inhomogeneous system.

Considering the increase in linewidth at low coverages first of all, it must be noted that this linewidth increase is seen below 0.3 ML, and this is the coverage at which Lauth *et al.* observe their lowest coverage LEED structure as shown in figure 5.2. This suggests that below this coverage, the CO overlayer does not possess regular order, at least not on a length scale suitable to generate a LEED pattern. Such “disorder” could also lead to heterogeneous broadening which would explain the linewidth increase. The first stable LEED pattern observed is a (3×1) structure (top left of figure 5.2) which demonstrates that there is a repulsive interaction between the CO molecules along the direction of the Ru{10$\bar{1}$0} ridges, ([$\bar{1}2\bar{1}0$] direction), and an attractive interaction perpendicular to the ridges ([000$\bar{1}$] direction). It therefore seems likely that as the coverage is built up from zero, chains may form along the direction perpendicular to the ridges, driven by the attractive interaction.

These chains may initially be of differing lengths, and have differing separations between them along the direction of the ridges. These differences in the chemical environments of the individual CO molecules would account for the heterogeneous broadening. The lack of symmetry would also make it impossible to observe a LEED pattern. Such a scheme of molecular chains at low coverage is shown in figure 5.24. Once the coverage reaches 0.3 ML the repulsive inter-

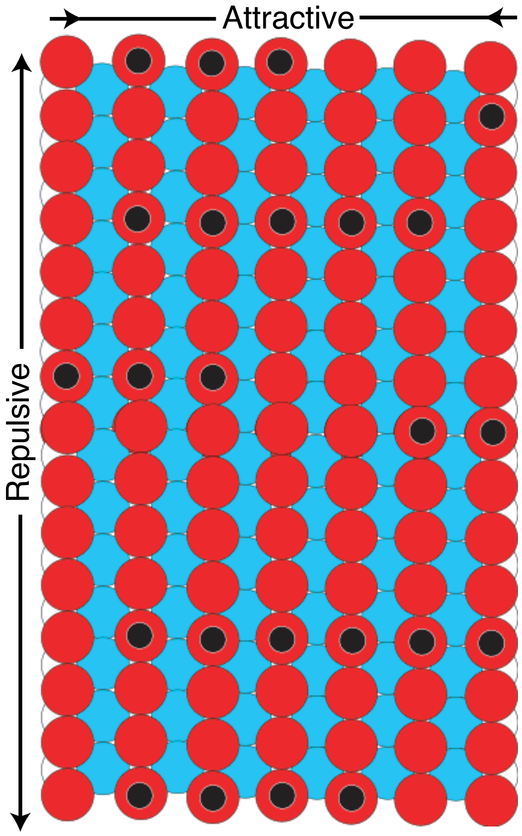

Figure 5.24: Proposed CO chains on Ru{10$\bar{1}$0} at low coverage (< 0.3 ML).

action along the ridges orders the chains to be at a regular separation, and the chain lengths will by then stretch right across the sample i.e. we reach the (3 × 1) structure. Such a regular quasi-infinite arrangement of CO molecules would not be heterogeneously broadened and would give a sharp LEED pattern.

Such chains of CO molecules have indeed been observed, running perpendicular to the ridges on a Cu{110} surface, by a recent STM study by Briner *et al.* [124]. Cu{110} has a similar symmetry to Ru{10$\bar{1}$0}. An STM study of CO/ Ru{10$\bar{1}$0} would therefore prove useful in confirming this conclusion.

Returning to the lack of inhomogeneous broadening at high coverage, an effect described by Persson *et al.* for CO on Ru{0001} [125, 126] could explain this observation. The effect, known as the *exchange model*, is well known for isotopic mixtures in highly coupled systems in which intensity stealing of low frequency oscillator peaks by high frequency peaks occurs due to (a) higher frequency oscillators screening the incoming electric field at lower frequencies and (b) lower frequency oscillators enhancing the electric field at higher frequencies. This may also happen between high and low frequency components of the same finite width peak. This means that the peaks of the observed spectra are blueshifted, and become asymmetric with a tail at lower frequencies. Indeed this seems to be the case for our data. This can also be viewed as strong dipolar interactions delocalising the vibrational resonance and thus the discreet oscillator frequency model is replaced by a band structure. For a more quantitative explanation of this phenomenon in our system a full isotope study at varying composition would be needed as performed by Persson *et al.* using RAIRS for the CO/Ru{0001} system [126]. The intense dipole-dipole coupling in our system at high coverage would cause such an effect.

5.5.3 Comparison with the Close Packed Surface

Bonn, Hess and Wolf *et al.* have performed a detailed broadband sum frequency study of CO on the close packed Ru{0001} surface [127, 128, 115, 129, 130, 131]. With a 400 Hz repetition rate femtosecond laser system and an OPA giving up to 11 μJ of IR to the surface they can: (a) measure spectra for much lower coverages of CO than we practically can (down to around 0.01 ML); (b) acquire spectra much more quickly; and (c) observe the $v = 1 \rightarrow 2$ "hot-band" vibrational transition (at 1961 cm^{-1} c.f. their measurement of the fundamental at 1990 cm^{-1}). They observe asymmetric, narrower than expected spectra at high coverages, which they too attribute to dipole-dipole coupling and the consequent delocalisation of the vibrational excitation. From their hot-band observation they calculate the value of the anharmonicity of the vibrational potential to be 13.6 cm^{-1}. It has not been possible for us to see this hot band because we cannot obtain spectra at low enough coverages. The band-structure effect caused by dipole-dipole coupling seen at even very low coverages (0.025 ML for Ru{0001}), described in the previous section, prevents the hot band being observed. They also give two FID measurements, both at 0.33 ML coverage. One, measured at 95 K gives T_2=1.94 ps and the other at 340 K gives T_2=1.16 ps, compared with T_2=1.08 ps for our surface at this coverage and 200 K. They point out that as the pure vibrational relaxation is due to electron-hole pair excitation [132], it should be temperature independent and hence the temperature dependence of T_2 is due purely to the temperature dependence of T_2^*.

To investigate this for our system, we performed temperature dependent studies of the frequency and linewidth. CO was adsorbed at the appropriate coverage, then SF spectra were taken for various sample temperatures. The frequency shift for saturation coverage is shown in figure 5.25, and that for 0.9 ML in figure 5.26, with an indication of the order in which the data were taken. The linewidths show no change within the experimental error over this temperature range for these coverages. The last three points for saturation coverage were taken with the chamber background filled with CO (10^{-9} mbar) to counteract desorption at these temperatures.

The hysteresis in the saturation coverage plot is probably due to accumulation of hydrogen from the background on the surface over the long time these experiments took to perform (at 15 minutes per point for the accumulation, plus time for temperature equilibration). Indeed, with the exception of this 0.9 ML data set, at lower coverages this hysteresis makes the data unusable; species other than hydrogen (including of course CO) can accumulate on the surface as well at low coverages. A shift of 3.5 cm^{-1} is seen over the temperature range of 108–270 K

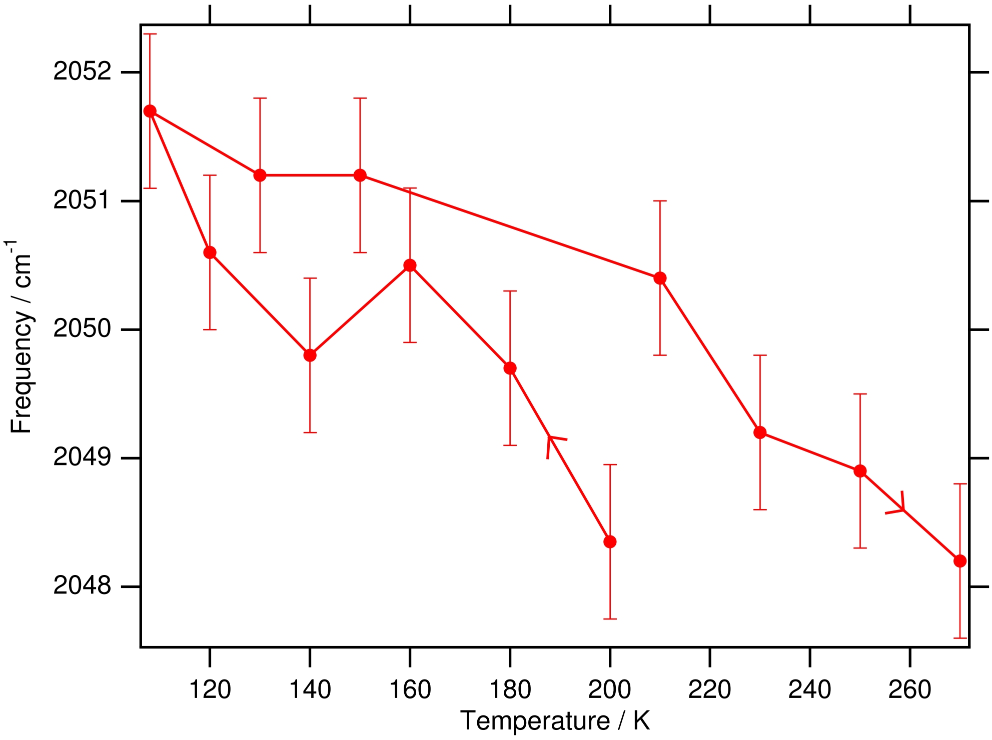

Figure 5.25: Temperature dependence of CO stretch frequency of Ru{10$\bar{1}$0} at saturation coverage. Arrows show the order in which the data were taken. For the last three points the chamber was background filled with CO to counteract desorption at these temperatures.

($\simeq$ 0.021 cm^{-1}K^{-1}) for saturation, and 7.0 cm^{-1} over the range 100–260 K ($\simeq$ 0.043 cm^{-1}K^{-1}) for Θ = 0.9 ML.

The change in frequency is probably due to coupling with the frustrated translation phonon mode of the CO overlayer, which is populated at higher temperatures in many systems. This was suggested for CO/Ru{0001} by Jakob and Persson [133] in which they report a ~10 cm^{-1} frequency shift over a temperature range of 50–350 K at Θ = 0.33 ML (~0.033 cm^{-1}K^{-1}). Bonn *et al.* also attribute the temperature dependence of T_2 described above to this effect. The coupling process of the C-O stretch with the lower frequency frustrated translation mode

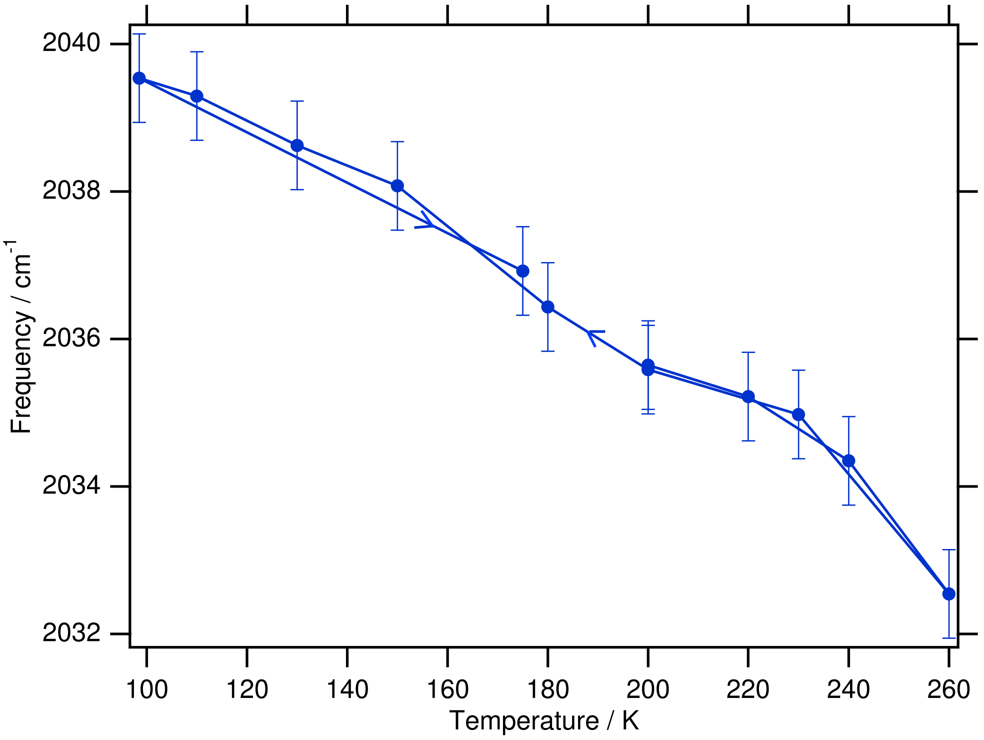

Figure 5.26: Temperature dependence of CO stretch frequency on Ru{10$\bar{1}$0} at $\Theta = 0.9$ ML. Arrows show the order in which the data were taken.

(47 cm^{-1} on Ru{0001} [134]) leads to an exchange interaction which redshifts the C-O stretch spectra. It can be thought of as the lateral translation weakening the C-O bond. The increased change in frequency in our data with respect to temperature at lower coverage could be due to: (a) the frequency of the frustrated tranlation changing with coverage as the surface becomes more or less packed or (b) the strength of coupling between the frustrated translation and the C-O stretch changing with coverage. Unfortunately, there seems to be no work in the literature on the frequency of phonon modes of CO on Ru{10$\bar{1}$0} so it is difficult to draw any quantitative conclusions. It could be the case that the frustrated rotation plays a significant rôle for our system, especially given the CO tilting predicted by Lauth *et al.* at high coverages (figure 5.2).

5.5.4 Summary

We have measured the CO stretch frequency and linewidth on Ru{10$\bar{1}$0} using broadband sum frequency generation, as a function of CO surface coverage. We have shown that by carefully including the temporal characteristics of our system obtained by the methods in chapter 4, we can use FID measurements to measure T_2 (Γ) with much less instrumental shortening (broadening) than with spectral measurements of the linewidth. The free induction decay peaks exhibit a positive temporal displacement with respect to the time zero of pulse overlap (obtained from the fit), which is in agreement with previous theoretical studies of FID curves with finite laser pulse widths.

Dipole-dipole coupling has been shown to be important in this system at high coverages due to the very tight packing of CO oscillators into a quasi-hexagonal array. At lower coverages we suggest the formation of chains perpendicular to the surface ridges leads to heterogeneous broadening of the linewidth.

A temperature dependent C-O stretch frequency shift of 0.021 $\mathrm{cm^{-1}K^{-1}}$ is observed at saturation coverage and 0.043 $\mathrm{cm^{-1}K^{-1}}$ at 0.9 ML. These shifts are attributed to coupling with the frustrated translation mode as seen for the close packed surface.

Even though our Ru{10$\bar{1}$0} sample had poor mid and long range order, as highlighted by the LEED data, the spectral data sets taken before and after electrochemical polishing are identical despite an improvement in the LEED pattern after polishing. We are therefore confident that the spectral effects observed in this study arise from short range order effects, and are unaffected by the problems with the sample at larger length scales.

The CO/Ru{10$\bar{1}$0} system has proved to be an interesting first system to study using the broadband / femtosecond SF spectrometer. The Ru{10$\bar{1}$0} sample has now been removed from the UHV chamber to make way for pump-probe studies of CO on Pt{110} and for NO on Ir/Au, as described in the next chapter. However, whilst it was still in place, experimental setups for IR-pump SF-probe, photon echo and VIS-pump SF-probe, were designed, implemented and attempted for the CO/Ru{$10\bar{1}0$} system. This is the subject of the next chapter.

Chapter 6

Pump-Probe and Conclusions

Whilst the Ru$\{10\bar{1}0\}$ sample was in the UHV chamber, three other types of time resolved femtosecond spectroscopy were attempted on the system. This chapter briefly outlines the theory, experimental setup and results for each, and then suggests how these must be improved for future studies.

6.1 IR-Pump SF-Probe

6.1.1 Theory

This is a technique to directly measure T_1 (see for example [135, page 130]). An intense IR pump pulse tuned to the vibrational resonance is incident on the surface and populates the $v = 1$ vibrational level. After a time delay, a VIS-IR SF probe is sent in to probe the relative populations of the $v = 1$ state. The longer the time delay, the more population decay from $v = 1$ to $v = 0$ will have occurred. From equation 2.29 and figure 2.3 one can see that the resonant susceptibility is proportional to the population difference between the ground and $v = 1$ states, and given the SF intensity is proportional to the square of this susceptibility, then the population difference will be proportional to the square root of the SF intensity so that [136]

$$1 - \left[\frac{I_{\mathrm{SF}}(\tau)}{I_{\mathrm{SF}}(0)}\right]^{\frac{1}{2}} = \Delta n_1(\tau) - \Delta n_0(\tau)$$

where I_{SF} is the SF intensity (at time delays τ and zero), and $\Delta n_0(\tau)$, $\Delta n_1(\tau)$ are the pump induced changes in the fractional populations of the $v = 0$ and $v = 1$ levels respectively.

These experiments have been successfully carried out on, for example: H / Si{111} [137] where $T_1 = 795$ ps; CO / Cu{100} [138], where $T_1 = 2.0$ ps; and CH_3S / Ag{111} [139] where a bi-exponential decay was seen.

6.1.2 Experimental Implementation

To provide a pump IR beam, the IR beam from the OPA was split using a 50% beamsplitter from a RAIRS spectrometer (with thanks to Dr. Frederic Thibault-Starzyk), on the small chamber mounted optical table. The Standa translation stage was then used to advance the pump IR with respect to the probe IR. In this way, the VIS and probe IR beams can remain temporally overlapped, and only one stage needs to be moved to perform the experiment. The pump beam enters the chamber along roughly the same path as the VIS beam and temporal and spatial overlap is achieved by observing the SF signal on the potassium covered surface of the pump IR and VIS beam. This arrangement is shown in figure 6.1.

6.1.3 Results

In the following experiment, the pump IR intensity is 1.2 μJ at the surface, and the probe IR is 2.0 μJ, and 9 μJ of OPA output. The increased attenuation is due to the IR beamsplitter, and the addition of extra reflective optics in the IR paths. Four spectra are given in figure 6.2 showing pump-probe delays of −2 ps (pump

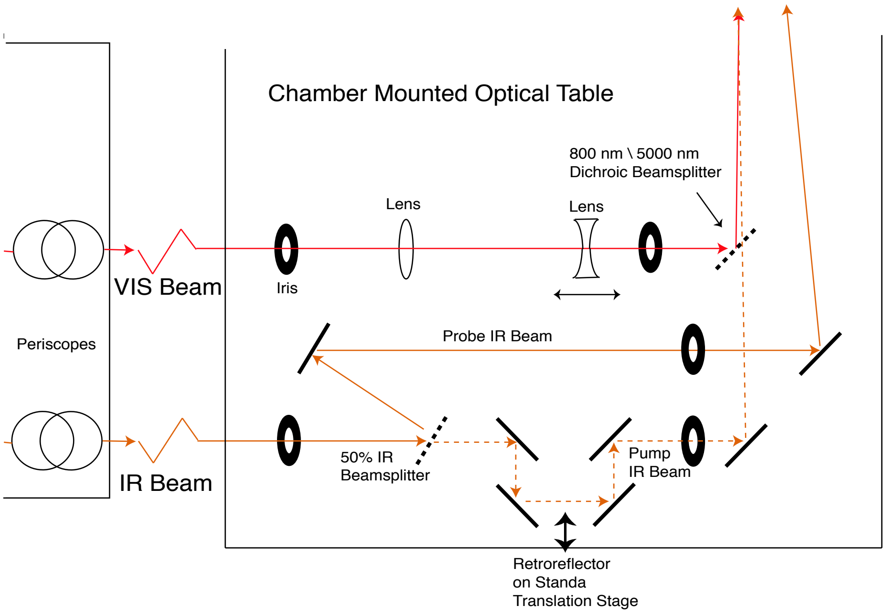

Figure 6.1: Changes to optical paths on the chamber mounted optical table for IR-pump SF-probe experiment. Sub-diagram of figure 3.33.

after probe), 0 ps, +1 ps and +2 ps. Unfortunately, all four spectra look identical. This is not entirely surprising. The 1.2 μJ of IR pump is simply not enough to saturate the $v = 1$ transition. As described in section 5.5.3, Bonn *et al.* [127, 128] only observe the hot band transition when the $v = 1$ level is saturated, at around 6 μJ of incident IR. Successful picosecond laser IR pump-probe experiments (e.g. on CO/Cu{100} [138]) were carried out with around 2–3 μJ of IR pump, but the energy of a one picosecond pulse will be around 6 times more concentrated on the actual vibrational frequency required than for our spectrally broader 150 femtosecond pulse. Successful IR pump-probe experiments with femtosecond lasers need higher pump energies.

However, I am pleased to say, that at the time of writing, we have just been awarded a grant to purchase a second OPA. This will be used for such experiments in the future to overcome this lack of pump energy and for two colour pump-probe studies as described in section 6.4.2.

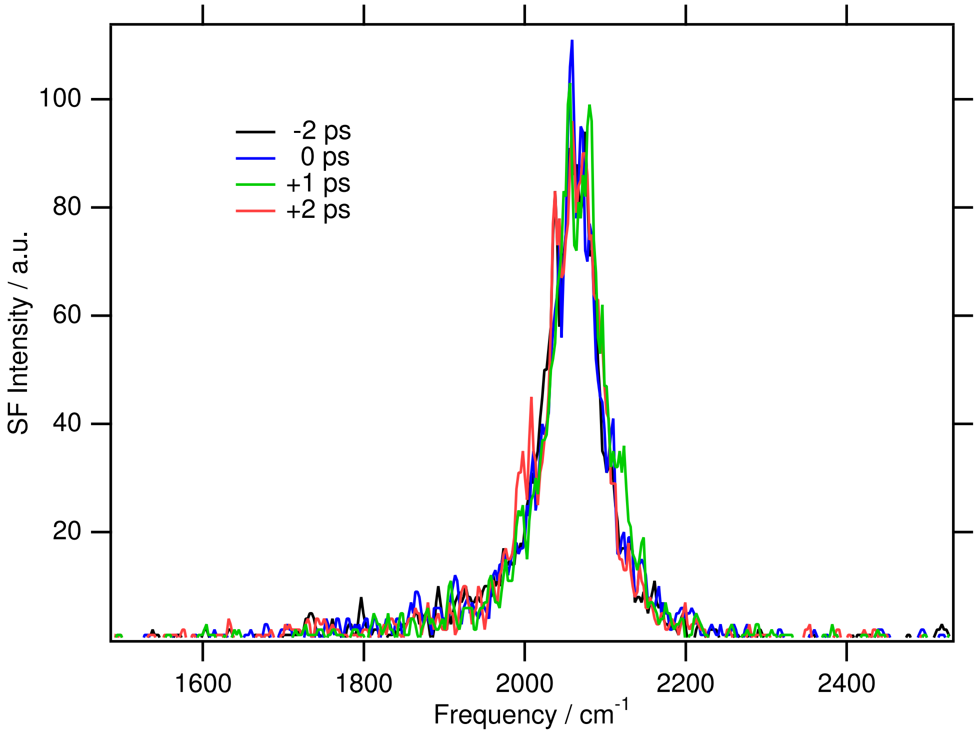

Figure 6.2: IR-pump, SF-probe spectra for CO on Ru$\{10\bar{1}0\}$. Saturation coverage, 200 K.

6.2 IR Photon Echo

6.2.1 Theory

In a vibrational photon echo experiment, two IR pump beams are used, with a VIS probe. The first IR pump induces a coherent vibrational polarisation in the adsorbate layer. This polarisation will then undergo the free induction decay process. After a time τ, the second pump is sent in which initiates a rephasing process of the dipoles. After a further equal time delay, τ, the dipoles will once again vibrate coherently and emit a short pulse of light — the photon echo. This photon echo emission is detected by upconversion with the VIS probe. However, due to interactions with the phonons there are fluctuations in the oscillator frequencies, which increase the homogeneous linewidth. So as τ is increased, these fluctuations have a greater effect and the size of the photon echo signal is reduced. This provides a method to measure the pure homogeneous linewidth from the Fourier transform of the echo decay curve.

A good analogy of this, from [140], is that of runners in a race. The first pump pulse can be thought of as the starting gun. The runners start to race, and of course some are faster than others. In this particular race though, a second gun (pump) is fired and the runners turn around and start to run back to the starting line. If their individual speeds are constant, they will all arrive back at the line at the same time in phase. However, if there are fluctuations in their speeds, then there will not be perfect rephasing.

Echos were originally seen for spins in NMR [141], and later for photons [142]. These experiments have been carried out on surfaces, for example, H / Si{111} [64].

6.2.2 Experimental and Results

The experimental setup is almost the same as that used for the IR-pump, SF-probe experiment described in section 6.1.2, and in figure 6.1. In the photon echo experiment, the VIS beam is scanned with the large translation stage on the main table, and τ is changed with the Standa stage on the chamber mounted table. The "probe" IR path in figure 6.1 is that used for the first IR pulse (IR1), and the "pump" path is used for the second (IR2). Energies are the same as for the IR pump-probe experiment.

The direction of the SF signal from the photon echo is given by [64]

$$\mathbf{k}_{\mathrm{SF}} = 2\mathbf{k}_{\mathrm{IR2}} - \mathbf{k}_{\mathrm{IR1}} - \mathbf{k}_{\mathrm{VIS}}$$

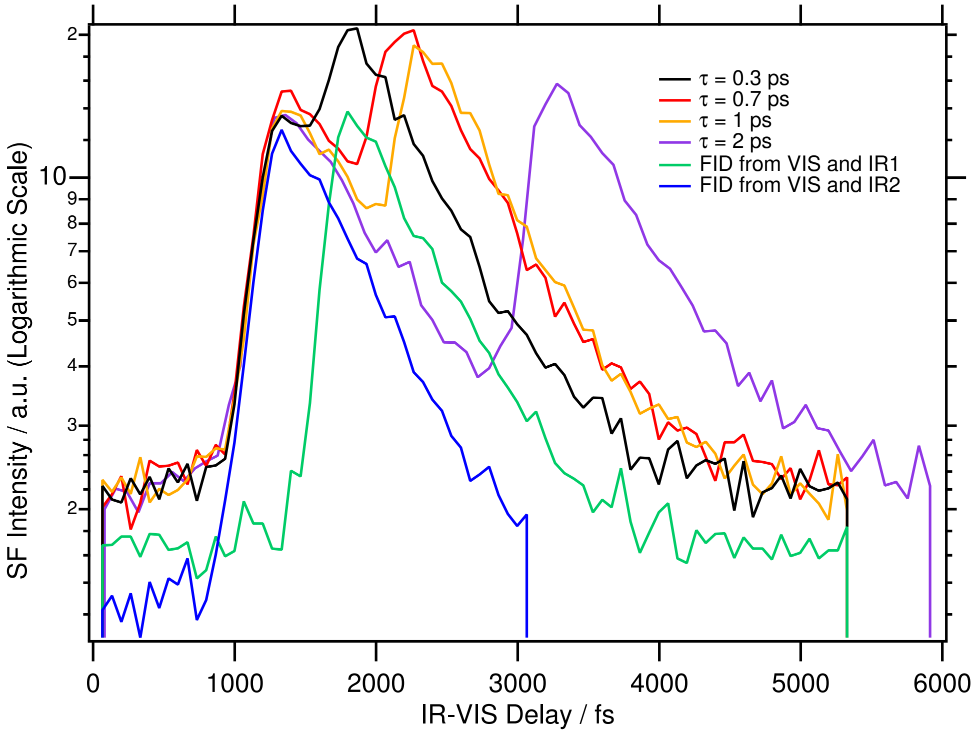

Figure 6.3: Photon echo results for CO/Ru$\{10\bar{1}0\}$. Saturation coverage, 200 K. Also shown are the FIDs from IR1 and IR2. See text for details.

$$\Rightarrow \frac{1}{\lambda_{\mathrm{SF}}} \sin\theta_{\mathrm{SF}} = \frac{2}{\lambda_{\mathrm{IR2}}} \sin\theta_{\mathrm{IR2}} - \frac{1}{\lambda_{\mathrm{IR1}}} \sin\theta_{\mathrm{IR1}} + \frac{1}{\lambda_{\mathrm{VIS}}} \sin\theta_{\mathrm{VIS}}$$

and with the geometry of our experiment this means that the photon echo should be produced just half a degree away from the VIS beam from the usual SF signal.

Figure 6.3 shows results from CO on Ru$\{10\bar{1}0\}$, for four values of the IR-IR delay, τ. Also shown are the individual free induction decays from each of the IR beams alone with the VIS beam. For each of the four photon echo experiments, the FIDs are observed from each of the IR pulses, due to the closeness of the directions of these signals to the echo direction in our experiment. According to [64] the echo should be of a similar magnitude to the FID signal, however, no photon echo is seen at $t \sim 2\tau$ unfortunately.

6.3 VIS-Pump SF-Probe

6.3.1 Experimental Implementation

These experiments were designed to investigate the effect of an 800 nm pulse arriving shortly before the SF VIS and IR pulses. In order to align a pump beam in space and time with the IR and VIS beams, we used the potassium layer method to look for the sum frequency of the pump with the VIS beam. However, this placed severe restrictions on which UHV chamber window (figure 3.24) was to be used for the pump beam entry, as we had to be able to detect the outgoing SF to align the system. It was decided to align the pump beam along virtually the same path as the IR beam, so the SF of the pump-VIS and probe-VIS would emerge spatially in-between these two beams, and could be detected by rotating the sample to direct the signal into the spectrometer.

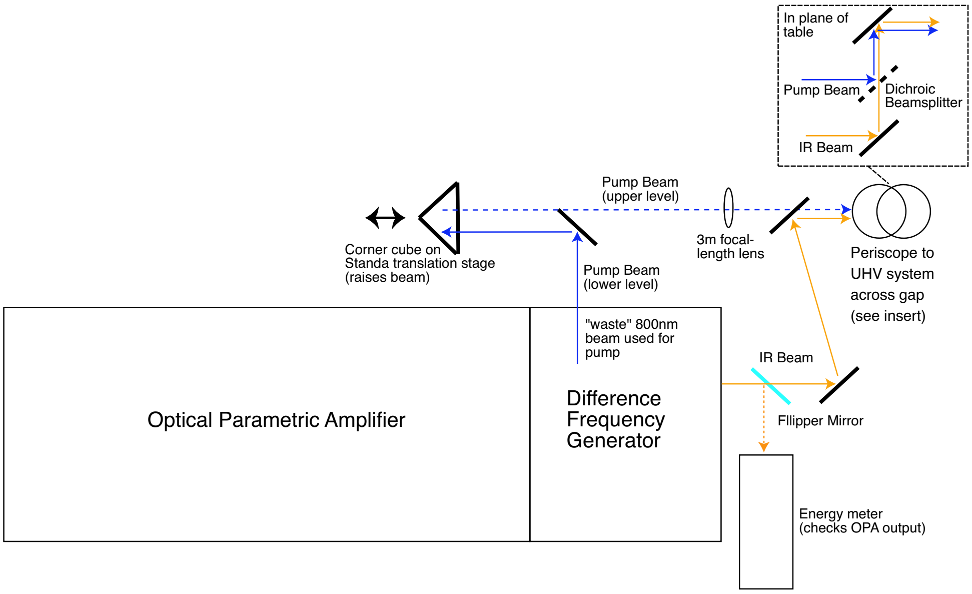

Figure 6.4: Changes to optical paths on the main optical table for VIS pump SF-probe experiment. Sub-diagram of figure 3.32.

Figure 6.4 shows the alterations made to the optical set up given in figure 3.32. The waste 800 nm beam (up to 1 mJ) from the OPA is used for the pump. The time delay is introduced by a broadband reflective (Al coated) *corner cube* mounted on the Standa translation stage, which reflects an outgoing beam parallel to the incoming beam. The beam height is raised by this corner cube and it then passes through a 3 m focal length lens which, in combination with the CaF_2 lens at the chamber window, focuses the pump beam on to the surface. The beam then passes onto an appropriate dichroic beamsplitter, where it joins the path of the IR beam until it reaches the sample. In order that the pump beam does not enter the detector, it is steered so that it rises very slightly along its path and thus exits the chamber very slightly above the other beams. Given that it follows the IR path, it is not very likely to enter the detector anyway as the SF path is much closer to the VIS probe path, the latter remaining the same as that given in figures 3.32 and 3.33.

6.3.2 Results

Various attempts were made to perform an 800 nm pump SF experiment and the most successful is discussed here. The energy of the pump was around 250 μJ, and 40% of this was reflected at grazing incidence. From an estimate of the pump-probe overlap this gives the absorbed fluence to be 24 $\mathrm{J\,m^{-2}}$. The sample temperature was 100 K, coverage 0.9 ML. While the surface was potassium covered, a check was made for any nonlinear interaction signals entering the detector (e.g. pump-VIS + probe-IR) other than the probe SF signal and none were observed. The program given in Appendix C to perform pump-probe experiments by changing the Standa stage time delay was used to take 10 SF spectra over a time delay range of ±13.4 ps around time zero, and these are shown in figure 6.5. They are also represented in a different form in figure 6.6. A redshift of 5.2 $\mathrm{cm^{-1}}$

is seen in the spectra around time zero, as shown in figure 6.7. The time-constant of the $t < 0$ rise is around 0.95 ps and that of the $t > 0$ recovery is around 5.3 ps, if fitted to an exponential function.

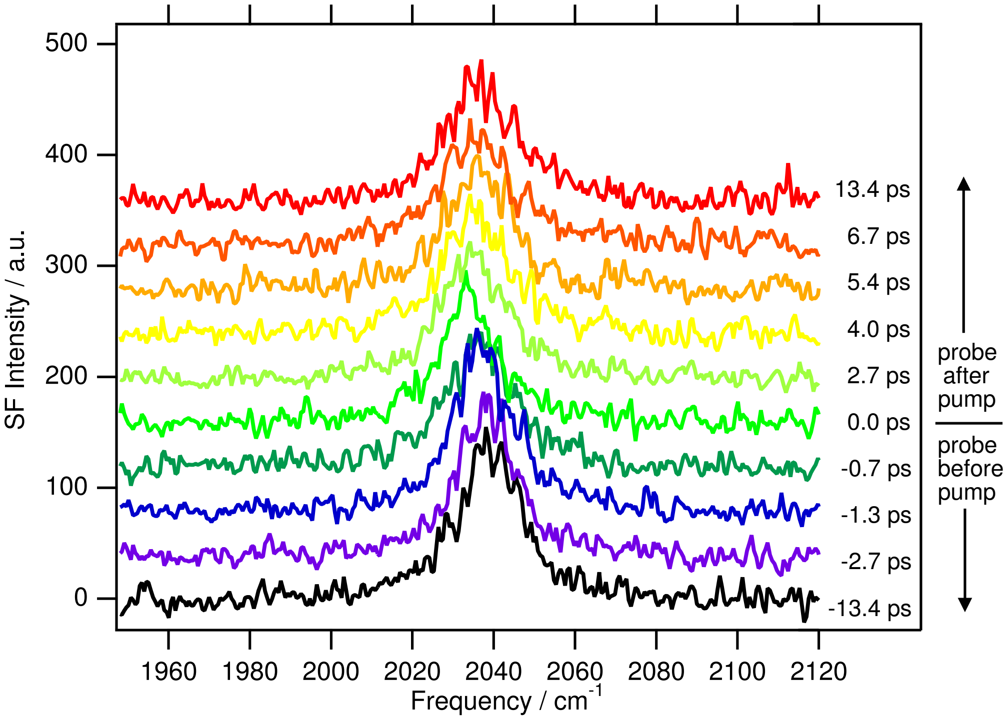

Figure 6.5: VIS-pump, SF-probe spectra from CO on Ru$\{10\bar{1}0\}$, as a function of pump-probe delay. Sample temperature 100 K, coverage 0.9 ML.

6.3.3 Discussion

Bonn, Hess and Wolf *et al.* [130] performed a similar experiment on the CO/ Ru{0001} surface in which a redshift of around 20 cm^{-1} in the CO spectra was seen around time zero for 19 J m^{-2} of incoming pump fluence at 0.33 ML coverage. They attribute this to the transient heating effect of the 800 nm beam leading to increased coupling with the frustrated translation mode at the higher temperature. At this fluence no desorption should occur. This effect was already seen by

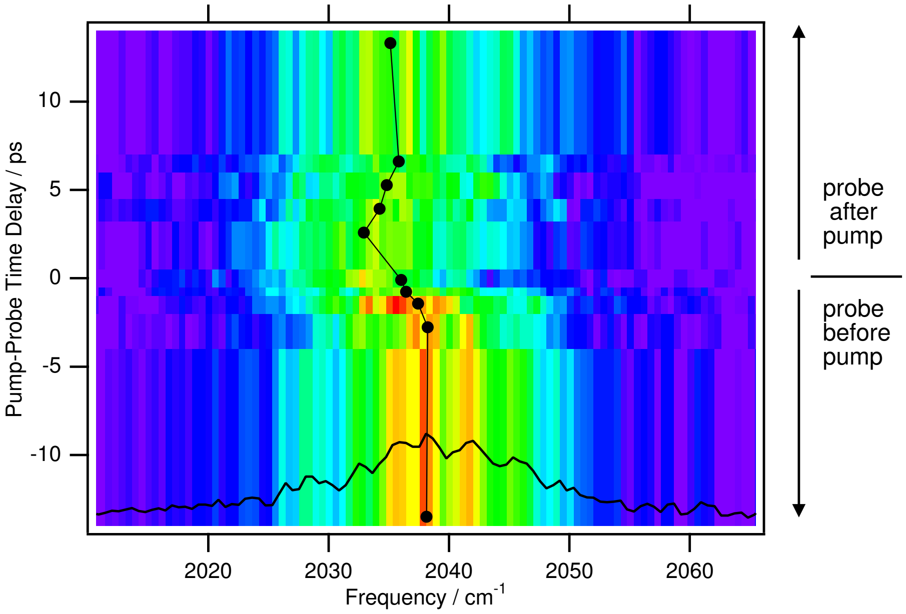

Figure 6.6: VIS-Pump, SF-Probe results from CO on Ru$\{10\bar{1}0\}$. The example spectrum at the bottom is for -13.4 ps, the intensities of the others are represented by a colour scheme to clearly show the frequency shift. The vertical black line plots the position of the fitted peak.

them at negative time delays due to the VIS pump arriving after the IR pulse and hence disturbing the free induction decay on a timescale of T_2. This is an example of a *coherent artifact* (see e.g. [135, page 140]) and can often be minimised by changing the polarisation of the pump pulse.

The effect we observe has a faster decay than that observed by Bonn *et al.*, which lasted several tens of picoseconds, but then we are dealing with a very different surface and coverage. It is unlikely that the effect is simply a coherent artifact. Checks were made with the K covered surface for other nonlinear interactions and none were seen. Also, the trace is quite clearly asymmetric with respect to time.

These data have been modelled assuming that the observed frequency shift is

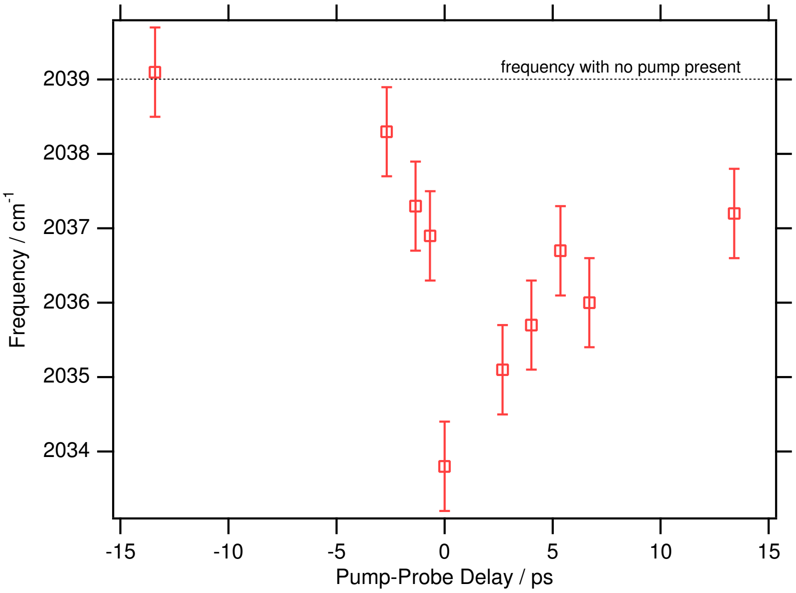

Figure 6.7: Change in CO stretch frequency with pump-probe delay.

due to laser heating. A FORTRAN program, previously used to model the benzene desorption experiments [42, 43] was employed to model the lattice, electronic and adsorbate temperatures after heating by an incoming 800 nm laser pulse. This program is based upon the two temperature model proposed by Anisimov *et al.* [143], used extensively in the literature to model laser heating. The program numerically solves the following coupled differential equations:

$$C_e \frac{\partial T_e}{\partial t} = \kappa \nabla^2 T_e + g\left(T_l - T_e\right) + S\left(z, t\right) \tag{6.1}$$

$$C_l \frac{\partial T_l}{\partial t} = -g\left(T_l - T_e\right) \tag{6.2}$$

$$C_a \frac{\partial T_a}{\partial t} = -g_e\left(T_a - T_e\right) - g_l\left(T_a - T_l\right) \tag{6.3}$$

where: T_e, T_l and T_a are the electronic, lattice and adsorbate temperatures; g, g_l and g_e are the electron-lattice, adsorbate-lattice and adsorbate-electron coupling constants; κ is the thermal conductivity; C_l is the lattice heat capacity and C_e is the electronic heat capacity, assumed to be of the form $C_e = \gamma T_e$, where γ is a constant. $S\,(z,t)$ is the laser source term given by

$$S\,(z,t) = 2I\,(t)\,(1-R)\,\frac{\exp(-2z/\delta)}{\delta}, \tag{6.4}$$

where $I\,(t)$ is the laser intensity as a function of time, R is the substrate reflectivity, z is the depth of the substrate and δ is the optical skin depth.

Parameter	Source[†]	Value
κ	[144]	117 $\mathrm{Wm^{-1}K^{-1}}$
C_l	[145]	2.9×10^{6} $\mathrm{Jm^{-3}K^{-1}}$
C_a/g_e	E	10 ps[‡]
C_a/g_l	[31]	1 ps
g	[144]	185×10^{-16} $\mathrm{Wm^{-3}K^{-1}}$
γ	[144]	400 $\mathrm{Jm^{-3}K^{-2}}$
δ	[144]	16.2 nm
Fluence[§]	M	24 $\mathrm{Jm^{-2}}$
Pulse Width	M	150 fs
Sample Temp.	M	100 K

Table 6.1: Modelling parameters for lattice, electronic and adsorbate heat for CO/Ru$\{10\bar{1}0\}$ after laser heating. † [n] = reference #n, M = measured, E = estimated. ‡ Assumed to be little adsorbate-electron coupling therefore large. § Empirical reflectivity of 40% at grazing incidence already factored in.

The parameters used in the model are given in table 6.1, and a plot of the three temperatures versus time is given in figure 6.8. From the work on the dependence of the CO stretch frequency on sample temperature described in section 5.5.3, at $\Theta = 0.9$ ML, we get $\mathrm{d}\nu/\mathrm{d}T = 0.043$ $\mathrm{cm^{-1}K^{-1}}$ (figure 5.26). The *adsorbate* temperature curve in figure 6.8, for it is the adsorbate temperature which would excite any CO phonon mode, was multiplied by this gradient to estimate the laser

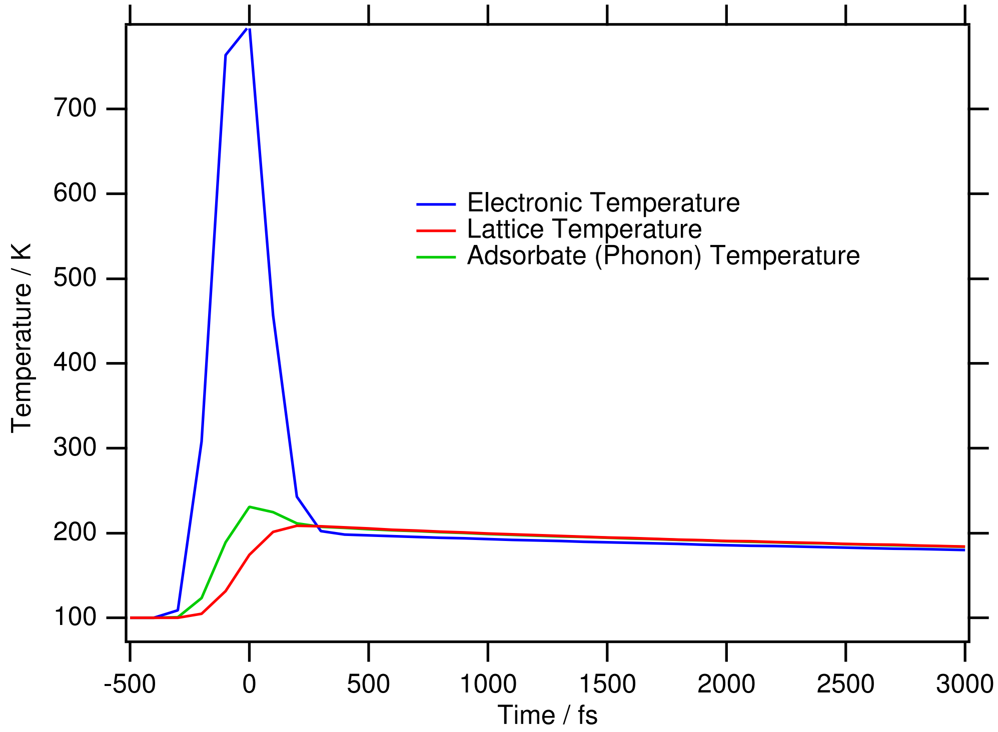

Figure 6.8: Calculation of electronic, lattice and adsorbate temperatures for CO/Ru{$10\bar{1}0$} due to 150 fs, 24 Jm^{-2} laser heating. See table 6.1 for other parameters.

induced frequency change and this is compared with the pump-probe results in figure 6.9. No attempt has yet been made in this model to account for the coherent interaction which causes the change in frequency prior to $t = 0$.

The fit to the data is quite good, although the recovery of the frequency in the model is still somewhat slower than from the experiment. It seems likely then that the process is thermally driven, and as such is probably due to coupling to the frustrated translational or rotational CO phonon mode. However, one cannot rule out electronic effects as proposed for the pump-probe results on CO/Ni{111} by Bandara *et al.* [38]. It is possible that pump laser excited electrons in the substrate could couple either directly to the CO stretch or via one of the phonon modes.

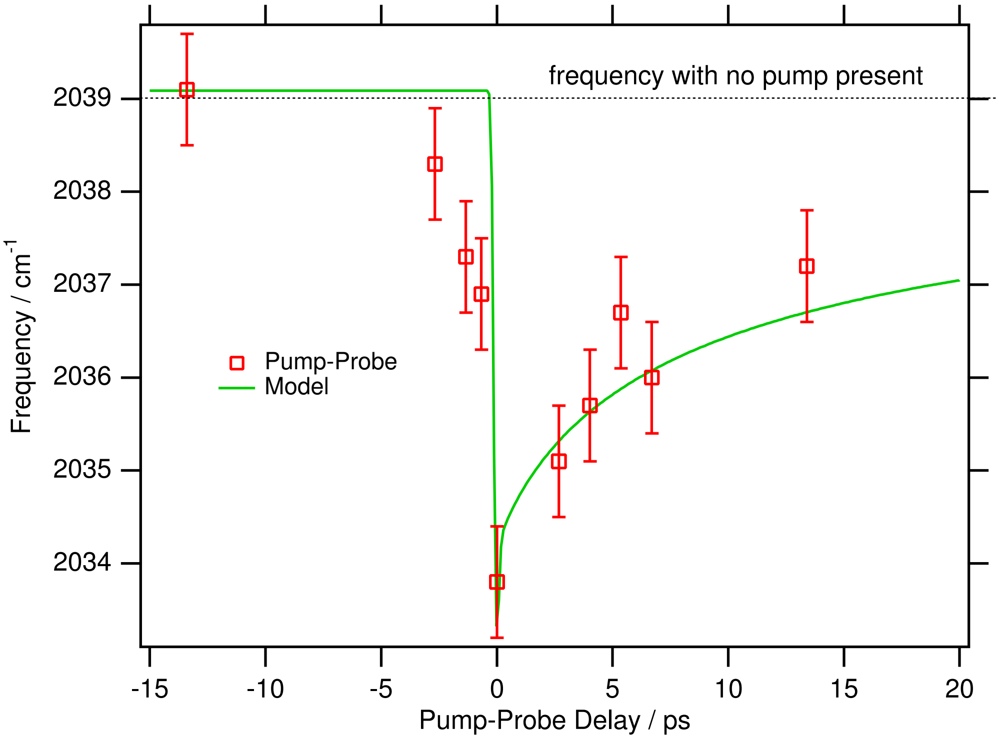

Figure 6.9: Comparison of thermal model with pump-probe data.

The analysis of these results is ongoing prior to their publication.

6.4 Future Work

Apart from the work on the photocatalytic decomposition of water described in section 1.1.3 the following two projects are to follow on from the work in this thesis.

6.4.1 C / CO oxidation on Pt{110}

Our group has already produced a large body of work from its molecular beam [6] and DFT [4] facilities on the reaction of carbon and oxygen on Pt{110}. Work completed just before my arrival in the group and soon to be published [146] on laser induced reactions between CO, C and ethylene co-adsorbed with molecular oxygen on Pt{111} show that the second harmonic (400 nm) of the TSA can induce reactions to produce CO_2, CO and $CO_2 + H_2O$ respectively. These were detected with the mass spectrometer, in a similar setup to the benzene work described in section 1.3 and the C_2H_4 / H_2 desorption work described in Appendix A. It is hoped to follow the reactions of $C + O \rightarrow CO$ and $CO + O \rightarrow CO_2$ on Pt{110} in real time and hence gain an understanding of the transition states in these industrially and environmentally important reactions (C may be deposited by heating adsorbed ethylene).

A major hurdle to be overcome in this experiment will be that of refreshing the sample. In the work described in [42, 43, 146] and Appendix A the laser beam was scanned across the surface so that each pulse was directed at an un-reacted / un-desorbed piece of surface. Whilst this could perhaps be overcome in the CO + O reaction by backfilling the chamber with the reagents, certainly for the C + O reaction each pulse would have to be directed at a new piece of the surface. For three overlapping laser beams in space and time it would be practically impossible to scan all three beams. A solution to this problem is to move the sample.

One could motorise the x, y and z motions of the sample mount (section 3.2.2). However, given the axes of motion do not correspond to the incoming beam orientation with respect to the crystal, a more complicated system is required. This would have to move the x and y axes in combination according to some algorithm. It is also possible that a HeNe beam reflected from the surface could provide real-time feedback on the sample position. Such a system is currently being investigated, and we thank Professor Charles T. Campbell for many useful discussions on this matter.

Problems with the availability of optics which are suitable for use both with

UV and IR light would make a colinear UV-pump/IR setup difficult, so a different beam path will have to be used, whilst still allowing emergence of the correct SF signals for alignment purposes.

In setting up the CO/Ru$\{10\bar{1}0\}$ experiment we originally tried CO/Pt{111} (described in section 3.3.4) and found no SF signal. This is probably because the experiment was not optimised at the time as well as it is now, but Bourguignon *et al.* [147] do report a much smaller SF signal at these wavelengths for CO/Pt{111} than is seen for ruthenium with a comparable laser system such as that of Bonn and Wolf *et al.*

The Pt{110} crystal has been installed in the UHV chamber in place of the Ru$\{10\bar{1}0\}$ sample and is being bulk cleaned at the time of writing.

6.4.2 The Toyota Project

The object of this project, sponsored by the Toyota Motor Corp. is ultimately to develop a NO_x decomposition catalyst without the need for reductants. It is in conjunction with the STM, DFT and RAIRS facilities within the group. The system under study will be NO on an iridium surface with a layer of gold deposited, along with the Ru$\{10\bar{1}0\}$ and Pt{110} surfaces also available. The gold layer on the iridium should enhance the SF signal. The plans for the femtosecond lab are:

- VIS-Pump SF-Probe of NO_x to investigate its decomposition in real time
- Measure the anharmonicity of the N-O bond, by exciting the hot band transition with an intense IR field. Thus one can calculate the dissociation energy of this bond
- SF photon echo experiments

- Two colour IR-IR-VIS SFG to examine the coupling between identical oscillators on different surface sites. One species is excited by the first IR pulse, and then the amount of vibrational energy transfer is monitored by a time delayed second IR pulse of a different frequency.

The last three points will require a second OPA, and we have just (at the time of writing) been awarded a grant to purchase one. Changes to the TSA will be needed to provide enough energy to pump both OPAs and it it hoped that this may be achieved by replacing the stretcher and compressor gratings with the more modern and efficient types now available.

Another problem is presented by the fact that the N-O stretch frequencies, at around 1800 cm^{-1}, are in the same spectral region as the IR absorbance of water in air. With the long ($\sim$ 3 m) IR path length we presently use this could greatly attenuate the amount of IR reaching the surface. A solution to this is to enclose the beam paths and purge with dry nitrogen.

A gold evaporator has already been purchased and installed in the UHV chamber.

6.4.3 General Suggestions

Upgrading the laser amplifier and amplifier pump to a 400 Hz or 1 kHz repetition rate system would substantially improve shot to shot energy fluctuations and data acquisition times, and hence allow much lower surface coverages and molecules with weaker dipole moments to be studied. The author feels that such an upgrade should be given the utmost consideration in any future grant applications. More modern laser systems are also inevitably easier to maintain and require less attention as technology has become much more “commercial” in the last few years. We recently borrowed a diode pumped 60 fs laser oscillator for a demonstration at an exhibition [148] which requires no user alignment whatsoever; its only control is the on/off switch.

A much less easily addressable problem is that of the laser and UHV system sharing the same laboratory environment. The chamber bakeouts required every time a fault develops in the UHV system, or when the sample needs changing, are very disruptive indeed given the laser alignment needed afterwards due to temperature gradients in the laboratory. The Leiden femtosecond laser group, which do not have this arrangement, inform me that their Light Conversion TOPAS OPA has not required realignment and as such is treated as a “black box” by workers. Some local environmental separation of these systems at least should be considered in the future.

The need for emergence of light from nonlinear interactions between the various pump and probe beams for alignment purposes puts restrictions on the already limited choice of optical windows (figure 3.24). Therefore re-orientating the chamber with respect to the laser system might be considered, or replacing the chamber mounted optical table with one that offers a scope of 360° around the chamber.

If absorption of mid-IR light in air becomes a problem, then the DFG module(s) of the TOPAS(s) could be removed and mounted on the chamber table. Then the shorter wavelength signal and idler beams could then be sent across the inter-table periscopes to the DFG module(s) to produce the mid-IR light in closer proximity to the sample.

6.5 Concluding Remarks

On an experimental level, the femtosecond sum-frequency spectrometer is now fully operational and capable of broadband spectral, free induction decay and VIS-pump SF-probe experiments; and *in principle* IR-pump SF-probe and photon echo experiments.

The coverage dependent study of the CO stretch frequency on Ru$\{10\bar{1}0\}$ by comparison with the HREELS work of Lauth *et al.* [106] gives confidence in the new spectrometer and its spectral calibration. The linewidth measurements have shown an increase at low coverage, sharply levelling off at the same coverage (0.3 ML) as the first stable LEED pattern (3 × 1). An isotopic study has shown that dipole-dipole coupling is important in this system, as for CO/Ru{0001}, leading to spectral narrowing at high coverages due to an exchange interaction between high and low frequency oscillators. At low coverages the formation of chains in the [0001] direction of varying length and separation is suggested to explain the heterogeneous broadening at low coverage.

The work in chapter 4 gives a novel and general technique for the temporal characterisation of ultrafast laser beams on surfaces *in vacuo*, and this has been used to accurately fit free induction decays for the CO/Ru$\{10\bar{1}0\}$ system, giving linewidths without instrumental broadening. The successful choice of a fitting model with a single exponential decay backs up the conclusions on the importance of the exchange interaction at high coverages.

The stretch frequency is dependent upon sample temperature and the change is more pronounced at $\Theta = 0.9$ ML (0.043 $\text{cm}^{-1}\text{K}^{-1}$) than at 1 ML (0.021 $\text{cm}^{-1}\text{K}^{-1}$). The effect is due to coupling with a thermally excited CO adlayer phonon mode, either the frustrated translation or rotation. The VIS-pump SF-probe experiment yields a redshift of 5.2 cm^{-1} in the CO stretch frequency for 24 J m^{-2} of incoming 150 fs pump fluence for 0.9 ML of CO coverage at 100 K. The time constant of the rise is ∼ 0.95 ps and for the recovery ∼ 5.2 ps. A model of the adsorbate temperature after laser heating, coupled with the sample temperature dependent data, accounts largely for the observed frequency shift being thermal in origin, suggesting coupling with one of the adlayer phonon modes. Such a fast effect could also be due to the CO stretch coupling to electrons excited in the substrate layer by the laser.

Appendix A

Laser Induced Desorption of C_2H_4 / H_2 from Pt{111}

During the first year of my PhD we undertook a time-of-flight study of the laser induced desorption of ethylene on Pt{111}, during downtime of the OPA. Ethylene was chosen as it is the precursor to surface carbon for a proposed study of the $C + O \rightarrow CO$ reaction on Pt{111} (section 6.4.1). Whilst not directly related to the rest of the work in this thesis, and ultimately proving inconclusive, the experiments and results are summarised here for completeness. A more thorough account is to be found in my end of first year report [44].

Experimental Details

The 800 nm output of the TSA was doubled to 400 nm using a BBO crystal. This beam was then scanned across the Pt{111} sample with adsorbed ethylene in the UHV chamber using a computer controlled scanner unit which consists of two motor driven mirrors for the x and y planes, at a pitch of 100 μm, placing around 1000 laser pulses on the crystal per experiment. The fluence could be attenuated

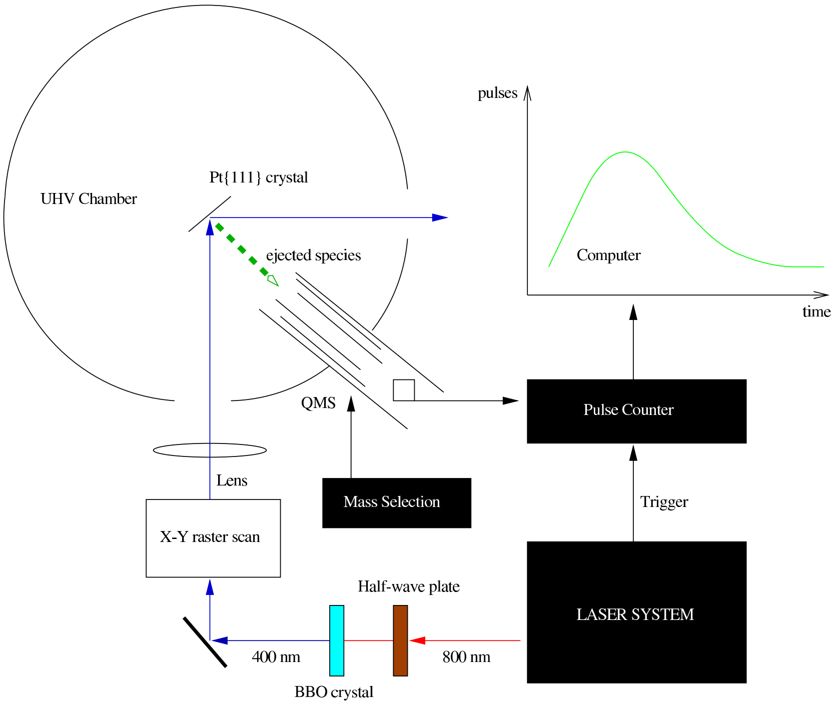

Figure A.1: Laser Desorption Experiment.

with a half-wave plate before the BBO crystal. The mass spectrometer on the UHV chamber was used to detect desorbed species. Pulses from the mass spectrometer channeltron were counted using a PC based multi-channel scaler to build up a histogram of counts versus time, where time zero is defined by the laser trigger. The time resolution is 2 µs. The experimental set up is shown in figure A.1.

Results

Results for ethylene (at mass 28) show a very fast peak at 9 µs and a slower peak which can be fitted to a Maxwell-Boltzmann disribution, corresponding to a kinetic temperature of 321 K for the measured pulse energy of 140 ± 20 µJ, figure A.2.

The fast peak is present at *all* mass spectrometer mass settings. Suspecting

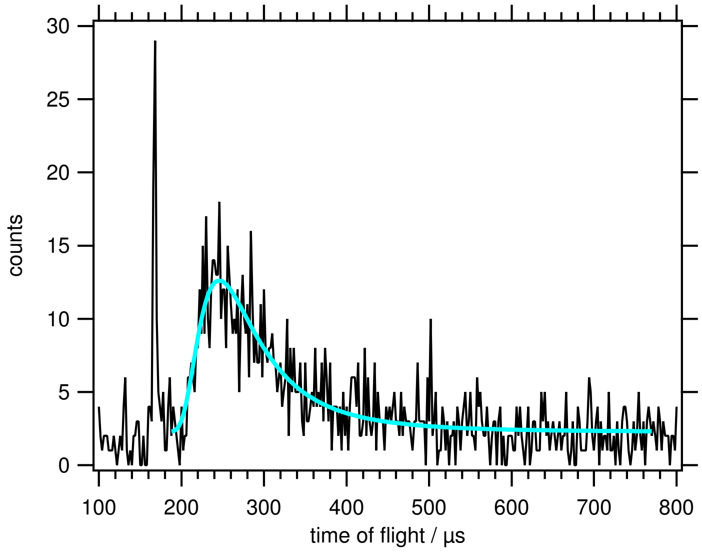

Figure A.2: Time-of-flight study of C_2H_4 on Pt{111}, at mass 28. Time zero is at 155 µs.

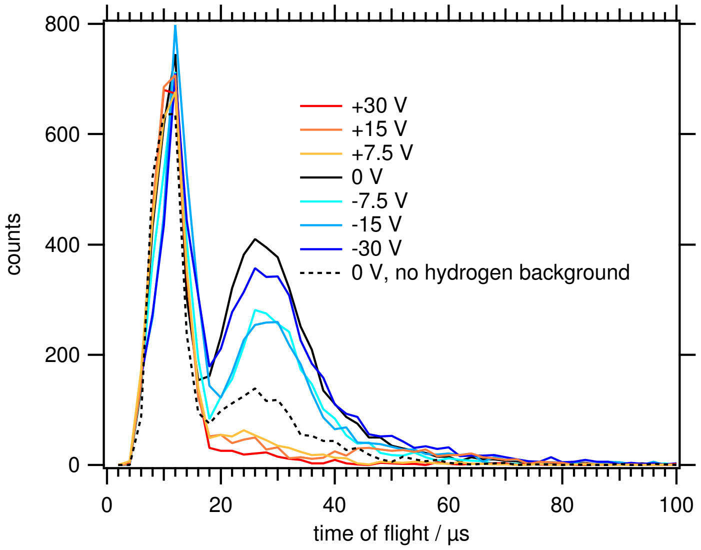

Figure A.3: TOF data from H_2 on Pt{111}, mass independent.

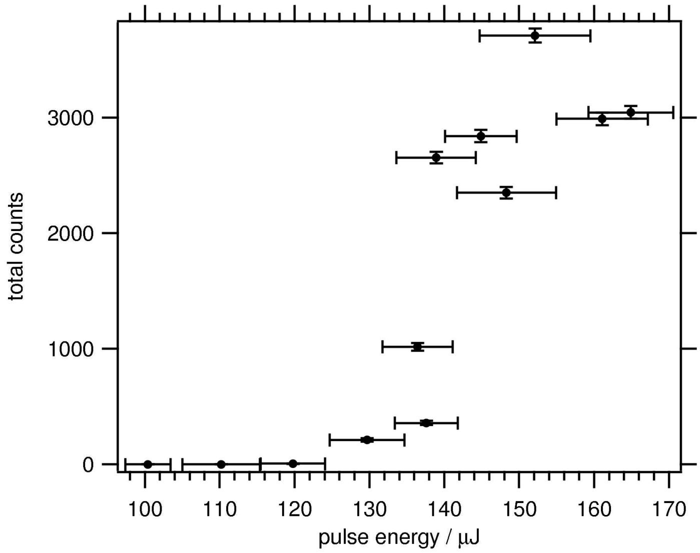

Figure A.4: Laser fluence dependence of the yield of the fast peak for H_2 on Pt{111}.

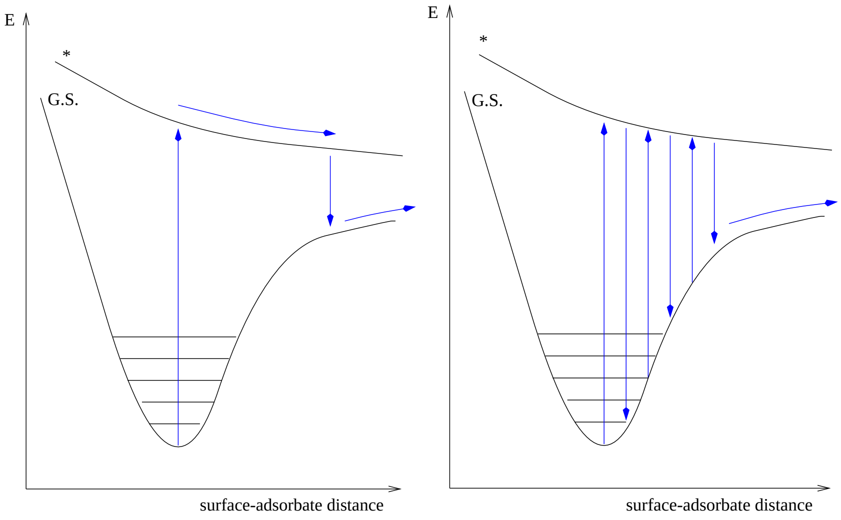

Figure A.5: The DIET (left) and DIMET (right) laser desorption processes.

a species which is so fast (and hence light) that it passes through the quadrupole undeviated, we turned our attention to adsorbing hydrogen. The fast peak was still seen, with a slightly slower and broader peak appearing also at 23 µs. Suspecting a charged H species to be responsible we electrically biased the sample, and figure A.3 shows the results. From this it must be concluded that the fast peak is caused by a neutral species and the slower peak by a negatively charged species.

Finally, a fluence dependence study of the fast peak was undertaken, and the results are given in figure A.4. A highly non-linear fluence dependence was seen, with a sharp threshold of around 50 mJ cm^{-2}.

Discussion

Concentrating on hydrogen, the most likely candidate for the fast peak is H and for the slower peak H_2^-. Laser induced desorption from surfaces, other than thermal desorption, is classified into two regimes [28]. Desorption Induced by Electronic Transition (DIET) is a process in which the laser excites an atom from its ground state to an excited state where it gains enough potential energy to leave the surface by the conversion of this to kinetic energy. The second process is known as Desorption Induced by Multiple Electronic Transitions (DIMET) and occurs by the atom being repeatedly promoted to the excited state (and decaying back to ground state) by successive photons in a very intense beam. DIMET shows a strongly non-linear dependence upon laser fluence. These processes are summarised in figure A.5.

It is rather difficult to attribute the process in this case to either DIET or DIMET. The very fast time is characteristic of a DIET process, but the very non-linear fluence dependence is characteristic of DIMET. The lattice temperatures for both peaks were calculated by solving the differential heat equations (numbers 6.1 & 6.2 in chapter 6) as described in section 6.3.3 and the results are given in figure A.6.

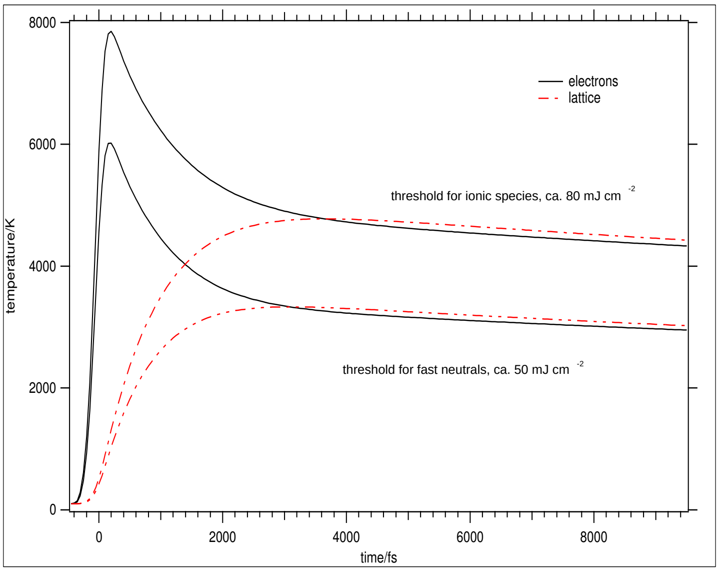

Figure A.6: Lattice and electron temperatures for fast (neutral) and slower (ionic) peaks versus time.

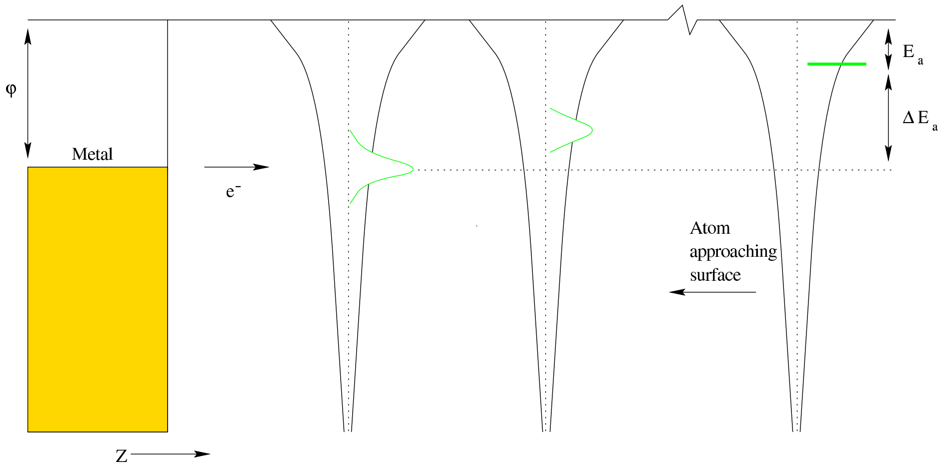

Figure A.7: Lowering and broadening of the electron affinity of an atom or molecule when approaching a metal surface. E_a is the electron affinity of the atom at infinity, and ΔE_a is the change in the affinity as the atom approaches.

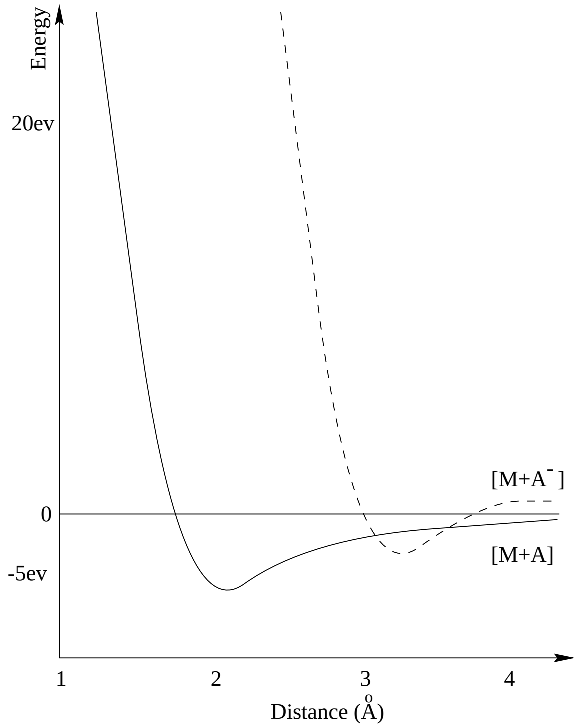

Figure A.8: Approximate potential energy curves involved in oxygen ion desorption from tungsten.

The presence of a negatively charged species could be explained by the following scenario: when the hydrogen atom approaches the metal its electron affinity decreases and broadens due to an interaction with an image of the affinity level in the metal [149]. This is illustrated in figure A.7.

Antoniewicz has suggested [150] that negative ion desorption (of oxygen ions from tungsten) occurs when the ground state (state V_0 in figure A.8, adapted from [150]), is at an energy above the $[M+A^-]$ state (dotted line) and electron tunnelling occurs from the substrate to the neutral thus leading to negative ion desorption.

More work would be needed to reach more concrete conclusions on this data, as our mass spectrometer was not at the time capable of ion differentiation, but has been very recently converted to do so.

Appendix B

Standa Stage Driver

The following program is written in C under the LabWindows CVI environment and libraries to run on a Windows based PC containing the Standa stage controller card. When compiled into an executable it provided a DOS style command `stage <signed number of microns>`. This is then called by any Andor BASIC program which needs to move the Standa stage.

The ISA stage controller card is controlled with two registers, one input and one output register. The program contains a routine `poke` which writes a value to the input register, whilst polling the output register for ready and confirmation signals, finally sending a synchronisation byte. A sequence of 21 half-bytes needs to be sent to the card for each movement, and the main routine of the program converts the distance parameter to the correct multi-half-byte form and sends this to the card via the `poke` routine along with all the other required parameters. These may of course be changed in the program if the user should wish, for example, to change the speed of the stage.

```
/* Move the Standa Stage. Syntax when compiled: stage <microns> */
/* J.P.R. Symonds 2002 */

#include <userint.h>
#include <analysis.h>
#include <easyio.h>
#include <visa.h>

#include <Ivi.h>
#include <cviauto.h>
#include <formatio.h>
#include <utility.h>
#include <ansi_c.h>
#include <lowlvlio.h>

/* Front End */

int main (int argc, char *argv[])
{
void stage(int,int);
int steps, dirn;
char dummy;

/* Check number of Arguments */

if (argc!=2)
{
printf("%s","Standa Stage Driver\nSyntax: stage <signed number of microns>");
printf("%s","\nJ.P.R. Symonds 2002\n\nHit enter to continue...");
dummy=getchar();
}
```

```
else

{

steps=atoi(argv[1]);

/* Determine Direction from Argument */

dirn=1;
if (steps<0)
{
dirn=−1;
steps=abs(steps);
}
stage(steps,dirn);

}
}

/* Move the Stage */

void stage(int number, int dir)

{
void poke(int);
int n4,n3,n2,n1,m;

/* ’modify’ number of steps */
if ((number%256) != 0) {number+=256; }

/* Divide number of steps up into 4 x 4 bits */
```

```
n1=number%16;
n2=(number/16)%16;
n3=(number/256)%16;
n4=(number/4096)%16;

/* Send half bytes in correct order to card using poke subroutine */
/* Number of Steps*/
poke(n4);
poke(n3);
poke(n2);
poke(n1);
/* Deceleration step (LSBs) */
poke(0);
poke(2);
/* Speed */
poke(15);
poke(15);
/* Accn per step */
poke(5);
/* Pulse Width Decrement (MSB)*/
poke(2);
/* Deceleration step (MSB) */
poke(1);
/* Pulse Width Decrement (LSB)*/
poke(0);
m=1;
if (dir==1) { m=0; }
/* Limit flags */
poke(m);
/* Sync Mode*/
poke(0);
/* Sync */
poke(0);
```

```
/* Mode */
poke(0);
/* Repetiton */
poke(0);
poke(0);
poke(0);
poke(1);
/* Step Size */
poke(0);

}

/* Send half bytes to card */
void poke(int value)

{
int state;
state=0;
/* wait for card ready */
do
        {
state = inp (772);
        } while (state != −17);


/* Send “HalfByte” */

outp (768, value);

/* wait for card accept */

do
        {
```

```
state = inp (772);
        } while (state != −1);

 /* Send sync */

outp (768, 80);

}
```

Appendix C

Acquisition Programs

All the following are written in Andor BASIC and run under the i-Star control program.

Move the VIS-IR (Aerotech) stage

The commands sent to the Aerotech controller via the RS232 port follow a “menu” control paradigm. ASCII 4 (control-D, or EOF) is sent to get to the top of the “menu” nest. Then successive single letter commands are sent to traverse the menus to get to what is needed, followed by any numerical parameters. If the controller is pre-set with parameters to set acceleration, top speed and deceleration then the ASCII sequence `CAD<distance in µm>` — Command, presets `A`, `Drive` — will move the stage.

```
rem Moves the VIS-IR stage
rem J Symonds 2001
input("how far (microns)",s)
baud(2,19200)
comwrite(2,chr$(4)) : rem Reset stage
```

```
delay(1000) : rem wait 1 s
comwrite(2,"CAD(";str$(s);")") : rem move it
```

Move the pump (Standa) stage

This uses the Standa stage driver given in appendix B.

```
rem Move the Pump Stage
rem J.Symonds 2002
input("PUMP STAGE: microns",mic$)
execute("c:\stage.exe ";mic$)
end
```

Scan the VIS-IR stage symmetrically about starting point

Used to cross-correlate VIS and IR beams.

```
rem Program to Scan stage whilst taking successive scans
rem J. Symonds 2001
SetAcquisitionType(0): rem take signal rather than background
SetTriggerMode(1) : rem external trigger

cls()
k=key("Do you want to save the data? (y/n)")
if (k==’y’) or (k==’Y’) then
        input("Filename base for Save", f$)
endif
input("Number of accumulations per scan",a)
SetAccumulate(0.017,a,0.1): rem Accumulate (exposure time, number, delay time)
input("Number of steps",n)
while (mod(n,2) != 0)
        input("Number of steps (div. by 2!!!!!)",n)
```

```
wend
input("Step size (microns)",s)
print(n;" steps at ";s;" micron step size")
print(a;" accumulations per scan")
if (k==’y’) or (k==’Y’) then
    print("Saving data with ";f$;" prefix into C:\Users\Scans directory")
endif
t=n*s : rem total distance to move
h=(t/2) : rem half this distance
baud(2,19200)
print("Initialising stage.....")
comwrite(2,chr$(4)) : rem Reset stage
delay(1000) : rem wait 1 s
comwrite(2,"CAD(-";str$(h);")") : rem Put stage to beginning of scan
delay(4000)
counter = 1
while counter < (n + 1)
    run() : rem acquire
    #counter = #0 : rem spectrum number
    d=(counter*s)-h
    InfoText(#counter, d;" microns from overlap centre") : rem annotate data
    comwrite(2,"D(";str$(s);")") : rem move stage
    if (k==’y’) or (k==’Y’) then
    rem save data
    SaveAsciiXY(#counter,"C:\Users\Scans\";f$;str$(counter);".asc")
    if (counter!=1) then
        CloseWindow(#(counter - 1))
    endif
    endif
    p=(counter/n)*100
    print(p;"% done")
    counter = counter + 1
    delay(1000)
```

```
wend
delay(2000)
comwrite(2,"D(-";str$(h);")") : rem Put stage back to centre
delay(2000)
print("Finished!")
```

Measure a Free Induction Decay

Performs an unsymmetrical scan of the VIS-IR beams, as the decay time is longer than the rise time. Moves back 1/4 of the total distance, then scans, then moves 3/4 of the total, back to the centre.

```
rem Free Induction Decay
rem J. Symonds 2001
SetAcquisitionType(0): rem take signal rather than background
SetTriggerMode(1) : rem external trigger

cls()
k=key("Do you want to save the data? (y/n)")
if (k=='y') or (k=='Y') then
        input("Filename base for Save", f$)
endif
input("Number of accumulations per scan",a)
SetAccumulate(0.017,a,0.1): rem Accumulate (exposure time, number, delay time)
input("Number of steps",n)
while (mod(n,4) != 0)
        input("Number of steps (div. by 4!!!!!)",n)
wend
input("Step size (microns)",s)
print(n;" steps at ";s;" micron step size")
print(a;" accumulations per scan")
```

```
if (k==’y’) or (k==’Y’) then
        print("Saving data with ";f$;" prefix into C:\Users\Scans directory")
endif
t=n*s : rem total distance
h=(t/4) : rem 1/4 of that distance
baud(2,19200)
print("Initialising stage.....")
comwrite(2,chr$(4)) : rem Reset stage
delay(1000) : rem wait 1 s
comwrite(2,"CAD(-";str$(h);")") : rem Put stage to beginning of scan
delay(4000)
counter = 1
while counter < (n + 1)
        run()
        #counter = #0 : rem spectrum number
        d=(counter*s)−h
        InfoText(#counter, d;" microns from overlap centre") : rem annotate data
        comwrite(2,"D(";str$(s);")") : rem move stage
        if (k==’y’) or (k==’Y’) then
        rem save data
        SaveAsciiXY(#counter,"C:\Users\Scans\";f$;str$(counter);".asc")
        if (counter!=1) then
                CloseWindow(#(counter − 1))
        endif
        endif
        p=(counter/n)*100
        print(p;"% done")
        counter = counter + 1
        delay(1000)
wend
delay(2000)
comwrite(2,"D(-";str$(3*h);")") : rem Put stage back to centre
delay(2000)
```

```
print("Finished!")
```

Scan Pump Stage

For pump-probe type experiments.

```
rem Program to Scan PUMP stage whilst taking successive scans
rem J. Symonds 2002
SetAcquisitionType(0): rem take signal rather than background
SetTriggerMode(1) : rem external trigger

cls()
k=key("PUMP STAGE. Do you want to save the data? (y/n)")
if (k=='y') or (k=='Y') then
    input("Filename base for Save", f$)
endif
input("Number of accumulations per scan",a)
SetAccumulate(0.017,a,0.1): rem Accumulate (exposure time, number, delay time)
input("Number of steps",n)
input("Step size (microns)",s)
print(n;" steps at ";s;" micron step size (PUMP stage)")
print(a;" accumulations per scan")
if (k=='y') or (k=='Y') then
    print("Saving data with ";f$;" prefix into C:\Users\Scans directory")
endif
t=n*s
counter = 1
while counter < (n + 1)
    run()
    #counter = #0 : rem spectrum number
    execute("c:\stage.exe ";str$(s)) : rem move stage
    if (k=='y') or (k=='Y') then
```

```
    rem save data
    SaveAsciiXY(#counter,"C:\Users\Scans\";f$;str$(counter);".asc")
    if (counter!=1) then
        CloseWindow(#(counter − 1))
    endif
    endif
    p=(counter/n)*100
    print(p;"% done")
    counter = counter + 1
    delay(1000)
wend
delay(2000)
print("Finished!")
```

Appendix D

FID Modelling Program

The following program is written in C and provides a UNIX style shell command `fid` <`amplitude`> <T_2> <`time zero,` T_0> <`temporal` $2\sigma_{\mathrm{IR}}$> <`VIS-IR delay,` τ> <`temporal` $2\sigma_{\mathrm{VIS}}$> <`resonant polarisability,` α> <`non-resonant polarisability,` β> <`integration accuracy`> <`time conversion factor`>. When executed it then returns the value to standard output of the FID curve for all the supplied parameters, based upon equation 5.1 in section 5.4.1, assuming Gaussian forms for the VIS and IR beams. It uses the GNU scientific library to perform the integrations, which is a free open source C library available to download from the GNU website [151]. The parameter <`integration accuracy`> is the fractional error to which the adaptive integration algorithms are performed. <`time conversion factor`> is a scaling factor for all the time parameters which has to be carefully selected to avoid overflow and underflow errors during the calculation.

Wavemetrics Igor Pro is used as the fitting application. The modelling program was written in C for speed, due to smaller system overheads and the availability of adaptive integration routines. However, Igor provides a very powerful graphical fitting environment. The second program in this appendix is the Igor routine which provides the free induction decay C program to Igor for fitting.

```c
/* Free Induction Decay Function Generator */
/* J. Symonds 2002 */
/* GNU Scientific Library Version */
/* This program generates the amplitude of a FID for a given time delay */
/* Command parameters: laser_amplitude T2 ir_centre ir_width*/
/* tau vis_width resonant_polarizability nonresonant_polarizability*/
/* integration_accuracy time_conversion_factor */

#include <stdio.h>
#include <stdlib.h>
#include <math.h>
#include <gsl/gsl_integration.h>

/* Gaussian Function */

double gaussian(double x, double x0, double dx)

{

  return exp(-pow(x-x0,2.0)/pow(dx,2.0));

}



/* Exponential Decay Function */

double decay(double x, double x0, double dx)

{
```

```
  return exp(−(x−x0)/dx);

}



/* Generate Resonant Contribution */

struct res_params { double max; double decay_c; double ir_c; double ir_w; };

double pol_res(double tp, void * p)

{
  struct res_params * params = (struct res_params *) p;

  double t = (params–>max);
  double T2 = (params–>decay_c);
  double ir_centre = (params–>ir_c);
  double ir_width = (params–>ir_w);
  double result;

  result = gaussian(tp,ir_centre, ir_width)*decay(t,tp,T2);

  return result;

}


/* Integrate Resonant and Non-Resonant IR contribs. -inf to t */

struct int_params { double delay; double vis_w; double ir_c; double ir_w;
double decay_c; double a; double b; double accuracy; };
```

```
double intensity(double tp, void * p)

{
  struct int_params * params = (struct int_params *) p;

  double t = (params->delay);
  double vis_width = (params->vis_w);
  double ir_centre = (params->ir_c);
  double ir_width = (params->ir_w);
  double T2 = (params->decay_c);
  double alpha = (params->a);
  double beta = (params->b);
  double acc = (params->accuracy);
  double res, error, result;

  gsl_integration_workspace * w2 = gsl_integration_workspace_alloc(1000);

  struct res_params pass = { tp, T2, ir_centre, ir_width };
  gsl_function F;
  F.function = &pol_res;
  F.params = &pass;

  gsl_integration_qagil (&F, tp, 0, acc, 1000, w2, &res, &error);

  gsl_integration_workspace_free(w2);

  result = pow(gaussian(tp, t, vis_width)*(alpha*res+beta*gaussian(tp, ir_centre,
ir_width)),2.0);

  return result;

}
```

```
int main(int argc, char *argv[])

{

   double amp;
   double acc, cnv;
   double result,error;
   struct int_params pass;

   gsl_integration_workspace * w = gsl_integration_workspace_alloc(1000);

   cnv=atof(argv[10]);

   amp=atof(argv[1]);
   pass.decay_c=atof(argv[2])*cnv;
   pass.ir_c=atof(argv[3])*cnv;
   pass.ir_w=atof(argv[4])*cnv;
   pass.delay=atof(argv[5])*cnv;
   pass.vis_w=atof(argv[6])*cnv;
   pass.a=atof(argv[7]);
   pass.b=atof(argv[8]);
   pass.accuracy=atof(argv[9]);

   gsl_function G;
   G.function = &intensity;
   G.params = &pass;

   gsl_integration_qagi (&G, 0, pass.accuracy, 1000, w, &result, &error);

   result*=pow(amp,4.0);

   printf("%.12g",result);
```

```
  return(0);
}
```

Here is the Igor routine to call the C program. Wavemetrics will supply an expensive add-on for Igor to allow it to call C programs directly, but I have found a good workaround worth mentioning. I use an Apple Macintosh G4 under Mac OS X to run these programs, and on Apple machines Igor allows embedded *AppleScript*™ programs to be called, and then stores their standard output in a special text variable. However, AppleScript routines can call UNIX commands under OS X and thus the AppleScript embedded within the following routine simply calls the `fid` command detailed above. The remainder of the code converts the numerical fitting parameters to text form to pass to the UNIX command, and then converts the response back to a number.

```
#pragma rtGlobals=1          // Use modern global access method.

// J.P.R. Symonds 2003
// Calls C F.I.D.   function for fitting. Mac OS X only, as does it via
// AppleScript, no PC equivelent provided in PC Igor for some reason.

function fid(t,amp,T2,ir_centre,ir_width, vis_width,alpha,beta,offset,acc,conv)
variable t,amp,T2,ir_centre,ir_width, vis_width,alpha,beta,offset,acc,conv
variable ans

// Concatenate string containing AppleScript code
String com = "Do Shell Script \"/home/jprs2/progs/fid "+num2str(1.0) + " " +
num2str(T2) + " " + num2str(ir_centre)+ " " + num2str(ir_width) + " " +
num2str(t) + " " + num2str(vis_width) + " " + num2str(alpha) + " " +
num2str(beta)+ " " + num2str(acc) + " " + num2str(conv) + "\""
```

```
// Execute Applescript
ExecuteScriptText com

// Next line makes sure than result is read to sufficient precision - Important!
sscanf S_value,"\"%18f\"", ans

return amp*ans+offset
end



function fidfit(v,x)
Wave v; variable x
variable ans

// Print progress to IGOR history window
printf "%.10g%.10g %.10g %.10g %.10g %.10g %.10g %.10g %.10g\r",x,v[0],v[1],v[2],
v[3],v[4],v[5],v[6],v[7]

ans = fid(x,v[0],v[1],v[2],v[3],v[4],v[5],v[6],v[7],1e−4,4e−4)
return ans
end
```

Appendix E

Program to Calculate Dipole Sum

In section 5.5.1 it was required to calculate the term $\sum_{j=2}^{N}\left(1/R_{ij}^{3}\right)$ in equation 5.2 for all the dipole-dipole distances R_{ij} in a hexagonal layer of CO molecules. The C program presented here, to be run under a UNIX type system, performs this numerical calculation given the basic interdipole separation. It does this by taking a triangular 6th slice of the hexagonal symmetry (60°) and increments a counter `layer` with each iteration which represents the current row of the triangle, from the tip of the triangle at the centre of the hexagon outwards. For each of the `layer` atoms in the row, the distance is calculated to the central atom by the cosine rule, and these distances are cubed and summed over each row, and over the whole triangle until the iteration limit is reached. Then the sum is simply multiplied by 6 to give the correct value for the whole hexagonal overlayer.

```c
/* 1/r^3 sum for hexagonal overlayer */
/* J.P.R. Symonds 2003 */
#include <stdio.h>
#include <stdlib.h>
#include <math.h>

int main()

{

  double r0=6.0; /* centre-centre distance */
  int cycles=10000; /* Number of iterations */
  int atom;
  int layer;
  double theta=60*(M_PI/180);
  double corr=0.0;
  double x;
  double y;
  double r;


  for (layer=1; layer<=cycles; layer++)
    {
      for (atom=0; atom<layer; atom++)
        {
          x=atom*r0;
          y=layer*r0;
          r=sqrt(x*x+y*y-2*x*y*cos(theta));
          corr=corr+(1/(r*r*r));
          printf("Layer %i Atom %i Dist %g Correlation %g\n",layer,atom,r,corr);
        }
```

```
    }
printf("Total correlation = %g\n",corr*6);
}
```

Bibliography

[1] Kurt W. Kolasinski. *Surface Science: Foundations of Catalysis and Nanoscience*. John Wiley & Sons Ltd., 2002.

[2] D.P. Woodruff and T.A. Delchar. *Modern Techniques of Surface Science*. Cambridge University Press, 2nd edition, 1994.

[3] R. K. Sharma, W. A. Brown, and D. A. King. The adsorption of CO on Pt{110} over the temperature range from 90 to 300 K studied by RAIRS. *Surface Science*, 414(1-2):68–76, 1998.

[4] A. Michaelides, Z.P. Liu, C.J. Zhang, A. Alavi, D.A. King, and Hu. P. Identification of general linear relationships between activation energies and enthalpy changes for dissociation reactions on surfaces. *Journal of the American Chemical Society*, 125(13):3704–3705, 2003.

[5] W. A. Brown, R. Kose, and D. A. King. Femtomole adsorption calorimetry on single-crystal surfaces. *Chemical Reviews*, 98(2):797–831, 1998.

[6] D. T. P. Watson, J. J. W. Harris, and D. A. King. Distinctive roles of chemisorbed atomic oxygen and dioxygen in methane catalytic oxidation on Pt{110}. *Journal of Physical Chemistry B*, 106(13):3416–3421, 2002.

[7] F.H. Scholes, H. Kleine, and D. A. King. Surface infrared emission spectroscopy studies of CO on Pt{111} and Pt{110}, To be submitted. 2003.

[8] K. Johnson, Q. Ge, S. Titmuss, and D. A. King. Unusual bridged site for adsorbed oxygen adatoms: Theory and experiment for Ir{100}-(1x2)-O. *Journal of Chemical Physics*, 112(23):10460–10466, 2000.

[9] C. I. Carlisle and D. A. King. Direct molecular imaging of NO monomers and dimers and a surface reaction on Ag{111}. *Journal of Physical Chemistry B*, 105(18):3886–3893, 2001.

[10] K. A. Briggman, J. C. Stephenson, W. E. Wallace, and L. J. Richter. Absolute molecular orientational distribution of the polystyrene surface. *Journal of Physical Chemistry B*, 105(14):2785–2791, 2001.

[11] T. Sakata, K. Hashimoto, and T. Kawai. Catalytic properties of ruthenium oxide on n-type semiconductors under illumination. *Journal of Physical Chemistry*, 88(22):5214–5221, 1984.

[12] D. N. Denzler, Ch. Hess, R. Dudek, S. Wagner, Ch. Frischkorn, M. Wolf, and G. Ertl. Interfacial structure of water on Ru(001) investigated by vibrational spectroscopy. *Chemical Physics Letters*, 376(5–6):618–624, 2003.

[13] H. Eyring. The Activated Complex in Chemical Reactions. *Journal of Chemical Physics*, 3:107, 1935.

[14] M. G. Evans and M. Polanyi. Some Applications of the Transition State Method to the Calculation of Reaction Velocities, Especially in Solution. *Transactions of the Faraday Society*, 31:875, 1935.

[15] R.G.W. Norrish and G. Porter. *Nature*, 164:658, 1949.

[16] M. Eigen and L. DeMaeyer. In A. Weissberger, editor, *Techniques of Organic Chemistry*, volume 8 Pt. 2. Wiley, 1963.

[17] M. Hentschel, R. Kienberger, Ch. Spielmann, G.A. Reider, N. Milosevic, T. Brabec, P. Corkum, U. Heinzmann, M. Drescher, and F. Krausz. Attosecond Metrology. *Nature*, 414:509–513, 2001.

[18] D.R. Herchbach. *Angewandte Chemie*, 26:1221, 1987.

[19] A. H. Zewail. *Femtochemistry: Ultrafast Dynamics of the Chemical Bond*. World Scientific Publishing, Singapore, 1994.

[20] A. H. Zewail. *Voyage Through Time: Walks of Life to the Nobel Prize*. American University in Cairo Press, 2002.

[21] M. Dantus, M.J. Rosker, and A. H. Zewail. Real-time Femtosecond Probing of “Transition States” in Chemical Reactions. *Journal of Chemical Physics*, 87(4):2395–2397, 1987.

[22] M. Gruebele, I. R. Sims, E. D. Potter, and A. H. Zewail. Femtosecond probing of bimolecular reactions: The collision complex. *Journal of Chemical Physics*, 95(10):7763–7766, 1991.

[23] A. H. Zewail. Femtochemistry: Recent progress in studies of dynamics and control of reactions and their transition states. *Journal of Physical Chemistry*, 100(31):12701–12724, 1996.

[24] Jonathan P.R. Symonds. *Femtochemistry: Recent Literature Concerning the Clocking of Bimolecular Reactions*. Undergraduate literature review, Cavendish Laboratory, University of Cambridge, 1998.

[25] A. H. Zewail. Femtochemistry: Past, Present and Future. *Pure Applied Chemistry*, 72(12):2219–2231, 2000.

[26] H. Gerischer. *Faraday Discussions of the Chemical Society*, 58:219, 1974.

[27] T.J. Chuang. Laser-induced gas-surface interactions. *Surface Science Reports*, 3(1):1–105, 1983.

[28] R. Cavanagh, D. S. King, J. C. Stephenson, and T. F. Heinz. Dynamics of Nonthermal Reactions - Femtosecond Surface Chemistry. *Journal of Physical Chemistry*, 97(4):786–798, 1993.

[29] W. S. Fann, R. Storz, H. W. K. Tom, and J. Bokor. Electron Thermalization in Gold. *Physical Review B*, 46(20):13592–13595, 1992.

[30] J. A. Prybyla, T. F. Heinz, J. A. Misewich, M. M. T. Loy, and J. H. Glownia. Desorption induced by femtosecond laser pulses. *Physical Review Letters*, 64(1537–1540), 1990.

[31] M. Bonn, S. Funk, C. Hess, D. N. Denzler, C. Stampfl, M. Scheffler, M. Wolf, and G. Ertl. Phonon- versus electron-mediated desorption and oxidation of CO on Ru(0001). *Science*, 285(5430):1042–1045, 1999.

[32] E. J. Heilweil, R. R. Cavanagh, and J. C. Stephenson. Picosecond Study of the Population Lifetime of CO ($v = 1$) Chemisorbed on SiO_2-Supported Rhodium Particles. *Journal of Chemical Physics*, 89(8):5342–5343, 1988.

[33] J. D. Beckerle, M. P. Casassa, R. R. Cavanagh, E. J. Heilweil, and J. C. Stephenson. Time Resolved Studies of Vibrational-Relaxation Dynamics of CO ($v = 1$) on Metal-Particle Surfaces. *Journal of Chemical Physics*, 90(8):4619–4620, 1989.

[34] J. D. Beckerle, M. P. Casassa, R. R. Cavanagh, E. J. Heilweil, and J. C. Stephenson. Ultrafast Infrared Response of Adsorbates on Metal-Surfaces — Vibrational Lifetime of CO/Pt(111). *Physical Review Letters*, 64(17):2090–2093, 1990.

[35] J. D. Beckerle, R. R. Cavanagh, M. P. Casassa, E. J. Heilweil, and J. C. Stephenson. Subpicosecond Transient Infrared-Spectroscopy of Adsorbates — Vibrational Dynamics of CO/Pt(111). *Journal of Chemical Physics*, 95(7):5403–5418, 1991.

[36] T. A. Germer, J. C. Stephenson, E. J. Heilweil, and R. R. Cavanagh. Picosecond Measurement of Substrate-to-Adsorbate Energy- Transfer — the Frustrated Translation of CO/Pt(111). *Journal of Chemical Physics*, 98(12):9986–9994, 1993.

[37] B. Bourguignon, F. Fournier, W. Zheng, S. Carrez, and H. Dubost. Time Resolved Ultrafast Energy Transfer from Photoexcited Electrons of Pt{111} to Adsorbed CO During Photodesorption. In *Femtochemistry VI Conference*, Paris, 2003.

[38] A. Bandara, S.S. Kano, K. Onda, S. Katano, J. Kubota, K. Domen, C. Hirose, and A. Wada. SFG Spectroscopy of CO/Ni{111}: UV Pumping and the Transient Hot Band Transition of Adsorbed CO. *Bulletin of the Chemical Society of Japan*, 75(5):1125–1132, 2002.

[39] Z. Chen, Y. R. Shen, and G. A. Somorjai. Studies of polymer surfaces by sum frequency generation vibrational spectroscopy. *Annual Review of Physical Chemistry*, 53:437–465, 2002.

[40] Ahmed Zewail. Personal Communication whilst visiting this department, 2002.

[41] G. Roberts. Femtosecond chemical reactions. *Philosophical Transactions of the Royal Society of London Series A — Mathematical, Physical and Engineering Sciences*, 358(1766):345–366, 2000.

[42] H. Arnolds, C. E. M. Rehbein, G. Roberts, R. J. Levis, and D. A. King. Femtosecond near-infrared laser desorption of multilayer benzene on Pt{111}: spatial origin of hyperthermal desorption. *Chemical Physics Letters*, 314(5-6):389–395, 1999.

[43] H. Arnolds, C. Rehbein, G. Roberts, R. J. Levis, and D. A. King. Femtosecond near-infrared laser desorption of multilayer benzene on Pt{111}: A molecular Newton's cradle? *Journal of Physical Chemistry B*, 104(14):3375–3382, 2000.

[44] Jonathan P.R. Symonds. *Femtosecond Spectroscopy at Metal Surfaces*. Certificate of postgraduate study, University of Cambridge, 2000.

[45] B.I. Bleaney and B. Bleaney. *Electricity and Magnetism*. Oxford University Press, 1st edition, 1957.

[46] Robert W. Boyd. *Nonlinear Optics*. Academic Press, San Diego, 2nd edition, 2003.

[47] Neil Greenham and David Richards. *Optoelectronics*. Cavendish Laboratory, University of Cambridge, Part III Physics Course, 1998.

[48] Y.R. Shen. *The Principles of Nonlinear Optics*. John Wiley and Sons, New York, 1984.

[49] M. Born and E. Wolf. *Principles of Optics*. Pergamon Press, Oxford, 1975.

[50] J.A. Giordmaine and R.C. Miller. Tunable Coherent Parametric Oscillation in $LiNbO_3$ at Optical Frequencies. *Physical Review Letters*, 14(24):973–976, 1965.

[51] Alex Lambert. PhD thesis, University of Cambridge, 2001.

[52] P. Guyot-Sionnest, J. H. Hunt, and Y. R. Shen. Sum-Frequency Vibrational Spectroscopy of a Langmuir Film — Study of Molecular-Orientation of a Two-Dimensional System. *Physical Review Letters*, 59(14):1597–1600, 1987.

[53] P. Galletto, H. Unterhalt, and G. Rupprechter. The molecular orientation of CO on Pd(111): a polarization- dependent SFG study. *Chemical Physics Letters*, 367(5-6):785–790, 2003.

[54] N. Bloembergen and P. S. Pershan. Light Waves at the Boundary of Nonlinear Media. *Physical Review*, 128(2):606–622, 1962.

[55] P. Guyot-Sionnest, R. Superfine, J. H. Hunt, and Y. R. Shen. Vibrational Spectroscopy of a Silane Monolayer at Air Solid and Liquid Solid Interfaces Using Sum-Frequency Generation. *Chemical Physics Letters*, 144(1):1–5, 1988.

[56] J. H. Hunt, P. Guyot-Sionnest, and Y. R. Shen. Observation of C-H Stretch Vibrations of Monolayers of Molecules: Optical Sum-Frequency Generation. *Chemical Physics Letters*, 133(3):189–192, 1987.

[57] A. Tadjeddine, A. Le Rille, O. Pluchery, F. Vidal, W. Q. Zheng, and A. Peremans. Sum and difference frequency generation at the electrochemical interface. *Physica Status Solidi A — Applied Research*, 175(1):89–107, 1999.

[58] L. T. Richter, T. P. Petralli-Mallow, and J. C. Stephenson. Vibrationally resolved sum-frequency generation with broad- bandwidth infrared pulses. *Optics Letters*, 23(20):1594–1596, 1998.

[59] S. Roke, A. W. Kleyn, and M. Bonn. Femtosecond Sum Frequency Generation at the Metal-Liquid Interface. *in preparation*, 2003.

[60] T. Mii and H. Ueba. Influence of pulse duration on time-resolved sum-frequency generation of surface vibrations. *Surface Science*, 428:324–330, 1999.

[61] A. Abragam. *Principles of Nuclear Magnetism*. Oxford University Press, 1978.

[62] T.S. Jones, S. Holloway, and J.W. Gadzuk. Theoretical Study of the Vibrational Lineshape for CO/Pt{111}. *Surface Science*, 184:L421–L430, 1987.

[63] L. Allen and J.H. Eberly. *Optical Resonance and Two-Level Atoms*. Dover, New York, 1987.

[64] P. Guyot-Sionnest. Coherent processes at surfaces: Free-induction decay and photon echo of the Si-H stretching vibration for H/Si(111). *Physical Review Letters*, 66:1489–1492, 1991.

[65] J. C. Owrutsky, J. P. Culver, M. Li, Y. R. Kim, M. J. Sarisky, M. S. Yeganeh, A. G. Yodh, and R. M. Hochstrasser. Femtosecond Coherent Transient Infrared-Spectroscopy of CO on Cu(111). *Journal of Chemical Physics*, 97(6):4421–4427, 1992.

[66] S. Roke, A. W. Kleyn, and M. Bonn. Time vs. frequency-domain femtosecond surface sum frequency generation. *Chemical Physics Letters*, 370(1-2):227–232, 2003.

[67] H. Ueba, T. Sawabu, and T. Mii. Coherent optical effect on time-resolved vibrational SFG spectrum of adsorbates. *Surface Science*, 502–503:254–260, 2002.

[68] C.D. Bain, P.B. Davies, T.H. Ong, R.N. Ward, and M.A. Brown. Quantitative Analysis of Monolayer Composition by Sum-Frequency Vibrational Spectroscopy. *Langmuir*, 7(8):1563–1566, 1991.

[69] M. van der Voort, C.W. Rella, L.F.G. van der Meer, A.V. Akimov, and J.I. Dijkhuis. Dynamics of Si-H Vibrations in an Amorphous Environment. *Physical Review Letters*, 84(6):1236–1239, 2002.

[70] P. F. Moulton. Spectroscopic and Laser Characteristics of Ti-Al_2O_3. *Journal of the Optical Society of America B — Optical Physics*, 3(1):125–133, 1986.

[71] Orizio Svelto. *Principles of Lasers*. Plenum, New York, 4th edition, 1998.

[72] J. D. Simon. Ultrashort Light-Pulses. *Review of Scientific Instruments*, 60(12):3597–3624, 1989.

[73] N. H. Schiller, M. Foresti, and R. R. Alfano. Picosecond Pulses Produced by Mode-Locking a Nd-Glass Laser with Kodak Dye-26. *Journal of the Optical Society of America B — Optical Physics*, 2(5):729–731, 1985.

[74] D. E. Spence, P. N. Kean, and W. Sibbett. 60 fs Pulse Generation from a Self-Mode-Locked Ti-Sapphire Laser. *Optics Letters*, 16(1):42–44, 1991.

[75] H. Kapteyn and M. Murnane. Ultrashort light pulses: life in the fast lane. *Physics World*, 12(1):31–35, 1999.

[76] W. Sibbett, R. S. Grant, and D. E. Spence. Broadly Tunable Femtosecond Solid-State Laser Sources. *Applied Physics B — Lasers and Optics*, 58(3):171–181, 1994.

[77] D. E. Spence and W. Sibbett. Femtosecond Pulse Generation by a Dispersion-Compensated, Coupled-Cavity, Mode-Locked Ti-Sapphire

Laser. *Journal of the Optical Society of America B-Optical Physics*, 8(10):2053–2069, 1991.

[78] http://www.spectraphysics.com/.

[79] J.E. Geusic, H.M. Marcos, and L.G. Van Uitert. Laser Oscillations in Nd-doped Yttrium Aluminium, Yttrium Gallium and Gadolinium Garnets. *Applied Physics Letters*, 4:182–183, 1964.

[80] P. Maine, D. Strickland, P. Bado, M. Pessot, and G. Mourou. Generation of Ultrahigh Peak Power Pulses by Chirped Pulse Amplification. *IEEE Journal of Quantum Electronics*, 24(2):398–403, 1988.

[81] http://www.lightcon.com/.

[82] R. Danielius, A. Piskarskas, D. Podenas, P. Ditrapani, A. Varanavicius, and G. P. Banfi. High-Power, Subpicosecond, 750-1770 nm Tunable Pulses from Travelling-Wave Parametric Generator. *Optics Communications*, 87(1-2):23–27, 1992.

[83] P. Ditrapani, A. Andreoni, D. Podenas, R. Danielius, and A. Piskarskas. Ultrashort Pulses of High-Power and Spectral Quality Tunable between 1.6 and 4.8 μm. *Optics Communications*, 118(3-4):338–344, 1995.

[84] O. E. Martinez. 3000 Times Grating Compressor with Positive Group-Velocity Dispersion — Application to Fiber Compensation in 1.3-1.6 μm Region. *IEEE Journal of Quantum Electronics*, 23(1):59–64, 1987.

[85] J. Ahner, D. Mocuta, R.D. Ramsier, and J.T. Yates. Adsorbate-adsorbate repulsions — the coverage dependence of the adsorption structure of CO on Cu(110) as studied by electron-stimulated desorption ion angular distribution. *Journal of Chemical Physics*, 105(15):6553–6559, 1996.

[86] John T. Yates Jr. *Experimental Innovations in Surface Science*. Springer-Verlag, New York, 1997.

[87] Fiona Scholes. *Far-Infrared Emission Spectroscopy of C_6D_6 and CO on Pt(111) and Pt(110)*. PhD thesis, University of Cambridge, 2001.

[88] Gary Attard and Colin Barnes. *Surfaces*. Oxford Chemistry Primers. Oxford University Press, New York, 1998.

[89] Carol L. Hedberg. *Handbook of Auger Electron Spectroscopy*. Physical Electronics Inc., Minnesota, 3rd edition, 1995.

[90] A. Peremans, A. Tadjeddine, P. Guyot-Sionnest, R. Prazeres, F. Glotin, D. Jaroszynski, J. M. Berset, and J. M. Ortega. Adsorbate Vibrational Spectroscopy by IR Visible Sum-Frequency Generation Using Clio-Fel — CO from CH_3OH Electrochemical Decomposition on Pt. *Nuclear Instruments & Methods in Physics Research Section A — Accelerators Spectrometers Detectors and Associated Equipment*, 341(1-3):146–151, 1994.

[91] H. Arnolds, J.P.R. Symonds, V.L. Zhang, and D.A. King. In-situ characterisation of ultrafast laser pulses for sum frequency surface studies. *Review of Scientific Instruments*, 74(9):3943–3946, 2003.

[92] Rick Trebino. *Frequency Resolved Optical Gating: The Measurement of Ultrashort Laser Pulses*. Kluwer Academic Publishers, Norwell, MA, 2000.

[93] Rick Trebino, Patrick O'Shea, Mark Kimmel, and Xun Gu. Measuring Ultrashort Pulses Just Got a Lot Easier. *Optics and Photonics News*, pages 22–25, June 2001.

[94] P. O'Shea, M. Kimmel, X. Gu, and R. Trebino. Highly simplified device for ultrashort-pulse measurement. *Optics Letters*, 26(12):932–934, 2001.

[95] M. Bonn, C. Hess, and M. Wolf. The dynamics of vibrational excitations on surfaces: CO on Ru(001). *Journal of Chemical Physics*, 115(16):7725–7735, 2001.

[96] H. W. K. Tom, C. M. Mate, X. D. Zhu, J. E. Crowell, T. F. Heinz, G. A. Somorjai, and Y. R. Shen. Surface Studies by Optical 2nd-Harmonic Generation - the Adsorption of O_2, CO, and Sodium on the Rh(111) Surface. *Physical Review Letters*, 52(5):348–351, 1984.

[97] C. Schwab, G. Meister, A. Goldmann, and E. Bertel. Second-harmonic generation from Na-covered Cu(110): intensity enhancement by inter-surface-state transitions? *Surface Science*, 469(2-3):93–104, 2000.

[98] A. Liebsch. Theory of sum frequency generation from metal surfaces. *Applied Physics B — Lasers and Optics*, 68(3):301–304, 1999.

[99] G. Chiarello, A. Cupolillo, A. Amoddeo, L. S. Caputi, L. Papagno, and E. Colavita. Collective excitations of two layers of K on Ni(111). *Physical Review B*, 55(3):1376–1379, 1997.

[100] M. Simon, F. Träger, A. Assion, B. Lang, S. Voll, and G. Gerber. Femtosecond time-resolved second-harmonic generation at the surface of alkali metal clusters. *Chemical Physics Letters*, 296(5-6):579–584, 1998.

[101] J.C. Campuzano. The Adsorption of Carbon Monoxide by The Transition Metals. In D.A. King and D.P. Woodruff, editors, *The Chemical Physics of Solid Surfaces and Hetrogeneous Catalysis*, pages 389–469. Elsevier, 1990.

[102] H.P. Bonzel and T.E. Fischer. An UV photoemission study of NO and CO adsorption on Pt {100} and Ru$\{10\bar{1}0\}$ surfaces. *Surface Science*, 51(1):213–227, 1975.

[103] R. Ku, N.A. Gjostein, and H.P. Bonzel. Adsorption of NO and CO on a Ru$\{10\bar{1}0\}$ surface. *Surface Science*, 64:465–483, 1977.

[104] M. Kiskinova. Interactions of CO and Sodium Coadsorbed on Ru$\{10\bar{1}0\}$. *Surface Science*, 182(1-2):150–160, 1987.

[105] M. Kiskinova and M. Tikhov. Adsorption of CO on Ru$\{10\bar{1}0\}$ Doped with Different Amounts of K and Cs. *Surface Science*, 194(3):379–396, 1988.

[106] G. Lauth, T. Solomun, W. Hirschwald, and K. Christmann. The Interaction of Carbon-Monoxide with a Ruthenium $\{10\bar{1}0\}$ Surface. *Surface Science*, 210(1-2):201–224, 1989.

[107] G. Rotaris, A. Baraldi, G. Comelli, M. Kiskinova, and R. Rosei. Carbon monoxide adsorbed on Ru$\{10\bar{1}0\}$. *Surface Science*, 359(1-3):1–9, 1996.

[108] K. Harrison, R. M. Lambert, and R. H. Prince. Structure and Energetics of Potassium Overlayers on Ruthenium $\{10\bar{1}0\}$. *Surface Science*, 176(3):530–546, 1986.

[109] Klaus Christmann. Freie Universität Berlin, Personal Communication, 2002.

[110] K.J. Schmidt. PhD thesis, Freie Universität Berlin, 2002.

[111] Mintcho Tikhov. Dept. of Chemistry, Cambridge, Personal Communication, 2001.

[112] R. G. Musket, W. McLean, C. A. Colmenares, D. M. Makowiecki, and W. J. Siekhaus. Preparation of Atomically Clean Surfaces of Selected Elements — a Review. *Applied Surface Science*, 10(2):143–207, 1982.

[113] Heike Arnolds. *Fourier-Transform NMR of ^{6}Li/Ru(001)*. PhD thesis, Philipps-Universität, Marburg, 1996.

[114] Christian Hess. *Ultraschnelle Reaktionsdynamik und Schwingungsspektroskopie an Oberflächen*. PhD thesis, Freie Universität Berlin, 2001.

[115] M. Bonn, C. Hess, and M. Wolf. The dynamics of vibrational excitations on surfaces: CO on Ru(001). *Journal of Chemical Physics*, 115(16):7725–7735, 2001.

[116] A. Tokmakoff, D. Zimdars, B. Sauter, R. S. Francis, A. S. Kwok, and M. D. Fayer. Vibrational Photon-Echoes in a Liquid and Glass — Room Temperature to 10 K. *Journal of Chemical Physics*, 101(2):1741–1744, 1994.

[117] A. Tokmakoff, B. Sauter, A. S. Kwok, and M. D. Fayer. Phonon-Induced Scattering between Vibrations and Multiphoton Vibrational up-Pumping in Liquid Solution. *Chemical Physics Letters*, 221(5-6):412–418, 1994.

[118] A. B. McLean, C. E. J. Mitchell, and D. M. Swanston. Implementation of an Efficient Analytical Approximation to the Voigt Function for Photoemission Lineshape Analysis. *Journal of Electron Spectroscopy and Related Phenomena*, 69(2):125–132, 1994.

[119] A. Crossley and D.A. King. Infrared spectra for CO isotopes chemisorbed on Pt{111}: Evidence for strong adsorbate coupling interactions. *Surface Science*, 68:528–538, 1977.

[120] P. Jakob. Dynamics of the C-O stretch overtone vibration of CO/Ru(001). *Physical Review Letters*, 77(20):4229–4232, 1996.

[121] R.M. Hammaker, S.A. Francis, and R.P. Eischens. Infrared study of intermolecular interactions for carbon monoxide chemisorbed on platinum. *Spectrochimica Acta*, 21:1295–1309, 1965.

[122] G.D. Mahan and A.A. Lucas. Collective vibrational modes of CO. *Journal of Chemical Physics*, 68(4):1344–1348, 1978.

[123] M. Scheffler. The influence of lateral interactions of the vibrational spectrum of adsorbed CO. *Surface Science*, 81:562–570, 1979.

[124] B. G. Briner, M. Doering, H. P. Rust, and A. M. Bradshaw. Microscopic molecular diffusion enhanced by adsorbate interactions. *Science*, 278(5336):257–260, 1997.

[125] B. N. J. Persson and F. M. Hoffmann. Vibrational Phase Relaxation at Surfaces — the Role of Lateral Interaction. *Journal of Electron Spectroscopy and Related Phenomena*, 45:215–225, 1987.

[126] B. N. J. Persson and R. Ryberg. Dipole-Coupling-Induced Line Narrowing in Adsorbate Vibrational Spectroscopy. *Chemical Physics Letters*, 174(5):443–448, 1990.

[127] C. Hess, M. Bonn, S. Funk, and M. Wolf. Hot-band excitation of CO chemisorbed on Ru(001) studied with broadband-IR sum-frequency generation. *Chemical Physics Letters*, 327(5-6):448–448, 2000.

[128] C. Hess, M. Wolf, and M. Bonn. Direct observation of vibrational energy delocalization on surfaces: CO on Ru(001). *Physical Review Letters*, 85(20):4341–4344, 2000.

[129] M. H. Cho, C. Hess, and M. Bonn. Lateral interactions between adsorbed molecules: Investigations of CO on Ru(001) using nonlinear surface vibrational spectroscopies. *Physical Review B*, 65(20):205423, 2002.

[130] C. Hess, M. Wolf, S. Roke, and M. Bonn. Femtosecond time-resolved vibrational SFG spectroscopy of CO/Ru(001). *Surface Science*, 502:304–312, 2002.

[131] C. Hess, M. Cho, and M. Bonn. Doubly vibrationally resonant spectroscopy of CO on Ru(001). *Surface Science*, 502:123–128, 2002.

[132] P. Jakob and B. N. J. Persson. Infrared spectroscopy of overtones and combination bands. *Journal of Chemical Physics*, 109(19):8641–8651, 1998.

[133] P. Jakob and B. N. J. Persson. Dephasing of localized and delocalized vibrational modes: CO adsorbed on Ru(001). *Physical Review B*, 56(16):10644–10650, 1997.

[134] J. Braun, K. L. Kostov, G. Witte, and Ch. Wöll. CO overlayers on Ru(0001) studied by helium atom scattering: Structure, dynamics, and the influence of coadsorbed H and O. *Journal of Chemical Physics*, 106(19):8262–8273, 1996.

[135] H. Ueba. Vibrational Relaxation and Pump-Probe Spectroscopies of Adsorbates on Solid Surfaces. *Progress in Surface Science*, 55(2):115–179, 1997.

[136] A.L. Harris and L. Rothberg. Surface vibrational energy relaxation by sum frequency generation: Five-wave mixing and coherent transients. *Journal of Chemical Physics*, 94(4):2449, 1991.

[137] P. Guyot-Sionnest, P. Dumas, Y. J. Chabal, and G. S. Higashi. Lifetime of an Adsorbate-Substrate Vibration — H on Si(111). *Physical Review Letters*, 64(18):2156–2159, 1990.

[138] M. Morin, N.J. Levinos, and A.L. Harris. Vibrational energy transfer of CO/Cu(100): Nonadiabatic vibration/electron coupling. *Journal of Chemical Physics*, 96(5):3950, 1992.

[139] A.L. Harris, L. Rothberg, L. Dhar, N.J. Levinos, and L.H. Dubois. Vibrational energy relaxation of a polyatomic adsorbate on a metal surface: Methyl thiolate (CH_3S) on Ag(111). *Journal of Chemical Physics*, 94(4):2438, 1991.

[140] C.A. Walsh, M. Berg, L.R. Narashimham, and M. D. Fayer. Probing Intermolecular Interactions with Picosecond Photon Echo Experiments. *Accounts of Chemical Research*, 20:120, 1987.

[141] E.L. Hahn. Spin Echoes. *Physical Review*, 80:580–594, 1950.

[142] N.A. Kurnit, I.D. Abella, and S.R. Hartmann. Observation of a Photon Echo. *Physical Review Letters*, 13:567–568, 1964.

[143] S.I. Anisimov, B.L. Kapeliovich, and T.L. Perel'man. *Soviet Physics JETP*, 39:375, 1974.

[144] Stephan Funk. *Ultraschnelle Reaktionsdynamik an Oberflächen: Desorption und Oxidation von CO auf Ru(001) induziert durch Femtosekunden-Laserpulse*. PhD thesis, Freie Universität Berlin, 1999.

[145] Catalogue of Goodfellow Ltd., metal supplier.

[146] H. Arnolds and D.A. King. Femtosecond laser-induced reactions with O_2 on Pt{111}, to be submitted. *Surface Science Letters*, 2003.

[147] B. Bourguignon. Personal communication at the Surface Photochemistry conference, Les Houches, France, 2002.

[148] At the Royal Society's *Summer Science Exhibition*, exhibit name *Seeing is Believing*, July 2003.

[149] R. van Os. *Negative Ion Sourcery*. PhD thesis, Institute for Atomic and Molecular Physics, Amsterdam, 1989.

[150] P.R. Antoniewicz. Model for electron- and photon-stimulated desorption. *Physical Review B*, 21:3811–3815, 1980.

[151] http://www.gnu.org/software/gsl/gsl.html.

Endpiece

This thesis was typeset using LaTeX under Mac OS X and Sun Solaris. Data analysis and presentation were performed using Wavemetrics Igor Pro. Diagrams were prepared using Dia, Adobe Illustrator, the GIMP and xFig. Optical path simulation was done using Sarkomand Software's CyberRay. Program listings in the appendices were prepared with Lgrind.

The novel technique described in chapter 4 for in-situ laser characterisation is at the time of writing very soon to be published in the *Review of Scientific Instruments* [91]. The work on CO/Ru$\{10\bar{1}0\}$ from chapter 5 was presented by the author at the *Time Resolved Vibrational Spectroscopy* conference in Italy, May 2003. The work from chapters 5 and 6 is also being prepared for publication.